Continuous production of carbon nanotube-grafted fibres: A route to manufacture hierarchical composites

Doctoral Thesis

By Hugo Gilles De Luca

A thesis submitted in fulfilment of the requirements for the degree of Doctor of Philosophy and the Diploma of Imperial College London

Department of Materials
Imperial College London
London, SW7 2AZ, UK

Supervisors:

Prof. Milo S. P. Shaffer
Prof. Alexander Bismarck

March 2021

Declaration of Authorship

I hereby declare that the work presented in this thesis is entirely my own, except where specific reference has been made. The work presented was carried out in its entirety in Imperial College London using facilities provided by the Department of Materials, Chemistry, Chemical Engineering and Aeronautics. This work has not been previously submitted for the reward of a degree course at this institute, nor any other university.

Hugo Gilles De Luca

March 2021

The copyright of this thesis rests with the author and is made available under a Creative Commons Attribution Non-Commercial No Derivatives licence. Researchers are free to copy, distribute or transmit the thesis on the condition that they attribute it, that they do not use it for commercial purposes and that they do not alter, transform or build upon it. For any reuse or redistribution, researchers must make clear to others the licence terms of this work.

Abstract

The mechanical performance of structural composites depends strongly on the interface between the reinforcing fibres and the surrounding matrix. Nanoengineering this interface with carbon nanotubes (CNTs) improves its strength and toughness, yet has proved difficult to scale. Typically, the CNT coverage is heterogeneous, poorly oriented, or has an inappropriate thickness, whilst the grafting process degrades the properties of parent fibres. This thesis focuses on the development of a new process to produce CNT-grafted structural fibres continuously (1 to 5 $m.h^{-1}$), reel-to-reel, on whole tows in an open chemical vapour deposition (CVD) reactor. The process operates on both carbon (AS4) and quartz (Quartzel) fibres, following a continuous bi-catalyst precursor deposition step. The CNT coating coverage and thickness was optimised, following an in-depth investigation of a range of process variables, including reactive gas composition, catalyst reduction and growth duration, growth temperature and line speed.

The thickness of the CNT layer is a crucial factor; in the literature, most CNT layers are so long (compared to the primary fibre diameter) that the overall fibre volume is reduced. Here, the goal was to grow CNTs with lengths around a few hundred nanometres, to reinforce the interface without increasing the primary fibre separation. In the case of the quartz fibres, morphology improvement through fine-tuning of the catalyst deposition and CVD process variables produced a uniform CNT coating around 200 nm, throughout the fibre tow. Using single fibre pull-out tests, the coating was found to increase the interfacial shear strength (IFSS) with an archetypical epoxy to 90.3 ± 2.1 MPa (+12%) compared to commercially-sized quartz fibres. Percolation through the coating, predominantly parallel to the fibres, provided a high electrical conductivity (2.7 ± 0.3 S m^{1}) to the otherwise insulating quartz fibre composites. This conductive path displayed a piezoresistive response that allowed monitoring of both elastic strain and the onset of fibre breakage/debonding. The ability to detect the accumulation of damage was validated by comparison to simultaneous acoustic emission measurements collected during mechanical testing.

Grafting CNTs on carbon fibres is particularly challenging, as the catalyst for CNT growth intrinsically dissolves carbon and can accelerate gasification reactions; catalyst pitting is, therefore, common and typically reduces the underlying fibre mechanical properties. The application of an in-situ potential difference (300 V), between the fibres and a cylindrical graphite foil counter electrode, however, enhances the growth and significantly reduces damage to the parent fibres. The properties of the fibres were evaluated by bundle composite tensile tests. Uniform growth of small diameter ca. 10 nm and 300 nm long CNTs was found to improve the IFSS with epoxy to 96.7 MPa (+7.5%), compared to that of as-received carbon fibres. Interestingly, the interfacial strength improved further to 100.2 MPa

when combined with an epoxy system reinforced with 1 wt.% CNT. This synergistic effect between the nanoengineered epoxy and the nanoengineered carbon fibres was attributed to simultaneous reinforcement of both the interphase and the surrounding matrix. The interfacial improvements measured at the microscale, by single fibre tests, were investigated at the macroscale with the manufacture of short beam shear testing coupons. Continuous, reel-to-reel, CVD is a practical and scalable route to produce hierarchical fibre feedstocks in large quantities. It provides a path towards the manufacture of large multifunctional composites for commercial applications.

Acknowledgments

This past year has been quite challenging. Not only for me but for the people that took out of their time to help me. Having lived the lockdown life for close to a year now, deprived of most non-virtual social interactions, hence taking a toll on my mental health. I am really grateful to be surrounded by such loving people, including my parents who helped me see that there might be a bright future ahead despite the uncertainty associated with this never-ending pandemic.

I would first like to thank my main supervisor, Prof. Milo Shaffer, that helped me see this through, with weekly meetings, countless suggestions and words of encouragement. Thanks for the support you have kindly offered me during this difficult time. Thanks to Dr. David Anthony, for sharing his expertise on composite materials and the countless hours spent either discussing CNT-synthesis, reviewing technical drawings, scolding me for not buying any coffee beans for the office or just generally sharing a good time around a milky stout or two. I would also like to thank Prof. Alexander Bismarck for his help, often with equipment in the laboratory or through a late-night call for a paper submission. I cannot forget here Prof. Emile Greenhalgh for the guidance and support throughout this project with weekly group meetings and discussions on the fracture mechanisms of composite materials.

I would like to acknowledge the ministry of defence of Singapore (MINDEF), along with the Lloyd's Register Foundation (LRF) for the financial support of this work and the International Consortium of Nanotechnologies (ICON) for allowing me to join a worldwide network of experts in the field of nanotechnology.

Many thanks to the current and ex-members of the Nanostructured Hierarchical composites and Assemblies (NanoHAC) group, including Dr. Chris Roberts, Dr. David Buckley, Dr. Noelia Rubio Carrera, Mr. Tommaso Costantini, Mr. David Stringer for sharing their expertise on various characterisation techniques, helping with setting-up experiments, and the quality memes they shared. I'd also like to thank all members of the Polymer and Composite Engineering (PaCE) group in Vienna for organising our yearly symposium reunion. I would like to extend my sincere thanks to the Imperial College London's Chemical Engineering Workshop and in particular Mr. Jonathon Henton and Mr Richard Wallington for the fabrication of the composite moulds. Last but not least, my partner, Amanda Chan, for her encouragements and emotional support. I hope we will be reunited soon.

List of publications

Journal paper (Co-author): J. Wang, D.B. Anthony, C.A. Fuentes, H.G. De Luca, D. Zhang, A. Bismarck, A.W. Van Vuure, M.S.P. Shaffer, D. Seveno. Wettability of carbon nanotube-grafted carbon fibers and their interfacial properties in polypropylene thermoplastic composite. *Submitted*, *Composites Science and Technology*, 2021.

Journal paper (1st author): H.G. De Luca, D.B. Anthony, E.S. Greenhalgh, A. Bismarck, M.S.P. Shaffer. Piezoresistive structural composites reinforced by carbon nanotube-grafted quartz fibres. *Composites Science and Technology*, 198, 2020. DOI: 10.1016/j.compscitech.2020.108275.

Journal paper (Co-first author): B. Liu, C. Liu, H.G. De Luca, S.K. Raman Pilai, D.B. Anthony, J. Li, A. Bismarck, M.S.P. Shaffer, M.B. Chan-Park. Synthesis of epoxidized poly(ester carbonate)-b-polyimide-b-poly(ester carbonate): reactive single-walled carbon nanotube dispersants enable synergistic reinforcement around multi-walled nanotube-grafted carbon fibers. *Polymer Chemistry*, 10:1324-1334, 2019. DOI: 10.1039/C8PY01465E.

Journal paper (Co-author): D.B. Anthony, X. Sui, I. Kellersztein, H.G. De Luca, E.R. White, H.D. Wagner, E.S. Greenhalgh, A. Bismarck, M.S.P. Shaffer. Continuous carbon nanotube synthesis on charged carbon fibers. *Composite Part A: Applied Science and Manufacturing*, 112:525-538, 2018. DOI: 10.1016/j.compositesa.2018.05.027.

Journal paper (Co-author): F. De Luca, A. Clancy, N. Rubio Carrero, D.B. Anthony, H.G De Luca, M.S.P. Shaffer. Increasing carbon fiber composite strength with a nanostructured “brick-and-mortar” interphase. *Materials Horizons*, 5:668-674, 2018. DOI: 10.1039/C7MH00917H.

List of conferences

Oral presentation: H.G. De Luca, D.B. Anthony, E.S. Greenhalgh, A. Bismarck, M.S.P. Shaffer. Continuous Production of CNT-grafted Carbon Fibres: A Route to Manufacture Hierarchical Composites. *CNPComp2019 - 8th International Conference on Carbon NanoParticle based Composites*, Queen Mary University of London, United Kingdom, 2019.

Oral presentation: H.G. De Luca, D.B. Anthony, E.S. Greenhalgh, A. Bismarck, M.B. Chan-Park, M.S.P. Shaffer. Continuous production of carbon nanotube-grafted fibres: A route to manufacture hierarchical composites. *2018 MRS Fall Meeting & Exhibit*, Boston, MA, United States, 2018.

Poster presentation: H.G. De Luca, D.B. Anthony, A. Bismarck, M.S.P. Shaffer, E.S. Greenhalgh. Hierarchical fibre reinforced nanocomposites: A novel production route. *Composite Research Showcase*, Imperial College London, United Kingdom, 2018.

Poster presentation: H.G. De Luca, D.B. Anthony, H. Qian, E.S. Greenhalgh, A. Bismarck, M.S.P. Shaffer. Hierarchical fibre reinforced nanocomposites for multifunctional improvements in safety. *Lloyd's Register Foundation International Conference*, London, United Kingdom, 2018.

Oral presentation: H.G. De Luca, D.B. Anthony, E.S. Greenhalgh, A. Bismarck, M.S.P. Shaffer. Continuous production of carbon nanotube-grafted quartz fibres: Effect of carbon nanotube length on fibre/matrix adhesion. *PPS2017 – Europe Africa Conference of the polymer processing society*, Dresden, Germany, 2017.

Paper and oral presentation: H.G. De Luca, D.B. Anthony, E.S. Greenhalgh, A. Bismarck, M.S.P. Shaffer. Continuous production of carbon nanotube-grafted quartz fibres: Effect of carbon nanotube length on fibre/matrix adhesion. *ICCM21 – 21st International Conference on Composite Materials*, Xi'an, China, 2017.

Poster presentation: H.G. De Luca, D.B. Anthony, H. Qian, E.S. Greenhalgh, A. Bismarck, M.S.P. Shaffer. Hierarchical fibre reinforced nanocomposites for multifunctional improvements in safety. *1st ICON Conference*, Athens, Greece, 2017.

Paper and poster presentation: H.G. De Luca, D.B. Anthony, H. Qian, E.S. Greenhalgh, A. Bismarck, M.S.P. Shaffer. Non-damaging and scalable carbon nanotube synthesis on carbon fibres. ECCM17 – 17th European Conference on Composite Materials, Munich, Germany, 2016.

Table of contents

Chapter 1 : Introduction 18

1.1. A brief history of hierarchical composites 18

1.2. Motivation and scope of work 19

Chapter 2 : Literature Review 21

2.1. Carbon nanotubes (CNTs) 22

2.1.1. Introduction to CNTs 22

2.1.2. Structure and properties of CNTs 23

2.1.3. Synthesis of CNTs 26

2.1.4. Growth mechanisms of CNTs 26

Common catalyst precursors 27

Substrates and catalyst particle formation 27

Active gases composition, growth accelerators and catalyst poisoning 29

2.2. Fibre-reinforced polymer composites (FRPs) 31

2.2.1. Introduction to FRPs 31

2.2.2. Carbon fibres 31

Common precursors, production and properties 31

Conventional surface treatments 33

2.2.3. Quartz fibres 34

Production and application 34

2.2.4. Role of the interface/interphase on the mechanical performance of FRPs 34

2.3. CNT-nanoengineered FRPs 38

2.3.1. Bulk resin reinforcement 40

2.3.2. Interlaminar reinforcement 43

2.3.3. Targeted reinforcement of the fibre/matrix interface 45

Fibre-matrix interfacial properties 48

Multifunctional interphases 59

2.3.4. Mechanical properties of CNT-nanoengineered FRPs 63

Chapter 3 : Materials and methods 73

3.1. Materials 74

3.1.1. Fibres 74

3.1.2. Carbon nanotubes 74

3.1.3. Catalyst precursors and gases 74

3.1.4. Matrices 75
3.2. Methods 75
3.2.1. Continuous deposition experimental set-up 75
3.2.1. Continuous CVD experimental set-up 78
3.2.2. Continuous CVD set-up equipment details 82
3.2.3. Continuous CVD synthesis method 83
3.3. Characterisation techniques 84
3.3.1. Scanning electron microscopy 84
3.3.2. Thermogravimetric analysis 85
3.3.3. Raman spectroscopy 85
3.3.4. Modified Wihelmy technique 85
3.3.5. Single fibre tensile test 86
3.3.6. Single fibre pull-out test 87
3.3.7. Bundle composite test with in-situ electrical conductivity and acoustic emission 89
3.3.8. Short beam shear test 92
Chapter 4 : Continuous synthesis of CNTs on quartz fibres 94
4.1. Growth of CNTs on quartz fibres 95
4.2. Characterisation of the CNT-grafted quartz fibres 97
4.2.1. Morphology of the CNT-grafted quartz fibres 97
4.2.2. CNT loading and quality 101
4.2.3. Single fibre mechanical and interfacial properties 103
4.3. Characterisation of CNT-grafted quartz fibres unidirectional composites 109
4.3.1. Piezoresistive response of unidirectional hierarchical composites 109
4.3.2. Mechanistic study using correlated acoustic emission data 114
4.4. Summary 118
Chapter 5 : Continuous synthesis of CNTs on carbon fibres 120
5.1. In-line continuous deposition of catalyst precursor on carbon fibres 121
5.1.1. Morphology of the carbon fibres 121
As-received carbon fibres 121
Plasma treated carbon fibres 122
5.1.2. Bi-catalyst precursors deposition on carbon fibres 123
5.1.3. Effect of bi-catalyst precursors composition on CNT synthesis 126
5.1.4. Effect of bi-catalyst precursors concentration on CNT synthesis 128
5.2. In-line CNT-synthesis via chemical vapour deposition 131

5.2.1. Continuous CVD parameter space 131
5.3. Refining the CVD parameter space for enhanced CNT synthesis 132
5.3.1. Effect of applied potential difference on CNT synthesis 132
5.3.2. Effect of the furnace temperature 135
5.3.3. Effect of active gases composition and flow rate 138
5.3.4. Effect of reduction and growth durations 140
Line-speed 141
5.4. Refined CVD conditions and repeatability 148
5.4.1. Morphology of the CNT-grafted carbon fibres 149
5.5. Summary 151
Chapter 6 : CNT-reinforced carbon fibre composites 152
6.1. Characterisation of carbon fibre/matrix interface 153
6.1.1. Interfacial shear strength of single fibre model composites 153
Polypropylene resin 153
Aerospace grade epoxy resin 154
6.2. Mechanical performance of carbon fibres 160
6.2.1. Tensile properties of unidirectional bundle composites 160
6.3. Characterisation of nano-reinforcements at the macroscale 162
6.3.1. Processing nano-reinforced short beam shear composites 162
6.3.2. Interlaminar shear strength of nano-reinforced short beam shear composites 166
First generation design 166
Second generation design 166
6.4. Summary 169
Chapter 7 : Conclusions and outlook 170
7.1. Summary of findings 170
Continuous bi-catalyst precursor deposition 170
Continuous CNT growth on quartz fibres 170
Continuous CNT growth on carbon fibres 171
7.2. Outlook 172
7.3. Future work 173

List of figures

Fig. 1.1 *Historical continuous CVD experimental set-up. Reproduced from [8].* *19*

Fig. 1.2 *CNT-nanoengineering composite approaches, including the CNT-grafted fibre approach developed in this work (left), CNT dispersion in epoxy investigated by collaborators in NTU (right) and the combination of both approaches (middle).* *20*

Fig. 2.1 *TEM images of (left) the first evidence for the tubular structure of nano-sized carbon filaments [10] and (right) multi-walled carbon nanotubes demonstrating the graphitic spacing (0.34 nm) between the nanotube walls. Reproduced from [11].* *23*

Fig. 2.2 *Schematic diagram of the 2D unit cell showing how a sheet of graphene is wrapped to form SWCNTs with different chirality (e.g. armchair and zig-zag) - reproduced from [21].* *24*

Fig. 2.3 *Fracture of a MWCNTs showing a "sword-in-sheath" failure mechanism. Reproduced from [27].* *25*

Fig. 2.4 *Schematic representation of the VLS mechanism, including the decomposition of the carbon-containing precursor on the surface of the catalyst particle, diffusion of carbon atoms through the particle as a solid solution, and precipitation of carbon and formation of a nanotube. Reproduced from [43].* *27*

Fig. 2.5 *Schematic representation of the growth mechanisms for CNTs, including (a) tip and (b) base growth. Reproduced from [51].* *28*

Fig. 2.6 *Schematic representation of nanoparticle formation and subsequent CNT growth on carbon-based substrates. Reproduced from [37].* *29*

Fig. 2.7 *C-H-O ternary diagram showing the successful active gases composition for the growth of CNTs in CVD processes. Reproduced from [54].* *30*

Fig. 2.8 *Schematic representation of a fibre-reinforced polymer composite (FRP). Reproduced from [57].* *31*

Fig. 2.9 *Schematic representation of the structure of a PAN-based carbon fibre. Reproduced from [59].* *32*

Fig. 2.10 *Schematic representation of the different microstructures in pitch carbon fibres. Reproduced from [60].* *32*

Fig. 2.11 *Schematic representation of the interphase formation characteristics in composite materials. Reproduced from [71].* *35*

Fig. 2.12 *Schematic representation of interphase formation for sized carbon fibres composites. (a) Graded interphase from the diffusion of sizing and matrix molecules, (b) distinct interphase due to poor compatibility of the sizing with epoxy and (c) magnified view of distinct interphase showing both chemisorption at the sizing/fibre interface and physisorption at the sizing/matrix interface. Reproduced from [65].* *36*

Fig. 2.13 *SEM micrographs of hierarchical structure examples present in nature as well as engineered: (a) osteons in equine metacarpal bone, (b) vascular bundles in bamboo, and (c) nano-engineered composite with CNT-grafted alumina fibres. Reproduced from [85].* *38*

Fig. 2.14 *Schematic representation of the length scales involved in nano-engineered FRPs. Adapted from [17].* *40*

Fig. 2.15 *SEM micrographs of CNT-nanocomposite fractured surfaces with (a, b) a soft epoxy resin showing CNT bridging and a ductile failure and (c, d) a stiffer epoxy resin showing a brittle failure and debonded CNTs suggesting poor interactions between the CNTs and the epoxy resin. Reproduced from [107].* *41*

Fig. 2.16 *Schematic illustration of fracture mechanisms in hierarchical FRPs with (a) homogeneously distributed CNTs and (b) engineered heterogeneities within the matrix. Adapted from [97].* *42*

Fig. 2.17 *Hierarchical nano-engineered composite architecture produced by the introduction of a CNT-rich layer at the interface between prepreg plies (also referred to as 'nanostiching'): (a) concept illustration of the nanostitched laminate interface. Representative SEM micrographs of: (b) conventional 90/45 FRP interface and (c) CNT-nanoengineered 90/45 FRPs interface showing CNTs filling the interlaminar region. Reproduced from [117].* *44*

Fig. 2.18 *CNT-grafted microfibers. (a) Radially aligned CNT growth with a 'mohawk' splayed configuration, (b) randomly oriented CNT growth, and (c) CNT-containing size. Simulated configurations (left column) and SEM micrographs of practically realizable configurations (right column). Reproduced from [1].* *45*

Fig. 2.19 *Schematic representation of six types of fracture mechanisms during pull-out of a CNT-grafted fibre from a resin block. From left to right, most to least efficient interfacial fracture mechanism.* *47*

Fig. 2.20 *Schematic representation of the idealised hexagonal close packing in FRPs for a fibre volume fraction of 60%. (a) FRP with fibre-fibre separation distance of B, (b) hierarchical FRP with radial CNTs from adjacent CNT-grafted fibres touching (CNT length = B/2), (c) hierarchical FRP with CNT nesting from adjacent CNT-grafted fibre (CNT length ≥ B). Reproduced from [3].* *48*

Fig. 2.21 *Schematic diagrams of proposed failure mechanisms for (a) single fibre pull-out and (b) single fibre push-out before and after grafting CNT on the fibre surface. Reproduced from [144].* *50*

Fig. 2.22 *Collated literature values of apparent interfacial shear strength determined from single fibre fragmentation tests (SFFT), microdroplet debond (MD-SFPO), single fibre pull-out (SFPO) and single fibre push-out (SF-PushOut) for CNT-g-CF obtained from (a) chemical vapour deposition, (b) electrophoretic deposition and (c) chemical grafting and/or sizing. Mean values for unsized/desized CF, Sized CF and CNT-g-CF (open -square, -circle and –diamond, respectively) with standard deviation (bracket) and minimum-maximum range (green-, violet- and red- rectangles) associated.* [1]*Data point obtained from the combination of CNT-g-CF with a SWCNT-reinforced epoxy system [4].* [2]*Outlier not included in the measurement of the mean. Values generated in this work (filled data points; orange and pink) with statistical difference indicated (asterisks).* *58*

Fig. 2.23 *Schematic representation illustrating the change in electrical resistance transmission mode after a crack progresses in the interphase. Reproduced from [193].* *60*

Fig. 2.24 *Piezoresistivity of MWCNT/epoxy sensor for different CNT loading, as compared to conventional resistance strain gauge (K = 2). Reproduced from [196].* *61*

Fig. 2.25 *Relationship between electrical conductivity and sensor sensitivity (gauge factor). Reproduced from [196].* *61*

Fig. 2.26 *(a) Digital image correlation contour plot of shear strain in a CFRP SBS specimen (side view). (b) Micrograph of a polished SBS specimen with 0/90 degree plies. Reproduced from [213].* *64*

Fig. 3.1 *Photographs of the continuous pre-catalyst deposition line set-up with close-ups on the (a) IR-furnaces, (b) in-lane plasma jet, (c) catalyst precursors deposition bath and (d) collection spool.* *77*

Fig. 3.2 *Photograph of the continuous reel-to-reel CVD set-up.* *78*

Fig. 3.3 *Schematic representation of the CVD line equipped with an open 3-zone tubular furnace consisting of internal quartz sections forming the inert (N_2), reductive (2.4 vol.% H_2 in N_2) and growth (1.3 vol.% C_2H_2 in N_2) gas sleeves. Location of the electrodes for the capacitor-like arrangement indicated.* *79*

Fig. 3.4 *Close-up schematic of the concentric quartz tubes which determine the reaction regions, with reactor gas inlet/outlets highlighted. Reproduced from [3]. Graphite foil counter-electrode not included.* *79*

Fig. 3.5 *(a) 3D representation of the co-axial capacitor arrangement inside the reactor (inner tube right, as defined in Fig. 3.4) including the connection made to graphite foil with stainless steel wire (b) Circuit diagram, the inclusion of the switch is to ensure complete discharge from the set-up at the end of the experiment.* *80*

Fig. 3.6 *Schematic of (a) the catalyst precursor deposition line with collection of the bi-catalyst decorated quartz fibres (after drying in infrared radiation (IR) furnaces) on the right-hand side reel; (b) The bi-catalyst deposited quartz fibres are introduced in the continuous chemical vapour deposition set-up for CNT-synthesis.* *81*

Fig. 3.7 *Schematic representation of the daisy-chained bi-catalyst precursors deposited carbon fibres. The red crosses indicate the location of the Zepellin bend knots joining the one meter long carbon fibre sections together.* *84*

Fig. 3.8 *Representation of the modified Wihelmy set-up with five carbon fibres fixed onto a hanger connected to a balance.* *86*

Fig. 3.9 *Single fibre tensile (a) 25 mm gauge specimen and (b) testing unit with 20 N loading cell.* *87*

Fig. 3.10 *Single fibre pull-out rig with (a, b) fibre embedding kit including a built-in heating stage for pre-curing the epoxy bead and (c, d) single fibre pull-out testing unit with force sensor and piezo-translator. 88*

Fig. 3.11 *Schematic representation of the single fibre pull-out test equipment with a close-up view of the microscale carbon fibre debonding. 89*

Fig. 3.12 *photographs of the unidirectional bundle composite mould, (a) without and (b) with the lid on. 90*

Fig. 3.13 *Photograph of the bundle composite tensile test set-up with in-situ AE and electrical conductivity measurement. The video gauge camera and associated software records the pixel displacement from two painted marks on the sample surface. The sample is illuminated using a light source to ensure a suitable contrast for the video gauge software to track the points accurately. The force and displacement outputs from the Instron were also recorded in-situ with the strain measurements to ensure simultaneous data acquisition via an analogue to digital converter. In conjunction with these recordings acoustic emission events were detected though sensors placed on the sample's surface and processed by the AE chassis and associated software. Similarly, a fixed voltage was applied to the sample, in the loading direction, and the current recorded using a potentiostat to evaluate strain-dependent resistivity. 91*

Fig. 3.14 *Photograph of a hierarchical bundle composite under tensile loading (in the enclosure) with in-situ electrical conductivity and AE detection. AE sensors were clamped to the specimen using purpose-built aluminum jigs. Painted marks for the video gauge tracking were made close to the clamps situated at each end of the sample. 92*

Fig. 3.15 *Short Beam Shear testing requirements as specified by ASTM D2344 [256]. 93*

Fig. 3.16 *Short beam shear testing set-up with a span-length of 8 mm, loading nose of 6 mm and supports diameter of 3 mm. 93*

Fig. 4.1 *Effect of different bi-catalyst precursor stoichiometry on the growth of CNTs on quartz fibres with (a) $NiFe_2$, (b) NiFe and (c) Ni_2Fe. 96*

Fig. 4.2 *SEM micrographs of (a) as-received sized, (b) heat-treated (thermally desized) and (c) bi-catalyst decorated quartz fibres 97*

Fig. 4.3 *Photograph of quartz fibres tow sections (two meter long) after different chemical and/or thermal treatment conditions (left to right: as-received, heat-treated, bi-catalyst decorated, short CNT grafted, long CNT grafted). The catalyst precursor deposition was performed on as-received sized quartz fibres. 98*

Fig. 4.4 *SEM micrographs of the hierarchical fibres produced with (a, b, c) a short and uniform CNT coverage, namely CNT-g-QF (S) and (d, e, f) long "mohawk" CNT arrays, referred to as CNT-g-QF (L). Arrows correspond to the scalpel cutting locations and directions, both scale bars in the inserts (c) are 200 nm. 99*

Fig. 4.5 *High-magnification SEM micrographs of (a) CNT-g-QF (S) and (b) CNT-g-QF (L). The shorter CNTs can only be easily viewed 'end on', whilst the Mohawk arrangement of the longer CNTs facilitates a transverse view. 100*

Fig. 4.6 *TGA curves of as-received sized, heat-treated (thermally desized), bi-catalyst decorated and CNT-grafted quartz fibres with different growth duration; 12 min (S) and 24 min (L), respectively. 101*

Fig. 4.7 *Raman spectra for (a) as-received sized, heat-treated (thermally desized) and bi-catalyst decorated quartz fibres. ❖ Baseline for QF-HT was not subtracted due to the absence of modes resulting in significant noise. Raman spectra normalised to the G-peak for (b) CNT-g-QF (S) and CNT-g-QF (L), corresponding to a residence time in the furnace hot-zone of 15 min and 30 min, respectively. 2D-mode (2700 cm^{-1}), G-mode (1582 cm^{-1}) and D-mode (1350 cm^{-1}) and corresponding I_G to I_D ratio are included. 102*

Fig. 4.8 *Apparent interfacial shear strength obtained from single fibre pull-out tests (top) and typical single fibre pull-out test curves for heat-treated and short CNT-grafted quartz fibres (bottom). The green area corresponds to the debonding region where the fibre/epoxy interface has not yet failed; the blue area highlights the extraction region. 103*

Fig. 4.9 *Collated single fibre pull-out data including linear fits. The slope of the fits corresponds to the apparent IFSS tabulated in* ***Table 4.1****. 105*

Fig. 4.10 *SEM micrographs of fracture surfaces after pull-out from cured epoxy droplets with corresponding Raman spectra normalised to the G-peak for (a, b) CNT-g-QF (S) and (c, d) CNT-g-QF (L), respectively. Red arrows indicate the location of CNTs whilst blue arrows show epoxy-CNTs agglomerates. 107*

Fig. 4.11 *Raman spectra normalised to the G-peak of (a) CNT-g-QF (S) and (b) CNT-g-QF (L) after single fibre pull-out, away from the fracture surfaces with D-mode (1350 cm^{-1}), G-mode (1582 cm^{-1}) and 2D-mode (2700 cm^{-1}).* *107*

Fig. 4.12 *Tensile properties of as-received quartz fibres before and after all thermal and/or chemical treatments, measured through single fibre tensile tests with a gauge length of 25 mm. Error bars correspond to standard error. A minimum of 13 specimens were tested per data set.* *108*

Fig. 4.13 *(a) Representative stress-strain curve with real-time electrical conductivity measurements for CNT-g-QF (S). (b) Influence of CNT loading in composites on electrical conductivity for CNT-g-QF (S) (open squares) and CNT-g-QF (L) (open triangles) bundles both in the fibre direction (longitudinal). For comparison, various CNT/epoxy systems (filled circle) [98] and CNT/epoxy glass fibre composites (filled diamond) [106, 200, 264-266]. The typical CNT weight fraction upper limit for CNT/epoxy viable incorporation in composites (dashed vertical line) is included for reference. (c) Collated electrical conductivity for all CNT-g-QF (S) and CNT-g-QF (L) bundles. (d) Resistance variation $\Delta R/R_0$ for all hierarchical bundle composites; (dashed horizontal line) corresponds to a break in the ordinate with the upper part plotted on a logarithmic scale, for clarity.* *111*

Fig. 4.14 *Ex-situ electrical conductivity of the UD hierarchical bundle composites (longitudinal and transverse directions in relation to the loading direction) with standard error associated.* *112*

Fig. 4.15 *A 3D model of a quartz fibre with a homogeneous coverage of short CNTs* *113*

Fig. 4.16 *Signal amplitude (left column) and peak frequency (right column) from acoustic emission events measured for all bundle composites (AR-QF-S, QF-HT, QF-BiCat, CNT-g-QF (S) and CNT-g-QF (L)) during tensile testing, and associated resistance-change ($\Delta R/R_0$) for UD hierarchical bundles. Vertical and horizontal dashed line correspond to 65 dB threshold and the onset of fibre/matrix debonding, respectively. Coloured peak frequency ranges were obtained from [271]. 0 – 150 kHz (yellow): matrix cracking; 200 – 300 kHz (green): fibre/matrix debonding; 400 – 500 kHz (blue): fibre failure; 500 – 600 kHz (red): fibre pull-out.* *116*

Fig. 5.1 *SEM micrographs of as-received (left) sized and (right) unsized AS4 carbon fibres.* *122*

Fig. 5.2 *SEM micrographs of bi-catalyst deposited AS4-S fibres. Red arrows indicate the presence of catalyst precursor-polymer aggregates, while the blue arrow shows a typical agglomeration between two adjacent carbon fibres.* *124*

Fig. 5.3 *SEM micrographs of CNT growth on bi-catalyst deposited AS4-S fibres produced with CVD_H synthesis conditions (refer to* ***Table 5.4*** *for details on CVD_H growth conditions).* *124*

Fig. 5.4 *SEM micrographs of CNT growth on bi-catalyst deposited untreated AS4-US fibres (left) and plasma treated P-AS4-US fibres (right) under CVD_H synthesis conditions.* *125*

Fig. 5.5 *SEM micrographs of CNT growth on carbon fibres using varying bi-catalyst stoichiometries: (a) 1:0.33, (b) 1:0.5, (c) 1:0.64, (d) 1:1 and (e) 1:2 mol.% Ni:Fe. The deposition was performed in batch conditions on untreated AS4-S fibres with a EtOH concentration of 1 wt.% $Ni(acac)_2$ + $Fe(NO_3)_3$. The growth was performed using CVD_H synthesis conditions.* *127*

Fig. 5.6 *SEM micrographs of CNT-grafted carbon fibres produced from deposition in (a) 0.1 wt.%, (b) 0.5 wt.% and (c) 1.0 wt.% bi-catalyst (Ni:Fe, 1:0.64 mol.%) solutions.* *130*

Fig. 5.7 *SEM micrographs of CNT-g-CF from CVD_H conditions using a potential difference of (a) 0 V, (b) 300 V, and (c) 1000 V.* *133*

Fig. 5.8 *SEM micrographs of CNT-g-CF from CVD_H conditions with sequentially increased potential difference starting from 0 V.* *134*

Fig. 5.9 *SEM micrographs of CNT-g-CFs synthesised for a growth temperature of (a) 670, (b) 720, (c) 770, (d) 820, (e) 870, (f) 920, and (g) 970 °C.* *136*

Fig. 5.10 *SEM micrographs of CNT-g-CFs with fine temperature variation around the control temperature: (a) 750, (b) 760, (c) 770, (d) 780, and (e) 790 °C.* *138*

Fig. 5.11 *SEM micrographs of CNT-g-CFs synthesised with a C_2H_2:H_2 ratio of (a) 1:10, (b) 1:19.3, (c) 1:30, (d) 1:40, and (e) 1:80.* *139*

Fig. 5.12 *Schematic representation of the quartz tube arrangement along with the furnace temperature profile in the stable hot-zone. 141*

Fig. 5.13 *SEM micrographs of CNT-g-CFs synthesised at a line speed of (a) 0.6, (b) 1.2, (c) 2.4, (d) 4.8, and (e) 6.7 $m.h^{-1}$. 142*

Fig. 5.14 *SEM micrographs of CNT-g-CFs produced at different line-speed using (a) configuration 1, (b) configuration 2, (c) configuration 3, (d, e) configuration 4, and (f, g) configuration 5. ..... 145*

Fig. 5.15 *SEM micrographs of CNT-g-CFs produced at 2.4 $m.h^{-1}$ using (a) the control configuration 1 and (b) configuration 2 with a halved growth duration. 148*

Fig. 5.16 *Repeatability and robustness of the CVD system after dismantling and cleaning procedures over four quarters (CVD system was dismantled at least once per quarter). CNT-g-CFs were synthesised using CVD_{α} conditions. 150*

Fig. 6.1 *Fractography micrographs of microdroplet fibre-polypropylene model composites, a) sized CF, b) unsized CF, c) HRBC-CF, d) CNT-g-CF, e) CNT-g-CF high magnification of fracture surface circled in d), with residual PP indicated with a black arrow and fractured CNTs indicated by the white arrow. f) Relationship between the equilibrium contact angle of CFs in diiodomethane (DIM) and the IFSS results from microdroplet PP single fibre composites. Reproduced from [276]. 154*

Fig. 6.2 *(a) Polyimide (PI) linker and (b) triblock copolymer PMACEP-PI-PMACEP (TB3b). Adapted from [4]. .. 155*

Fig. 6.3 *TEM micrographs of dispersed SWNTs with TB3b at different magnifications. Adapted from [4]. 155*

Fig. 6.4 *(a) UV-Vis-NIR absorption spectra of SWCNTs/TB3b dispersant at different SWCNT concentrations. (b) Absorbance of the different dispersions at 700 nm fitted with a linear least square fit (slope a). 156*

Fig. 6.5 *Maximum force as a function of fibre embedded area for (a) unsized carbon fibres and (b) CNT-g-CFs in neat epoxy, (c) unsized carbon fibres and (d) CNT-g-CFs in TB3b-dispersed SWCNTs (0.1 wt.%) reinforced epoxy, (e) unsized carbon fibres and (f) CNT-g-CFs in TB3b dispersed SWCNTs (1.0 wt.%) reinforced epoxy. Average apparent interfacial shear strength is calculated from the linear fit (red line). 157*

Fig. 6.6 *Single fibre pull-out test results for carbon fibres without (plain)) and with CNTs grafted (hatched) on their surface, embedded in (A) neat epoxy, (B) 0.1 wt.% TB3b dispersed SWNT-reinforced epoxy, and (C) 1.0 wt.% TB3b-dispersed SWNT-reinforced epoxy. Error bars represent standard errors. 158*

Fig. 6.7 *Fibre surfaces after single fibre pull-out tests for (a) unsized carbon fibre and (b) CNT-g-CF in neat epoxy, (c) unsized carbon fibre and (d) CNT-g-CF in TB3b-dispersed SWCNT (0.1 wt.%) reinforced epoxy, (e) unsized carbon fibre and (f) CNT-g-CF in TB3b-dispersed SWCNT (1.0 wt.%) reinforced epoxy - scale bars = 2 µm. 159*

Fig. 6.8 *Effective single fibre stress-strain curve under tension for AR-AS4-US (black) and CNT-g-AS4 (red). CNT-g-AS4 data were offset by 0.2 % strain for clarity. 161*

Fig. 6.9 *Tensile strength and modulus of unidirectional CFRP bundle composites made of as-received AS4-US, AS4-BiCat and CNT-g-AS4. Error bars correspond to standard errors. 161*

Fig. 6.10 *(a) photograph of the first generation short beam shear stainless steel mould. (b) Schematic representation of the winding process ensuring an angle of 3.0° (± 1.5°) between two successive plies; specimen locations indicated by cutting marks (black lines). (c, d) Photographs of the SBS specimens after curing and cutting (dimensions in mm). 163*

Fig. 6.11 *Photographs of the second generation short beam shear stainless steel mould (a) with the different fabrication steps including, (b) moulds assembly, (c, d) fibre winding, (e) top inserts for securing the tows, cutting and separation of the moulds, (f) introduction of the mould lateral inserts and tacky tape for (g) pouring epoxy and (h) addition of the mould lid. 164*

Fig. 6.12 *Second generation mould with flow media intercalated between the PTFE release film and the peel ply. 165*

Fig. 6.13 *Interlaminar shear strength measurements for both (a) AR-AS4-US and (b) CNT-g-CF in neat epoxy (L20:EPH161) from SBS specimen produced with the first-generation mould design. Ellipses highlight the onset of interlaminar failure. 166*

Fig. 6.14 *Interlaminar shear strength measurements for AR-AS4-S with (a) 20ULV and (b) L20:EPH161 epoxy resins and for AR-AS4-US with (c) 20ULV and (d) L20:EPH161 epoxy resins. 168*

Fig. 7.1 *3D illustration of the combination of CNT-g-CF with sub-micron scale CNT reinforcements in epoxy. Red line suggests the propagation of a crack in the epoxy rich regions (not to scale) with grafted CNTs pushing the crack away from the critical fibre-matrix interface. 175*

List of tables

Table 2.1 *Mechanical, electrical and thermal properties of CNTs. 25*

Table 2.2 *Reported apparent interfacial shear strength (IFSS), for CNT-grafted-CFs obtained from various physico-chemical techniques (e.g. chemical grafting, sizing, EPD, ESD, CVD) embedded in epoxy; determined from single fibre fragmentation test and compared to baseline. Critical fibre length (l_c), fibre strength at critical length (σ_{lc}) and fibre diameter (d_f). 52*

Table 2.3 *Reported apparent interfacial shear strength (IFSS), for CNT-grafted-CF obtained from various physico-chemical techniques (e.g. chemical grafting, sizing, EPD, CVD) embedded in epoxy; determined from single fibre pull-out, single fibre push-out and microdroplet debonding tests. Embedded fibre length (l_e), maximum force (F_{max}) and fibre diameter (d_f)..... 54*

Table 2.4 *Multifunctional properties of CNT-grafted GF/epoxy systems obtained from various CNT-grafting techniques, all performed in batch. 62*

Table 2.5 *Interlaminar shear strength (ILSS) and in-plane strength of CF/epoxy composites reinforced with CNTs using different approaches. 65*

Table 3.1 *Details for both carbon and quartz fibres from manufacturer's datasheet with associated sample name used consistently throughout the thesis. 74*

Table 3.2 *List of epoxy systems used in this thesis..... 75*

Table 3.3 *Quartz tubes dimensions as manufactured by Robson Scientific, GB. 82*

Table 4.1 *Single fibre pull-out test results with interfacial shear strength (IFSS) determined using fibre diameter after pull-out with standard error associated. Embedded area shown in* ***Fig. 4.9****..... 104*

Table 4.2 *Mechanical and in-situ electrical properties of the unidirectional bundle composites measured in tension with standard error provided. Tensile properties were normalised to a nominal fibre mass fraction of 65 wt.% following ASTM D4018 standard, which corresponds to a Quartzel® fibre volume fraction of 49 vol.%.. 109*

Table 5.1 *Contact angle measurements of carbon fibres in water, before and after APO treatment..... 123*

Table 5.2 *Final bi-catalyst precursors deposition parameters..... 129*

Table 5.3 *CVD line equipment list and associated process variables..... 131*

Table 5.4 *CVD_H synthesis conditions..... 132*

Table 5.5 *Ratio of acetylene to hydrogen with associated gas flow..... 140*

Table 5.6 *Quartz tubes (B and C_1) arrangements of the reduction zone with associated process variables..... 144*

Table 5.7 *Quartz tube (C_2) dimension and associated process variables including line speed, reduction and growth duration within the growth zone 147*

Table 5.8 *CVD_α synthesis conditions..... 148*

Table 6.1 *Mechanical properties of the epoxy systems. 165*

Table 6.2 *Collated ILSS data for AR-AS4-US and AR-AS4-S with 20ULV and L20:EPH161 epoxy resins. 169*

Chapter 1 : Introduction

1.1. A brief history of hierarchical composites

Hierarchical composites, such as wood and bone, are ubiquitous as structural materials in Nature. Although often formed from relatively weak constituents, they demonstrate both efficient reinforcement and embedded multifunctionality, exploiting architectures specified at every lengthscale. Manmade composites, combining microscale structural fibres with polymer matrices, are the current state-of-the-art materials for lightweight mechanical performance. However, they offer little, if any, control of the microstructure at length scales between the primary reinforcing fibre (diameters ~ 10 μm) and the molecular structure of the polymer (~ 1 nm). Recent developments in the synthesis of nanomaterials, particularly carbon nanotubes (CNTs) with exceptional intrinsic specific performance, have enabled to translate nature's hierarchical strategy into the design of novel engineered composite architectures combining high performance nano- and micro-scale reinforcements [1]. The main approaches to incorporate CNTs into conventional fibre-reinforced polymer composites consist in dispersing CNTs throughout the matrix [2], attaching CNTs directly onto the primary reinforcing fibres [3] or a combination thereof [4]. The dispersion approach is generally limited to relatively low CNT volume fractions due to significant increase in matrix viscosity and self-filtration [4]. On the other hand, the incorporation of CNTs in the interphase region between fibres and polymer matrices alleviates the latter constraint and provides crucial reinforcements in regions where stress concentrations dominate, addressing current limitations in compressive and transverse performance of conventional fibre-reinforced composite materials [5, 6]. Among all existing CNT-incorporation techniques, the direct chemical vapour deposition (CVD) growth of CNTs on the primary fibres provides a promising approach to produce hierarchical architectures in industry-relevant contexts. Furthermore, CVD also offers key controls over CNT orientation, yielding either random or radially aligned and dense CNT structures [5].

Previous extensive investigations in the group have demonstrated the value of the CVD approach, using batch processing to produce short sections of CNT-grafted fibres; despite improvements in interfacial properties, reductions in the tensile strength of the grafted carbon and silica fibres were reported, as high as 54 and 30 %, respectively, caused by fibre damage during CVD treatment [6, 7]. Subsequent work in the group has demonstrated a proof of concept for a continuous CNT CVD growth on fibre tows (**Fig. 1.1**), scaling up the production of grafted fibres. The continuous growth, did not produce excessive carbon fibre damage, owing to the application of a modest potential difference between the fibres and a cylindrical graphite foil counter-electrode [3]. However, limited scalability of

the process, due to a lack of thorough CVD parameter studies and the development of large-scale catalyst precursor deposition techniques, has not allowed for the production of substantial amount of CNT-grafted fibres required for the manufacture of macro-scale composite specimens.

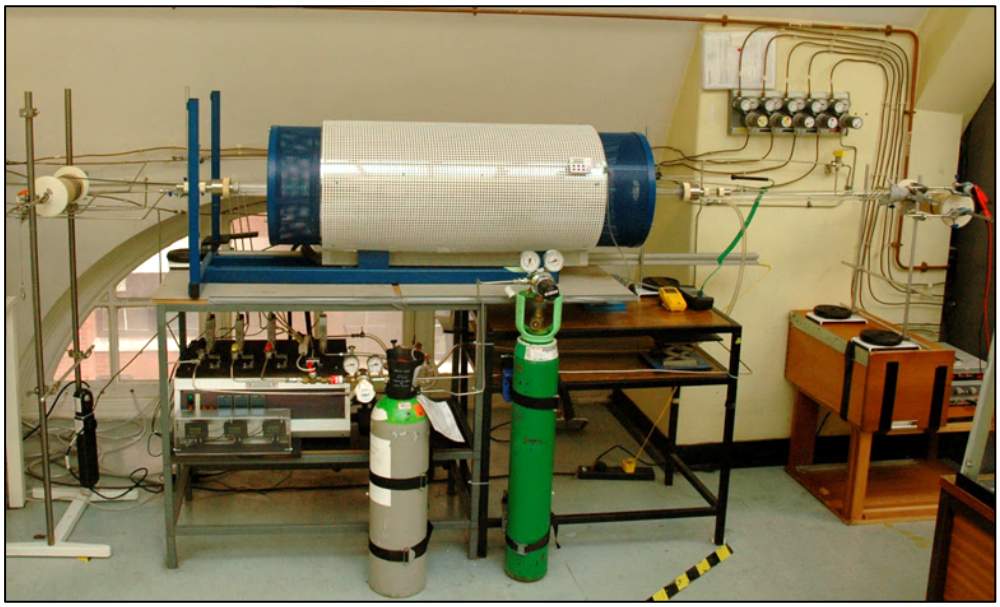


Fig. 1.1 Historical continuous CVD experimental set-up. Reproduced from [8].

1.2. Motivation and scope of work

The principal aim of the project is to scale-up the production of CNT-g-CFs whilst ensuring CNT coverage uniformity and repeatability of the growth process. Hierarchical fibres have been shown to improve drastically the fibre/matrix interphase, yet mainly limited to microscale systems, a novel route to produce large hierarchical coupons should be developed to investigate the macroscale mechanical properties. Growing CNTs via chemical vapour deposition (CVD) strongly depends on precise process conditions to ensure an even coverage, ideal CNT length and avoid pitting of the carbon fibre surface. The current procedure for CVD, including catalyst precursor deposition, needs to be developed so that reproducible specimens may be obtained. The CNT-g-CFs and subsequent hierarchical composites produced should be adequately characterised to evaluate their mechanical performance in contrast with existing novel composites. Failure mechanism of the CNT-g-CF hierarchical composites should also be investigated. Furthermore, combination of carbon nanotubes reinforced matrices with CNT-g-CFs will be explored as the use of both nano-engineered components simultaneously should offer a synergistic effect (**Fig. 1.2**).

The history and context of both conventional fibre and CNT-reinforced fibre composites are discussed in **Chapter 2**, with a particular emphasis on interphase reinforcement through CVD growth of CNTs. This thesis presents the work undertaken to develop and enhance a continuous CNT growth process

on fibre tows. Development of the historical continuous growth experimental set up and of a process methodology, including the continuous deposition of catalyst precursor on fibre tows are described in detail in **Chapter 3**. The improved set up and methodology were first applied to the growth of CNTs on silica fibres; inorganic oxide fibres being a well-established stable substrate for CNT growth (**Chapter 4**). The effect of the nanostructured interphase formed with epoxy was assessed at the single fibre level as well as at the scale of a fibre tow composite. The process was then adapted to the more challenging CNT growth on carbon fibres, by means of a comprehensive parameter study to establish the key dependencies, providing insights into the nature of the mechanisms at play, and assess the stability and consistency of the CNT growth (**Chapter 5**). The mechanical performance of the hierarchical fibres obtained from continuous growth on fibre tows was assessed *via* the production and testing of composites with both aerospace grade and CNT-reinforced epoxy. The mechanical evaluation was carried out at both the single fibre and fibre tow levels, as well as on small-scale composite coupons (**Chapter 6**). Overall, the thesis lays out the basis for a practical and scalable route to produce hierarchical fibre reinforcements in large quantities for structural and multifunctional composites applications. The conclusions and prospects for future developments are discussed in **Chapter 7**.

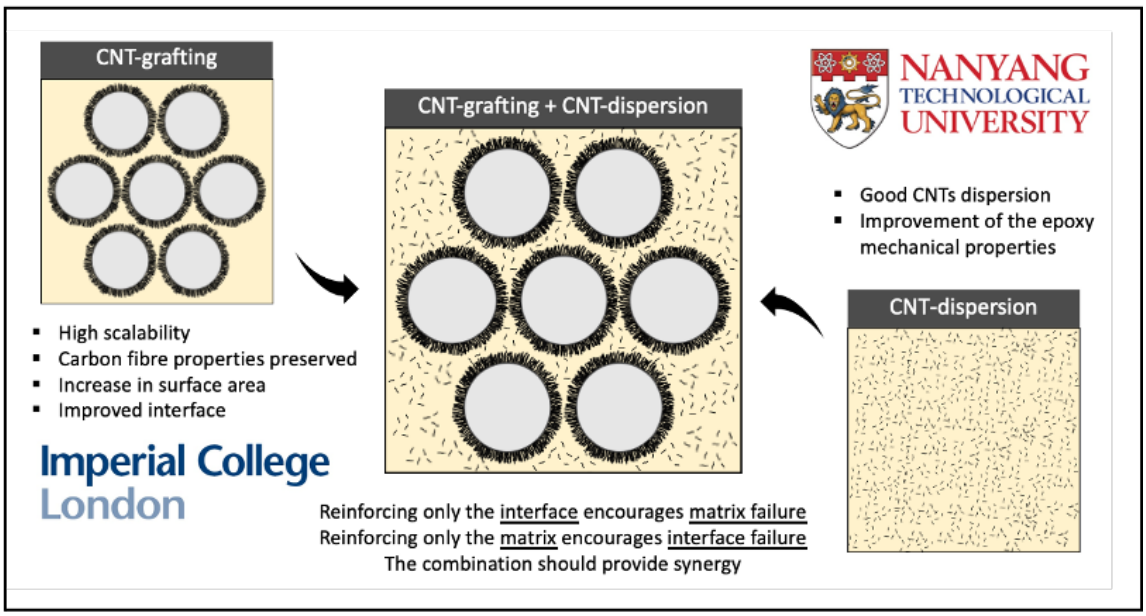


Fig. 1.2 CNT-nanoengineering composite approaches, including the CNT-grafted fibre approach developed in this work (left), CNT dispersion in epoxy investigated by collaborators in NTU (right) and the combination of both approaches (middle).

Chapter 2 : Literature Review

This chapter contains a brief review of the structure, properties, synthesis and growth mechanisms of carbon nanotubes along with current advances in manufacturing CNT-based hierarchical composites. Whilst an exhaustive list of the different techniques used to introduce CNTs into conventional fibre-reinforced composites is provided, the following review focuses on CNT-grafted microscale reinforcements, particularly glass and carbon fibres. Continuous CNT-grafting processes, needed for large scale industrial production, are extensively discussed. The mechanical performance of fibre-reinforced polymer composites and the role of interfaces (or interphases) is presented for both micro- and macro-scale epoxy-based systems. Finally, the multifunctional properties and applications of CNT-enhanced hierarchical composites are discussed.

2.1. Carbon nanotubes (CNTs)

2.1.1. Introduction to CNTs

It is only with the discovery of Buckminsterfullerene (C_{60}) in 1985 [9] – which prompted the reclassification in 1991 of graphitic filaments (**Fig. 2.1** - synthesised and imaged 40 years prior [10]) as multi-walled carbon nanotubes (MWCNTs) [11] – that carbon nanomaterials were finally considered as a new class of carbonaceous materials; an addition to conventional macroscopic carbon forms (graphite and diamond). From the early 90s, carbon nanotubes (CNTs) have galvanised the attention of scientists. Their unprecedented intrinsic properties [12], including high strength, high stiffness, low density, large aspect ratio, and exceptional thermal and electrical conductivities [13, 14] have allowed for the conception of a new range of potential applications [15]. The ability to mimic nature's complex hierarchical designs, ingeniously branching nanoscale and macroscale, yet with the superior properties of CNTs, has triggered a "nano" hype as the next generation of strong, stiff, tough and lightweight composite materials was within arm's reach. Whilst the interest for CNTs grew exponentially with the ever-increasing prospect for diverse multifunctional applications, such as sensing, structural health monitoring, de-icing and electromagnetic shielding [16-18], the high demand for CNTs was quickly met with a high production cost along with numerous processing difficulties [19]. From a flourishing number of proofs of concept, to a decline in tedious and rather unprofitable scaling-up projects, CNTs failed to live up to expectations. In 2004, scientific attention quickly shifted towards a new carbon allotrope, called graphene, a two-dimensional carbon sheet which had long been discussed theoretically but had only recently been isolated from graphite with a simple mechanical exfoliation method known as the "scotch-tape" method [20]. After recent progress in understanding the physical properties of these carbon nanostructures, advances in processing (e.g. CNT individualisation) and the significant decrease in CNT production cost, the pursuit for the next state-of-the-art composites is finally back on track. The past decade has witnessed a recrudescence in large scale experimental studies, driving the development of hierarchical composites for industrial applications [1].

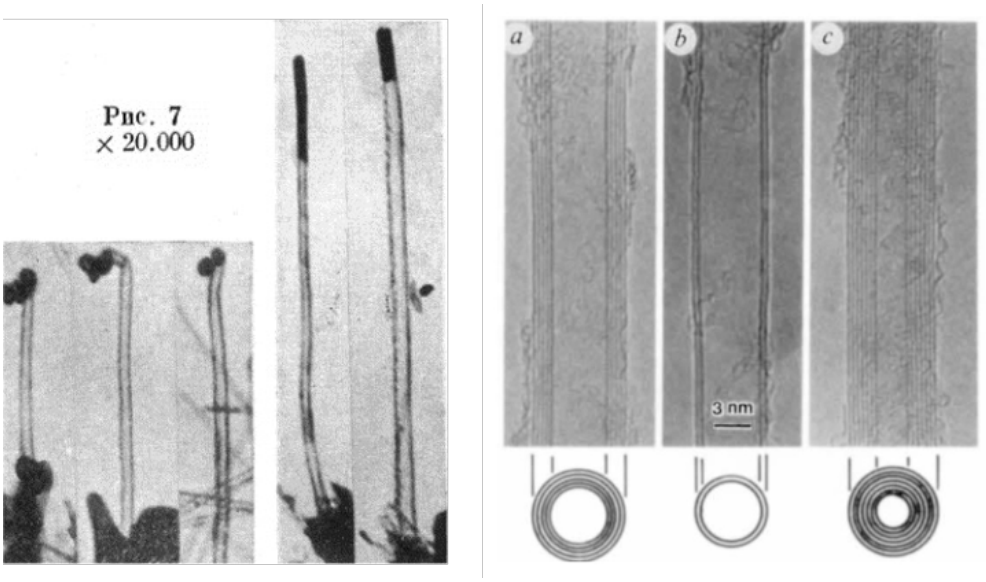


Fig. 2.1 TEM images of (left) the first evidence for the tubular structure of nano-sized carbon filaments [10] and (right) multi-walled carbon nanotubes demonstrating the graphitic spacing (0.34 nm) between the nanotube walls. Reproduced from [11].

2.1.2. Structure and properties of CNTs

Carbon nanotubes can be visualised as a sheet of graphene wrapped up into a seamless cylinder (**Fig. 2.2**). Unlike diamond, where carbon forms a three-dimensional crystal structure with four nearest neighbours arranged together into a tetrahedron, graphene forms as a two-dimensional sheet, with carbon atoms in a hexagonal arrangement (sp^2- hybridized carbon) and a conjugated π-bond system over its entire sheet. Whilst such a sheet, referred to as "graphene" when isolated, can be rolled up into a single-walled carbon nanotube (SWCNT); multilayer graphene (or "graphite") typically forms a multi-walled carbon nanotube (MWCNT). These seamless cylinders can be open ended, closed by hemispheres of fullerene or a combination thereof. The versatile properties of these CNTs depend mainly on the atomic arrangement, in other words, how the sheets of graphene are rolled. The angle of wrapping, which dictates the tube chirality, or helicity, along with its diameter can be represented by a 2D unit cell (**Fig. 2.2**) which is defined by the chiral vector $\overrightarrow{C_h}$ (see Eq. 2.1) and the chiral angle θ (associated with the degree of twist of the CNT);

$$\overrightarrow{C_h} = n\overrightarrow{a_1} + m\overrightarrow{a_2} \qquad \text{Eq. 2.1}$$

where $\overrightarrow{a_1}$ and $\overrightarrow{a_2}$ are the graphene lattice unit vectors, and (n, m) integers which determine the metallic (Armchair) or semiconducting (Zig-Zag) behaviour of the SWCNTs and, therefore, their electrical properties.

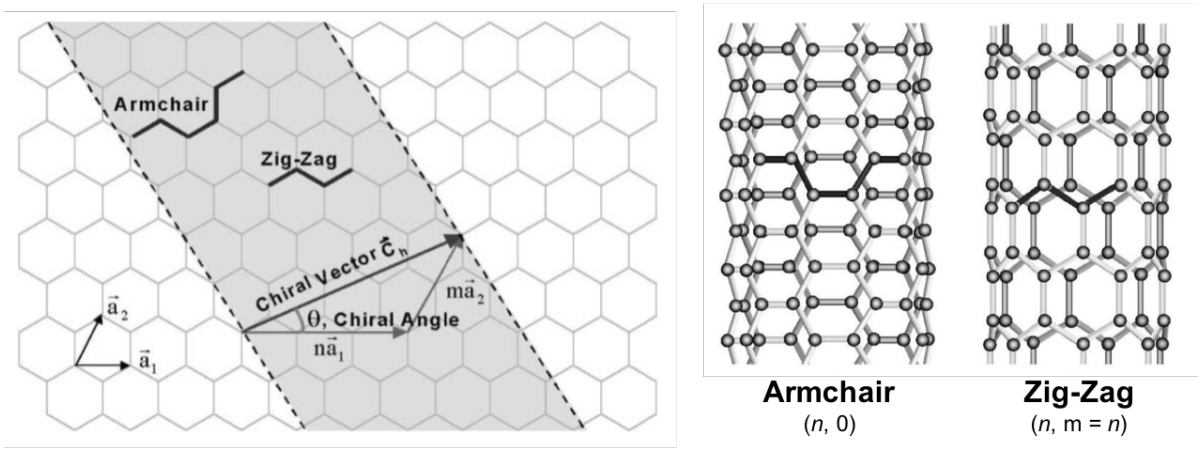


Fig. 2.2 Schematic diagram of the 2D unit cell showing how a sheet of graphene is wrapped to form SWCNTs with different chirality (e.g. armchair and zig-zag) - reproduced from [21].

SWCNTs are typically 1 nm in diameter, with an aspect ratio often around 1000 [22], yet drastic variation in length, from tens of nanometres to several centimetres has been observed [23], thus bridging molecular and macroscopic scales. MWCNTs structure differ to SWCNTs' as they comprise multiple tubes encased in one another, akin to matryoshka dolls. MWCNTs are therefore larger in diameter than their single walled counterpart, typically ranging between 5 and 20 nm, although they can exceed 100 nm.

MWCNTs stacked tubes, of diverse electronic structures, are held together by Van der Waals forces. These relatively weak inter-wall interactions lead to a non-uniform current redistribution over individual tubes and, therefore, much more complex electrical conductivities than SWCNTs. Whilst a correlation between chirality and the mechanical properties of CNTs has been reported – zig-zag tubes showing lower strength and lower ultimate strain than armchair tubes [24] – the presence of defects, including vacancies, walls discontinuities, pentagons, heptagons and Stone-Wales defects, have shown a much more pronounced effect on the fracture process and mechanical properties of CNTs [24-26]. Given the MWCNTs structure, only the outermost layer is considered to carry the load as it is strongly bonded to the carbonaceous deposit, whilst the shear strength between layers are relatively small due to weak Van der Walls interactions [27]. MWCNTs layers can translate with respect to one another (interlayer shear), which leads to MWCNTs interlayer bonding failure (referred to as "sword-in-sheath") instead of nanotubes undergoing structural deformation as observable in SWCNTs. The tensile strength and modulus of carbon nanotubes can be estimated by scaling the carbon-carbon covalent bond of graphite whiskers, 20 and 700 GPa, respectively [28]. In principle, perfect CNTs should exceed those values, with theoretical studies predicting SWCNT strength and modulus of up to 150 GPa and 3.6 TPa, respectively [29]. However, it was experimentally found that the tensile strength and modulus of MWCNTs ranged from 11 to 63 GPa and 12 to 1000 GPa,

respectively. The CNTs ends were attached to an atomic force microscope (AFM) tips and longitudinally loaded while imaged *in-situ* with a scanning electron microscope (SEM). The *in-situ* SEM images (**Fig. 2.3**) showed that the MWCNTs broke in the outermost layer ("sword-in-sheath" failure) followed by pull-out [27]. CNTs properties are collated in **Table 2.1**.

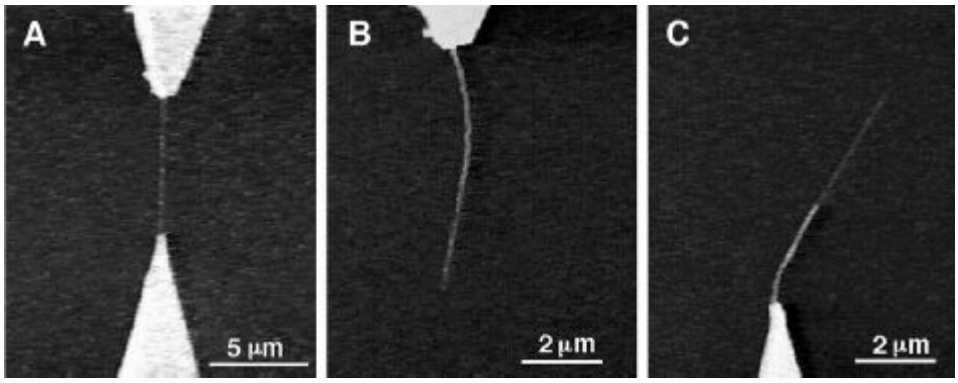


Fig. 2.3 Fracture of a MWCNTs showing a "sword-in-sheath" failure mechanism. Reproduced from [27].

Table 2.1 Mechanical, electrical and thermal properties of CNTs.

	Tensile		Electrical resistance ($\Omega.\mu m^{-1}$)	Thermal conductivity ($W.mK^{-1}$)
	Strength (GPa)	Modulus (GPa)		
SWCNTs	13 - 52 [30]	300 - 1300 [30]	3.3×10^3 [31]	3500 - 6000 [32]
MWCNTs	11 - 63 [33]	†600 - 1000 [34] ‡12 - 50 [34]	8.6×10^4 [14]	1400 - 3000 [32, 35]

MWCNTs produced from † arc-discharge and ‡ CVD.

2.1.3. Synthesis of CNTs

CNTs synthesis can be carried out by means of different high temperature techniques, such as laser ablation, arc discharge, and chemical vapour deposition (CVD). In the latter method, catalyst precursors can be pre-deposited on a substrate prior to CNT-synthesis, introduced *via* an aerosol (AACVD) or through injection of a hydrocarbon/catalyst precursor mixture (iCVD). CVD can also be plasma enhanced (PECVD), which has the ability to produce highly aligned arrays of CNTs [36].

Chemical vapour deposition is the prevailing carbon nanotube synthesis method owing to higher degree of control and scalability. CVD CNTs can be grown on a variety of substrates, including carbon substrates (carbon fibres, diamond, graphite) [37] and non-carbon-based substrates such as silicon, silica fibres [7], and many others. CVD implies the catalytic conversion or dissociation of a gaseous precursor (i.e. carbon monoxide, acetylene, ethylene, etc.) into a solid material at the surface of either a reactive catalyst particle or a continuous catalyst film [38]. This mechanism requires the surface or bulk diffusion of carbon intermediates species in the catalyst particle. Aligned CNT "forest", comparable to CNTs grown through PECVD can be obtained through CVD synthesis by ensuring a high catalyst precursor loading and dense arrangement [39, 40]. Catalyst precursor deposition can be performed with a number of different methods including sputtering, electrodeposition, colloidal suspension and incipient wetness.

2.1.4. Growth mechanisms of CNTs

A tremendous number of publications covers the growth of CNTs *via* CVD. However, a lack of structural control over CNT chirality, nature and density of defect implies that many aspects of the growth mechanism remain poorly understood. Vapour-liquid-solid (VLS) theory, in which a vapour feedstock is absorbed by a liquid catalyst particle until saturation occurs and subsequent carbon precipitation, is considered to describe CNT-growth mechanism for metal catalyst particles (**Fig. 2.4**). Catalyst particles provide a nanoscale template for the nucleation and growth of nanotube, and aid keeping a reactive nanotube rim. The physical state of the catalyst particles (i.e. liquid or solid) and their size influence the solubility of carbon and its diffusion rate, with smaller catalyst particles exhibiting a lower melting point to that of the bulk material and thus an increased carbon solubility [41, 42]. CVD growth of CNTs is often referred to as "grafting"; however, the term creates confusion as it also refers to the chemical grafting of *ex-situ* grown CNTs. Whilst the CVD growth mechanism is a "grafting from" approach, chemical grafting is a "grafting to" process. Ideally, a consensus should be reached in the field to choose a term that helps better differentiate between the two mechanisms. However, for simplicity, and for the remainder of the manuscript, "grafting" will be used interchangeably with "CVD growth".

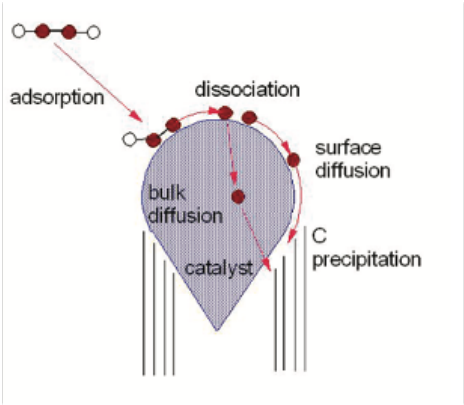


Fig. 2.4 Schematic representation of the VLS mechanism, including the decomposition of the carbon-containing precursor on the surface of the catalyst particle, diffusion of carbon atoms through the particle as a solid solution, and precipitation of carbon and formation of a nanotube. Reproduced from [43].

Common catalyst precursors

The role of a catalyst is to accelerate a thermodynamically-allowed chemical process by creating a transition state of lower energy. Numerous metal catalyst particles, including "typical" (Ni, Fe, and Co) which exhibit high carbon solubility and "atypical" (Al, In, Ti, Pt, K, Mg, Pd, Cs, Mn, W, Na, Mo, etc.), have been shown to catalyse the growth of CNTs [44]. Binary mixtures of active catalysts such as Ni, Fe, and Co are often more effective than individual elements [45], mainly due to alterations in the physical and chemical properties of the resulting co-catalysts nanoparticles, including melting point, vapour pressure, carbon solubility and wetting behaviour [46]. It has been reported that Ni-Fe alloy possesses a reduced eutectoid temperature compared to the pure constituents, allowing for carbon diffusion through the catalyst particles over a wider range of temperature [47]. Ni and Fe are less toxic than Co and, therefore, usually preferred when used in large proportions. Whilst low quality CNTs are typically synthesised from Fe, due to high carbon diffusion and solubility, more resilient nanotubes with a higher degree of crystallinity can be produced from Co and Ni, yet at a lower growth rate [48]. Moreover, the use of nickel-rare earth metal catalysts has been shown to increase the nucleation rate drastically with the postulate that charge transfer may play an important role as it can promote the formation of the pentagons and heptagons required to induce local curvatures of tube nuclei [49]. Recent work even demonstrated the CVD growth of CNTs with non-metallic catalysts, using a reagent-grade common sodium-containing compounds found in table salt [50].

Substrates and catalyst particle formation

Two different growth mechanisms can occur depending on the catalyst-support interaction. When the catalyst-substrate interaction is weak, the particle is lifted off the support while CNT grows, referred

to as “tip-growth”. However, when the catalyst-substrate interface is preserved due to strong interaction, the “root-growth” or “base-growth” process occurs (**Fig. 2.5**).

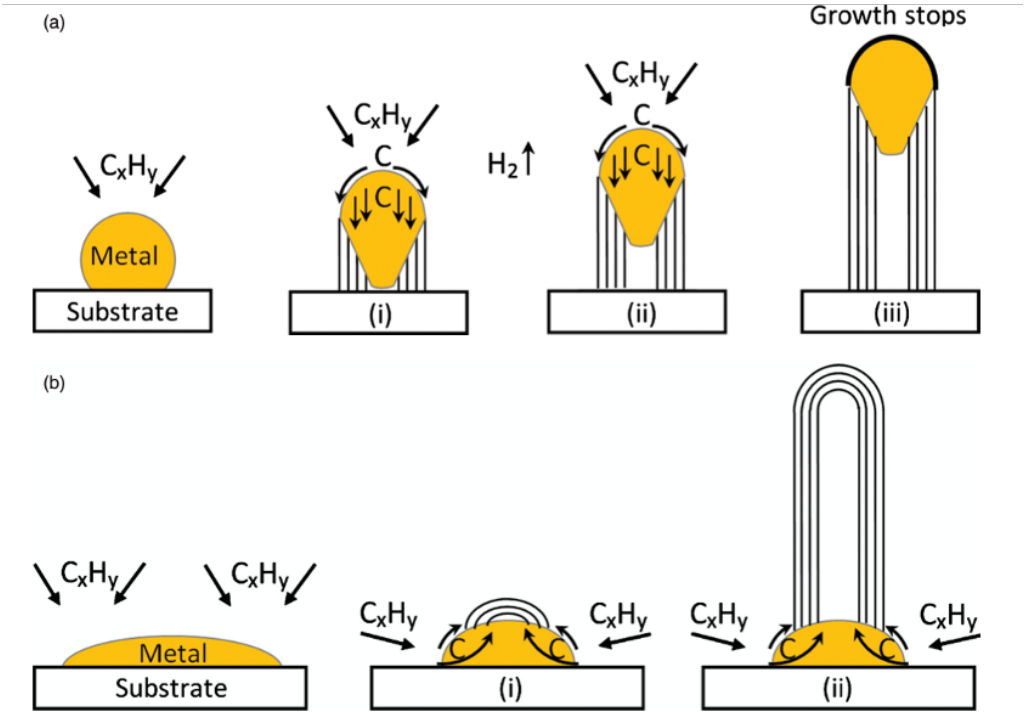


Fig. 2.5 Schematic representation of the growth mechanisms for CNTs, including (a) tip and (b) base growth. Reproduced from [51].

Whilst the substrate-catalyst interface should be preserved in order to continuously grow CNT without disrupting the gaseous precursor supply; interactions between the catalyst and the substrate should neither be too strong nor too weak, according to the Sabatier principle. Ratio of sp^2:sp^3 hybridised carbon has been found to strongly affect the CNT yield; while sp^3 rich carbon leads to poor catalyst-support interaction and low CNT yield with particles evolving towards larger sizes (Ostwald ripening), sp^2 rich carbon exhibits stronger catalyst-support interaction and promotes the controlled growth of dense CNT forests (**Fig. 2.6**) [37]. In addition, both alumina and silica when used as support, showed increased nucleation sites as compared to carbon-based support, correlated to low Ostwald ripening and mild sub-surface diffusion rates, leading to a much narrower catalyst particle size distribution.

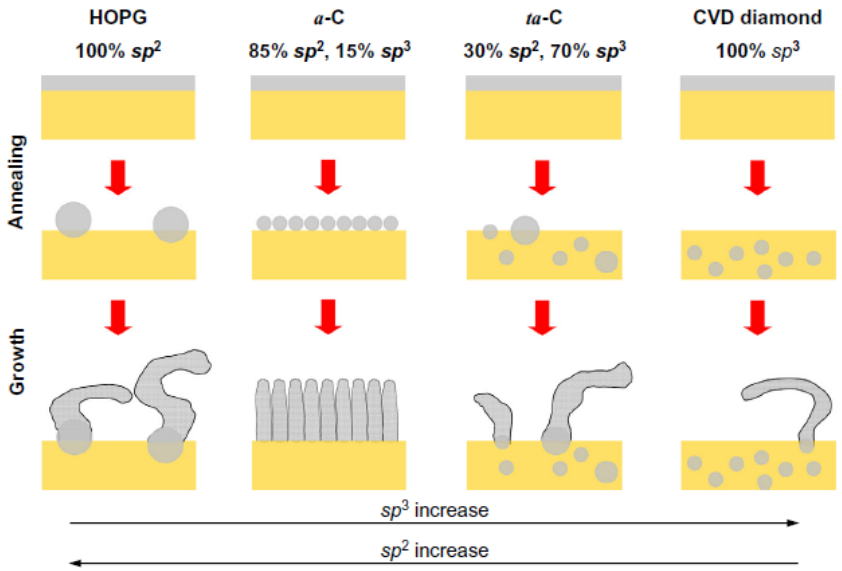


Fig. 2.6 Schematic representation of nanoparticle formation and subsequent CNT growth on carbon-based substrates. Reproduced from [37].

Active gases composition, growth accelerators and catalyst poisoning

The catalytic growth of CNTs not only requires high temperatures but also the presence of gaseous carbon-containing molecules. Whilst CNTs can be synthesised from pure carbon, as commonly achieved *via* arc discharge and laser ablation, the gaseous carbon precursors used in CVD often incorporate other elements that can affect the synthesis, such as hydrogen and/or oxygen. The CVD gaseous environment can therefore be represented by a ternary diagram of three active elements, i.e. carbon-hydrogen-oxygen (**Fig. 2.7**). Upon catalyst deposition and so that CNTs may be grown, catalyst oxide particles must be reduced into catalyst metal particles to allow carbon feed-stock diffusion to occur. During CNT synthesis, catalyst particles may become inactive due to a carbon "cap" forming on top of the particle when excess carbon feedstock is introduced in the chamber. This mechanism may be avoided using growth accelerators also known as weak oxidisers (such as water), etching amorphous carbon from the catalyst particle surface, thus avoiding the formation of inactive caps. Hence, the introduction of oxidisers, which increases the CNT growth rate and allows CNT growth at a low temperature of 400-500 °C, has been reported through an oxidative dehydrogenation reaction between acetylene and carbon dioxide [52, 53]. Extensive studies regarding carbon-hydrogen-oxygen (C-H-O) gas stoichiometry were performed to look into the elementary molar composition of gases necessary for the growth of CNTs in CVD processes [54]. Although, oxygen is present in several cases, it is not considered essential to form CNTs and could potentially react with the carbon-based substrates, which may be unfavourable to its mechanical properties. [55] Adjusting the carbon to hydrogen ratio is much more crucial for the success of the CNT growth. Carbon-based substrates, such

as carbon fibres, has the fundamental problem of support diffusion (surface or bulk) in the catalyst particle, leading to substrate damage, but can be limited by extensive control upon temperature, catalyst particle size, gases composition and respective flow. It should also be noted that carbon fibres that have been annealed at high temperatures are more likely to give controllable CNT growth than amorphous carbon, due to higher sp^2 content and inherent resistance to dissolution by the metal catalyst (**Fig. 2.6**) [37].

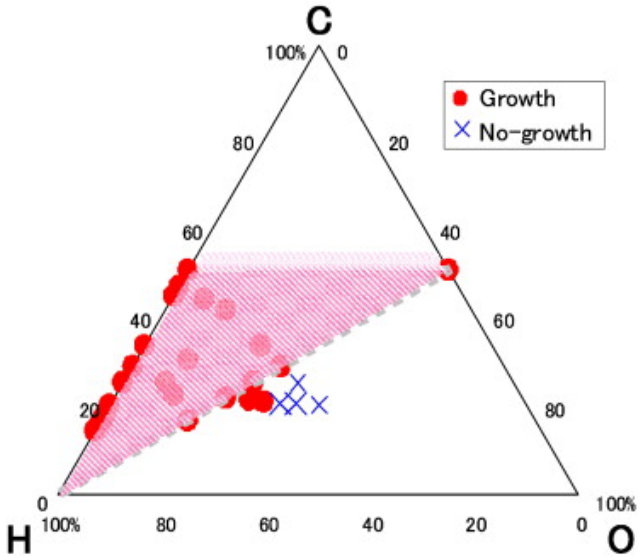


Fig. 2.7 C-H-O ternary diagram showing the successful active gases composition for the growth of CNTs in CVD processes. Reproduced from [54].

2.2. Fibre-reinforced polymer composites (FRPs)

2.2.1. Introduction to FRPs

A composite material is formed of at least two constituents with complementary characteristics, which when combined, form a material that outperforms the individual components. A composite generally contains a stiff constituent referred to as the reinforcement, e.g. carbon fibres, and a soft binder referred to as the matrix (**Fig. 2.8**). The latter component facilitates the transfer of stress to the reinforcing structure and can be either a thermoset or a thermoplastic, depending on the composite properties desired. Thermoplastics matrices become malleable above a specific temperature and returns to a solid state upon cooling. On the other hand, thermosets (epoxy) undergo an irreversible chemical reaction or curing process, also known as cross-linking, that cannot be further altered. This cross-linking effect tends to produce stiffer composites that maintain their shape and integrity at elevated temperatures. Composites exhibit excellent in-plane mechanical properties that can be tailored by laminates' arrangements as well as reinforcement volume fraction. Composites are intrinsically anisotropic due to defined alignment of the reinforcement, but methods such as cross-ply laminating promotes isotropic properties. The matrix/reinforcement interface is of utmost importance, with poor adhesion leading to premature failure of the composite given the inability to transfer stress [56]. Despite limitations including relatively weak compression and interlaminar properties, conventional fibre-reinforced polymer composites (FRPs) have made a huge impact over the past 60 years in several industrial sectors including automotive, aeronautic and sporting goods.

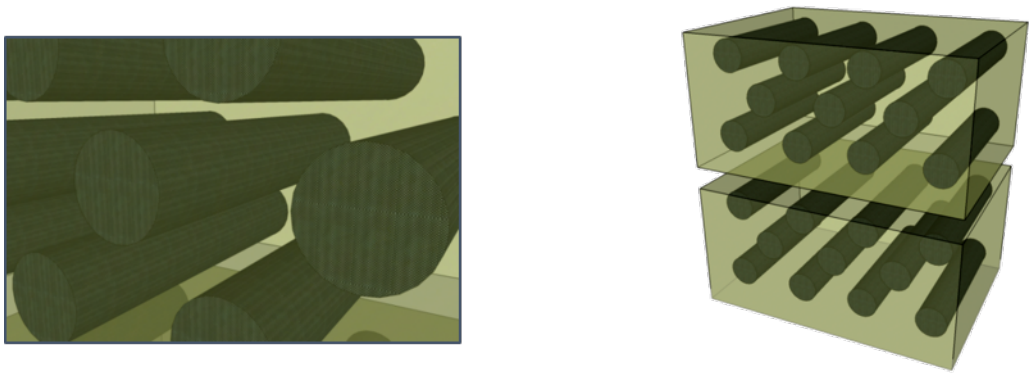


Fig. 2.8 Schematic representation of a fibre-reinforced polymer composite (FRP). Reproduced from [57].

2.2.2. Carbon fibres

Common precursors, production and properties

Carbon fibre is a micro-scale material of continuous length which contains 90 wt. % carbon or above. It is commonly used for structural applications due to excellent properties, including high tensile

strength and modulus, low densities, and good electrical and thermal conductivity [58]. Carbon fibre properties are strongly affected by their precursor composition and structure, with the two most important precursors in the carbon fibre industry being mesophase pitch (MP) and polyacrylonitrile (PAN). The structure of a carbon fibre consists of graphite planes of variable orientation constructing a semi-ordered to ordered tubular structure. The most popular precursor is PAN, which can produce high strength carbon fibres due to a higher degree of orientation of the graphitic structure along the fibre axis, reducing the probability of crack propagation throughout the fibre. Although, the outer layers or "skin" of the PAN-based carbon fibres display a perfect structure when observed under scanning electron microscopy (SEM), their inner core exhibits a disorganised cross-sectional texture, also referred to as "turbostratic texture" (**Fig. 2.9**).

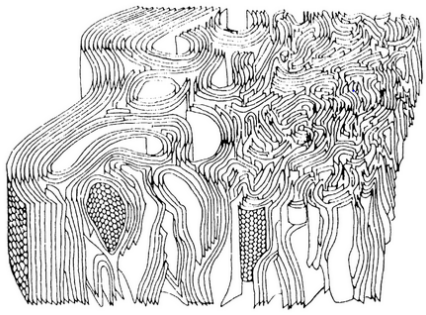


Fig. 2.9 Schematic representation of the structure of a PAN-based carbon fibre. Reproduced from [59].

Pitch-based fibres are the second most manufactured carbon fibres. Those fibres exhibit a number of different orientations of the graphitic planes. Despite a lower strength, pitch-based carbon fibres have superior electrical conductivities due to their highly graphitic regions along the fibre axis (**Fig. 2.10**).

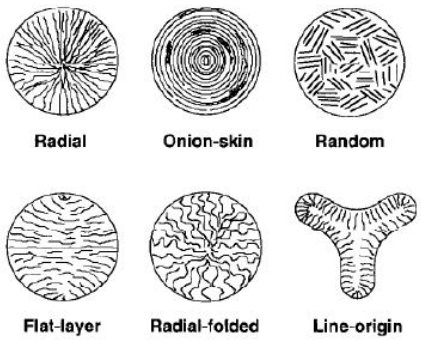


Fig. 2.10 Schematic representation of the different microstructures in pitch carbon fibres. Reproduced from [60].

Even though carbon fibres manufacture requires different conditions depending on the precursor used, the different stages are quite similar. Precursor fibres are first oxidised in air at a temperature

of 200 - 400 °C. The stabilized fibres are then carbonised at a high temperature of 1000 °C in inert atmosphere. Carbonised fibres are finally subjected to an even higher temperature of 1300 - 3000 °C for step known as "graphitisation" which grant higher carbon content and Young's modulus. In terms of mechanical properties, fibres can be classified from low-modulus (LM) to ultra-high modulus (UHM) tailored by the heat treatments conditions. High strength fibres are obtained by stretching during the graphitisation step [58]. PAN-based carbon fibres have typically tensile strength and Young's modulus ranging from 4000 to 7000 MPa and 230 to 450 GPa, respectively [61]. On the other hand, pitch-based carbon fibres have a higher modulus, inherent to their superior density, ranging from 620 to 935 GPa and a slightly inferior tensile strength ranging from 1000 to 3800 MPa [62]. Carbon fibres can also be prepared from lignin, often considered a "greener" alternative, but do not exhibit properties that fits industry prerequisites yet.

Conventional surface treatments

After a final heat treatment step in carbonisation and graphitisation furnaces, the commercial carbon fibres reach their ultimate mechanical properties. However, they exhibit an inert, non-polar, and rather smooth surface due to their highly crystallised graphitic basal planes, resulting in poor wettability with most polymer resins [63]. At this stage of the manufacturing process, carbon fibres are referred to as "*untreated*". To improve their interaction with polymer matrices (e.g. epoxy), carbon fibres are surface treated. These surface treatments remove the weak outer fibre layer initially present on the fibres after carbonisation, and add surface chemical groups, which considerably improves the fibre wettability with polymers [64]. Conventional surface treatment methods includes plasma oxidation, which activates the edges of the graphitic basal planes and the formation of micropores [65]. An increase in surface area is commonly observed after oxidative treatments through the roughening of the carbon fibre surfaces with the formation of micropores and adsorbent sites, resulting in enhanced fibre-matrix interactions [66]. Whilst changes in fibre topography have a limited impact on the interactions with epoxy and reactive resins, mechanically keyed surfaces are particularly of interest for a range of matrices, including more challenging thermoplastic systems that do not form strong covalent bonds and relies mostly on hydrogen bonding. After the critical surface treatment step, carbon fibres are referred to as "*oxidised*" or "*unsized*". Finally, carbon fibres are surface coated with polymeric materials which formulation depends on the manufacturer; this step applies for most man-made fibres at the final stage of their production. These surface coatings, named "*finish*" or more commonly "*sizing*", are usually 100 - 200 nm thick and compatible with the polymeric matrix [67]. The sizing protects the fibres from handling damage and improve processability, retaining the high strength of carbon fibres during composite manufacture. In addition, sizing is a key component in the formation and properties of the fibre/matrix interface, acting as a coupling agent between the

reinforcing fibres and bulk resin, and influencing the final performance of composite. The aim is to reach a fibre/matrix interfacial adhesion energy superior to the cohesive energy of the matrix. Hence, carbon fibres are specifically coated with an epoxy-like polymer given their common use with epoxy resins, improving fibre wettability and, therefore, adhesion to the matrix.

2.2.3. Quartz fibres

Production and application

Novel engineered composites are also developed for specific applications, where structural integrity is required over a large range of temperature. A prime candidate includes quartz fibres (QFs), a homogeneous, non-porous, continuous, amorphous, ultrapure silica glass (99.999 % SiO_2). Quartz fibres combine high-temperature resistance (up to 1090 °C [68] with virtually no shrinkage) and superior transparency to ultraviolet (UV) and longer wavelength radiation, as compared to commercial glass fibres. When used in a composite radome, they protect delicate radar equipment from flying objects, lighting and static discharge. In addition, they have superior resistance to corrosion and heat, along with dielectric properties. On the other hand, they exhibit poor mechanical properties as compared to carbon fibres, with a 4-fold decrease in Young's modulus and a generally lower tensile strength. Quartz fibres are typically formed by downdrawing preforms or by dry spinning a viscous tetraethylorthosilicate (TEOS) solutions [68]. Similar to carbon fibres, quartz fibres are surface treated and sized. The sizing typically consists of a protective polymer layer which is chosen to be compatible with the matrix; an adhesion promoter, generally a silane coupling agent (SCA) and lubricating agents. Due to the large selection of matrices commonly used with glass fibres, ranging from polar (e.g. polyamine, polycarbonate) and non-polar (e.g. polypropylene, polyethylene) thermoplastics to diverse thermoset resins, such as epoxy, polyester and vinyl ester, a broad variety of sizing coatings can be applied to glass fibres. Sizing formulation and application is one of the major challenges associated with glass fibres production and is the main commercial advantage individual manufacturers have over their competitors, which explains its highly secretive aspect.

2.2.4. Role of the interface/interphase on the mechanical performance of FRPs

Fibre-reinforced polymer composites (FRPs) exploit the remarkable mechanical properties of microscale reinforcements (e.g. quartz and carbon fibres), which are combined with matrix materials of dissimilar physico-chemical natures, thus generating interfaces. An interface can be seen as the surface formed by a common boundary between two layers of different chemistry and/or microstructure, in this instance, the reinforcing fibre and the matrix. The interface exhibits unique mechanical properties, differing from those of the fibres and the matrix. Two-dimensional interfaces

are rarely free from chemical interactions, hence a region of finite volume extends therefrom, with mechanical, chemical and physical properties varying either gradually or in a stepwise manner from one phase to the other [69, 70]. This region is called the interphase, as represented in **Fig. 2.11**.

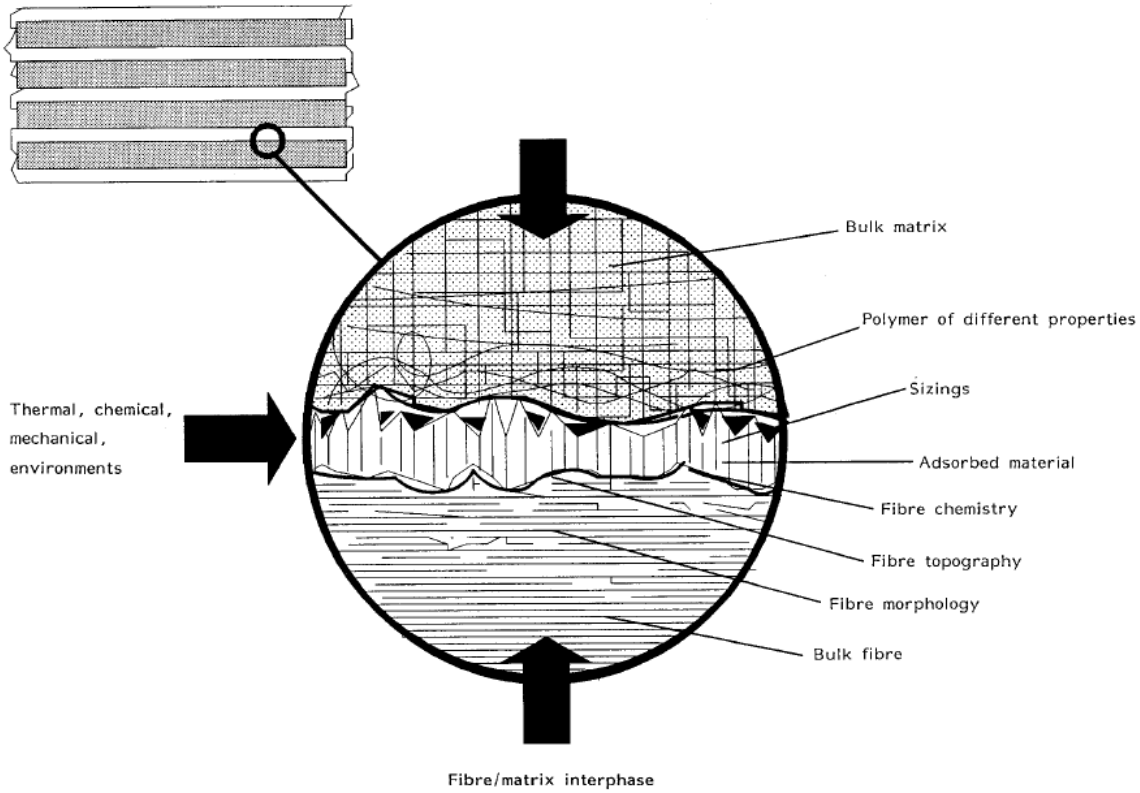


Fig. 2.11 Schematic representation of the interphase formation characteristics in composite materials. Reproduced from [71].

The notion of interphase in composite materials was first introduced in 1974 [72] and later described in further details by Drzal *et al.* in 1983 [67]. Both studies note that during the formation of a composite, and more specifically the infiltration of reinforcing fibres by a polymeric resin, a region of finite volume, different in structure and composition near the fibre/matrix interface is generated. As represented in **Fig. 2.11**, the interphase is a complex three-dimensional region that starts from a location near the fibre surface where the properties differ from those of the bulk fibre, through the fibre/matrix interface (the two-dimensional domain in contact between fibre and matrix), and ends at the matrix region where the properties are equal to those of the bulk matrix. In other words, the interphase is the volume of materials affected by the interactions occurring at the fibre/matrix interface. These interactions can be physico-chemical, frictional or a combination thereof, and includes adsorption and wetting, electrostatic attraction, chemical bonding, reaction bonding and exchange reaction bonding [69]. The frictional component of adhesion, which relates to the surface topography of the fibre, can be tailored by surface roughening/mechanical keying but is typically less

important than the physico-chemical contributions, particularly when combined with a highly reactive epoxy system. However, it is of interest for promoting toughening mechanisms with fibre surface crenulations acting as local obstacles to the propagation of a crack, leading to crack bifurcation and larger amount of energy dissipated. The surface condition of the fibres is therefore an important factor for the formation of the interphase. Sizing typically dissolves into the bulk matrix to different extents depending on the compatibility between the polymeric sizing and the resin [65]. Whilst a sizing with a relatively poor compatibility with the bulk matrix (e.g. an insoluble cross-linked epoxy) tends to form a distinct interphase (**Fig. 2.12**b, c), a soluble sizing is more likely to diffuse and form a larger interphase with graded mechanical properties (**Fig. 2.12**a). Thus, the dimensions of the interphase depend on the length scale over which diffusion occurs [73].

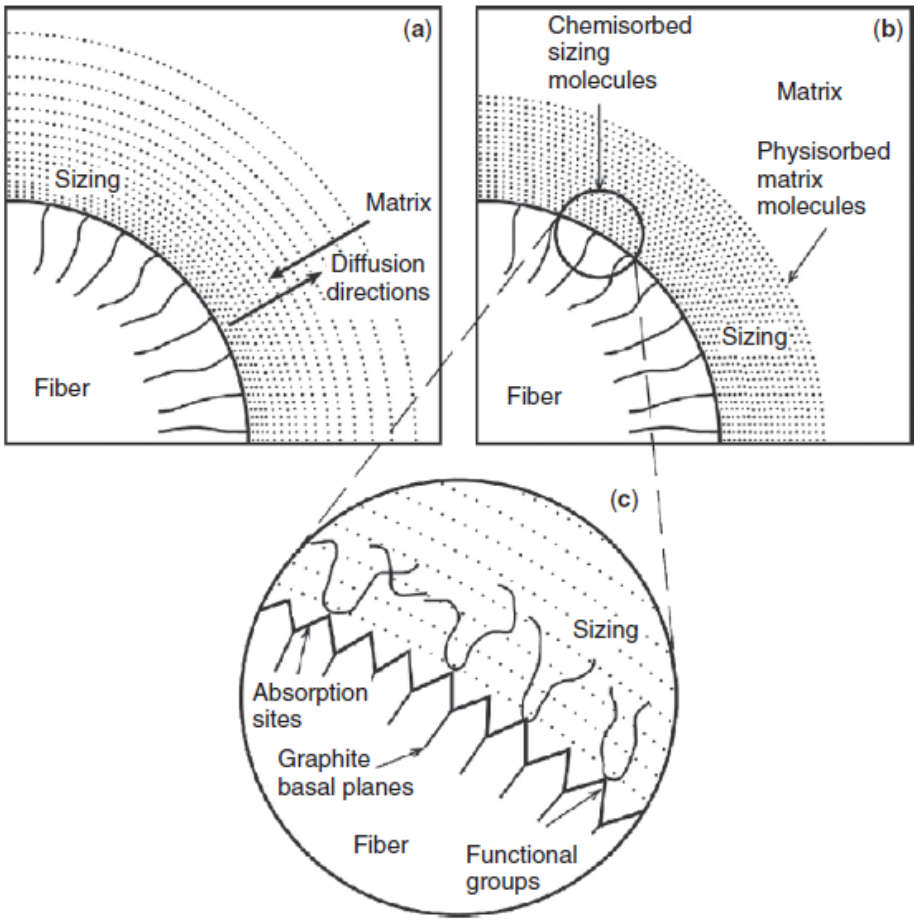


Fig. 2.12 Schematic representation of interphase formation for sized carbon fibres composites. (a) Graded interphase from the diffusion of sizing and matrix molecules, (b) distinct interphase due to poor compatibility of the sizing with epoxy and (c) magnified view of distinct interphase showing both chemisorption at the sizing/fibre interface and physisorption at the sizing/matrix interface. Reproduced from [65].

Interestingly, an interphase is also formed in the absence of surface coatings. Unsized fibres, which have been oxidised have a functional microporous structure that strongly adsorbs epoxy molecules.

In addition, it has been shown that amine-based hardeners may preferentially adsorb on unsized fibre surfaces, altering the epoxy/curing agent stoichiometry near the interface [74]. Therefore, a lower (or higher) cross-linking density in the interphase region may result in a lower (or higher) shear modulus and strength.

The mechanical properties of FRPs depend on the properties of the fibre/matrix interface where stress concentrations prevail. These high local stresses or "*stress risers*" are a result of a mismatch in properties between the reinforcing fibre and the matrix. More specifically, a transverse stiffness imbalance, leading to an early onset of damage in composites, which not only affects the ultimate mechanical properties in the off-axis direction but also along the fibre direction This mismatch typically ranges from 5 to 10 times for carbon fibres and around 30 times for glass fibres embedded in epoxy [75]. Moreover, these high stress concentrations are exacerbated when increasing the fibre volume fraction and "non-ideal" fibre packing, results of fibre-fibre contacts.

The fibre-matrix adhesion ensures that high stress levels can be maintained along the interface and transferred from the fibres to the matrix. In addition, the degree of adhesion governs the failure mode; a poor adhesion prompts frictional debonding, whereas strong adhesion promotes interfacial crack growth or radial matrix fracture if the intrinsic resin strength is exceeded [74]. Subsequently, weak interfaces do not exploit the full potential of the fibres and drastically reduce the load-bearing capacity of composite materials.

After an isolated fibre break, the interface controls the redistribution of stresses in the fibre and surrounding matrix [76]. At the failure site, the fibre loses its capability to transfer stresses but recovers it some distance away; this distance is referred to as the ineffective length and gets shorter for the stronger the fibre/matrix interface. Thus, a fragmented fibre can still carry load and reinforce the material. The interface is therefore a critical component in composite materials as it controls the micromechanics of failure and thus its durability. In addition, the stress concentration on fibres adjacent to the fibre break can be reduced by allowing the interphase to distribute the load across a larger volume [77], limiting the formation of cluster of fibre breaks and premature failure of the composite.

Similarly, the toughness of a composite material is strongly related to the interfacial properties between the fillers and the matrix. Whilst poor interfaces typically favour fibre/matrix debonding and frictional sliding which dominates energy dissipation at the microscale [78], strong interfacial bonding often results in the rapid growth of transverse matrix cracks quickly followed by fibre breaks and catastrophic failure of the composite. Despite the apparent mutual exclusivity of high strength and high toughness in brittle composite materials, several research groups have investigated the potential

of intermittent bonding as an attempt to improve both properties at once. The concept was initially proposed by Atkins *et al.* [79, 80], arranging fibres with alternating sections of high and low shear strength (low and high toughness, respectively) *via* intermittent surface coating of the fibres. Following on this concept, alteration of the interfacial structure/geometry rather than the common chemical bonding approach was also investigated; the formation of epoxy beads, referred to as intermittent beading [81], and laser-induced shape modulation of carbon fibres [82], were both successful in providing a strong interface and a weak (modified) region that enabled localised plastic deformation of the interfacial layer and redistribution of stresses around defects and cracks.

2.3. CNT-nanoengineered FRPs

Nature has developed a number of ingenious solutions to complex problems, notably designing organised structures across multiple length scales, generating both strong and tough materials through synergistic effects. Bones, for example, exhibit a rich hierarchical structure, self-assembled through seven levels of hierarchy, with mineral particles at the nanoscale and collagen fibres at the microscale forming a hierarchical composite that balances strength and toughness at the macroscale [83]. Similarly, bamboo exhibits remarkable mechanical properties combining strong fibrils and a soft matrix with radial density gradients on different length scales [84]. These examples from nature show that despite the use of relatively weak materials, the system obtained as a whole is consistently superior to the sum of its individual components. It has finally become conceivable, with the recent developments in the synthesis of nanomaterials – and more specifically carbon nanotubes (CNTs), resulting in an increased production – to pursue nature's hierarchical strategy and manufacture novel architecture combining high performance nano- and micro-scale reinforcements (**Fig. 2.13** and **Fig. 2.14**).

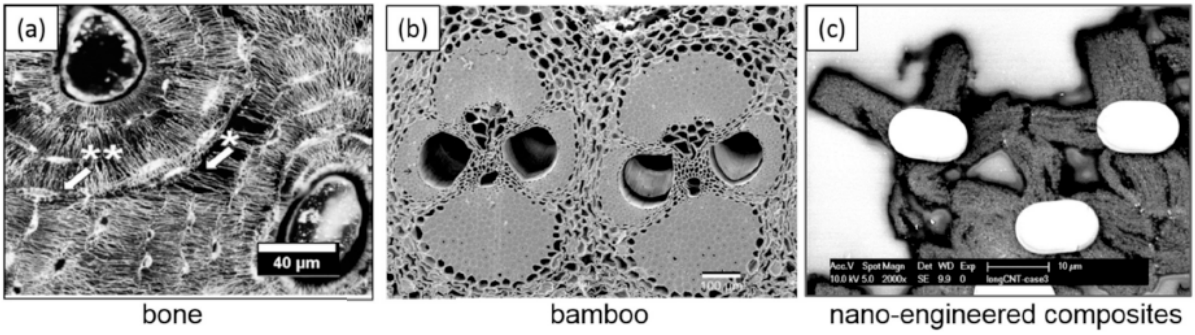


Fig. 2.13 SEM micrographs of hierarchical structure examples present in nature as well as engineered: (a) osteons in equine metacarpal bone, (b) vascular bundles in bamboo, and (c) nano-engineered composite with CNT-grafted alumina fibres. Reproduced from [85].

In fact, structural design strategies exploiting the outstanding intrinsic mechanical properties of CNTs to reinforce state-of-the-art FRPs has been largely investigated in the past few decades [1, 21, 86].

However, despite some improvements in a wide range of composite properties including electrical and thermal conductivity [2, 32], absolute increases in the mechanical properties have been somewhat limited. Transferring these CNT nanoscale properties to a macroscale composite material is challenging, mainly due to processing issues and the complex interdependent mechanisms that take places in hierarchical FRPs. As mentioned previously, a complex situation develops around an inclusion in a matrix, such as shrinkage-induced stresses, areas of imperfect bonding, high stress gradients, voids and microcracks, all impacting the composite performance to various degrees [87]. Moreover, these effects may be exacerbated by the introduction of CNTs which generates more interfaces. Thus, the requirement for sufficient interfacial bonding between CNT and matrix, but also high CNT quality (i.e. tensile strength) is of upmost importance to further enhance the mechanical properties of FRPs [85].

Indeed, the main motivation behind the addition of CNTs in conventional FRPs is to address the current limitations associated with matrix dominated properties, including the resistance to delamination and through-thickness performance, yet without degrading the in-plane properties. CNTs are found to provide additional micro- and nano- scale fracture mechanisms, such as crack diffusion/branching, suppression of stress concentrations and CNT debonding/pull-out [17, 88, 89]. However, the literature shows a large variability in hierarchical FRPs performance; the improvement in strength, stiffness and fracture toughness have been rather inconsistent if not non-existent [90, 91]. Hence, a complete mechanistic study of a nano-reinforced composites requires an extensive set of experiments that allows for the investigation of the different scales of reinforcements at which mechanisms of degradation occur, including diffuse intralaminar damage (e.g. fibre/matrix interfacial failure) at the microscale, transverse cracking at the mesoscale and delamination at the macroscale [91]. Nevertheless, from the collated literature data on CNT-nanoengineered composites, a number of variables stand out. CNT -loading, -dispersion, -orientation, -location, -length, -diameter, but also -surface chemistry have been shown to strongly relate to the efficiency of these nanoscale materials as reinforcements in FRPs. Moreover, the wide interest in CNT-based hierarchical designs has led to the development of a variety of CNT-nanoengineering techniques, with some, potentially practical and scalable [92-97]. These methods can be separated into three main groups, depending on the location of the nanoscale reinforcements, including bulk resin reinforcements, interlaminar reinforcements and the targeted reinforcements of the fibre/matrix interface that are described in further detail in the following sections.

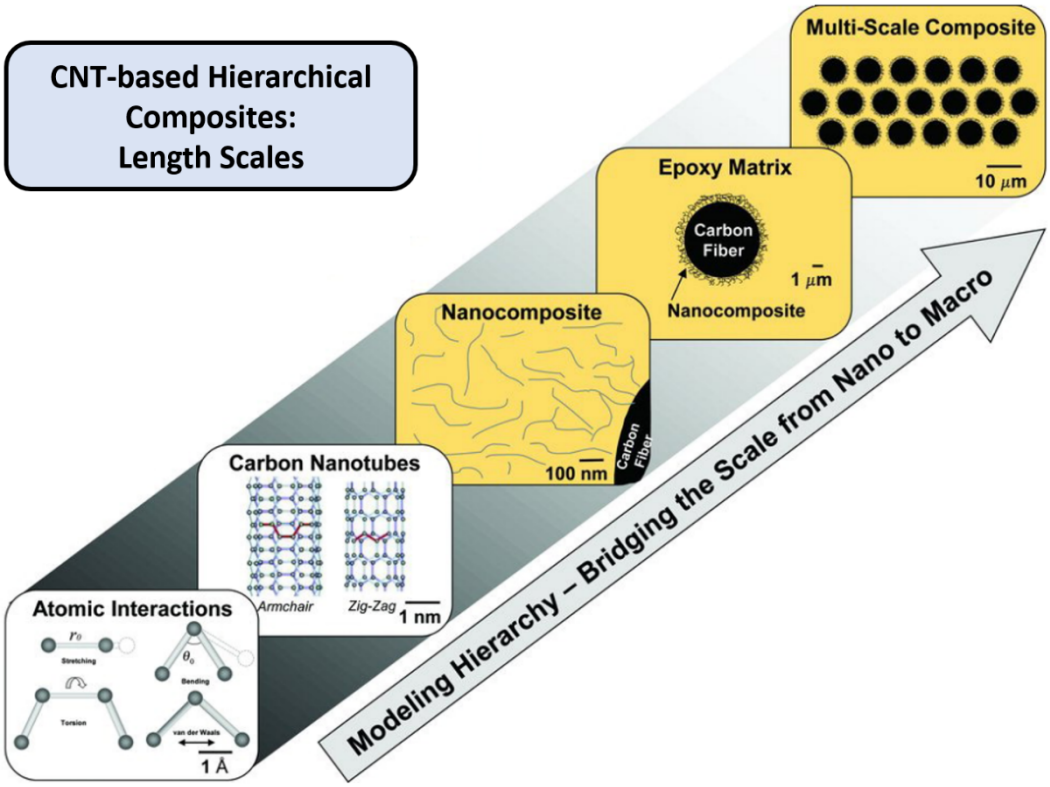


Fig. 2.14 Schematic representation of the length scales involved in nano-engineered FRPs. Adapted from [17].

2.3.1. Bulk resin reinforcement

There is already a large body of literature on the dispersion of CNTs in polymer matrices. The relative simplicity of this approach and the large interest from researchers to dope polymers with CNTs unprecedented physical and chemical properties has led to hundreds of scientific studies using a wide range of polymers, including epoxy, polyaniline, polycarbonate, polyethylene, poly(methyl methacrylate), polypropylene, polystyrene and various copolymer systems [17, 21, 98, 99]. The introduction of CNTs *via* dispersion into polymer matrices is usually performed by surface functionalisation [99], shear mixing [19], sonication [100], or calendaring [101]. These techniques, however, tend to be damaging to the CNTs, with sonication-induced scission [102] or the introduction of defects on the CNT walls as a result of acid treatments. In addition, CNT loading is typically limited (< 1 wt.%) as they tend to entangle and/or aggregate due to strong van der Walls interactions, leading to an increase in resin viscosity, which reduces the processability of the matrix, and introduces voids and stress concentrations, both detrimental to the nanocomposites mechanical properties [103].

The combination of these nanocomposites with conventional microscopic reinforcements, such as glass and carbon fibres has also received a lot of attention [86, 104] which is particularly due to their

compatibility with conventional resin infusion/impregnation techniques, including resin transfer moulding (RTM) and vacuum-assisted resin transfer moulding (VATRM). These industrial techniques, however, suffer from processing issues especially when coupled with nanocomposites, as high viscosity tends to cause incomplete matrix infusion. In addition, the formation of CNT agglomerates can lead to filtering effect against the primary fibres, resulting in a heterogeneous distribution of CNTs, which may significantly degrade the composites performance [105, 106]. Solutions to these processing issues include reducing CNT loading (< 1 wt.%) and/or their length (< 1 μm), which is not ideal as it limits the reinforcing potential of CNTs in FRPs. Recently, an alternative based on a wet powder impregnation process, similar to industrial pre-pregging, has led to CNT loading fractions of up to 25 wt.% whilst ensuring a homogenous distribution and minimal void content in the final composites [2, 97]. Despite the aforementioned limitations, CNT doping in FRPs has clearly shown some large increases in terms of fracture toughness [91] and interlaminar shear strength (ILSS) [97], namely due to the addition of micro- and nano-scale toughening mechanisms such as crack diffusion/branching and CNT debonding/pull-out throughout the matrix (**Fig. 2.15**). However, the reinforcement role of CNTs was found to be highly dependent on the original mechanical properties of the matrix and the functionalisation of CNTs. In the absence of CNT surface functionalisation, relatively soft and ductile epoxy systems were more prone to improve their tensile strength, modulus and fracture toughness, as compared to stiffer counterparts which form poor CNT/matrix interfaces [107].

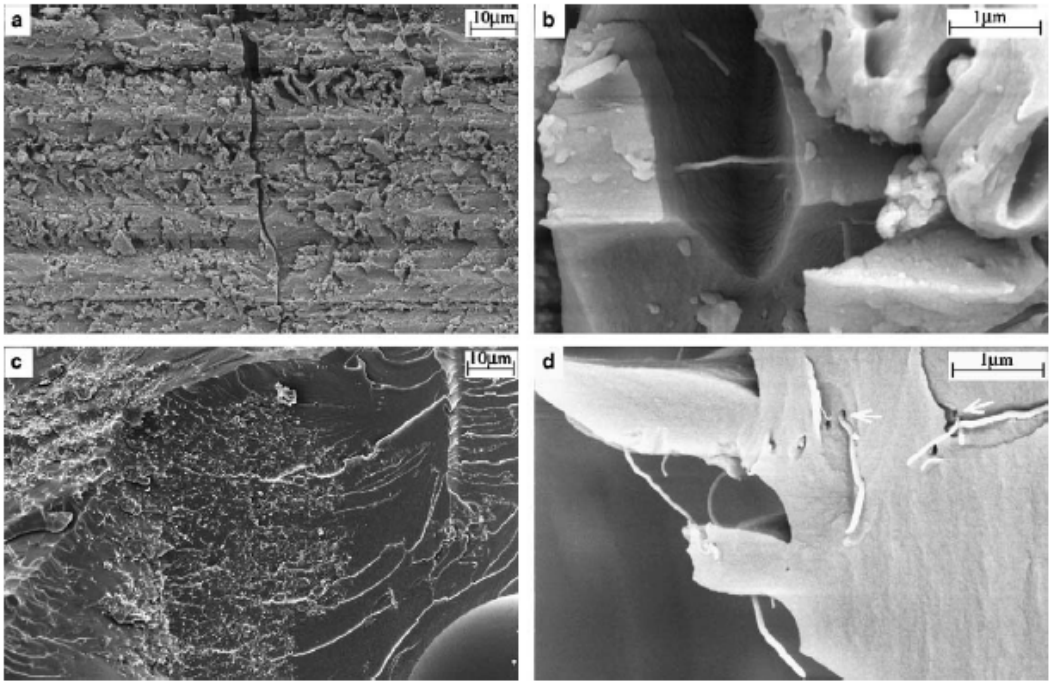


Fig. 2.15 SEM micrographs of CNT-nanocomposite fractured surfaces with (a, b) a soft epoxy resin showing CNT bridging and a ductile failure and (c, d) a stiffer epoxy resin showing a brittle failure and debonded CNTs suggesting poor interactions between the CNTs and the epoxy resin. Reproduced from [107].

Interestingly, designing microstructural heterogeneity within the matrix, by adjusting the spatial separation of CNT-rich regions, was found to provide superior improvement in the fracture toughness when compared to homogeneously dispersed CNTs with similar loading. A propagating crack in the homogeneous system was deflected from the toughened matrix to the fibre/matrix interface, devoid of CNTs, whilst the heterogeneous system promoted cohesive matrix failure and an increase in crack tortuosity. Similarly, recent modelling studies suggest that randomly oriented and uniformly distributed CNTs only have minimal effect on stress concentrations in FRPs, whilst spatially oriented and distributed CNTs reduce significantly the presence of stress risers; the optimised nanostructure allows for the redistribution of stress throughout the material [75, 89]. In other words, agglomerated CNTs act as stiff microscopic reinforcing entities which generates secondary stress risers, potentially detrimental to the composite if not minimised by further spatially oriented/distributed CNTs. On the other hand, uniformly distributed individual CNTs only produce nanoscale stiffness gradients, which are not as efficient in suppressing stress concentrations, particularly at the fibre/matrix interface. Moreover, nanoscale effects, such as CNT pull-out/fracture, do not contribute significantly to the success of CNTs in toughening FRPs. Mechanisms including damage diffusion, crack branching and the suppression of stress concentration (delaying the onset of damage) are more effective at dissipating energy in FRPs [88].

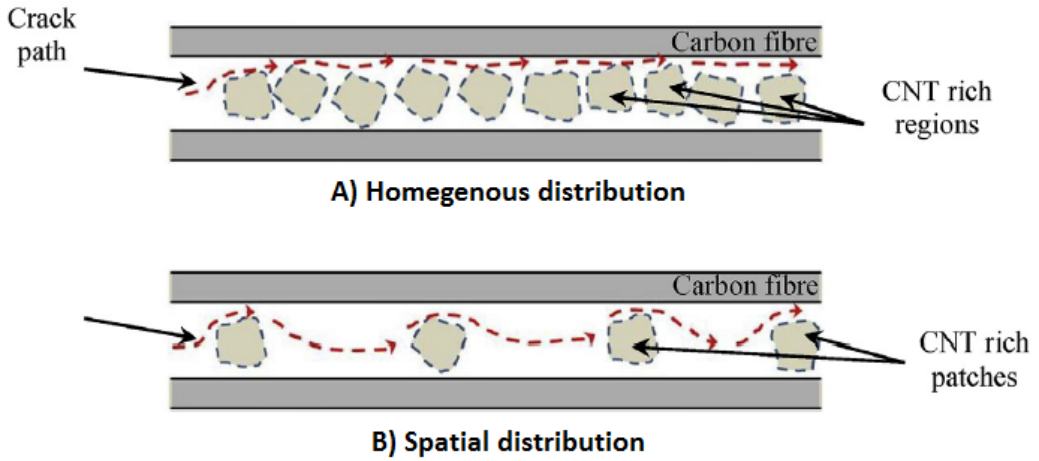


Fig. 2.16 Schematic illustration of fracture mechanisms in hierarchical FRPs with (a) homogeneously distributed CNTs and (b) engineered heterogeneities within the matrix. Adapted from [97].

From those recent studies, it becomes clear that only optimising the CNT/matrix interface is insufficient to fully exploit the potential of CNTs as bulk matrix reinforcements. CNTs spatial orientation and distribution should be tailored to the FRP design requirements. However, in practice, resin dispersion methods only offer little control over CNTs spatial orientation and/or distribution and, therefore, limit their performance as reinforcements [103].

2.3.2. Interlaminar reinforcement

Most FRPs failure results from the coalescence of nano and micro- scale damage mechanisms into mesoscale transverse cracking and macroscopic interlaminar delamination [108, 109]. Hence, the localised reinforcement of the interlaminar region is of great interest. In fact, the interlaminar strength is, arguably, considered the weakest link in FRPs, which could be greatly improved by a number of design strategies including interlayer toughening [110]. Reinforcement of the interlaminar region has long been sought as a mean to improve the through-thickness performance of FRPs. The development of techniques, such as z-pinning and stitching, have been quite successful. However, the introduction of these relatively large inclusions, typically in the sub-millimetre range – two orders of magnitude over conventional microfibril reinforcements – has led to significant decrease in the in-plane mechanical properties due to damage of the primary fibres [111]. On the other hand, interleaving nanomaterials do not compromise the primary reinforcement. Moreover, in direct comparison with CNT bulk reinforcement, CNT interleaving has the advantage of leaving the matrix viscosity unaltered.

The addition of CNTs in the interlaminar region is rather straightforward and typically requires only minimal processing. Techniques such as CNT spray-coating [112-114], the introduction of CNT/CNF buckypapers [115, 116] and more recently 'nanostiching' of densely packed CNT arrays at the centre of the laminate [117-119] were found to improve the interply fracture toughness and prevent delamination of FRPs. The latter method is particularly interesting as it offers both scalability and control over the orientation of the CNTs, particularly in the transverse direction; the high-density CNT arrays (A-CNTs) are produced with a high degree of alignment *ex-situ* via CVD before being transferred in the interlaminar region through a transfer-printing process, between prepreg plies. The A-CNTs fill the ply-to-ply interfacial region and diffuse to some degree in the intralaminar region (***Fig. 2.17***). The growth of a laminar crack in the corresponding nanostiched FRPs, subjected to three-point bending, was driven out from the reinforced mid-plane to the intralaminar region suggesting the requirement for additional intralaminar reinforcements (e.g. fibre/matrix interface) [120].

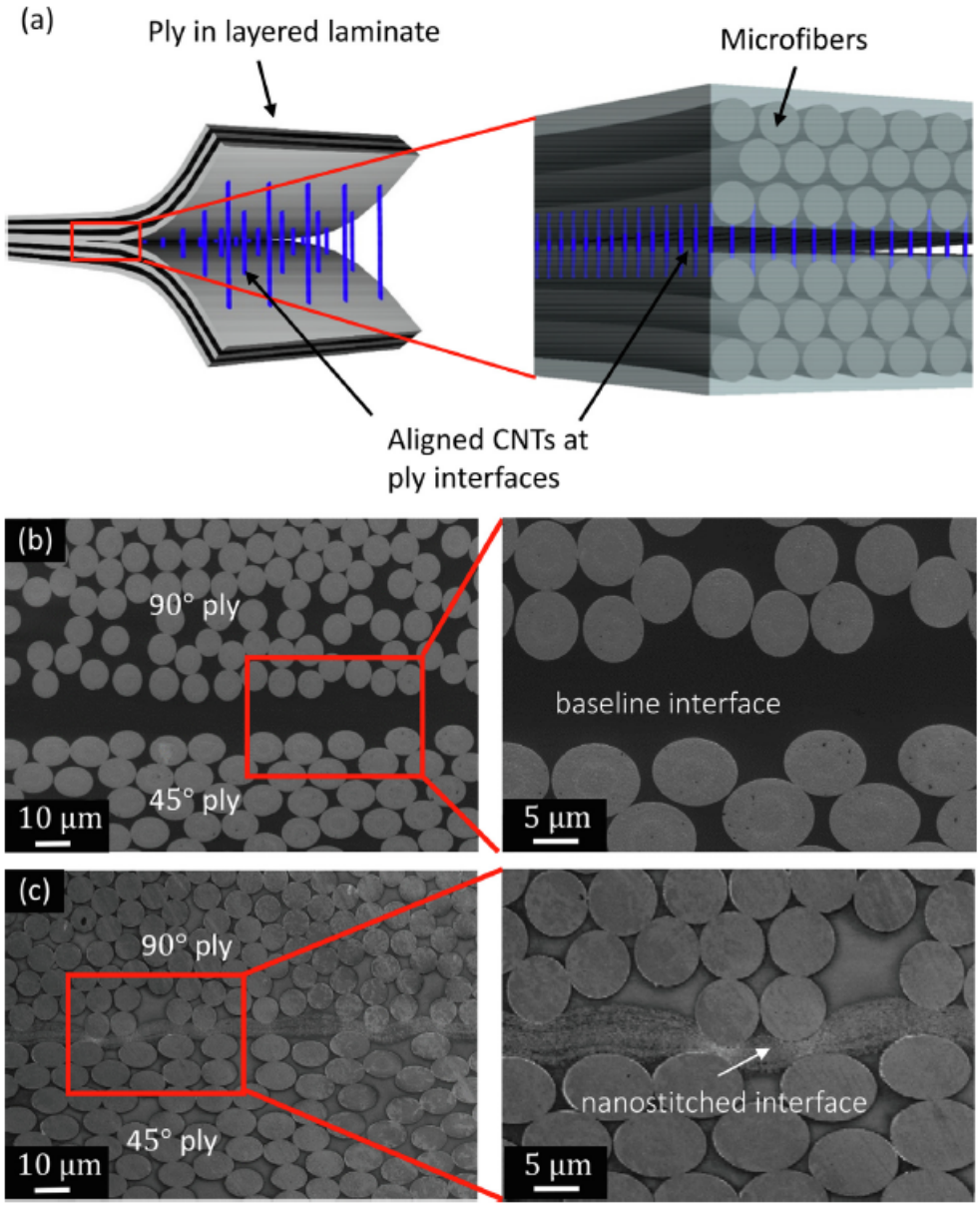


Fig. 2.17 Hierarchical nano-engineered composite architecture produced by the introduction of a CNT-rich layer at the interface between prepreg plies (also referred to as 'nanostiching'): (a) concept illustration of the nanostitched laminate interface. Representative SEM micrographs of: (b) conventional 90/45 FRP interface and (c) CNT-nanoengineered 90/45 FRPs interface showing CNTs filling the interlaminar region. Reproduced from [117].

Whilst some significant improvement in fracture toughness and ILSS have been reported, it is hard to distinguish whether the toughened response of the composite is the result of CNT addition or the introduction of a thicker matrix region between the plies. In fact, most studies do not include a resin-rich layer in their baseline FRPs. In addition, although resin-rich layers enhance the interlaminar toughness, they drastically reduce the longitudinal compression performance [121]. Moreover, the

production of bulkier FRPs – with thick ply-ply separations – is undesirable as it hampers the performance to weight advantage of composite structural materials.

2.3.3. Targeted reinforcement of the fibre/matrix interface

Ensuring sufficient stress transfer between reinforcing fibres and matrix has long been recognized as pivotal in the design of FRPs [67]. The direct reinforcement of the fibre/matrix interface through the use of CNTs is particularly interesting as it forms a nanostructured interphase with graded properties [122] that acts as a protective layer around the fibres, displacing the stress concentration away from the fibre/matrix interface to the end of the CNT layer [123].

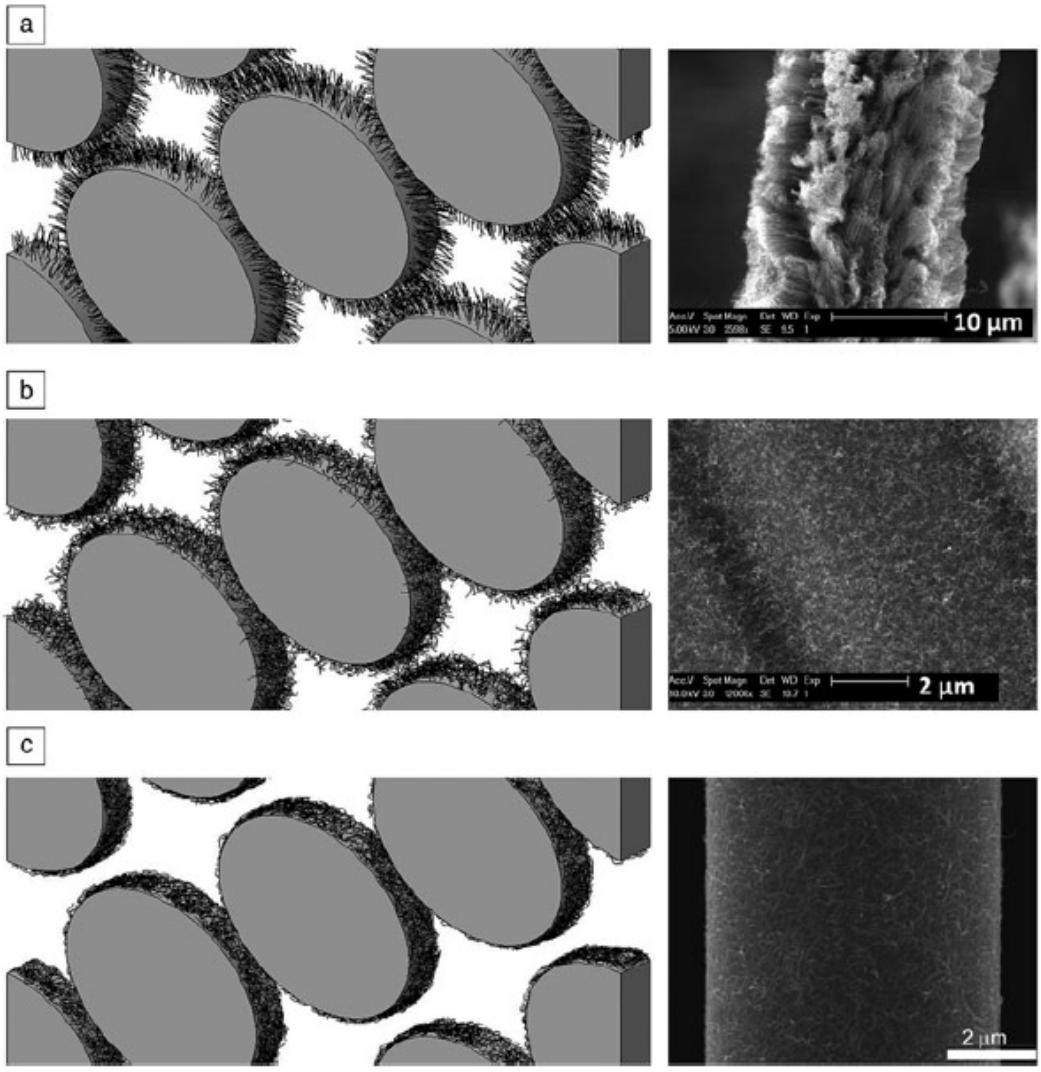


Fig. 2.18 CNT-grafted microfibers. (a) Radially aligned CNT growth with a 'mohawk' splayed configuration, (b) randomly oriented CNT growth, and (c) CNT-containing size. Simulated configurations (left column) and SEM micrographs of practically realizable configurations (right column). Reproduced from [1].

Numerous methods have been reported to deposit CNTs on microscopic fibres, including electrophoretic deposition (EPD) [96, 124-126], chemical grafting [127-130], the application of a CNT-containing sizes [92, 131, 132] and CVD [3, 133-136]. EPD, CNT-sizing and chemical grafting commonly provide CNTs with a random planar arrangement on the fibre surfaces (**Fig. 2.18**c), which is of interest for reducing crack opening displacement after fibre failure, but inefficient for enhancing transverse mechanical properties [137]. In contrast, CVD can control the CNT orientation, typically providing random or radially aligned structures (**Fig. 2.18**a, b) [5]. CVD also provides a more homogeneous CNT coverage and densities generally superior to all other means of production of hierarchical fibres, further increasing the fibres surface area, hence resulting in a larger interaction volume between fibre and matrix.

A huge variation in CNTs crystalline quality is typically observed with CVD. Highly crystalline CNTs – which correlate to superior mechanical properties – form at high temperature and low precursor pressure [138] and further exacerbate the measurement variability associated with the fibre/matrix interfacial properties. Similarly, although EPD, chemical grafting and CNT-sizing use well-characterised CNTs produced *ex-situ* from different industrial, large-scale, synthesis techniques, the requirement for additional processing steps including surface functionalisation, dispersion and sometimes the use of polymer linkers [130, 139, 140], tends to be detrimental to the CNTs, introducing defects in the CNT walls and reducing their strength.

In addition to CNT/polymer adhesion and CNT quality, the grafting strength between CNTs and fibres is particularly critical. Depending on the type of interactions formed (i.e. physical or chemical), intrinsic to the grafting method employed, the adhesion is expected to vary greatly. To exploit the full potential of CNTs as interfacial reinforcements, the grafting strength should be equal or superior to the CNTs tensile strength; thus, promoting CNTs breakage rather than their detachment from the fibres surface. A recent study investigated the fracture behaviour of CNTs, as synthesised *via* CVD on CF, and showed that both CNT detachment and fracture have an equivalent strength of ca. 60 GPa [141] – similar to previously reported experimental value for the strength of MWCNTs [33] – suggesting CVD as an prime candidate for the production of hierarchical fibres. Similarly, the adhesion strength of chemically grafted MWCNTs on CF *via* ester linkage [142] and poly-(amideoamine) bridging [140] was measured. Whilst the former only showed CNT breakage at ca. 30 GPa (a lower bound value potentially resulting from the harsh acid treatment of the CNTs), bridging the CNT/CF interface with a dendrimer led to the detachment of all tested CNTs, with grafting strength ranging from 0.7 to 16 GPa, characteristic of a poor CNT/CF adhesion. Most common chemical grafting reactions can therefore be separated into 'direct' and 'indirect' methods. The latter typically includes multiple step processes with amide,

siloxane and urethane linkers potentially acting as a weakest link and prompting CNT detachment [143].

Thereafter, six different failure mechanisms for CNT-grafted fibres embedded in resin can be identified (**Fig. 2.19**). Ideally, a type 1 or type 2 fracture would prove to be the most efficient reinforcement routes, with a cohesive failure in the matrix at the end of the CNT forest or within the forest with direct reinforcement through CNT breakage, respectively; both configuration corresponding to a larger effective fibre diameter. Type 3 is less likely and would typically occur for damaged CNTs, with their tensile strength being the limiting factor, breaking close to the parent fibre and subsequently pulling-out of the matrix. The latter would still be beneficial as it would provide nanoscale reinforcement including CNT breakage/pull-out. On the other hand, type 4 is characteristic of a poor CNT/matrix interaction prevalent in the absence of CNT surface functionalisation. Finally, type 5 and type 6 are the worst case scenarios. Whilst the former exhibit a poor CNT/fibre interaction therefore acting as a unsized/desized fibre, the latter is distinctive of fibre surface damage with a fracture of the outermost layer, usually observed for CFs [144].

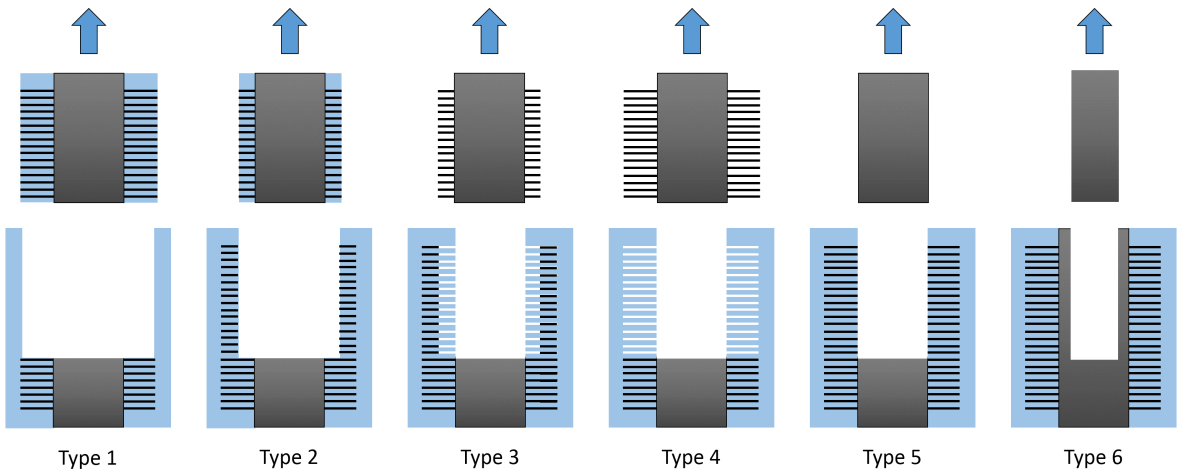


Fig. 2.19 Schematic representation of six types of fracture mechanisms during pull-out of a CNT-grafted fibre from a resin block. From left to right, most to least efficient interfacial fracture mechanism.

In order to achieve the most efficient reinforcing architecture from CNT-nanoengineered fibre/matrix interfaces, and to promote a matrix cohesive failure, one must ensure that all interfaces at play, including CNT/fibre, CNT/matrix and fibre/matrix are not a limiting factor. Thus, the development of a grafting procedure that allows for suitable CNT anchorage to the microfibril substrate and sufficient CNT/matrix adhesion is of utmost importance. The method should be scalable, and able to achieve high loadings of radially oriented CNTs as it is more likely to provide lateral support for the

load-bearing fibres. In addition, the nanoreinforcement dimensions should not hinder the highly packed structured of FRPs containing high fraction of reinforcing fibres (**Fig. 2.20**).

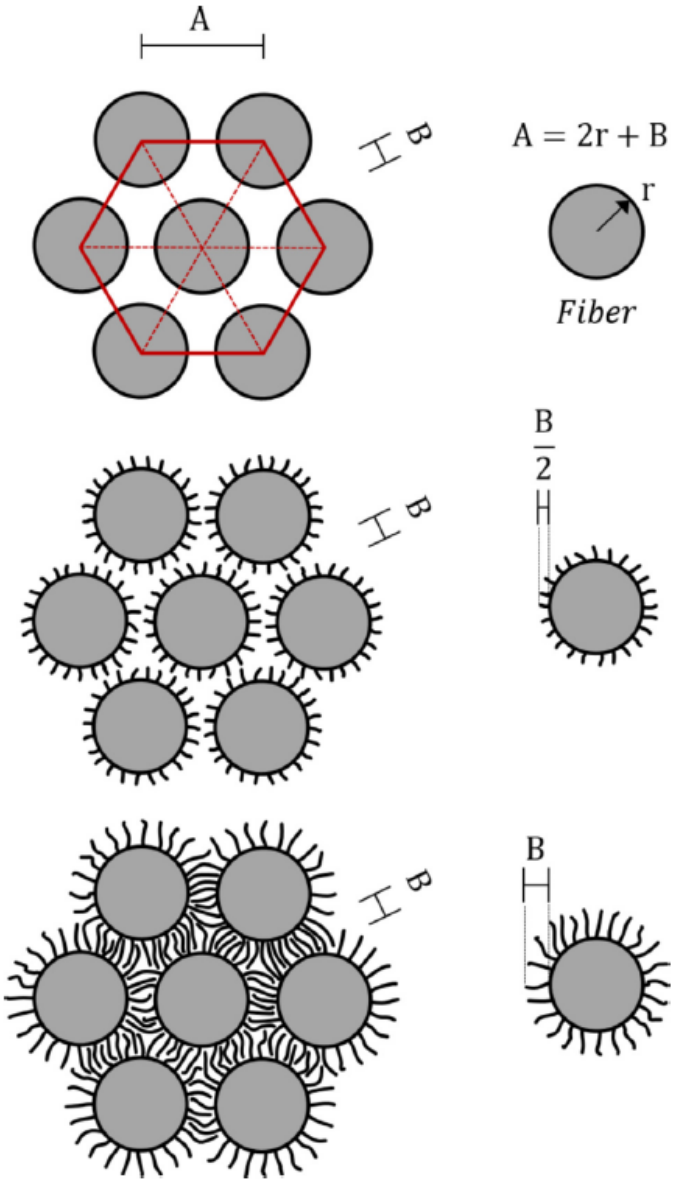


Fig. 2.20 Schematic representation of the idealised hexagonal close packing in FRPs for a fibre volume fraction of 60%. (a) FRP with fibre-fibre separation distance of B, (b) hierarchical FRP with radial CNTs from adjacent CNT-grafted fibres touching (CNT length = B/2), (c) hierarchical FRP with CNT nesting from adjacent CNT-grafted fibre (CNT length ≥ B). Reproduced from [3].

Fibre-matrix interfacial properties

Many micro-mechanical test methods have been developed and are extensively used in the field of composite materials, including single-fibre fragmentation (SFFT), single-fibre pull-out (SFPO), microdroplet-debond (MD-SFPO) and single-fibre push out (SF-PushOut), representing great experimental tools for the qualitative determination of fibre/matrix interfaces and their effect on

stress transfer. The quantitative results, however, cannot accurately predict macroscopic composite performance. The absolute values obtained from SFPO, for example, are affected by a number of micro-mechanical effects which do not represent large scale composite behaviour; the formation of a meniscus region [74], fibre end effect [145], and the absence of neighbouring fibres constraining the surrounding matrix, all make the IFSS estimation challenging. In addition, these micromechanical test methods require a lot of data acquisition given the small sections typically assessed (< 1 mm for SFPO) and are thereby especially sensitive to local variations in the chemical, physical and morphological nature of the fibre along its length. However, despite the difficulties with translating IFSS to bulk composite performance, several research groups have found correlating trends when comparing micromechanical (IFSS) and macro-mechanical (ILSS) test results [95, 131, 146, 147].

Hence, relative percentage differences between the baseline (as-received sized or unsized fibres) and nano-engineered fibres are typically preferred rather than absolute values. However, the choice of a suitable baseline is also problematic. Whilst as-received sized fibres should be favoured, as they represent the industrial benchmark in terms of adhesion to epoxy; a large body of research studies remove the matrix-compatible sizing, either thermally or chemically, thus deteriorating the baseline fibre-matrix interactions even further than that of as-received unsized fibres, which are oxidised. In addition, the terminology commonly used in the research field creates confusion; terms such as ‘raw’, ‘pristine’, ‘barren’, ‘virgin’ and ‘untreated’ do not clearly define the surface conditions of the reference fibres. It is frequently unclear whether the performance of the grafted fibres exceeds the commercial sizing or not. These terms should therefore be avoided without the designations ‘as-received unsized’, ‘as-received sized’ or ‘desized’.

In direct comparison with the commonly used SFFT, which involves multiple fibre fracture events, SFPO consists solely of one interface failure and is therefore independent of fibre strength, avoiding potential measurement variations caused by fibre damage. The SFPO test provides a lower bound IFSS; upon initial interface failure, the process zone progresses (unless mechanical interlocking or frictional forces dominate) until complete failure. On the other hand, SFFT generates multiple failure events before a fragment saturation is reached, providing an ultimate interfacial shear strength value. In addition, the discrepancy in IFSS commonly observed between SFFT and SFPO/MD-SFPO could originate from a variation in bulk matrix properties. In the case of highly volatile curing agents, relatively small epoxy microdroplets were found to have lower mechanical properties when compared to the matrix surrounding single fibres in SFFT, likely due to a diffusion-driven variation in epoxy/curing agent stoichiometry [148]. Other research papers suggest that transverse normal stresses could be higher in SFFT specimens due to Poisson’s effects, resulting in a higher IFSS [149]. Unlike all other micro-mechanical testing methods, SF-PushOut has consistently shown unaltered or slightly

decreased interfacial properties for CNT-grafted CFs [150]. In fact, work carried out within the group showed an improvement of 57 % (118.3 MPa) and 2% (50.6 MPa, within error) in the IFSS of hierarchical CFs using SFPO and SF-PushOut, respectively [144]. An explanation for these results is the change in fracture mode of CNT-grafted CFs caused by difference in loading mechanisms. In SFPO, the fibre is loaded over a large region, and gradually transfers stress into the matrix through the meniscus region (**Fig. 2.21**), leading to a fracture in the CNT-rich interphase. In contrast, during SF-PushOut the fibre is loaded on a relatively small area, at the centre of the fibre, leading to internal cohesive failure (**Fig. 2.19**, Type 6). This difference in failure mode is most likely the result of CF damage during acid treatment and CVD synthesis [5, 151].

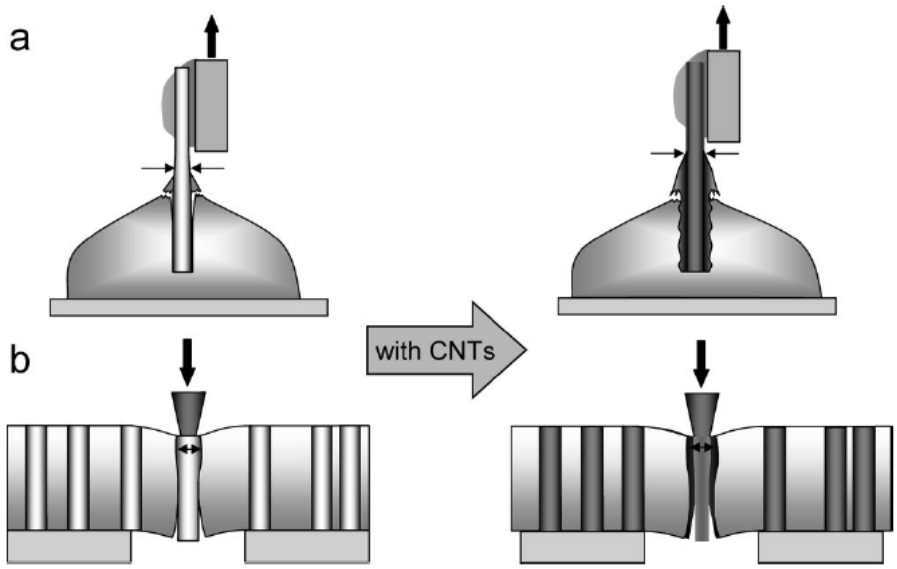


Fig. 2.21 Schematic diagrams of proposed failure mechanisms for (a) single fibre pull-out and (b) single fibre push-out before and after grafting CNT on the fibre surface. Reproduced from [144].

The presence of CNTs on the fibre surface, akin to polymer sizing, lead to the formation of a region of graded mechanical properties (referred to as the interphase, see Section **2.2.4**, pp. 35) extending from the primary reinforcing fibre into the matrix. The local stiffening of the interphase allows for smooth stress transfer across its entire volume and helps avoid stress concentration, which is the usual cause for premature failure. The interphase thickness of CNT-grafted CF/epoxy is dependent on the thickness of the CNT layer, usually in the micrometre range [147]. Commercial sized CFs features an interphase thickness generally inferior to 0.5 µm, as measured through force modulation atomic force microscopy (f-AFM) [95]. Interestingly, recent work showed that longer CNTs grown on CFs – although increasing the thickness of the interphase up to 8 µm – led to a reduced IFSS as compared to shorter CNTs [152]. Similarly, the application of a polymeric sizing with different thicknesses on unsized CFs was found to provide a maximal shear strength for the thinnest coatings of approximately 0.1 µm, with strength falling off as the thickness of the coating increased [153]. These results suggest that the

interphase thickness (i.e. CNT length) may require fine tuning, with the long CNTs typically obtained *via* CVD, potentially hindering the performance of CNT-grafted fibres as reinforcements.

The collated literature data for the IFSS of CNT-grafted CFs in epoxy is presented in **Table 2.2** and **Table 2.3**. The most common methods used to measure the fibre/matrix adhesion in composite materials, including SFFT, SFPO, SF-PushOut and MD-SFPO, are separated for clarity and comparison purposes. Surface condition of the baseline CFs, CNT-grafting technique with associated scale, CNT coverage, orientation and length are also included when available.

Table 2.2 Reported apparent interfacial shear strength (IFSS), for CNT-grafted-CFs obtained from various physico-chemical techniques (e.g. chemical grafting, sizing, EPD, ESD, CVD) embedded in epoxy; determined from single fibre fragmentation test and compared to baseline. Critical fibre length (l_c), fibre strength at critical length (σ_{lc}) and fibre diameter (d_f).

Fibre substrate[x]			Resin	CNT-grafting method	Scale	Interfacial properties of CNT-grafted fibres							Year	Ref.
Type	Surface condition	d_f [μm]				IFSS [MPa]	l_c [μm]	d_f [μm]	σ_{lc} [GPa] (%)	CNT				
										Coverage (CNT/μm²)	Orient.	Length[ƒ] [nm]		
I. Single fibre fragmentation test														
CF (T700)	Sized	7	Epoxy (DGEBA)	Chem. grafting	Batch	56.5 ± 6[†] (+43%)	585 ± 84 (-19%)[‡]	7	-	Scarce	Random (//)	35.2 ± 6.3[♠]	2013	[154]
CF (-)	Unsized	7	Epoxy (Bis. A)	Chem. grafting	Batch	102 (+168%)	-	-	-	Scarce	Random	-	2012	[155]
CF (T800)	Sized	5.2	Epoxy (GE)	Sizing	Batch	62.4 ± 5[◊] (+9.5%)[‡]	476 (-7.2%)	5.2	11.33 (+1.7%)	Scarce	Random (//)	37.4 ± 5.9[♠]	2019	[131]
CF (T700)	Desized	6.67	Epoxy (Bis. A)	EPD	Batch	69.6 (+45.2%)	533 (-28.6%)	6.82	10.88 (+8%)	Uniform	Random	20[†]	2017	[147]
CF (T700)	Desized	7	Epoxy (Bis. A)	EPD	Cont.	72 ± 7 (+33.3%)	-	-	-	Uniform	Random	< 400[†]	2017	[95]
CF (IM7)	Sized	5.2	Epoxy (Bis. A)	EPD	Batch	213 ± 27[†] (+207%)	-	-	-	Scarce	Random (//)	-	2017	[156]
CF (PX35)	Unsized	7.2	Epoxy (Bis. A/F)	ESD	Batch	111 ± 36 (+124%)	-	-	-	Uniform	Random	< 1000[†]	2011	[157]
CF (M40)	Unsized	6.6	Epoxy (Bis. A)	CVD	Batch	55.9 ± 5.3 (+134%)	338 ± 36 (-39%)	-	-	Uniform	Random	> 2000[†]	2018	[158]
CF (T700)	Unsized	7	Epoxy (DGEBD)	CVD	Batch	34.4 ± 8.4 (+104%)	575 ± 67 (-47%)	-	5.6 ± 0.7 (+8.5%)[‡]	-	-	-	2018	[159]
CF (AS4C)	Sized	7	Epoxy (DGEBA)	CVD	Cont.	101 ± 5 (-2%)[‡]	351 ± 20 (-1%)[‡]	7.0	10.1 ± 0.4	Uniform	Random	126 ± 69	2018	[3]
CF (HTR40)	Unsized	7[†]	Epoxy (TGDDM)	CVD	Batch	37.4 ± 4[◊] (+11%)[‡]	800 ± 130 (-1%)[‡]	7[†]	8.48 ± 0.48 (+3.3%)[‡]	Uniform	Random	1000 - 2000	2015	[135]
CF (-)	Unsized	5.2[†]	Epoxy (Bis. A)	iCVD	Batch	18.1 ± 0.4 (+44.6%)	900 ± 100 (-25%)	-	5.43 (+8.4%)	Uniform	Random	> 3000[†]	2015	[160]

CF (T700)	Sized	7	Epoxy (Bis. A)	CVD	Batch	66.0 ± 4.2 (+228%)	277 ± 14.3 (-66.5%)	7[†]	5.22 ± 0.05 (+8.7%)	Uniform	Random	~ 10000	2014	[161]
CF (T-300)	Sized	7	Epoxy (DGEBA)	CVD	Batch	65.7 ± 9.9 (+24%)	310 ± 40 (-29.5%)	7	5.7 ± 0.6 (-13.6%)	Uniform	Random	~ 2000	2013	[162]
CF (T700)	Sized[†]	7	Epoxy (Bis. A)	CVD	Batch	91.5 ± 10.9 (+474%)	305 ± 34 (-68.9%)	7	5.732 (+30.2%)	Uniform	Random	< 1000[†]	2013	[163]
CF (M40B)	Unsized	6.6	Epoxy (Bis. A)	CVD	Batch	32.0 ± 6.1 (+14%)[‡]	395 ± 115 (-11.8%)[‡]	6.6[†]	3.83 ± 0.05 (-1.6%)[‡]	Uniform	Random	< 1000[†]	2013	[164]
CF (UKN-M)	Sized[†]	7.5 ± 0.5	Epoxy (Bis. A)	CVD	Batch	65 ± 9[◊] (+132%)	262 ± 15[†] (-66.1%)	7.5[†]	4.6 ± 0.8 (-19.3%)	Uniform	Random	< 1000[†]	2012	[165]
CF (T-300)	Sized	7 ± 0	Epoxy (DGEBA)	CVD	Batch	70.0 ± 12.5 (+90%)	480 ± 80 (-27.3%)	17.1 ± 0.4	3.3 ± 0.35 (-51.5%)	Uniform	Random	~ 5000[†]	2012	[166]
CF (T300)	Desized	7.5	Epoxy (Bis. A)	iCVD	Batch	47.8[◊] (+175%)	320 (-58%)	7.5	4.07 (-15.3%)	Mohawk	Aligned (⊥)	47200	2011	[167]
CF (M40B)	Unsized	6.6	Epoxy (Bis. A)	CVD	Batch	31.5 (+11%)	395 (-11.8%)	-	3.77 (-1.6%)	-	-	-	2010	[6]
CF (T650)	Sized	7.3	Epoxy (Bis. F)	CVD	Batch	86.6[◊] (-15%)	229 (-40%)	6.5	5.98 (-43.5%)	Uniform	Random	3000 - 10000[†]	2009	[5]
CF (YS-50-30S)	Desized	7[†]	Epoxy (DGEBF)	CVD	Batch	- (+15%)	-	-	-	Uniform	Random	< 1000[†]	2002	[168]

[ᵍ] = used as control including any surface treatment (unsized = as-received/never sized, sized = as-received/sized by manufacturer, desized = sizing removed by thermal or chemical treatments). [†] = thickness of CNT layer perpendicular to carbon fibre surface. [†] = details not readily available or specified in text and are taken from graphs using Graph Grabber (V2.0.1, Quintessa Ltd, UK), previous papers, or from a manufacturer data sheet. [‡] = mean values generated are within error, when error is presented. // and *⊥ = denotes the preferential orientation of the CNT coverage with regards to the carbon fibre substrate. [♠] = thickness of the coating estimated via AFM subtracting control fibre surface roughness from CNT-grafted-CFs. [◊] = additional coating present on the carbon fibre including pyrolytic carbon, polymeric functional coating poly(styrene-alt-[dipotassium maleate]), SiO_2 and $MgSO_4$. Epoxy: DGEBA = Bisphenol-A diglycidyl ether; GE = Glycidyl-ether; DGEBD = butanediol diglycidyl ether; TGDDM = tetraglycidyl diaminodiphenylmethane; DGEBF = Bisphenol-F diglycidyl ether.*

Table 2.3 Reported apparent interfacial shear strength (IFSS), for CNT-grafted-CF obtained from various physico-chemical techniques (e.g. chemical grafting, sizing, EPD, CVD) embedded in epoxy; determined from single fibre pull-out, single fibre push-out and microdroplet debonding tests. Embedded fibre length (l_e), maximum force (F_{max}) and fibre diameter (d_f).

Fibre substrate[ꝺ]			Resin	CNT-grafting method	Scale	Interfacial properties of CNT-grafted fibres							Year	Ref.
Type	Surface condition	d_f [µm]				IFSS [MPa]	l_e [µm]	d_f [µm]	F_{max} [mN]	CNT				
										Coverage (CNTs/µm²)	Orient.	Length[†] [nm]		
II. Single fibre pull-out test														
CF (AS4)	Unsized	7.0 ± 0.3	Epoxy (Bis. A)	CVD	Cont.	96.7 ± 2.3 (+8%)	28 - 102	6.8 ± 0.4	70 - 230	Uniform	Random	~ 200	2019	[4]
CF ()	Desized	7	Epoxy (-)	CVD	Batch	28.2 ± 1.3[†] (+41%)	25 - 125[†]	-	14 - 96[†]	Uniform	Random	> 5000[†]	2018	[152]
CF (AS4C)	Sized	6.9	Epoxy (DGEBA)	CVD	Cont.	73.3 ± 1.6 (-8%)	31 - 89	7.0	47 - 165	Uniform	Random	126 ± 69	2018	[3]
CF (C320.00A)	Unsized	~ 7.5	Epoxy (TGDDM)	CVD	Batch	118.3 ± 1.9 (+57%)	18 - 42[†]	~ 7.5	43 - 119[†]	Uniform	Random	~ 500	2008	[144]
III. Single fibre push-out test														
CF (UTS50)	Sized	7.0	Epoxy (Bis. A)	EPD	Cont.	- 0%	30	7.0	66[†]	Moderate	Random (//)	-	2014	[94]
CF (T700)	Sized	7	Epoxy (Bis. A)	CVD	Batch	36.3 ± 8.3[†] (-36%)	15 - 40	~ 8	-	Uniform	Random	~ 1000	2017	[150]
CF (C320.00A)	Unsized	~ 7.5	Epoxy (TGDDM)	CVD	Batch	50.6 ± 2.8 (+2%)[‡]	15 – 40	~ 7.5	-	Uniform	Random	~ 500	2008	[144]
IV. Microdroplet debonding test														
CF (-)	Desized	7	Epoxy (Bis. A)	Chem. grafting	Batch	87.2 (+75.8%)	-	7	-	Scarce	Random	86.6[♠]	2019	[169]
CF (-)	Desized	6 - 7	Epoxy (Bis. A)	Chem. grafting	Batch	105.8[◊] (+117.7%)	-	-	-	Scarce	Random (//)	-	2018	[127]
CF (T300)	Desized	7.0 ± 0.3	Epoxy (Bis. A)	Chem. grafting	Batch	76.5 ± 12.5 (+223%)	42.6 - 127.8	7.0 ± 0.6	86 - 192	Uniform (59 ± 14)	Random	-	2018	[128]

CF (-)	Desized	6.5	Epoxy (Bis. A)	Chem. grafting	Batch	95.8[◊] (+104%)	-	-	-	Scarce	Random (//)	-	2015	[170]
CF (-)	Desized	-	Epoxy (Bis. A)	Chem. grafting	Batch	114.6[◊] (+114%)	40 - 80	-	-	Scarce	Random (//)	55[♠]	2014	[129]
CF (T300)	Sized	7	Epoxy (Bis. A)	Chem. grafting	Batch	71.2 (+41.6%)	-	-	-	Moderate (36 ± 6)	Random	-	2013	[171]
CF (-)	Desized	7	Epoxy (Bis. A)	Chem. grafting	Batch	87 (+190%)	-	-	-	Scarce	Random	-	2012	[155]
CF (T300)	Desized	7	Epoxy (Bis. A)	Chem. grafting	Batch	91[◊] (+111%)	-	-	-	Scarce	Random (//)	-	2012	[172]
CF (T300)	Desized	6.9	Epoxy (Bis. A)	Chem. grafting	Batch	117[◊] (+170%)	40 - 100	7.0	-	Scarce	Random	-	2011	[173]
CF (T300)	Unsized	7	Epoxy (GA)	Chem. grafting	Batch	106.6 (+150%)	-	-	-	Scarce	Random (//)	-	2009	[174]
CF (-)	Unsized	-	Epoxy (GE)	Sizing	Cont.	80.1[◊] (+77%)	-	-	-	Scarce	Random (//)	-	2018	[175]
CF (IM2C)	Sized	5.2	Epoxy (Bis. F)	Sizing	Batch	105.9 ± 12.4[◊] (+18.1%)[‡]	-	-	-	Uniform	Random (//)	-	2014	[176]
CF (-)	Unsized	-	Epoxy (GE)	Sizing	Cont.	81.3[◊] (+69.6%)	-	-	-	Scarce	Random (//)	-	2013	[177]
CF (T700)	Desized	7	Epoxy (Bis. A)	EPD	Batch	91.3 (+89.4%)	-	-	-	Moderate	Random (//)	< 200[†]	2018	[146]
CF (-)	Desized	7	Epoxy (DGEBA)	EPD	Batch	71.8 (+114.3%)	-	-	-	Uniform	Random	< 5000[†]	2014	[178]
CF (-)	Desized	-	Epoxy (Bis. A)	EPD	Batch	113.6 (+68.8%)	60 - 80	-	-	Uniform	Random	< 200[†]	2011	[179]
CF (-)	Sized[†]	5 - 8	Epoxy (PPEDGE)	Flame growth	Batch	46.8 ± 1.1[†] (+71%)	-	-	15 - 61[†]	Uniform	Random	∼ 300[†]	2016	[180]
CF (T300)	Sized	7	Epoxy (Bis. A)	CVD	Batch	67 ± 10.2 (+123.3%)	-	-	-	Uniform (336 ± 16)	Random	> 1000	2019	[181]
CF (-)	Desized	-	Epoxy (-)	CVD	Batch	70 (+30%)	53 - 111[†]	-	69 - 162[†]	Uniform	Random	< 5000[†]	2019	[182]
CF (T700)	Desized	7	Epoxy (Bis. A)	CVD	Cont.	85.3 (+84.4%)	-	-	-	Uniform	Random	< 1000[†]	2018	[183]

Table 2.3 (Continued)

Fibre substrate[¤]			Resin	CNT-grafting method	Scale	Interfacial properties of CNT-grafted fibres							Year	Ref.
Type	Surface condition	d_f [μm]				IFSS [MPa]	l_e [μm]	d_f [μm]	F_{max} [mN]	CNT				
										Coverage (CNTs/μm²)	Orient.	Length[†] [nm]		
CF (-)	Sized	7 - 10	Epoxy (-)	CVD	Batch	55 ± 6[†◊] (+28%)	-	-	-	Sporadic	Random	5000 - 20000	2014	[141]
CF (T-300)	Sized	-	Epoxy (Bis. A)	CVD	Batch	166 (+37%)	-	-	-	Uniform	Random	~ 1000[†]	2012	[184]
CF (T300)	Unsized	7.0 ± 0.1	Epoxy (DGEBA)	AACVD	Batch	126 ± 9 (+94%)	58 - 85[†]	7.0 ± 0.1	117 - 250[†]	Uniform	Random	> 5000[†]	2012	[185]
CF (T300)	Unsized	7.0 ± 0.1	Epoxy (DGEBA)	CVD	Batch	135 ± 9[◊] (+108%)	58 - 85[†]	7.0 ± 0.1	125 - 268[†]	Mohawk	Aligned (⊥)	> 20000	2011	[186]
V. Miscellaneous methods														
CF (TR30)	Sized	-	Epoxy (Bis. A/F)	CVD	Batch	31.8 ± 5.0 (+11%)[‡]	-	-	-	Uniform	Aligned (⊥)	> 20000	2016	[187]
CF (M46J)	Sized	5.23 ± 0.20	Epoxy (EPN)	Sizing	Batch	38.4 ± 0.1[◊] (+70.6%)	-	-	-	Scarce	Random (//)		2014	[188]

[¤] = used as control including any surface treatment (unsized = as-received/never sized, sized = as-received/sized by manufacturer, desized = sizing removed by thermal or chemical treatments). [†] = thickness of CNT layer perpendicular to carbon fibre surface. [†] = details not readily available or specified in text and are taken from graphs using Graph Grabber (V2.0.1, Quintessa Ltd, UK), previous papers, or from a manufacturer data sheet. [‡] = mean values generated are within error, when error is presented. // and ⊥ *= denotes the preferential orientation of the CNT coverage with regards to the carbon fibre substrate. [♠] = thickness of the coating estimated via AFM subtracting control fibre surface roughness from CNT-grafted-CFs. [◊] = additional coating present on the carbon fibre including melamine, diazonium salts, PAMAM, polymeric sizing agents, silane, pyrolytic carbon, Al_2O_3. Epoxy: GA = Glycidyl-amine; GE: = Glycidyl-ether; PPEGGE = diglycidyl ether of polypropylene glycol; EPN = Epoxy phenol novolac.*

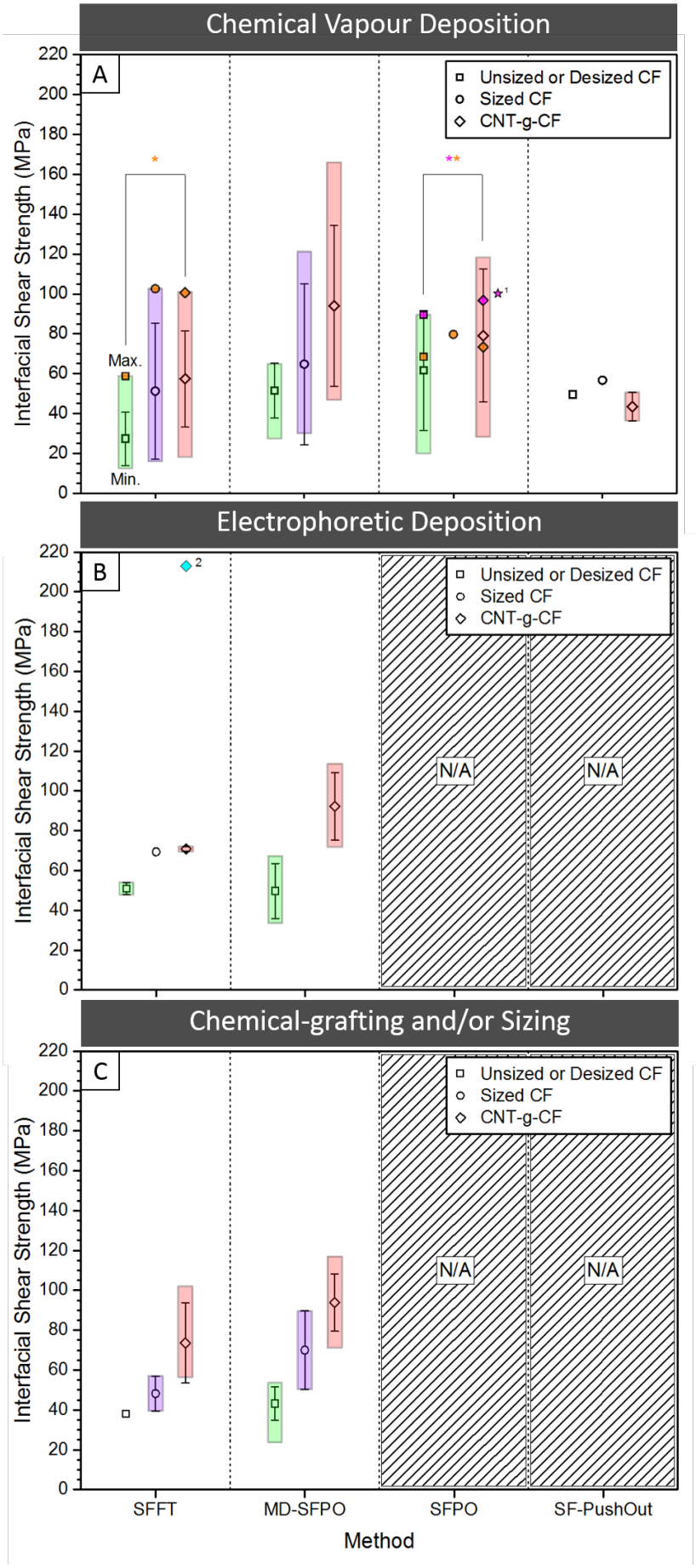

Chemical Vapour Deposition
A
Unsized or Desized CF
Sized CF
CNT-g-CF
Interfacial Shear Strength (MPa)
Max.
Min.
Electrophoretic Deposition
B
N/A
N/A
Chemical-grafting and/or Sizing
C
N/A
N/A
SFFT
MD-SFPO
SFPO
SF-PushOut
Method

Fig. 2.22 Collated literature values of apparent interfacial shear strength determined from single fibre fragmentation tests (SFFT), microdroplet debond (MD-SFPO), single fibre pull-out (SFPO) and single fibre push-out (SF-PushOut) for CNT-g-CF obtained from (a) chemical vapour deposition, (b) electrophoretic deposition and (c) chemical grafting and/or sizing. Mean values for unsized/desized CF, Sized CF and CNT-g-CF (open -square, -circle and –diamond, respectively) with standard deviation (bracket) and minimum-maximum range (green-, violet- and red- rectangles) associated. [1]Data point obtained from the combination of CNT-g-CF with a SWCNT-reinforced epoxy system [4]. [2]Outlier not included in the measurement of the mean. Values generated in this work (filled data points; orange and pink) with statistical difference indicated (asterisks).

As anticipated, among all the CNT-grafting methods presented in **Table 2.2** and **Table 2.3**, only CVD is able to provide radially aligned CNTs. However, even though some large improvements in IFSS were achieved (up to +175%) over desized CFs [167], the length obtained for these configurations were all equal or superior to 3 µm which is expected to hamper the highly packed arrangement of primary fibres in FRPs. These relatively long CNTs were the result of CFs pre-treatment with an alumina, silica or magnesium sulfate coating which drastically affects the CNT growth kinetics yet generates another potentially weak CF/coating interface [167, 186, 187]. Indeed, work by Sager *et al.* showed that a CNT coverage with an aligned arrangement produced *via* CVD (and promoted by a $MgSO_4$ pre-treatment) led to similar IFSS as unsized CFs whilst a uniform, random, CNT coverage generated an IFSS increase of 71% over that of the unsized baseline [5]. On the other hand, untreated CFs (i.e. carbon-based growth substrates), led to uniform CNT coverages with a random normal arrangement rather than the predominantly planar arrangement observed for chemical grafting, sizing and EPD. In addition, CVD, similarly to EPD, allows for some control of the thickness/length of the CNT layer within the range of interest, namely between 0.1 and 1 µm. On the other hand, chemical grafting shows limited CNT thicknesses, generally inferior to 100 nm. One recent study showed the potential of chemical grafting for tailoring CNT loading with increased concentration of 1,3-propodiamine linker leading to higher CNT density and improved IFSS (+42% over that of sized CFs) [171]. However, the maximum CNT loading obtained through chemical grafting was one order of magnitude lower than that conventionally achieved *via* CVD [181]. Chemical grafting is also the only CNT-nanoengineering method that has been suffering from limited scalability, with the entire body of work grafting CNTs onto small batches of short fibre sections.

Additionally, an issue that is recurrent with the reported values of IFSS for all grafting techniques and test methods, is the diameter used for its determination. Most study use the as-received fibre diameter (whilst some do not specify) which leads to an overestimation of the IFSS [166]. Indeed, it is suggested that the CNT layer lead to a reduction/suppression of stress concentration close to the primary fibre surface [123], with the CNT-grafted fibres experiencing high local stress concentrations around the tips of the CNTs, thus generating a fibre with a larger effective diameter. Therefore, the

diameter should be evaluated after failure, firstly, as an attempt to determine whether the fracture has occurred at the end of the CNT forest/sizing, secondly, to measure the effective interaction surface area and apparent IFSS.

The literature values of IFSS for all four grafting techniques are collated in **Fig. 2.22**. The general trend when focusing on the mean IFSS values is similar for all grafting methods, with unsized/desized CFs showing the poorest adhesion, as expected from their low compatibility with epoxy, and sized CFs on average inferior to CNT-grafted CFs. SF-PushOut stands out in that the CNT-grafted CFs exhibit a lower IFSS than unsized/desized CFs, likely due to a different loading mechanism, as previously mentioned. Given the number of variables presented so far, associated with the adhesion efficiency of CNT-grafted CFs, and the lack of in-depth multi-scale experimental studies, it remains a challenge to conclude which nano-engineered architecture would be best depending on the dominant/critical loading situation. Although, the recent development of multi-scale models does help understand how the beneficial effects of CNT-grafting can be maximised [85]. CNT strength being of utmost importance, it is important to develop a method that allows for processing of high quality CNTs in a highly scalable and robust manner.

Multifunctional interphases

Grafting CNTs on the surface of microfibril reinforcements do not only provide structural benefits but a number of new functionalities, including electrical conductivities, thermal conductivities and sensing (e.g. strain, damage) [16]. This approach becomes particularly interesting when combined with insulating materials (e.g glass/quartz fibres). The formation of an interconnected network of CNTs at the fibre/matrix interface, where stress concentration dominates, can provide monitoring of both the elastic strain along the fibre direction and the onset of fibre breakage/debonding. The monitoring of fibre deformation can operate through various mechanisms, including deformation of the CNT network conductive path [189], changes in the intertube tunnelling resistance (**Fig. 2.23**) [190], the inherent piezoresistivity of CNTs [191] and breakup of the in-plane CNT conductive path [192].

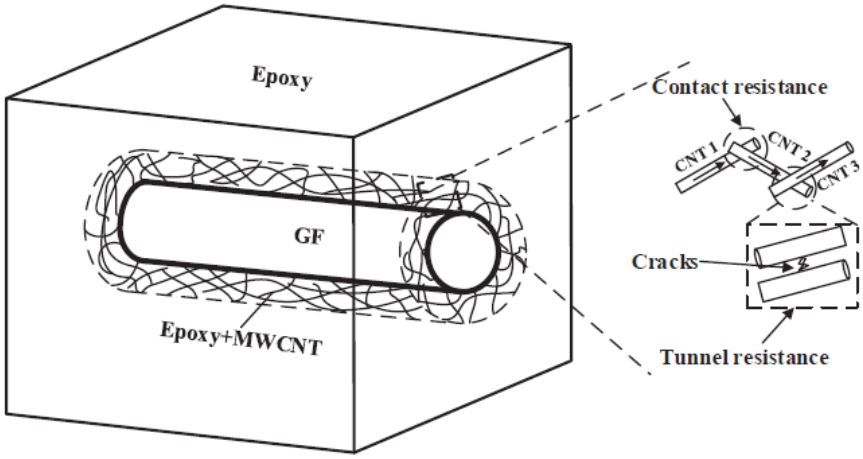


Fig. 2.23 Schematic representation illustrating the change in electrical resistance transmission mode after a crack progresses in the interphase. Reproduced from [193].

The introduction of CNTs in the interphase region leads to a relatively low percolation threshold as compared to random CNT/polymer percolated networks, which can be attributed to the efficient network formation, result of the CNT arrangement at the fibre/matrix interface [194]. Analogous selective localisation of CNTs has been found particularly efficient in co-continuous polymer blends and double percolated structures [195]. Whilst CNT/polymer systems can act as sensitive strain sensors [196, 197], as well as respond to matrix microcracking, providing insights into the nature, onset and evolution of matrix-dominated fracture mechanisms (including transverse microcracking and ply delamination [198]), these composite matrices are, however, poorly sensitive to fibre breakage [192]. The percolation through the coating, predominantly parallel to the fibres, provides an anisotropic behaviour as in-plane electrically conductive pathways form more easily along the fibre direction [199, 200]. The latter can be of interest depending on lay-up geometry (e.g. bouligand) for the non-invasive detection of in-service damage and the development of life prediction methodologies [201, 202].

It should be noted that CNT/epoxy nanocomposites exhibit a strong correlation between CNT loading and network sensitivity to strain (**Fig. 2.24**). Indeed, a lower concentration of CNTs, close to the critical percolation threshold, is more sensitive to changes in network geometry [190]. However, high CNT loadings (up to 10 wt.%) still show a two-fold improvement in strain sensitivity (also referred to as gauge factor, K) over traditional resistance stain gauge (e.g. constantan) [196].

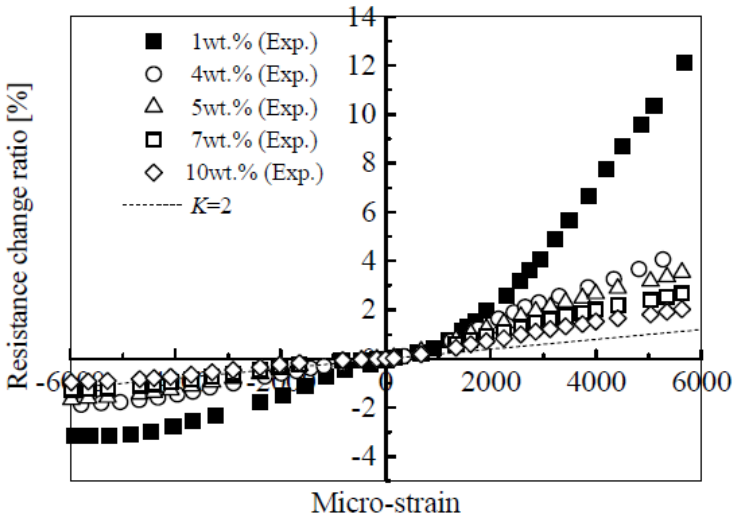


Fig. 2.24 Piezoresistivity of MWCNT/epoxy sensor for different CNT loading, as compared to conventional resistance strain gauge (K = 2). Reproduced from [196].

Similarly, a relationship between electrical conductivity of nanocomposites and strain sensitivity exists (**Fig. 2.25**). It appears clearly that specimens with higher resistances (i.e. lower CNT loading) possess higher strain sensitivity.

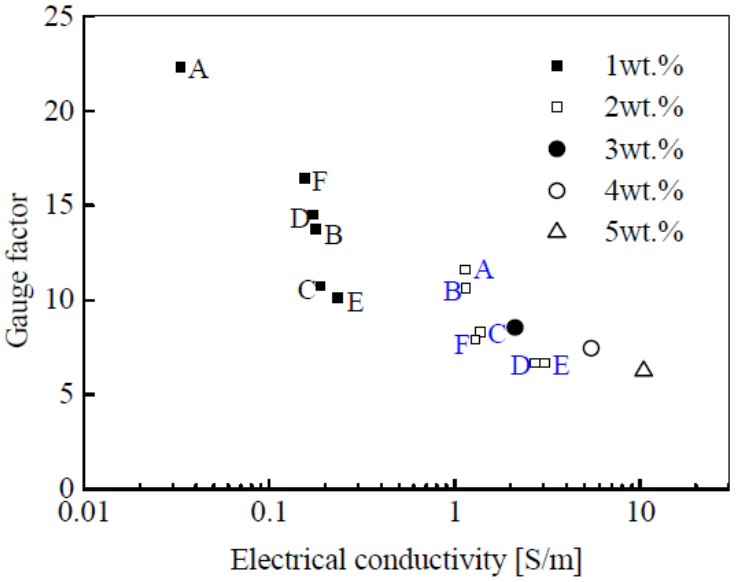


Fig. 2.25 Relationship between electrical conductivity and sensor sensitivity (gauge factor). Reproduced from [196].

CNT-grafted GF/epoxy networks are expected to behave similarly to CNT/epoxy nanocomposites, as presented in **Fig. 2.24** and **Fig. 2.25**. Hence, a fine tuning of the CNT loading/length and network architecture is necessary so that the nanostructured, conductive, interfacial region can combine piezo-resistive response, improved interfacial properties and electrically-monitored damage detection. Numerous studies have confirmed the multifunctional potential of adding CNTs in the

interphase region of glass fibres, with significant improvement in both mechanical and electrical properties as collated in **Table 2.4**. Interestingly, one recent study stands out, which reports the highest in-plane conductivity for CNT-grafted GF/epoxy of up to 100 $S.m^{-1}$ [203]. However, the composite's mechanical performance, including IFSS and flexural strength, was drastically lowered by as much as 36 % and 30 %, respectively. In fact, CNT length equal or superior to 2.5 μm affected the composite performance negatively, mainly due to CNT excessive length reducing the GF volume fraction.

The manipulation of the interface/interphase properties in glass/epoxy composites through the addition of CNTs, altering the relative conductivity of the composites, provides great opportunities for multifunctional applications, including static charge dissipation in composite radomes, electromagnetic interference shielding and protection from lightning-strike damage. However, the CNT-grafted fibre/epoxy systems typically produced and studied so far have been limited to batch experiments performed on single fibres [7, 204-207], yarns/rovings [193, 208] and GF fabric preforms [200, 203, 209, 210]. Hence, the requirement for large scale studies and commercial application relies on the development of a continuous, reel-to-reel process.

Table 2.4 Multifunctional properties of CNT-grafted GF/epoxy systems obtained from various CNT-grafting techniques, all performed in batch.

Fibre substrate[ᵡ]		CNT-grafting method	CNT content (wt. %)	IFSS [MPa]	ILSS [MPa]	In-plane Electrical cond. σ ($S\ m^{-1}$)	Gauge factor K	Year	Ref.
Type	Surface condition								
E-GF fabric	Sized	Spray-coating	0.75	-	48 (+5%)[‡]	1.34 ± 0.13x10^{-3}	6.5 ± 0.2	2019	[210]
GF yarn	Sized	Dip-coating	-	38 (+26%)	-	-	-	2018	[193]
S2-GF fabric	Sized	CVD	1.5	33 (+8%)	-	2	-	2017	[203]
E-GF fabric	-	Sizing		-	-	< 5	2.04 ± 0.23	2015	[200]
E-GF	Unsized + γ-APS	Dip-coating	-	65 ± 6 (+45%)	-	0.79	-	2014	[207]
E-GF fabric	Sized	EPD	-	-	83 (+80%)	1	-	2013	[209]
ARG-GF	Unsized	EPD	0.05	- (+30%)		0.01	~ 0.5[†]	2010	[206]
Silfa-GF	Sized	iCVD	-	24 (+156%)	-	-	-	2010	[7]
E-GF	Sized	Sizing	0.5	109 ± 29 (+91%)	-	-	-	2010	[208]
ARG-GF	Unsized	Dip-coating	-	-	-	0.03	1.3	2010	[194]

[g] = used as control including any surface treatment (unsized = as-received/never sized, sized = as-received/sized by manufacturer, desized = sizing removed by thermal or chemical treatments). [†] = details not readily available or specified in text and are taken from graphs using Graph Grabber (V2.0.1, Quintessa Ltd, UK), previous papers, or from a manufacturer data sheet. [‡] = mean values generated are within error, when error is presented. γ-APS = gamma-aminopropyltriethoxysilane. If several CNT configurations were presented, the one showing the best mechanical improvement, i.e. IFSS, was selected.

2.3.4. Mechanical properties of CNT-nanoengineered FRPs

Structural macroscopic delamination is typically characterised *via* three-point bending, double-cantilever beam (DCB) and end-notched flexure (ENF). These techniques allow for the estimation of the interlaminar shear strength (ILSS), mode I and mode II fracture toughness, respectively. The ILSS quantifies the resistance to the initiation of cracks whilst the fracture toughness evaluates the resistance to crack propagation. Although CNT-based bulk resins and interlaminar reinforcements are known to provide significant improvement in fracture toughness, the introduction of CNTs in the interphase region predominantly improves the ILSS. As a result, this section will mainly discuss the literature associated with the evaluation of the ILSS for CNT-based hierarchical composites.

The three most widely used composite laminate techniques for the characterisation of shear properties includes in-plane shear (or off-axis [±45] tensile), Iosipescu shear and short beam shear (SBS) [71]. Even though the former two methods are well-accepted shear test methods in the composite community, the latter is usually preferred because of its reliability, simplicity and relatively modest specimen dimensions, reducing the need for significant quantity of raw materials and making it an attractive materials screening test. Despite the simplicity of the SBS test and the reasonable values of shear strength typically generated, the short length of the beam coupled with stress concentrations at the loading and support points, creates a complex stress state in the composite (**Fig. 2.26**), rather than the parabolic shear distribution desired, and suggested from the classical beam theory [211]. For small span-length to thickness ratio, high stress concentrations on the compressive face may lead to premature failure by crushing [212]. It is therefore necessary to combine SBS testing with fractographic observations to ensure that non-shear or mixed mode failure – which would invalidate the data – are avoided.

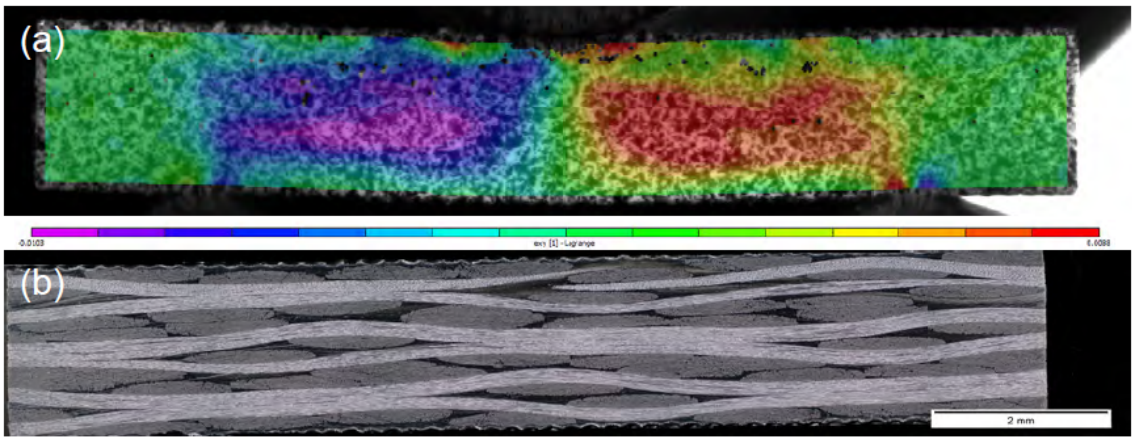


Fig. 2.26 (a) Digital image correlation contour plot of shear strain in a CFRP SBS specimen (side view). (b) Micrograph of a polished SBS specimen with 0/90 degree plies. Reproduced from [213].

It should be noted that the mesoscale architecture (i.e. ply lay-up) has a significant effect on the evaluation of the ILSS. Indeed, fibre bridging, specifically in the case of unidirectional (UD) composites, where the fibres of adjacent plies bridge the delamination plane and act as crack arrestors, tends to artificially enhance both the ILSS and the fracture toughness. The failure initiation in these UD composites is typically less sensitive to microfibre interface changes [214]. It is suggested that a matrix failure initiation may be prevailing in UD composites, in contrast to woven systems, where crimp may result in the preponderance of fibre/matrix debonding and pull-out, leading to a larger dependence on IFSS.

The main design strategies for the production of CNT-nanoengineered FRPs presented in the three previous sections, including bulk resin reinforcement, interlaminar reinforcement and the targeted reinforcement of the fibre/matrix interface with associated mechanical properties are collated in **Table 2.5**.

Table 2.5 Interlaminar shear strength (ILSS) and in-plane strength of CF/epoxy composites reinforced with CNTs using different approaches.

Materials[†]		CNT-nanoengineering techniques	Scalability	Effect on the mechanical properties		Testing methods	Comments	Year	Ref.
Fibre	Resin			ILSS [MPa]	In-plane US variation				
I. Interlaminar reinforcement									
UD CF (*sized*) prepreg (AS4/8552)		Nanostitch A-CNTs (CVD) across all ply-ply interface	Batch[1] (3 x 4 cm^2)	96.2 ± 0.9 (+1.3%)[‡]	-0.3% (tension)[‡] +14% (comp.)	SBS, OHC, Tension bearing, Micro-CT	Insensitivity of SBS due to complex failure mechanisms, modelling suggest a 20% improvement in ILSS given a 50% increase in interlaminar toughness.	2019 /2016	[117, 118]
UD CF (*sized*) thinpreg (HTS40/Q-1112)		Nanostitch A-CNTs (CVD) at the centre of the laminate	Batch	80.6 ± 0.6 (+5.2%)	-	SBS, 3D SRCT	50% increase in the interlaminar regions thickness potentially causing an increase in interlaminar toughness hence ILSS.	2018	[119]
UD CF (*sized*) prepreg (T700/epoxy)		CNT buckypaper placed at the centre of the laminate	Batch (2.5 x 20 cm^2)	87.0 ± 3.8[¤] (+29%)	-	SBS, ENF	73% improvement in mode-II interlaminar fracture toughness. Control should include a resin-rich baseline.	2015	[115]
UD CF (*sized*) prepreg (TR30S/epoxy)		CNF buckypapers placed in the 3 central planes of the laminate	Batch	69.3 ± 4.7[¤] (+31%)	-	SBS, ENF	Low CF volume fraction. Tough response potentially due to thickening of the resin rich region between plies.	2012	[116]
WO CF (*sized*) fabric (T300)	Epoxy (Bis. A)	A-CNTs (CVD) array placed at the centre of the laminate	Batch (2.5 x 1.2 cm^2)	25.6 (+2.5%)[‡]	-	Iosipescu shear	CNT array ca. 500 µm long greatly influence the spacing between the central plies. Shear modulus doubled.	2008	[215]
UD CF (*sized*) prepreg (AS4/3501-6)		f-SWCNT (RONa) /3501-6 films placed in the 9 central planes	Batch (30 x 30 cm^2)	96.8 ± 2.8[¤] (+1.7%)[‡]	-	SBS	Visible micron-scale SWCNTs aggregates present after dispersion in epoxy and solvent removal.	2006	[216]

UD CF (*sized*) fabric (T700)	Epoxy (TGDDM)	Spray coating SMA-grafted MWCNTs	Batch (10 x 15 cm^2)	69 ± 5 (+43.8%)	-	SBS, 3-point bend	Effect of SMA on interfacial properties not studied.	2018	[112]
UD CF (*sized*) fabric (T700SC)	Epoxy (E51, DGEBA)	Spray coating f-MWCNTs (COOH)/ Epoxy (E20)	Batch	49.8 (+12.6%)	+2.2% (tension)‡	SBS, DCB, ENF, tensile, 3-point bend	Epoxy binder (E20) may explain the increase in toughness and ILSS. Control sprayed (E20) without CNTs not investigated.	2013	[113]
II. Reinforcement of the bulk matrix									
CF tow (*sized*) (AS4C-GP)	Epoxy (Bis. A)	Powder impregnation[2] MWCNTs	Cont.	81 ± 1 (+32%)	-	SBS, DCB	CNT content of up to 25 wt.% achieved. Heterogeneously distributed CNTs results in enhanced fracture toughness.	2019	[97]
CF tow (*desized*) (T700S)	Epoxy (Bis. A)	Shear mixing/ Ultrasonication f-MWCNTs (COOH)	Batch	73.3 (+4.8%)‡	+10.4% (tension)	SBS, SFFT, tensile	UD laminates. No sized CF control.	2017	[147]
WO CF (*sized*) fabric (-)	Epoxy (-/Amine)	Shear mixing MWCNTs	Batch	46.7 (+4.7%)‡	-	SBS, DCB, ENF	Mode I and mode II fracture toughness doubled.	2017	[217]
UD CF (*sized*) fabric (IMS60)	Epoxy (-/Amine)	Calendaring and spray coating MWCNT/Epoxy mixture	Batch	67 ± 4 (-4.3%)‡	-	SBS, DCB, DMA	No improvement of the mechanical properties. Increase in through-thickness conductivity.	2017	[218]
WO CF (*sized*) fabric (T300)	Epoxy (DGEBF)	Shear mixing CNTs	Batch	43 (+11%)‡	+10.3% (tension)‡	SBS, OHT, FWT	No significant improvement of the composite mechanical properties.	2016	[219]
WO CF (*sized*) fabric (HTA)	Epoxy (Bis. A)	Shear mixing MWCNTs	Batch	43.1 ± 1.2 (-0.2%)‡	-	SBS, ENF, impact, compression	Higher damage tolerance observed for CNT-reinforced CFRPs.	2014	[220]

Table 2.5 (Continued)

Materials[†]		CNT-nanoengineering techniques	Scalability	Effect on the mechanical properties		Testing methods	Comments	Year	Ref.
Fibre	Resin			ILSS [MPa]	In-plane US variation				
WO CF (*sized*) fabric (-)	Epoxy (DGEBF)	Calendering f-XDCNTs (NH_2)[3]	Batch	44.3 ± 0.6 (+21.8%)	-	SBS, DMA	Covalent reaction between primary amine of f-XDCNTs and silane in CF sizing.	2014	[221]
CF tow (*sized*) (TR30S)	Epoxy (Bis. A)	Shear mixing f-MWCNTs/ surfactant + prepregging	Semi-cont.	63 ± 5[¤] (+11%)[‡]	-	SBS, 3-point bend, in-plane shear	No significant changes in ILSS nor flexural properties. CF volume fraction relatively low, ca. 40 ± 5%.	2009	[222]
CF tow (*sized*) (-)	Epoxy (DGEBA)	Calendering MWCNTs/ compatibilizer (prepregging)	Semi-cont. (30 x 200 cm^2)	66 ± 5[¤] (+0.2%)[‡]	-8% (tension)	SBS, DCB, tensile	CNT aggregates act as micro-centres of stress concentration around broken fibres reducing the strength of UD composites along the fibre direction.	2009	[223]
III. Targeted reinforcement of the fibre/matrix interface									
CF (*desized*) fabric (T700)	Epoxy (Bis. A)	EPD – f-MWCNTs (COOH)	Batch	58.2 (+55%)	-	SBS, Microdrop debonding	No control sized CF/epoxy. Two-fold decrease in moisture absorption upon CNT-grafting.	2018	[146]
UD CF (*sized*) fabric (HTS45)	Epoxy (Bis. A)	EPD – MWCNTs DI-water dispersion	Cont.	65.6 ± 1.3 (+0.6%)[‡]	-	SBS, 3-point bending	Ca. 40% decrease in flexural strength due to water induced misalignment.	2018	[96]
CF tow (*desized*) (T700S)	Epoxy (Bis. A)	EPD – f-MWCNTs (COOH)	Cont.	88.25 (+10.5%)	+1.3% (tension)[‡]	SBS, SFFT	No control sized CF/epoxy tested for ILSS. Flexural strength and modulus improved by 9.4 and 15.4%, respectively.	2017	[95]

CF tow (*desized*) (T700S)	Epoxy (Bis. A)	EPD – f-MWCNTs (COOH)	Semi-cont.	80.78 (+15.5%)	+24.4% (tension)	SBS, SFFT, tensile	No sized CF control.	2017	[147]
UD CF (*desized*) fabric (-)	Epoxy (-)	EPD – f-MWCNTs (COOH)	Batch	58.2 (+58.6%)	-	SBS	No commercial sized CF control. CNT grafting density marginally improved via ultrasonically assisted EPD.	2016	[126]
CF tow (*desized*) (T700)	Epoxy (Bis. A)	EPD – f-MWCNTs (COOH)	Cont.	58.87 (+60.2%)	-	SBS	Large CNT aggregates. No sized CF reference. CF bridging effect observed.	2015	[93]
CF tow (*sized*) (UTS50)	Epoxy (Bis. A)	EPD – MWCNTs	Cont.	Up to 58.2 (+40%)‡	-	Double notched compression , SFPO	UD laminates. No correlation between ILSS and CNT loading. Large scatter in ILSS values.	2014	[94]
UD CF (*desized*) fabric (T700S)	Epoxy (DGEBF)	EPD – f-MWCNTs (ozone/PEI)	Batch	55 (+72%)	-	In-plane shear, DCB	Significant increase in fracture energy due to high levels of MWCNTS in the resin-rich interlaminar region.	2012	[125]
WO CF (*sized*) fabric (TR30)	Epoxy (Bis. A)	EPD – f-MWCNTs (NH_3^+)	Batch (8 x 8 cm)	72 (+13%)	-	SBS	Cu (anode) nanoparticles co-deposited with MWCNTs.	2011	[224]
WO CF (*sized*) fabric (IM7)	Epoxy (DGEBF)	EPD – f-CNFs (amine)	Batch (17 x 25 cm^2)	59.6 (+12.4%)	-	SBS, compression	Stiffer interphase due to f-CNFs/epoxy covalent interactions.	2011	[225]
WO CF (*desized*) fabric (IM7)	Epoxy (Bis. A)	EPD – f-MWCNTs (COOH)	Batch (10 x 15 cm^2)	49.5 ± 2.8ǂ (+25%)	-3.7% (tension)‡	SBS, tensile	30% improvement of out-of-plane electrical conductivity.	2007	[124]

Table 2.5 (Continued)

Materials[†]		CNT-nanoengineering techniques	Scalability	Effect on the mechanical properties		Testing methods	Comments	Year	Ref.
Fibre	Resin			ILSS [MPa]	In-plane US variation				
CF tow (*sized*) (JH-T800)	Epoxy (-/Amine)	Sizing – f-MWCNTs (COOH)	Batch	110.58 (+27%)	-	SBS, SFFT	UD laminates, SBS specimens may not fail solely in shear. 59% improvement of the flexural strength.	2019	[131]
CF tow (desized) (T700S)	Epoxy (Bis. A)	Sizing – f-MWCNTs (OH)	Cont.	75.06 (+13.4%)	-	SBS, 3-point bend, f-AFM	UD laminates. No sized CF control. CNT oriented axially with CFs. 20.3% increase in flexural strength.	2015	[92]
CF tow (*unsized*) (T300)	Epoxy (DGEBA)	Sizing – f-MWCNTs (COOH)	Batch	39.3 ± 2.5[⁑] (+67.1%)	+2.7% (tension)[‡]	SBS, single fibre tensile	Absence of commercial sized CF control.	2014	[226]
UD CF (*sized*) fabric (T700SC)	Epoxy (DGEBA)	Aqueous suspension f-MWCNTs (COOH)	Batch	35 ± 2.1 (+12.9%)	+11% (tension)[‡]	SBS, SFFT, tensile	Inhomogeneous CNT coverage. CNTs oriented axially with CFs.	2013	[154]
CF tow (*desized*) (-)	Epoxy (Bis. A)	Chemical grafting (CF-CNT-POSS)	Batch	86.84 (+31.6%)	-3.2% (tension)	SBS, single fibre tensile	No clear evidence of shear failure. Lack of sized CF control.	2015	[130]
CF tow (*sized*) (T700SC)	Epoxy (Bis. A)	Chemical grafting (CF-POSS-CNT)	Batch	110.2 (+33.6%)	0% (tension)	SBS, SFTT, drop-weight impact, f-AFM	Complex grafting procedure. CF-POSS without CNTs show a 18.1% ILSS improvement over as-received CFs.	2011	[139]
UD CF (*sized*) fabric (HTS45)	Epoxy (TGDDM)	CVD – A-CNTs grown on CF fabric at 480 °C	Batch (2 x 6.4 cm^2)	90.0 ± 1.5[⁑] (+3.9%)	-	SBS, X-ray micro-CT	Thermoplastic weft growth artefacts (absence of CNTs) due to localised variation in gas composition and CF surface chemistry.	2019	[214]

CF fabric (*desized*) (-)	Epoxy (Bis. A)	CVD – CNTs grown on CF fabric at 700 °C	Batch	14.4 ± 0.6⁑ (+102%)	-	SBS, tensile, 3-point bend, ENF	Long CNTs (>5 µm) hinders CF volume fraction. Low ILSS measured.	2018	[227]
CF tow (*desized*) (-)	Epoxy (Bis. A)	iCVD – MWCNTs grown on CF at 800 °C + PI-BDA wrapped SWCNT epoxy system	Batch	47.59 ± 2.26 (+103%)	-	SBS	Tensile strength of the CFs potentially damaged from CNT-grafting. Shear failure not confirmed with fractography. Sized CF control missing.	2017	[228]
WO CF (*sized*) fabric (HTA40)	Epoxy (RTM6, Hexcel)	CVD – A-CNTs grown on CF fabric at 480 °C	Batch (2 x 2.5 cm^2)	41.8 ± 2.3 (-34.5%)	-	SBS, DIC	ILSS decrease potentially due to CFs sizing in the bulk laminate thermally degrading.	2016	[213]

† *Used as control including any treatments. All carbon fibres included in this table are produced from PAN precursor.* ‡ *Mean values generated are within error.* ⁑ *Details not specified in the text, hence taken from graphs using Graph Grabber (V2.0.1, Quintessa Ltd, UK). Carbon fibres (CFs) are sized unless specified otherwise. (US: Ultimate strength; UD: Unidirectional; WO: Woven; SBS: Short beam shear; OHC: Open hole compression; SRCT: Synchrotron radiation computed tomography; ENF: End notch flexure; f-MWCNTs: Functionalised multiwalled-carbon nanotubes; DCB: Double-cantilever beam; CVD: Chemical vapour deposition, EPD: Electrophoretic deposition; SFFT: Single fibre fragmentation test; DMA: Dynamic mechanical analysis; FWT: Flatwise tension; f-AFM: Force modulation atomic force microscope; DIC: Digital image correlation).* [1] *Patent includes "continuous process" but has yet to be demonstrated in the literature [229].* [2] *Patented process consists in the impregnation of a fibre tow with a suspension of nanocomposite particles [230].* [3] *XD-grade CNTs consist of a blend of SWCNTs, DWCNTs, carbon black and metallic impurities [231].*

Surprisingly, the introduction of CNTs as interlaminar reinforcements did not provide substantial improvement in ILSS, with most reinforced systems showing similar ILSS than the control sized CF fabric/prepreg. The inclusion of a CNT and CNF buckypaper interlayer at the centre of the CFRP laminates showed a 29 % (87 MPa) [115] and 31 % (69.3 MPa) [116] improvement in ILSS, respectively. However, the absence of a suitable baseline with a resin-rich interlaminar region of similar thickness did not help identify whether the toughening effect and ILSS improvement were the result of the CNTs or of a bulkier epoxy region. Similarly, spray-coating of styrene maleic anhydride (SMA)-grafted MWCNTs on UD CF fabric led to a significant ILSS improvement of up to 44 % (69 MPa), yet the contribution from SMA on the toughness was not addressed [112]. Interestingly, nanostiching aligned CNT arrays across all ply-ply interfaces of aerospace grade prepregs provided a 14 % increase in compressive strength although the ILSS was left unaltered [117, 118].

The reinforcement of bulk epoxy, commonly performed *via* shear-mixing, have shown somewhat limited improvement in ILSS, with interesting increase in damage tolerance, mode I and mode II fracture toughness. One recent study, however, showed an ILSS improvement of up to 32 % (81 MPa) by adding as much as 5 wt.% CNTs in epoxy, a concentration 20 times superior to the conventional rheological percolation threshold [232], ingeniously adapting a thermoplastic-based powder impregnation route to epoxy systems [97]. Calendering of amine functionalised CNTs with epoxy was also found to enhance the ILSS by 22 % (44.3 MPa), likely due to the covalent reaction between primary amine on the CNTs surface and the silane present in the CF sizing, hence promoting the reinforcement of the interphase region [221].

The addition of CNTs directly at the fibre/matrix interface represents most of the literature for improving the shear properties of FRPs and include CNT-grafting techniques such as EPD, CVD, chemical grafting and sizing. EPD shows some significant improvement in ILSS over that of desized CFs, up to 72 % (55 MPa) for ozone-PEI functionalised CNTs [125]. However, the improvement compared to sized CFs remains rather limited with a 12 % (59.6 MPa) and 13 % (72 MPa) increase for amine functionalised CNFs [225] and amine functionalised CNTs [224], respectively. These limited increases could be the result of the harsh acid treatments associated with CNT functionalisation, thus deteriorating their mechanical properties. Surprisingly, only limited studies focusing on the growth of CNT through CVD led to the manufacture of SBS specimens, supposedly due to the limited dimensions of batch experiments, associated with furnace quartz tube diameters. Nevertheless, CNT growth on UD CF fabric was found to provide a mild improvement in ILSS of 4 % (90 MPa), which could have been potentially hindered by the presence of growth artefacts. In fact, it was hypothesised that the thermoplastic weft generated a local variation in reactive gases composition and CF surface chemistry leading to the absence of CNTs in those areas [214]. In contrast, CVD growth on woven CF fabric

drastically reduced the ILSS by 35 % (41.8 MPa), likely due to CNTs growing only locally on the exterior surfaces of the carbon fibre weaves and sizing thermally degrading in the intralaminar region where the failure could therefore initiate [233]. Interestingly, a recent study combining CNT-grafted CF (*via* CVD) to a SWCNT-reinforced epoxy system, led to a 102 % (47.6 MPa) improvement in ILSS over that of desized CF in epoxy. However, the relatively low ILSS value as compared to the neat as-received epoxy tensile strength (ca. 70.2 MPa) suggests complications with the preparation of the SBS specimens, including the control [228].

In contrast with conventional FRPs that exhibit relatively consistent mechanical properties through a range of experimental studies, CNT-nanoengineered FRPs do not show a systematic mechanical improvement due to both characterisation and processing variability. Scalability and, therefore, quality control is currently of utmost importance. Thus, developing a robust process is a major focus for the potential implementation of hierarchical composite production into pilot plants used for large-scale composite manufacture.

Therefore, it is crucial to investigate the potential of CNT-grafted fibres as reinforcement, both at the microscale and the macroscale thereby taking into consideration structural properties that are commonly used in the practical design of composites, as discussed in great details in **Chapter 4** and **Chapter 6** for quartz fibres and carbon fibres embedded in epoxy, respectively.

Chapter 3 : Materials and methods

This chapter introduces the materials, including fibres, catalyst precursors and matrices, and describes in detail the different apparatus used throughout the thesis. The continuous catalyst deposition process developed in this work is presented along with the modifications to the existing continuous CVD rig. The procedures developed for both the production and the characterisation of CNT-grafted fibres and their micro and macroscale model composites are also discussed.

3.1. Materials

3.1.1. Fibres

A continuous roving of 6000 filaments of sized quartz fibres, also referred to as "QFs" (Quartzel®, C14 1600 QS1318, average diameter ~ 14 µm, > 99.99% SiO_2, Saint-Gobain, FR) was kindly offered by the manufacturer and used in the preliminary studies for the growth of CNTs on a resilient substrate.

Subsequently, PAN-based carbon fibres (CFs), both unsized (AS4-12K-7D, HS-CP-5000 grade, average diameter ~ 7.1 µm, Hexcel, GB) and sized (AS4C-GP-12K-8, HS-CP-4000 grade, average diameter ~ 6.9 µm, Hexcel, GB) were used as whole tow (12000 filaments). To improve the surface chemical reactivity, the carbon fibres were oxidised through an in-line plasma treatment (details in Section **3.2.1** below). Details for the microscopic continuous fibres are collated in **Table 3.1**.

Table 3.1 Details for both carbon and quartz fibres from manufacturer's datasheet with associated sample name used consistently throughout the thesis.

Fibre substrate[†]					Sample name	Product	Company	Ref.
Type	Precursor	Surface condition	Number of fibres	d_f [µm]				
Carbon fibre (AS4C)	PAN	Sized	12K	6.9	AR-AS4-S	AS4C-GP-12K-8 (HS-CP-4000)	Hexcel	[234]
Carbon fibre (AS4)	PAN	Unsized	12K	7.1	AR-AS4-US	AS4-12K-7D (HS-CP-5000)	Hexcel	[235]
Quartz fibre (Quartzel)	Pure silica (SiO_2 >99.99%)	Sized	6K	14	AR-QF-S	Quartzel C14 1600 QS1318	Saint-Gobain	[236]

[†]*fibres were used in the form of a continuous tow. When denominated with the suffix AR-, the fibres were used as-received.*

3.1.2. Carbon nanotubes

Single-walled carbon nanotubes (P2SWCNTs, carbonaceous purity > 90%, diameter 4 - 5 nm, length 0.5 - 1.5 µm, Carbon Solutions Inc., US) purified by air oxidation were used as received for the manufacture of SWCNT-reinforced epoxy (refer to **Chapter 6**).

3.1.3. Catalyst precursors and gases

For catalyst precursor deposition, three different catalyst precursors were used as-received from the supplier, namely iron(III) nitrate nonahydrate ($Fe(NO_3)_3 \cdot 9H_2O$, CAS: 7782-61-8, ≥98% ACS reagent, Merck, GE), iron(III) acetylacetonate ($Fe(acac)_3$, CAS: 14024-18-1, ≥99% ACS reagent, Sigma-Aldrich,

GB) and nickel(II) acetylacetonate ($Ni(acac)_2$, CAS: 3264-82-2, ≥98%, VWR, GE), dissolved in ethanol (EtOH, 96%, Brenntag, AT).

The gases injected in the CVD furnace included acetylene in nitrogen (N_2: 98.7 vol.% and C_2H_2: 1.3 vol.%, C certificate), hydrogen in N_2 (N_2: 97.6 vol.% and H_2: 2.4 vol.%, C certificate) and N_2 (99.998 vol.% minimum) used respectively as carbon source, reduction and carrier gases. All gases were purchased from BOC gases, GB.

3.1.4. Matrices

A variety of epoxy resins were used for the manufacture of composite materials as summarised in **Table 3.2** with associated testing techniques.

Table 3.2 List of epoxy systems used in this thesis.

Epoxy system				Main reinforcement	Scale	Testing technique	Ref.
Resin	Hardener	Composition by weight	Curing cycle				
Epon 828	Jeffamine T-403	1:0.42	‡100 °C for 6 h	QF	Micro	SFPO	[237]
Prime 20 LV	ULV	1:0.19	T_{amb} for 24 h + 50 °C for 16 h	QF	Macro	Bundle test	[238]
L20	EPH161	1:0.25	‡100 °C for 20 h	CF	Micro	SFPO	[239]
Prime 20 LV	ULV	1:0.19	T_{amb} for 24 h + 50 °C for 16 h	CF	Macro	Bundle test	[238]
L20	EPH161	1:0.25	T_{amb} for 24 h + 60 °C for 15 h	CF	Macro	SBS	[239]

*‡ curing cycles were altered when compared to manufacturer's recommendation due to testing requirements (refer to Section **3.3.6**). SFPO: Single fibre pull-out, SBS: Short beam shear. T_{amb}: ambient room temperature.*

3.2. Methods

3.2.1. Continuous deposition experimental set-up

Catalyst precursors can be deposited on carbon fibres, both chemically or physically, using various methods, including electrodeposition [240], colloid deposition [241], incipient wetness [242] and physical vapour deposition [243]. Whilst some of these methods offer control over catalyst loading,

needs for specific environment, such as high vacuum, can hinder their scalability; they are preferentially used when processing small material batches (e.g. carbon fibre fabrics). Previous work within the group, by Qian [244] and Anthony [8], has shown that a simple metal-containing solution dipping method, adapted from the incipient wetness technique, could be successfully used as a route to decorate short sections of carbon fibre tows (< 10 cm) with catalyst precursor [6, 245]. However, when used on larger batches (~ 30 m), this solution dipping method was ineffective. Indeed, carbon fibre tow/tow and tow/support contact during drying led to both barren areas and catalyst agglomerates, forming inhomogeneous coverage of catalyst precursor particles. Difficulties in maintaining the carbon fibre tow under tension during deposition and the need for numerous handling steps was also a source of problems, leading to operator-induced carbon fibre misalignment within the tow. In any case, batch deposition processes are incompatible with truly large parametric studies due to their limited scalability and increased variability. Reducing handling and potential damage to the parent fibres underlying mechanical properties, through the use of an automated process, was therefore necessary. The developed continuous deposition process (**Fig. 3.1**) allows for the production of large quantities of catalyst precursor deposited carbon fibres. It was adapted from other in-line composite processing techniques [246], using the fibre processing line now located in the group of Prof Alexander Bismarck at the University of Vienna. At a speed of 20 $m.h^{-1}$, this line can process several hundreds of meters of carbon fibres within a day, providing enough material for extensive parametric studies to be conducted on the same "batch". The continuous deposition process also alleviates a number of issues encountered with its batch counterpart. Inhomogeneity in the catalyst precursor coverage can be avoided both by altering the fibre surface chemistry via plasma oxidation [247] and by maintaining tension in the line throughout the deposition process; tension in the tow can effectively spread the fibres and ensure infiltration of the metal-containing solution. Moreover, in-line drying, via infrared furnaces, helps avert drying artefacts and prevents tow/tow or tow/support contact.

The deposition process involves loading a carbon fibre spool onto a creel and establishing a closed-circuit tension control system with a DTH type tension detector (Max. 10 N, Ogura Clutch Co., LTD, Japan), which applies a constant tension of 0.4 - 0.5 N throughout the process. The fibre tow passes through a plasma jet several times (**Fig. 3.1**b) where the fibres are subject to an oxidative treatment of approximately 4 min by ionising the feed gas (oxygen or compressed air) at a pressure of 2.5 bar, flow rate of 35 $l.min^{-1}$ and using a power of 2.1 kW. After surface oxidation, the carbon fibres pass through a custom-made impregnation bath containing a metallic solution precursor with a residence time of approximately 2 min (**Fig. 3.1**c). A set of tensioning pins along with a pair of magnetic stirring plates maximise the spread of the fibres while the solution is kept under vigorous agitation, allowing

for a full impregnation of the tow. The catalyst precursor deposited carbon fibres are then dried in a set of IR-furnaces (**Fig. 3.1**a) at 40 and 70 °C, and subsequently collected on a spool wrapped in PTFE film. Once enough processed fibre has been collected (> 300 m), the spool (**Fig. 3.1**d) is removed from the pre-catalyst deposition line and transferred to the CVD line for CNT synthesis.

The deposition process was identical for quartz fibres with the exception of the in-line plasma oxidation step which was omitted since it was not required; the fibres are already relatively hydrophilic, and a good loading of catalyst precursor was readily achieved. Details regarding the choice of catalyst precursors for carbon fibres and quartz fibres can be found in **Chapter 4** and **Chapter 5**, respectively. It is worth noting that due to limited available laboratory space, the pre-catalyst deposition and CNT growth lines were not combined into a single line; the overall length required for the process exceeding 15 m. However, given that both lines operate creel-to-creel, there would not be any difficulty in integrating them together apart from small adjustments to the line-speeds so that they would match (approximately a 4-fold difference as it stands).

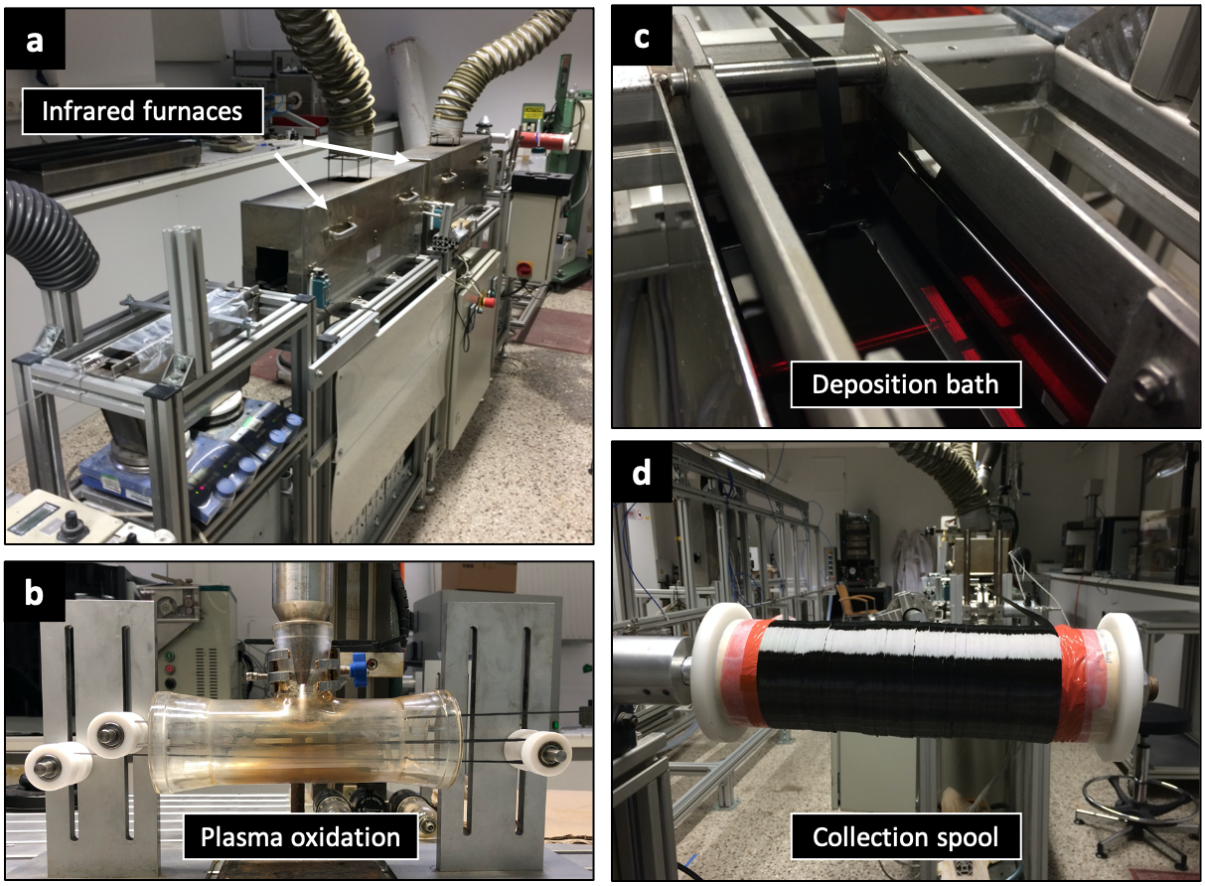


Fig. 3.1 Photographs of the continuous pre-catalyst deposition line set-up with close-ups on the (a) IR-furnaces, (b) in-lane plasma jet, (c) catalyst precursors deposition bath and (d) collection spool.

3.2.1. Continuous CVD experimental set-up

The continuous CVD line consists of three distinct regions (**Fig. 3.2**). Firstly, the deposited carbon fibres wind-off station, which comprises a tensioning unit along with electrical connections for the application of a potential difference, as described in **Fig. 3.5**. Secondly, The CVD furnace equipped with a temperature control unit and mass-flow controllers (MFCs). Finally, the wind-up section including a collection spool connected to a motorised pulley system which allows for real-time adjustments of the line speed.

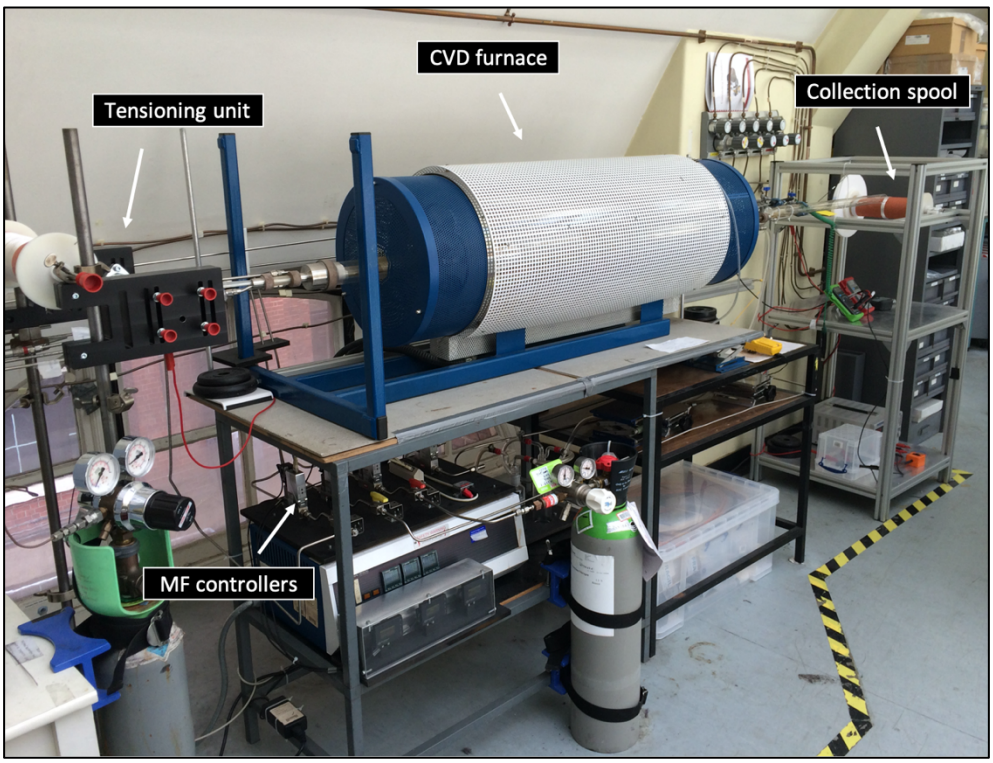


Fig. 3.2 Photograph of the continuous reel-to-reel CVD set-up.

The focus of the development was to create a continuous reel to reel process, implanting gas exchange regions to separate the catalyst reduction from the catalyst growth regions, and to isolate the reactive gases from the ambient environment. Therefore, an open 3-zone tubular furnace (PTF 15/-/610, Lenton, GB) containing an adjustable arrangement of internal quartz tubes was designed to define successive regions in which specific gas conditions can be achieved, while isolating each step of the process (heating under inert conditions, catalyst reduction and CNT growth, **Fig. 3.3**). Given the open nature of the furnace, and the CNT synthesis requirement for controlled environments, the furnace was subjected to an excess gas flow (> 10 $L.min^{1}$), avoiding infiltration of oxygen during synthesis and retaining the O/H/C ternary composition.

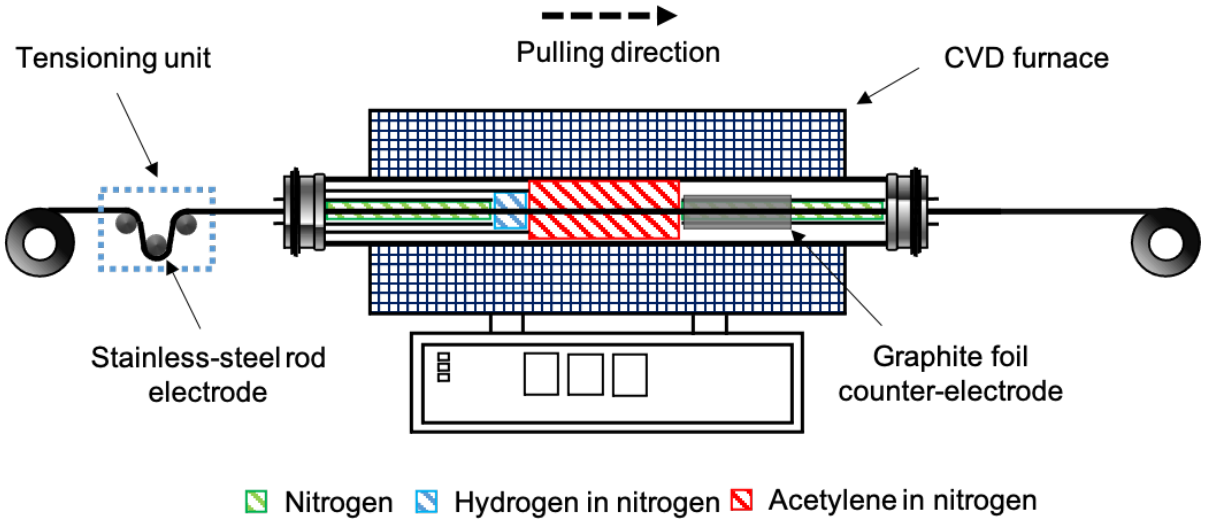


Fig. 3.3 Schematic representation of the CVD line equipped with an open 3-zone tubular furnace consisting of internal quartz sections forming the inert (N_2), reductive (2.4 vol.% H_2 in N_2) and growth (1.3 vol.% C_2H_2 in N_2) gas sleeves. Location of the electrodes for the capacitor-like arrangement indicated.

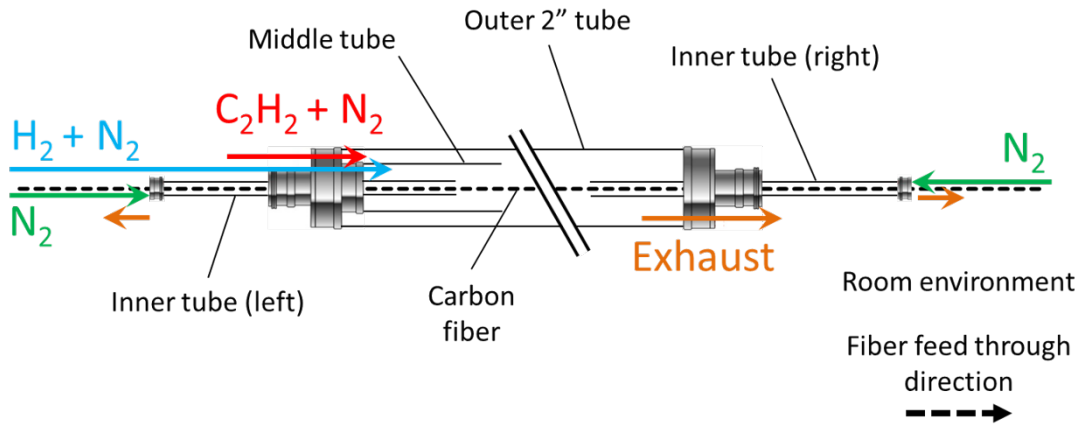


Fig. 3.4 Close-up schematic of the concentric quartz tubes which determine the reaction regions, with reactor gas inlet/outlets highlighted. Reproduced from [3]. Graphite foil counter-electrode not included.

Similar to batch CVD systems, both the reduction and growth regions are limited to the length of the furnace hot-zone, which is approximately 600 mm long in the aforementioned setup. Whilst the arrangement of the three quartz tubes highlighted in **Fig. 3.3** and **Fig. 3.4** allows for regions with specific gas conditions to be achieved (i.e. inert, reductive and growth environments), each tube length can be adjusted, offering direct control on the duration of both the reduction and growth steps.

Previous work within the group demonstrated that the application of a potential difference between the carbon fibres and a graphite foil counter electrode during CNTs synthesis significantly improved the uniformity of growth without compromising the tensile properties of the underlying fibres.

Improving upon the original design used by Anthony [8], a sheathed quartz tube was manufactured to contain and isolate the graphite foil counter-electrode from the carbon fibres. This sheath prevents broken carbon fibres causing a short-circuit and altering the applied potential to the system, which ultimately reduces intermittent variations along the fibre tow during CNT CVD synthesis (**Fig. 3.5**).

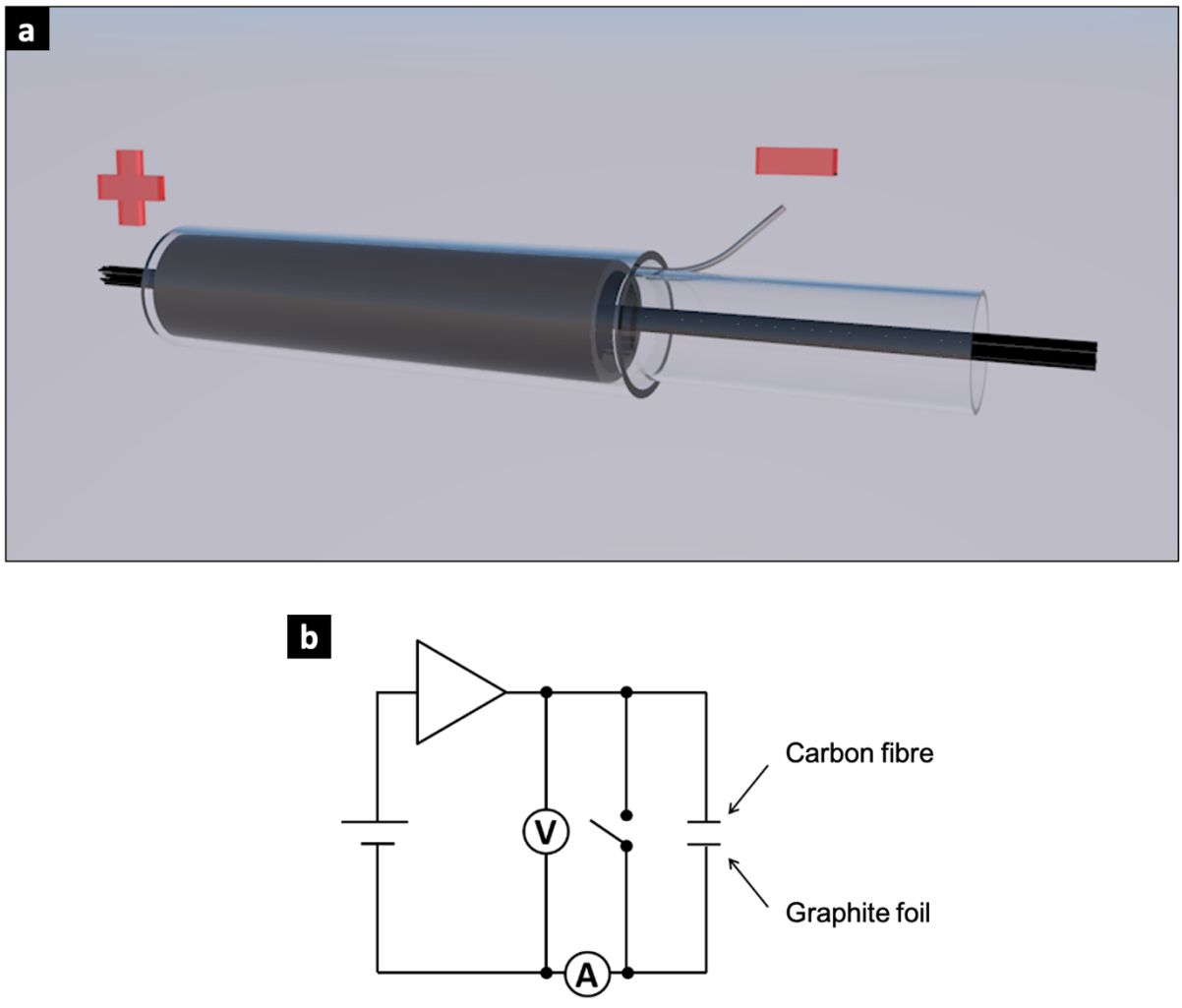


Fig. 3.5 (a) 3D representation of the co-axial capacitor arrangement inside the reactor (inner tube right, as defined in Fig. 3.4) including the connection made to graphite foil with stainless steel wire (b) Circuit diagram, the inclusion of the switch is to ensure complete discharge from the set-up at the end of the experiment.

Another modification to the CVD line was the addition of a custom-made tensioning unit consisting of three fixed stainless-steel rods rotating on ball bearings (**Fig. 3.2**, refer to **Annex 2** for the technical drawings). A slotted plastic frame, on which the ball bearings are supported, allows for vertical displacements of the rods, effectively adjusting the tension in the line. This alteration was deemed essential as recent findings evidenced CVD-induced reduction in both fibre strength and stiffness, caused by mechanochemical reorganisation of the underlying fibres when loosely heated at temperatures superior to 550 °C [248]. In addition, keeping the end of the fibre tow taut during growth

helped prevent fibre swaying and ensured the positioning of the tow at the centre of the furnace (and position relative to the counter electrode). A second modification consisted in changing the collection system, including pulleys and electrical motor, to extend the line speed range (0.1 to 10 $m \cdot h^{-1}$), thus reaching speed comparable to carbon fibre production lines. Additionally, mass flow controllers were re-configured to allow for higher gas flow rates, hence, preventing oxygen infiltration. A third modification involved re-designing the Swagelok gas lines in order to improve access, handling and facilitate the single-handed access point to the internal quartz tubes for re-configuration, replacement and cleaning, though the use of quick-release connections.

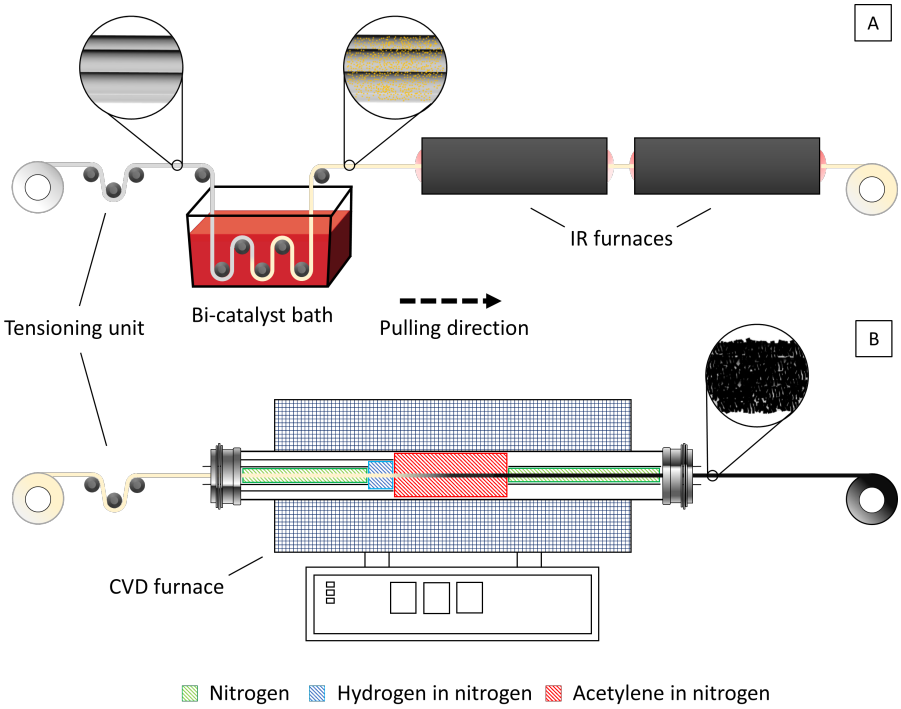


Fig. 3.6 Schematic of (a) the catalyst precursor deposition line with collection of the bi-catalyst decorated quartz fibres (after drying in infrared radiation (IR) furnaces) on the right-hand side reel; (b) The bi-catalyst deposited quartz fibres are introduced in the continuous chemical vapour deposition set-up for CNT-synthesis.

3.2.2. Continuous CVD set-up equipment details

Lenton furnace and thermometer

- PTF 15//610, Lenton, GB.
- Temperature probe: KHXL-IM30U-RSC-1000, Omega Engineering Ltd, GB.
- Thermometer: KM330 Single Channel, Temperature range, -50 °C to 1300 °C, accuracy, 0 to 1100 °C ± (0.2% of reading +1) °C, Kane-May by Comark, GB.

Quartz tubes and fittings

Table 3.3 Quartz tubes dimensions as manufactured by Robson Scientific, GB.

Quartz tubes	Length (mm)	Diameter (mm)	Wall thickness (mm)
Outer tube "A"	1600[¥]	51.0 ± 0.5	2.5 ± 0.2
Middle tube "B"	560; 600[¥]; 680	25.0 ± 0.2	2.5 ± 0.2
Inner tube (left) "C_1"	600; 640; 680[¥]; 720; 760	19.0 ± 0.3	2.5 ± 0.2
Inner tube (right) "C_2"	650[¥]; 900	19.0 ± 0.3	2.5 ± 0.2

[¥] *corresponds to the tubes used in the historical/control arrangement. All quartz tubes ends were flame polished.*

- Quick connect tube adaptors: bespoke concentric and cantilevered arrangement, stainless steel, LewVac LLP, GB. A variation of the stock item Hybrid Adapters: Quick Connect Adapters. The connection of the metal sleeve to the quartz tube is made using an O-ring seal to the outer surface of the quartz tube.

Motor, friction drive and creel

- Electrical motor: Crouzet, 82862202, 4.6 rpm with associated friction belt drive and custom-made PTFE pulleys.
- Creel structure: aluminium profiles bought from RS Components Ltd, GB, assembled in bespoke design by Imperial College London, Chemical Engineering Workshop, GB.

Power supply and electrical connections

- Power supply: Aim-TTi dual DC power supply, 30V, 2A.
- High voltage amplifier: MM3P1.5/12, 3 kV max, 0.5 mA max, 1:250, Spellman High Voltage Electronics, GB.
- Multimeter: IDM67, ± 0.7% voltage, ± 1.0% current, IEC 1010-1 CAT II 600V, ISO-Tech, GB.
- Steel pin electrode: ½" stainless steel tubing, Swagelok Company, US.

- Graphite foil counter electrode: 99.8%, C117933, Advent Research Materials Ltd, GB, approximate dimensions 100 mm x 500 mm x 0.2 mm.

Tensioning unit

- Custom-made plastic frame with two stainless-steel rods (½") free-rotating in a set of flanged bearings unit (½" ID), refer to **Annex 2** for technical drawings.

Mass flow controllers

Bronkhorst digital mass flow controllers were used with a computer interface, software FlowDDE V4.62 MBC Flow-Bus host with FlowView 10 V1.17, Bronkhorst UK Ltd, GB;

- Nitrogen: F-201CV-5K0-RAD-22-V, EL-FLOW Select, max flow 30000 sccm, ±0.5% reading plus ±0.1% full scale.
- Nitrogen with 2.4 vol.% hydrogen: F-201CV-5K0-RAD-22-V, EL-FLOW Select, max flow 30000 sccm, ±0.5% reading plus ±0.1% full scale.
- Nitrogen with 1.3 vol.% acetylene: F-201CV-200-RAD-22-E, EL-FLOW Select, max flow 2000 sccm, ±2% full scale.

3.2.3. Continuous CVD synthesis method

Catalyst-loaded carbon fibres are introduced into the continuous CVD system at room temperature and secured onto the creels. The furnace is then flushed with nitrogen (N_2, 10000 sccm) for at least 1 h. Once satisfactorily purged, the furnace temperature is increased at 10 °C.min^{-1} to 770 °C. During heating, further gas is added, namely hydrogen in nitrogen (2.4 vol.% H_2 in N_2, 3400 sccm) to reduce any potential inclusion of air into the system, whilst the tow is kept under tension and collected on the wind up unit at a speed of 1 m.h^{-1}. As an additional precaution, and to avoid damage to the carbon fibre tow, a potential difference (+ 300 V) was also applied during heating. Once the growth temperature is reached, acetylene (1.3 vol.% C_2H_2 in N_2, 325 sccm) is introduced in the furnace. The bi-catalyst precursor deposited carbon fibres are then continuously pulled through the furnace at speeds ranging from 1.2 to 10 m.h^{-1}, and exposed to different gas conditions in each gas sleeve (**Fig. 3.3**). As the tow enters the furnace, it is first exposed to an inert region (N_2, 10000 sccm) where the fibres are progressively heated. Once the tow reaches the hot-zone (about 770 °C), it is exposed to hydrogen diluted in nitrogen (2.4 vol.% H_2, 3400 sccm) for catalyst reduction. The hydrogen concentration was selected for safety on the basis that even at the furnace maximal temperature, the mixture would not be flammable. After reduction, the tow is then exposed to a gas mixture consisting of acetylene diluted in nitrogen (1.3 vol.% C_2H_2, 325 sccm), which acts as carbon source for CNT

synthesis. Finally, the fibres are passed through another inert region (N_2, 10000 sccm) before exiting the reactor unimpeded. In order to investigate various deposition parameters consecutively, and facilitate the collection of each type of processed fibres, one meter long tow sections were cut and combined using Zepellin bend knots (**Fig. 3.7**). Each tow section was separated by additional section of as-received AS4-US fibres to account for the length of the stable hot-zone (about 0.6 m), ensuring that the fibres generated for each condition were exposed to a complete CVD synthesis process including heat-up, catalyst precursors reduction, CNT growth and cool-down. All fibres present in the furnace when altering the processing variables, or during heating of the system were discarded.

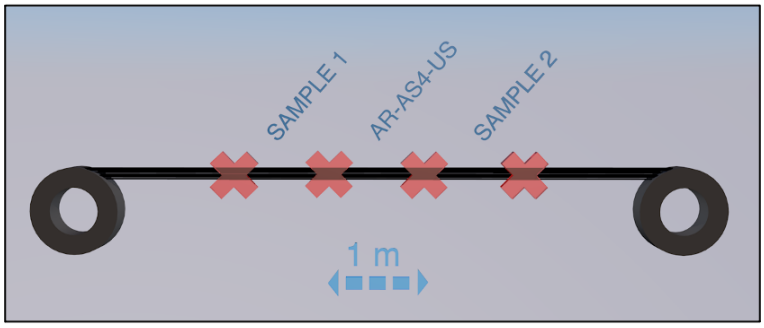


Fig. 3.7 Schematic representation of the daisy-chained bi-catalyst precursors deposited carbon fibres. The red crosses indicate the location of the Zepellin bend knots joining the one meter long carbon fibre sections together.

3.3. Characterisation techniques

3.3.1. Scanning electron microscopy

In order to confirm the formation of CNT, their morphology, and that of the fibre substrate, high resolution FE-SEM (LEO Gemini 1525) was used. These micrographs provide topographical images, detecting secondary electrons generated from the excitation of the sample by the primary electron beam [249]. To prevent charging of non-conductive specimens (i.e. AR-QF-S), an operating voltage of 1.0 kV was used. Conductive specimens, on the other hand, such as CFs and CNT-grafted QFs (CNT-g-QFs) were imaged at operating voltage of 5.0 kV, for improved resolution. The fibres were arranged in small bundles (ca. 100 filaments) on an aluminium stub and fixed using silver DAG (Agar Scientific, GB). SEM of CNT-g-QFs cross-sections were taken on specimens prepared by isolating a single fibre from the tow and using carbon tape to fix the fibre onto a slotted aluminium stub (AGG301D, Agar Scientific, GB). In order to limit observer bias and data misinterpretation, a statistical sampling approach was adopted for the analysis of SEM micrographs. A minimum of four sub-1000 filaments bundles were collected for each sample set. For analysis, the bundles were collected at two different locations along a one meter long section of processed tow, spaced by at least 50 cm. A minimum of two fibre bundles were collected per location, for SEM. Low magnification SEM

micrographs (about 0.5 to 1 k) allowed for full visualisation of the fibre bundles, but at the expense of resolving nanoscale features on the fibre surface. At this stage, 10 fibres were randomly selected and imaged at high magnification (about x200k), for a more detailed investigation of each sample set, evaluating the effect of deposition and growth conditions on the CNT coating thickness and coverage.

3.3.2. Thermogravimetric analysis

The thermogravimetric analysis technique measures weight as a function of temperature under a controlled atmosphere and can provide information about degradation temperatures and material composition. Hence, the thermal stability of QFs and CNT-g-QFs was assessed using a Mettler Toledo TGA/DSC 1 with a GC200 flow controller. Thermals scans were carried out in air (60 SCCM) from 100 to 850 °C at 10 °C.min^{-1}, after initially heating from 30 to 100 °C at 35 °C.min^{-1} and holding for 30 min, under N_2, to ensure a dry sample/system. CNT loading was estimated from TGA data as quartz fibres do not oxidise and remain as residue after the analysis.

3.3.3. Raman spectroscopy

Raman spectroscopy probes the structure of molecules based on the inelastic scattering of an incident beam of coherent light. The wavelength of the scattered light (characteristic of vibrational, rotational and other low -frequency modes [250]) is detected via a charge-coupled device (CCD) and an intensity spectrum is produced. The signature spectrum is dependent on the laser wavelength used and its interaction with the sample. This non-destructive technique, which has a high spatial resolution (0.7 μm) is commonly used for CNTs. Hence, the graphitic nature of the CNTs produced was investigated through Raman spectroscopy using a Renishaw inVia micro-Raman spectrometer with 532 nm (2.33 eV) DPSS diode laser (NA 0.8/50x, sample power 3.2 mW), in a backscattered geometry with relative spot size diameter of 1.2 μm [82]. Raman spectra in the range of 80-3200 cm^{-1} were collected and averaged for at least five different locations on the CNT-g-QFs tow. The intensity ratio of G- (1582 cm^{-1}) to D-mode (1350 cm^{-1}) (I_G/I_D), which characterises the degree of order of the sp^2 framework, was measured [250]. In addition, Raman mapping was performed along the CNT-g-QF fracture surfaces after single fibre pull-out in an attempt to identify the locus of failure.

3.3.4. Modified Wihelmy technique

The modified Wihelmy technique provides information on the wetting properties of microscopic fibres through their immersion in a liquid of known surface tension [251]. The technique was used to assess the efficiency of the oxidative plasma pre-treatment performed on CFs. The contact angle (θ) generated can be measured through the following equation:

$$\cos\theta = \frac{\Delta m.g}{n.\pi.d.\gamma_l}, \qquad \text{Eq. 3.1}$$

where Δm is difference in mass recorded during immersion or emersion of the fibres into the liquid resulting in advancing (θ_a) and receding (θ_r) contact angles, g the gravitational acceleration (9.80665 $m.s^{-2}$), n the number of fibres, d the fibre diameter and γ_l the liquid surface tension. The advancing contact angle (θ_a), measured on immersion, should be characteristic for the low-energy parts of the investigated surface whilst the receding contact angle (θ_r), determined on retrieving the fibres, i.e. during the de-wetting process, reflects the high-energy portion of the surface [252]. The contact angle hysteresis $\Delta\theta$, defined as the difference between θ_a and θ_r can be assumed to be a measure of the surface heterogeneity. Five CFs were fixed vertically onto a hanger (perpendicular to the liquid surface) using double sided tape and hung on a microbalance (MP8, Sartorius, Göttingen, Germany, ± 0.1 µg) [253], and slowly introduced in the liquid (DI water; γ_l = 72.8 $mN.m^{-1}$) at constant rate of 3 $\mu m.s^{-1}$ (**Fig. 3.8**). The weight difference was then recorded using a signal processing toolbox (MATLAB, Agilent VEE Pro, V.7.0.6310.9, 1991) data logger. The measurements were conducted on at least 5 single fibres.

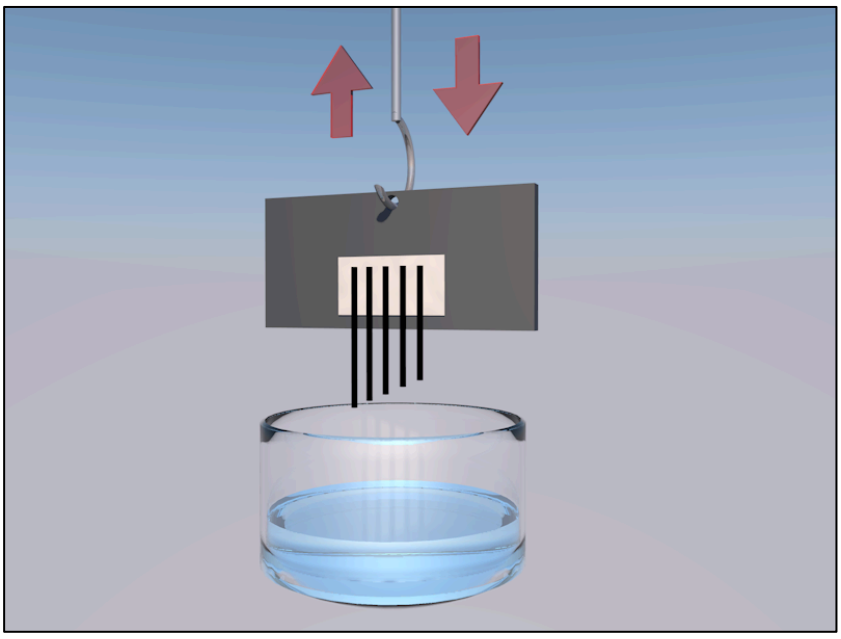


Fig. 3.8 Representation of the modified Wihelmy set-up with five carbon fibres fixed onto a hanger connected to a balance.

3.3.5. Single fibre tensile test

The single fibre tensile test is a simple and standardised technique that allows for the measurement of the effective fibre tensile strength, tensile modulus and strain to failure. The method was only used as a preliminary test for QFs given its time-consuming nature associated with the sample preparation.

Single fibre tensile tests were carried out on a TST350 Tensile Stress Tester (Linksys32, V1.9.1, Linkam Scientific Instruments Ltd., GB), following the standard BS EN ISO 11566, 1996, Method B [254]. The single fibre specimens were tested at a gauge length of 25 mm with a 20 N load cell at crosshead speed of 15 μm.s^{1}. A fibre was glued at both ends of a piece of cardboard using epoxy adhesive (**Fig. 3.9**a). Once secured in position in the tensile tester (**Fig. 3.9**b), the cardboard was cut so that only the fibre properties would be measured. The tensile strength (σ_t) was calculated from the following equation:

$$\sigma_t = \frac{F_{max}}{A_{CSA}} = \frac{F_{max}}{\pi r^2}, \quad \text{Eq. 3.2}$$

where F_{max} is the maximum force and A_{CSA} the cross-sectional area. The strain (ϵ) was calculated from the displacement from original position (Δ_x) and gauge length (L) such as:

$$\epsilon = \frac{\Delta_x}{L}, \quad \text{Eq. 3.3}$$

Finally, the tensile modulus was estimated from the gradient when σ_t was plotted as a function of ϵ. A minimum of 13 samples were measured for each data set.

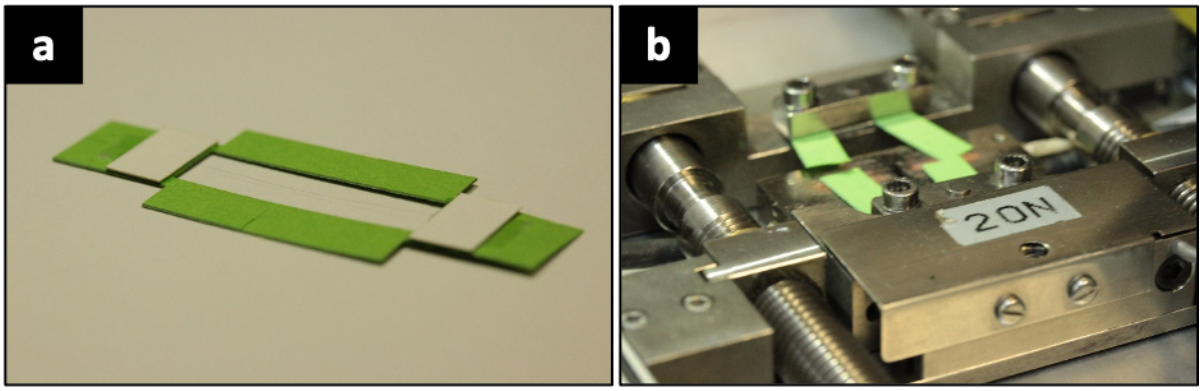


Fig. 3.9 Single fibre tensile (a) 25 mm gauge specimen and (b) testing unit with 20 N loading cell.

3.3.6. Single fibre pull-out test

Single fibre pull-out tests were carried out using a bespoke apparatus previously reported [145]. The technique allows for the measure of interfacial shear strength (IFSS), a measure of adhesion between a microscopic fibre and a resin. The specimens were prepared by embedding a single fibre in an epoxy droplet while altering the embedded length (ca. 30 - 100 μm) using a fine vertical adjustment screw (**Fig. 3.10**a, b). The epoxy resin was then heated using a built-in heating stage, removed from the holder, then placed in an oven for the completion of the curing cycle (see **Table 3.2** for details on curing cycle). The specimens were then mounted on the force sensor (using the tread of the screw), measuring the force with a resolution of 0.1 mN, while the free fibre end (ca. 10 mm) was glued

(cyanoacrylate) to a needle which was already attached (push fit) to a piezo-translator (**Fig. 3.10**c, d and **Fig. 3.11**) with linear resolution of 1.8 nm. The pull-out test was operated at a cross-head speed of 0.2 µm.s^{-1}. The apparent interfacial shear strength (IFSS, τ_{app}) was calculated using the following equation:

$$\tau_{app} = \frac{F_{max}}{A_e} = \frac{F_{max}}{\pi d_f l_e}, \qquad \text{Eq. 3.4}$$

where the fibre diameter (d_f), which includes any contribution from grafted CNTs, and embedded length (l_e) were measured *via* FE-SEM for each specimen after single fibre pull-out tests. A minimum of 13 specimens were tested for each sample set, and the average IFSS was obtained from a linear fit fixed at the origin of the population when pull-out peak force (F_{max}) is plotted as a function of embedded fibre area (A_e).

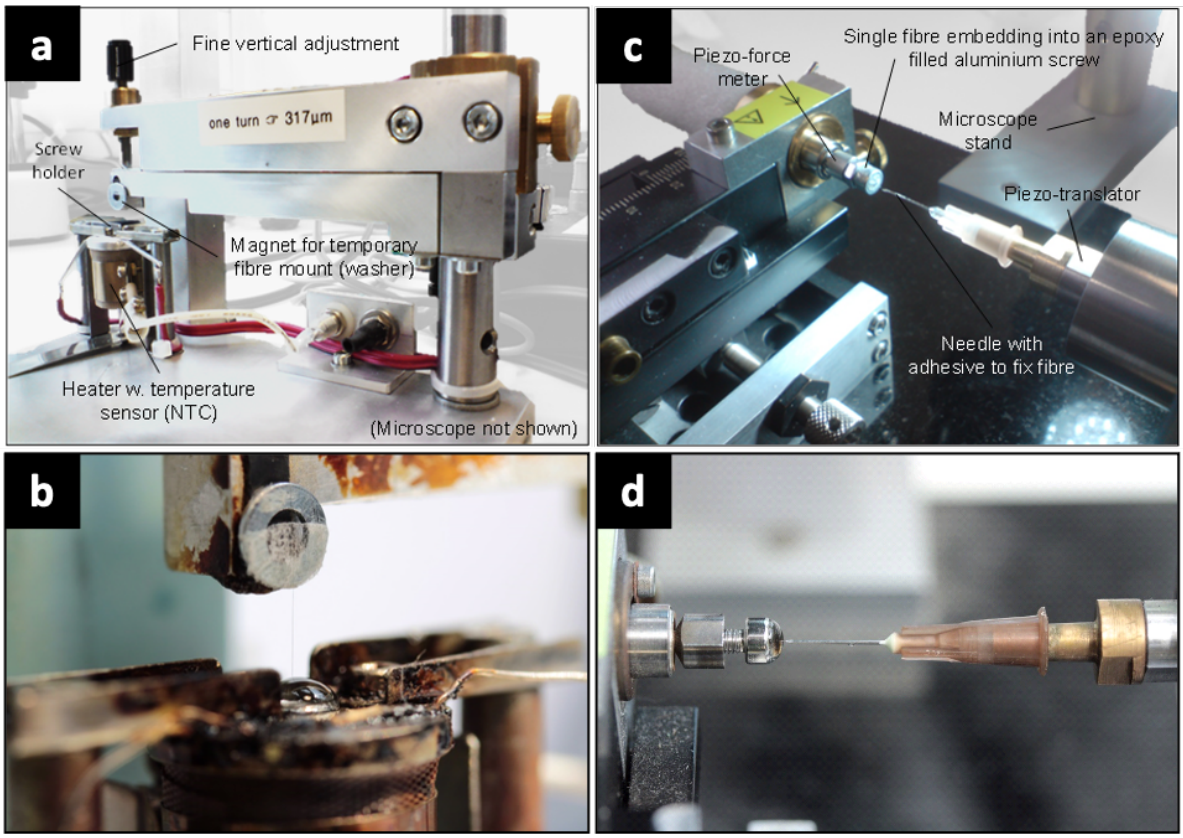


Fig. 3.10 Single fibre pull-out rig with (a, b) fibre embedding kit including a built-in heating stage for pre-curing the epoxy bead and (c, d) single fibre pull-out testing unit with force sensor and piezo-translator.

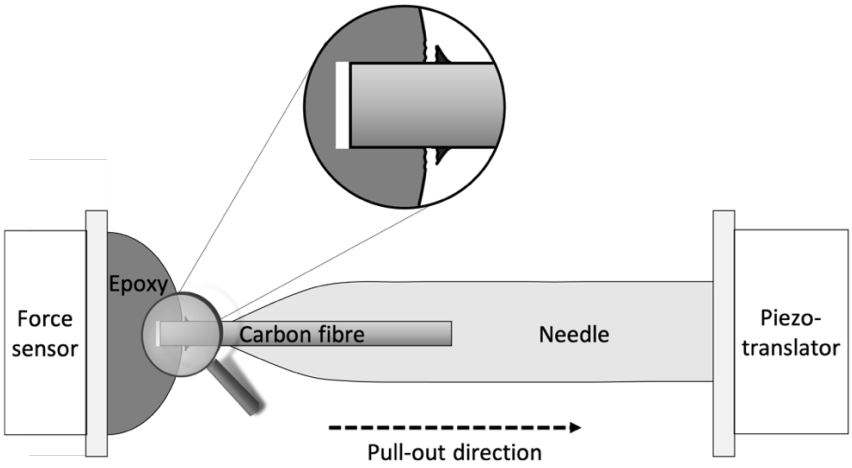


Fig. 3.11 Schematic representation of the single fibre pull-out test equipment with a close-up view of the microscale carbon fibre debonding.

3.3.7. Bundle composite test with in-situ electrical conductivity and acoustic emission

In order to directly assess the in-plane properties of CNT-grafted fibres and avoid the use of time-consuming techniques such as the single fibre tensile test, a fabrication method for unidirectional FRP bundle specimens was developed. A custom-made resin impregnation mould was designed to produce resin-infused tow specimens with a gauge length of 150 mm and a fibre volume fraction of approximately 30 vol.% and 45 vol.%, for CFs and QFs, respectively, in accordance with the ASTM D3039 standard [255]. The relatively low volume fraction specified in the ASTM standard helps alleviate fibre damage during the manufacture process and allow for the measurement of the effective fibre strength. For comparative purposes, the data were normalized to the largest volume fraction (49 vol.%) permitted in the standard, which approaches values most typically used in practical composites. Dry tow sections were gently placed under tension and inserted into the slotted stainless-steel mould (**Fig. 3.12**, refer to **Annex 3** for technical drawings). 30 g weights were attached to both ends of the tow to keep the fibres taut and ensure alignment. An ultra-low viscosity epoxy system (20ULV, Gurit) was then injected in the mould groove, directly onto the dry tow sections, using a syringe. Next, the mould lid was pressed down slowly until sitting flush with the mould inserts (**Fig. 3.12**), removing the excess of epoxy and adjusting the composite thickness. The epoxy was then left to cure following on the manufacturer's recommendations, i.e. 24 h at ambient temperature followed by 16 h at 50 °C. After cooling, the specimen was gently removed from the mould. End-tabs consisting of glass fibre reinforced polymer (GFRP) were used to sandwich the ends of the specimen using epoxy (Araldite 2011, Huntsman), providing suitable grips and, therefore, avoiding premature failure during mechanical testing.

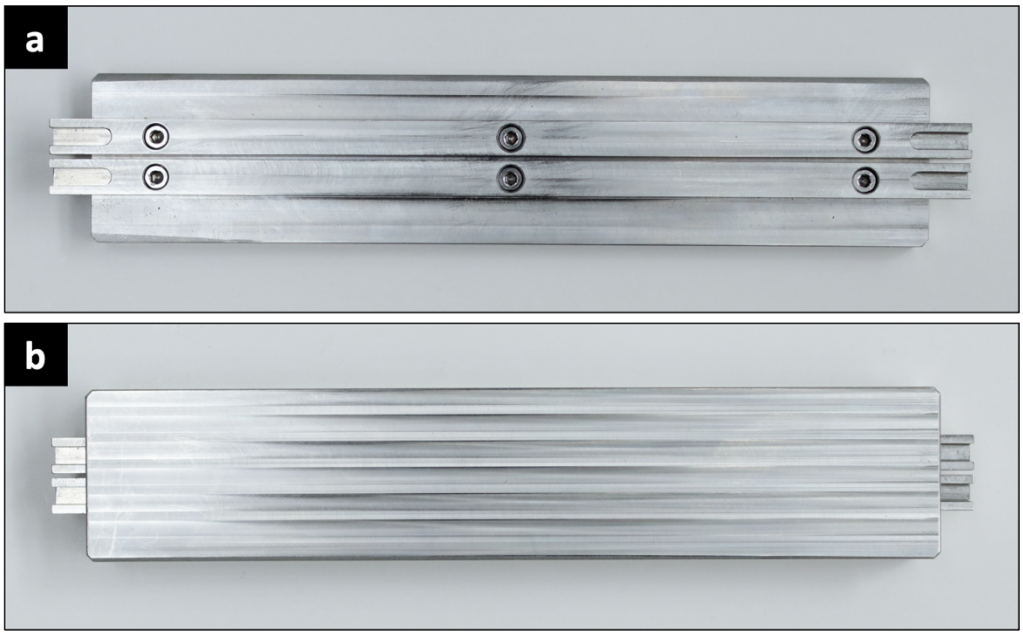


Fig. 3.12 photographs of the unidirectional bundle composite mould, (a) without and (b) with the lid on.

Tensile testing was carried out using an Instron 5980 equipped with a 250 kN load cell (**Fig. 3.13**) at quasi-static strain rate of 1 mm.min^{-1}. Strain was recorded tracking painted marks using a video gauge (iMETRUM MG223B PoE E0022522, iMETRUM Ltd, GB) equipped with a general purpose lens (iM-LENS GP006) with a focal length of 50 mm.

For CNT-g-QFs, *In-situ* electrical conductivity measurements were performed using a Gamry Instruments Interface 1000 potentiostat/galvanostat/ZRA, with Gamry Instruments Framework™ (v.6.24). UD hierarchical bundle composites had both ends, sticking out of the end-tabs (ca. 10 mm), silver painted and connected to the circuit with hook clips. A constant voltage of 500 mV was applied and the current measured using a sampling interval of 100 ms. The cross-sectional area along with the original length of each bundle specimens were measured to calculate the in-plane electrical conductivity. For clarity, plotting electrical conductivity and $\Delta R/R_0$ (the ratio of electrical resistance variation ΔR and initial electrical resistance R_0) as a function of strain, 30 and 10 data points were skipped between each displayed measurement, respectively.

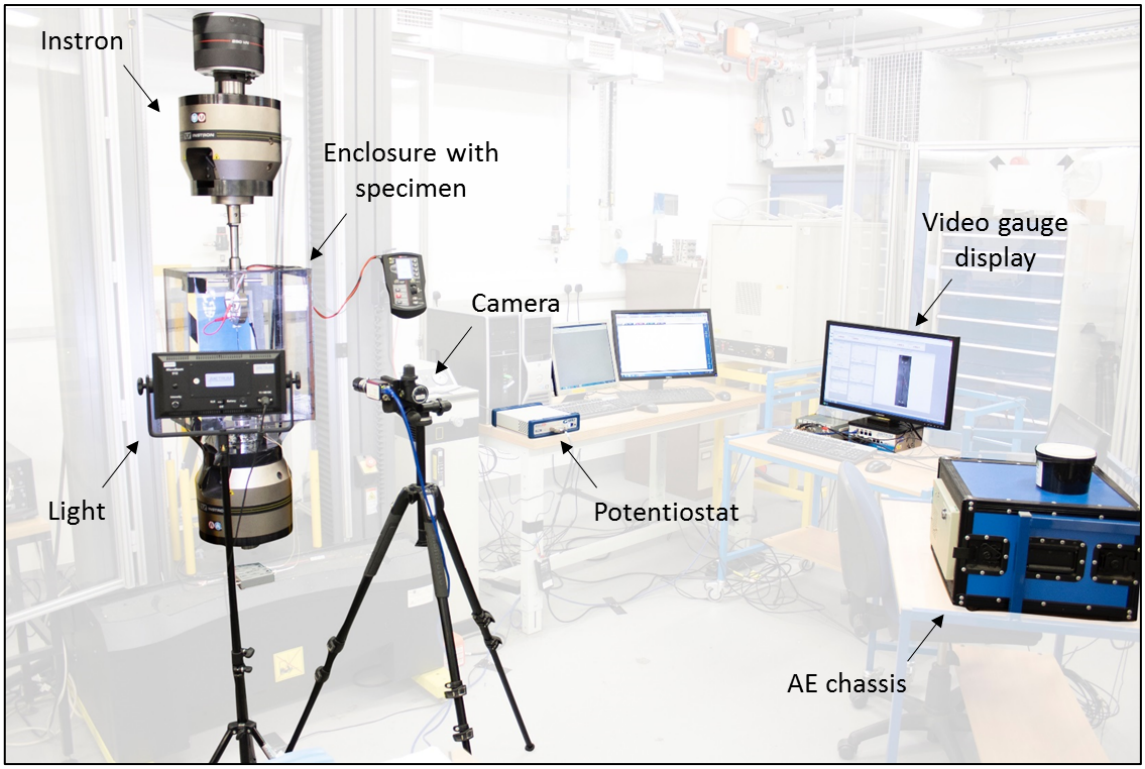


Fig. 3.13 Photograph of the bundle composite tensile test set-up with *in-situ* AE and electrical conductivity measurement. The video gauge camera and associated software records the pixel displacement from two painted marks on the sample surface. The sample is illuminated using a light source to ensure a suitable contrast for the video gauge software to track the points accurately. The force and displacement outputs from the Instron were also recorded *in-situ* with the strain measurements to ensure simultaneous data acquisition via an analogue to digital converter. In conjunction with these recordings acoustic emission events were detected though sensors placed on the sample's surface and processed by the AE chassis and associated software. Similarly, a fixed voltage was applied to the sample, in the loading direction, and the current recorded using a potentiostat to evaluate strain-dependent resistivity.

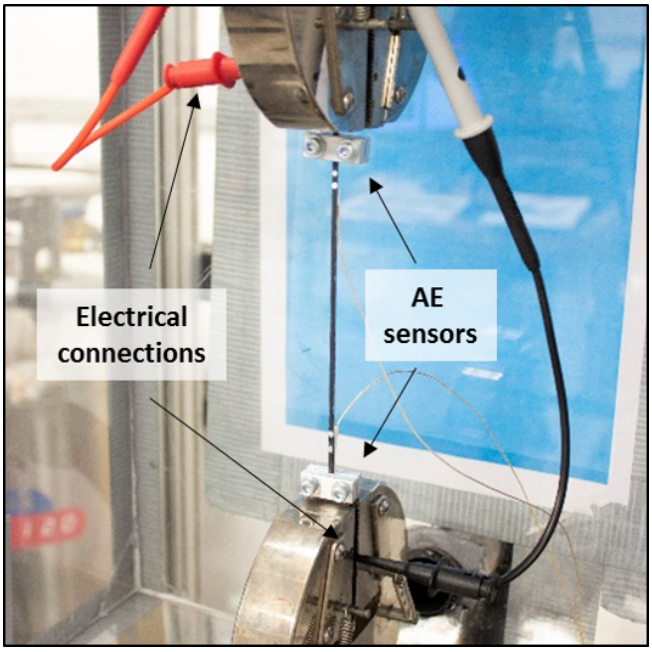


Fig. 3.14 Photograph of a hierarchical bundle composite under tensile loading (in the enclosure) with *in-situ* electrical conductivity and AE detection. AE sensors were clamped to the specimen using purpose-built aluminum jigs. Painted marks for the video gauge tracking were made close to the clamps situated at each end of the sample.

Acoustic emission (AE) events, characteristic of microcracking occurring in the composite under load and generally concentrated within the 10 - 550 kHz frequency range for GFRPs [256] were detected using a ultra-miniature wideband sensor (PICO, 200 - 750 kHz, Mistras Group Inc., Physical Acoustics Corporation, US). The sensor was held in place (ca. 10 mm from bottom end-tab) using a purpose-built aluminium clamp (**Fig. 3.14**) and contact to the specimen ensured with a coupling agent gel (Sonagel W1, Sonatest, GB). The AE sensor was used in association with a 2/4/6 preamplifier with 20 dB gain, AE Express-8 PCI chassis and AEwin software (version E5.71) from the same supplier. Amplitude threshold, peak definition time, hit definition time, time drive rate and hit lockout time were set to 65 dB, 100 ms, 200 ms, 10 ms and 200 ms, respectively.

3.3.8. Short beam shear test

The short beam shear (SBS) test is a well-known composite testing method for the measure of interlaminar shear strength (ILSS). It is often used in the composite field as a screening test due to the relatively low quantity of raw materials needed for sample production. In the SBS test, the composite coupon (20 x 10 x 2 mm) is subject to bending in a 3-point bend configuration (**Fig. 3.15**). A loading span length-to-specimen thickness ratio of 4.0 and a minimum specimen thickness of 2.0 mm was retained (refer to **Chapter 6** for details on SBS specimen production).

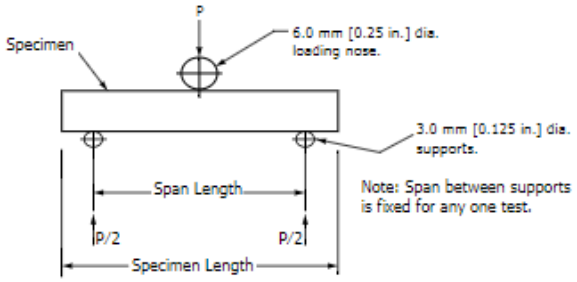


Fig. 3.15 Short Beam Shear testing requirements as specified by ASTM D2344 [257].

The short beam strength (F^{SBS}) is calculated from the following equation:

$$F^{SBS} = 0.75 \frac{P_m}{b.h}, \quad \text{Eq. 3.5}$$

where P_m is the maximum force (at which point delamination occurs) during testing, b the specimen width and h the specimen thickness. Testing was carried out using an Instron 5980 equipped with a 10 kN load cell (**Fig. 3.13** and **Fig. 3.16**) at quasi-static strain rate of 1 mm.min^{-1}.

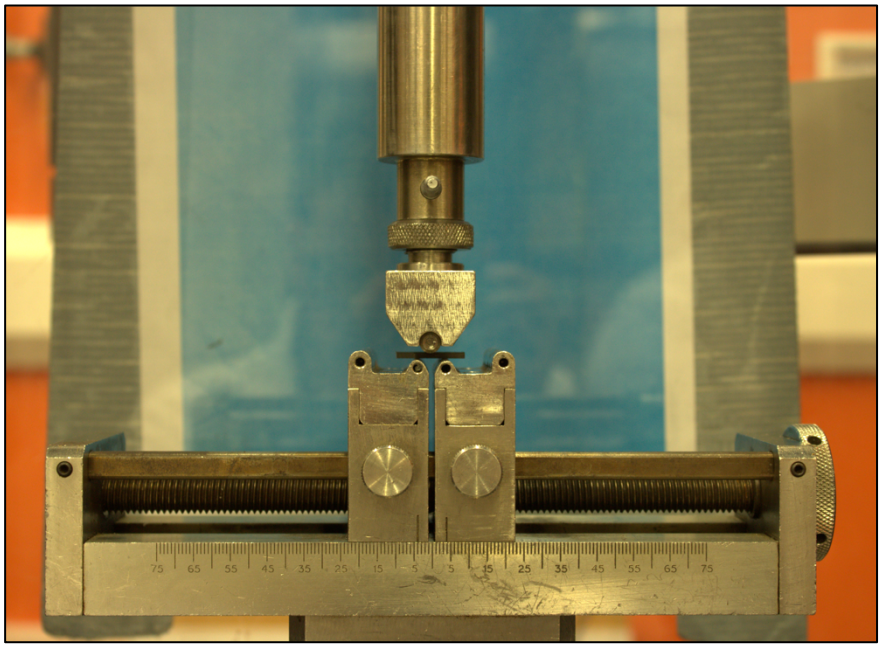


Fig. 3.16 Short beam shear testing set-up with a span-length of 8 mm, loading nose of 6 mm and supports diameter of 3 mm.

Chapter 4 : Continuous synthesis of CNTs on quartz fibres - A multifunctional interphase

The growth of CNTs on inorganic substrates is more straightforward than on carbon fibres. However, as the fibres need to be stable at the growth temperature required for CNT CVD synthesis (600 - 1000 °C) [46, 51], traditional glass fibres used for composites (S-glass and E-glass) cannot be used as they melt/soften at these typical growth temperatures whilst their mechanical properties degrade at temperatures as low as 250 °C [258]. Special purpose glass fibres, however, and more specifically quartz fibres, are designed for high in-use temperatures, and were therefore chosen for these experiments. Previous work produced a range of CNTs on silica fibres in batch process, usually with long CNTs (> 1 µm). To make practical composites, it was essential to control the length of the CNTs to be shorter than previous results in the literature. The effects of these shorter CNT grafts can then be studied at the single fibre scale – and more importantly, at larger scale, in full hierarchical composites with realistic loading fractions. Hence, this chapter describes the continuous, reel-to-reel, growth of CNTs on Quartzel® quartz fibres, performed on whole tows in an open CVD reactor. Both crystallinity and CNT loading were assessed via Raman and TGA, respectively. The effect of the CNT microstructure on the mechanical performance and failure of the fibre/matrix interface was investigated at the single fibre level. Unidirectional hierarchical bundle composites were manufactured, and their mechanical properties measured in tension. The introduction of a conductive, nanostructured, interfacial region demonstrating a piezo-resistive response, allowed the capability for structural health monitoring to be explored *via* simultaneous real time monitoring of both acoustic emission (AE) and electronic transport.

4.1. Growth of CNTs on quartz fibres

The continuous production of CNT-grafted quartz fibres (CNT-g-QFs) can be separated into two distinct stages as described in great details in **Chapter 3**. Prior to their insertion into the open chemical vapour deposition (CVD) reactor, the as-received sized quartz fibre (AR-QF-S) must be deposited with catalyst precursor. Whilst historically a mixture of nickel(III) nitrate ($Ni(NO_3)_3$) and iron(II) acetylacetonate ($Fe(acac)_2$) was found particularly compatible with carbon fibres [3], a mixture of nickel(II) acetylacetonate ($Ni(acac)_2$) and $Fe(acac)_2$ appeared more suitable for quartz fibres, adsorbing well on their polar, hydrophilic surface. In addition, the catalytic activity being dependent on the substrate (refer to Section **2.1.4**, pp. 27), various Ni:Fe bi-catalyst precursor stoichiometries were investigated including 2:1, 1:1 and 1:2 mol.%. The former showing the best CNT growth on quartz fibres was retained for the remainder of the study (**Fig. 4.1**c). Thereby, the tow was continuously pull-through a bath containing a mixture of 1 wt.% $Ni(acac)_2$ and $Fe(acac)_2$ (2:1 mol.) in ethanol for 2 min. The tow was kept under modest tension (ca. 0.4-0.5 N) during deposition to allow for sufficient spreading in the catalyst precursor containing bath. The QFs were then dried in a set of infrared-furnaces at temperature of ca. 40 °C and 70 °C, and collected on a reel. The bi-catalyst precursor coated QFs (QF-BiCat) were subsequently passed through the hot-walled CVD set-up (**Fig. 3.6**) and exposed sequentially in the hot-zone (770 °C) to a mixture of 2.4 vol.% H_2 in N_2 (3400 SCCM) for catalyst reduction and afterwards to a mixture of 1.3 vol.% C_2H_2 in N_2 (325 SCCM), acting as the carbon source. The growth of CNTs was completed for two different line speeds through the continuous CVD set-up: 1.2 and 2.4 $m.h^{-1}$, corresponding to a dwell time in the furnace stable hot zone of 30 and 15 min, respectively. As a control, similar conditions were used to produce heat-treated (thermally desized) fibres (QF-HT), exposed to high temperature (770 °C) for 30 min under an equivalent absolute flow of N_2 (11140 SCCM at a line speed of 1.2 $m.h^{-1}$) but in absence of active gases.

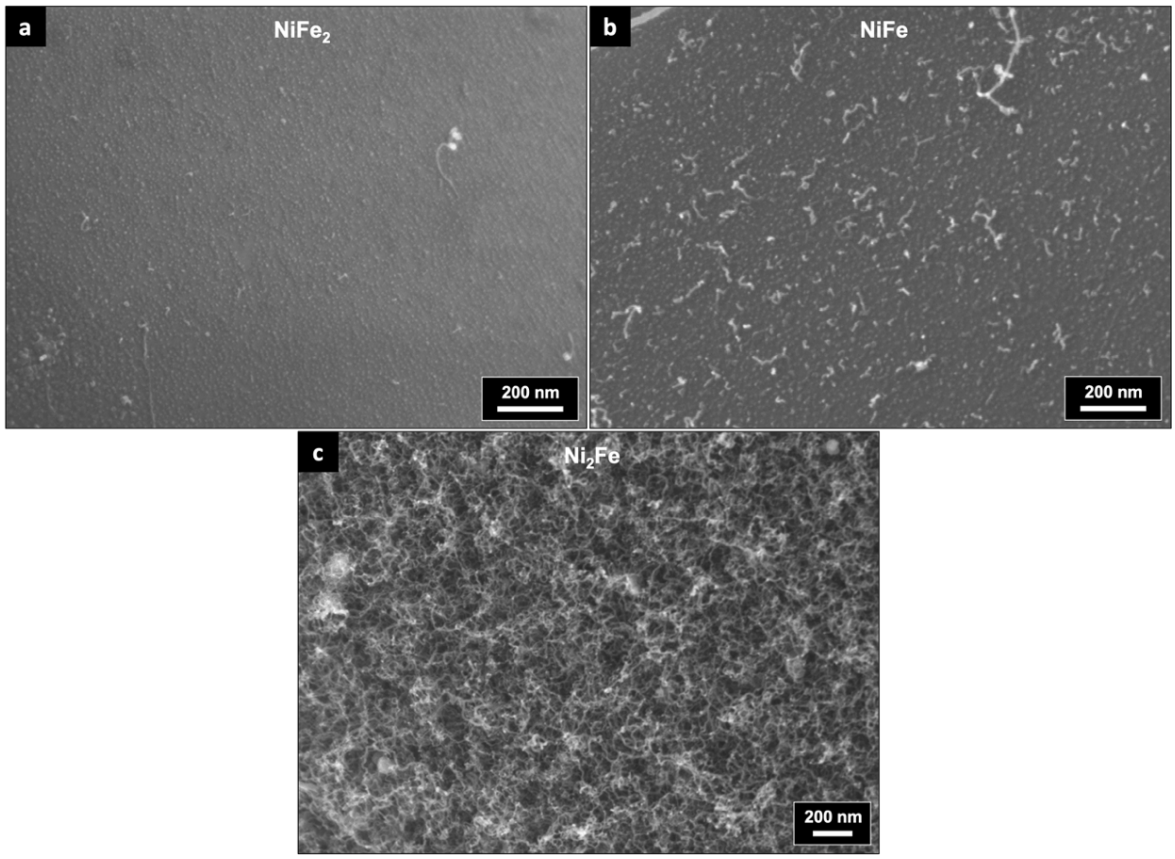


Fig. 4.1 Effect of different bi-catalyst precursor stoichiometry on the growth of CNTs on quartz fibres with (a) $NiFe_2$, (b) NiFe and (c) Ni_2Fe.

4.2. Characterisation of the CNT-grafted quartz fibres

4.2.1. Morphology of the CNT-grafted quartz fibres

As-received sized quartz fibres (AR-QF-S, **Fig. 4.2**a) exhibit a smooth surface alike to that of its heat-treated and bi-catalyst deposited counterparts (**Fig. 4.2**b, c). In addition, the absence of aggregates on QF-BiCat suggests a homogeneous distribution of catalyst particles (**Fig. 4.2**c).

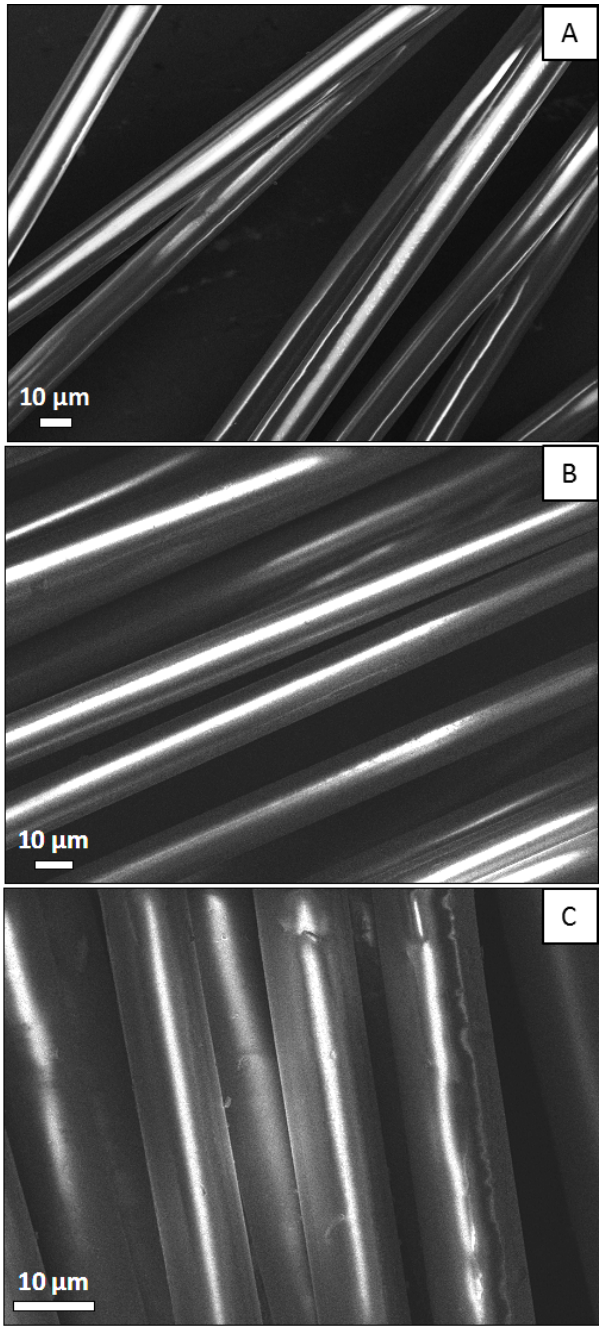


Fig. 4.2 SEM micrographs of (a) as-received sized, (b) heat-treated (thermally desized) and (c) bi-catalyst decorated quartz fibres

The presence of the catalyst particles on the QFs surface introduced a uniform yellow tinge to the previously colourless fibres, due to the presence of the metal salts (**Fig. 4.3**). After exposure to reactive gases, at high temperature, the tow turned black; longer dwell times produced a darker tint and noticeable fuzziness (**Fig. 4.3**). The continuous CVD process developed here allowed for the production of several metres of CNT-g-QFs.

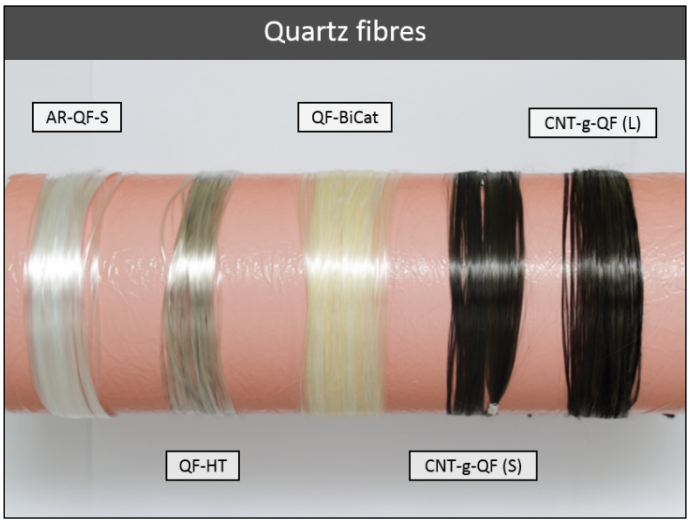


Fig. 4.3 Photograph of quartz fibres tow sections (two meter long) after different chemical and/or thermal treatment conditions (left to right: as-received, heat-treated, bi-catalyst decorated, short CNT grafted, long CNT grafted). The catalyst precursor deposition was performed on as-received sized quartz fibres.

Adjusting the reduction and growth times, *via* the pull-through speed, promoted distinctive CNT morphologies: shorter dwell time (12 min) produced a uniform, 200 nm thick layer of highly entangled CNTs (SEM, **Fig. 4.4**a, b and c); extended exposure (24 min) to the active gas grew much longer (up to 30 µm) CNT arrays (SEM, **Fig. 4.4**d, e and f). For these longer CNTs, the radial symmetry around the fibres was broken, with the formation of a splayed "Mohawk" morphology, as reported previously in similar geometries [122, 259, 260]. In addition, the resulting longer arrays had a rather uneven apparent length along the tow fluctuating from 5 to 30 µm (**Fig. 4.4**e, f). Both configurations, namely CNT-g-QF (S) and CNT-g-QF (L) exhibited CNT diameters of sub-20 nm (**Fig. 4.5**).

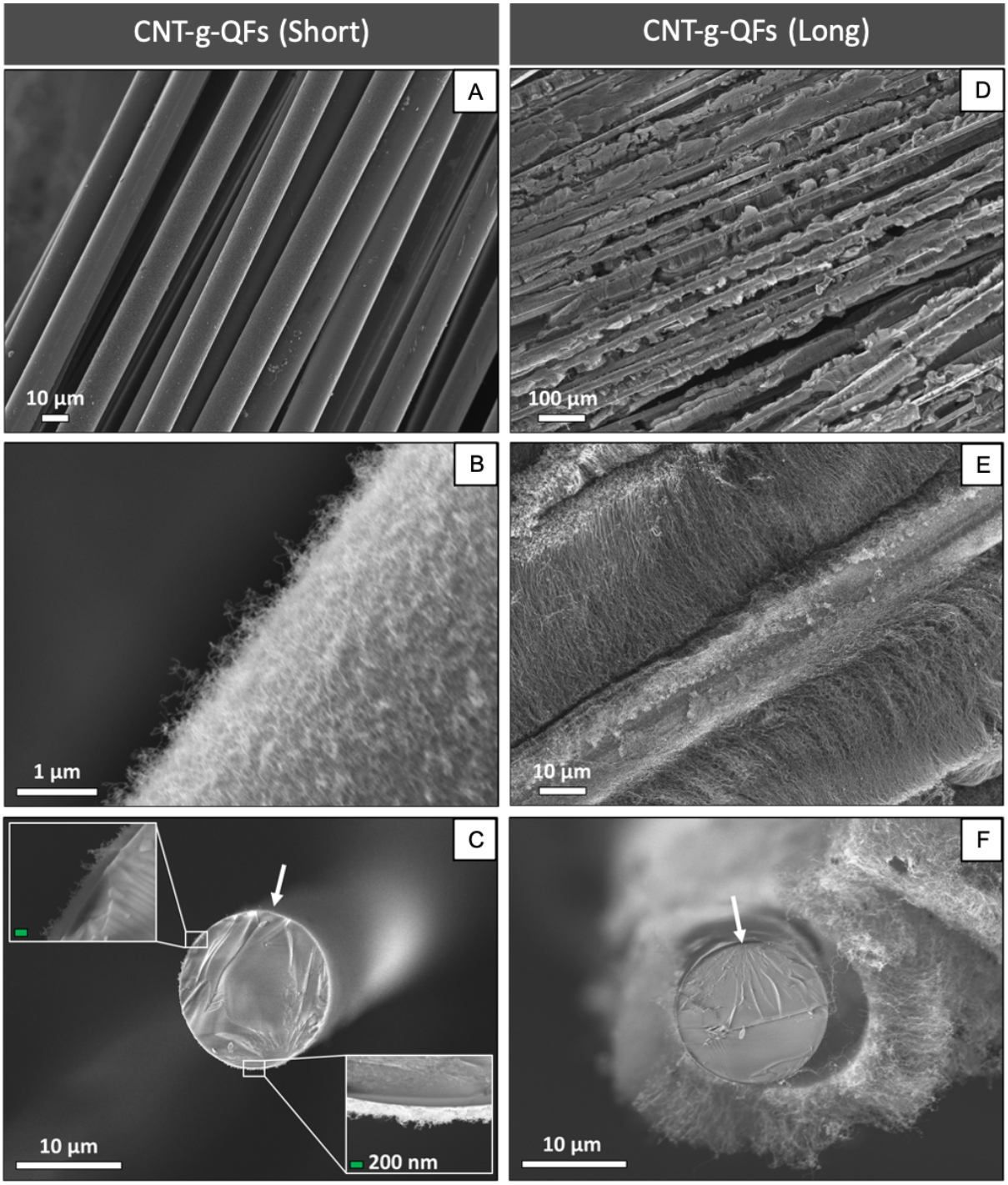


Fig. 4.4 SEM micrographs of the hierarchical fibres produced with (a, b, c) a short and uniform CNT coverage, namely CNT-g-QF (S) and (d, e, f) long "mohawk" CNT arrays, referred to as CNT-g-QF (L). Arrows correspond to the scalpel cutting locations and directions, both scale bars in the inserts (c) are 200 nm.

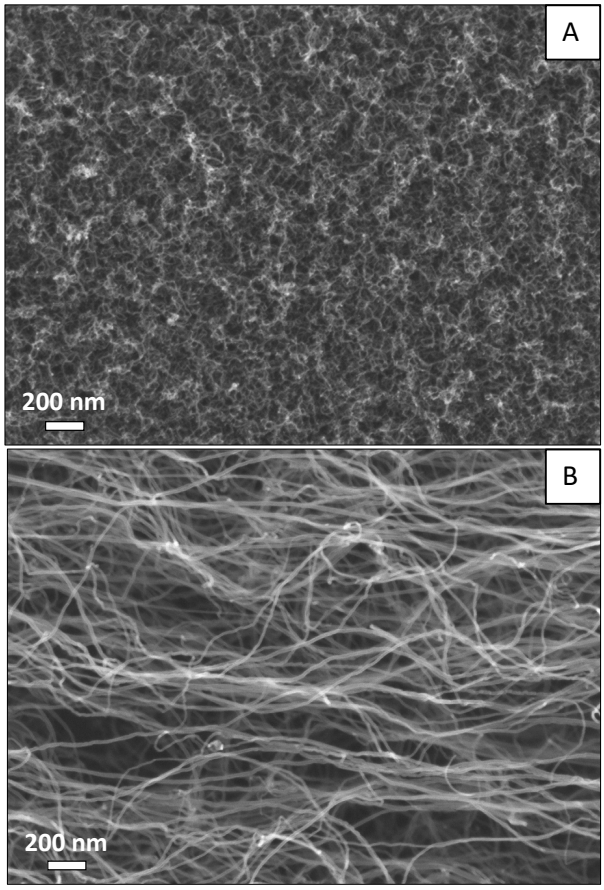


Fig. 4.5 High-magnification SEM micrographs of (a) CNT-g-QF (S) and (b) CNT-g-QF (L). The shorter CNTs can only be easily viewed 'end on', whilst the Mohawk arrangement of the longer CNTs facilitates a transverse view.

4.2.2. CNT loading and quality

Thermogravimetric analysis (TGA) in air (**Fig. 4.6**) provides information about the carbon/organic content and stability of samples. As-received (sized) QFs showed a mass loss (1.4 wt.%) at the lowest initial decomposition temperature (ca. 150 °C), corresponding to the degradation of the protective sizing present on their surface. Both QF-HT and QF-BiCat showed a delayed onset of degradation when compared to AR-QF-S at ca. 250 °C, likely due to the presence of partially carbonised residual sizing. CNT-g-QF (S) and CNT-g-QF (L) on the other hand were relatively stable up until ca. 450 °C, when the CNTs started to combust significantly. The weight ratio of CNTs introduced onto the QFs was estimated to be around 0.6 and 1.6 wt.% for CNT-g-QF (S) and CNT-g-QF (L), respectively. The thermal stability of the nanoengineered QFs make them an interesting reinforcement, particularly if combined with resin systems designed for high service temperatures.

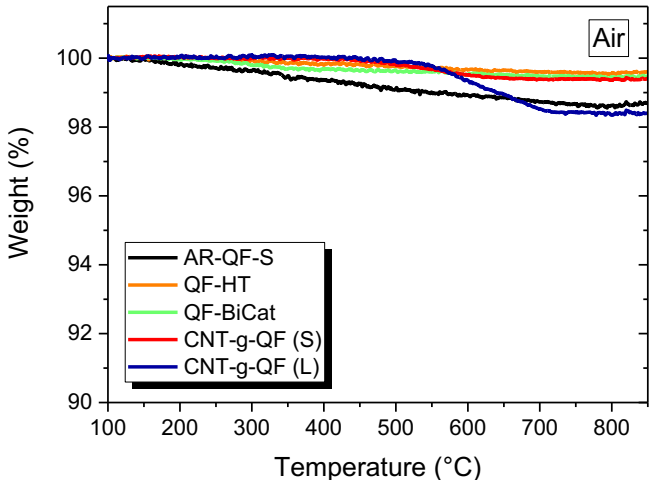


Fig. 4.6 TGA curves of as-received sized, heat-treated (thermally desized), bi-catalyst decorated and CNT-grafted quartz fibres with different growth duration; 12 min (S) and 24 min (L), respectively.

The Raman spectra for both AR-QF-S and QF-BiCat (**Fig. 4.7**a, c) showed characteristic features associated with fused silica, ranging from 450 to 1200 cm^{-1}. After thermal treatment of the QF-HT control at 770 °C in N_2, the silica signals were greatly weakened, likely due to overcoating with amorphous carbon from the decomposition of the sizing, leading to a relatively featureless spectrum, with a rising fluorescent background (**Fig. 4.7**b). In contrast, in addition to the weak silica signal, the CNT-g-QF (S) sample showed strong D- and G-modes at ca. 1340 and 1580 cm^{-1}, respectively, characteristic of the graphitic carbons such as CNTs (**Fig. 4.4**d). The CNT-g-QF (L) showed similar graphitic features (**Fig. 4.4**h), but the silica modes were lost, due to the increased thickness of the CNT layer. The longer CNT array obtained for CNT-g-QF (L) was relatively crystalline with the appearance of a 2D-mode (also referred to as G') around 2700 cm^{-1}. The CNT-g-QF (L) also exhibited a higher intensity ratio of the G-mode to the D-mode (I_G/I_D) when compared to CNT-g-QF (S), 1.37 ± 0.01 and

1.11 ± 0.01, respectively, indicating greater ordering of the sp^2 bonded graphitic domains. This morphological difference can be attributed to the transition from an unconstrained disordered growth (with a lower nucleation density [44]) to the concerted growth of arrays [261], at higher nucleation density [262]. In addition, the altered growth kinetics and more specifically the prolonged exposure to H_2 may also reduce the defect concentration [263], shifting from random to aligned CNT growth [264].

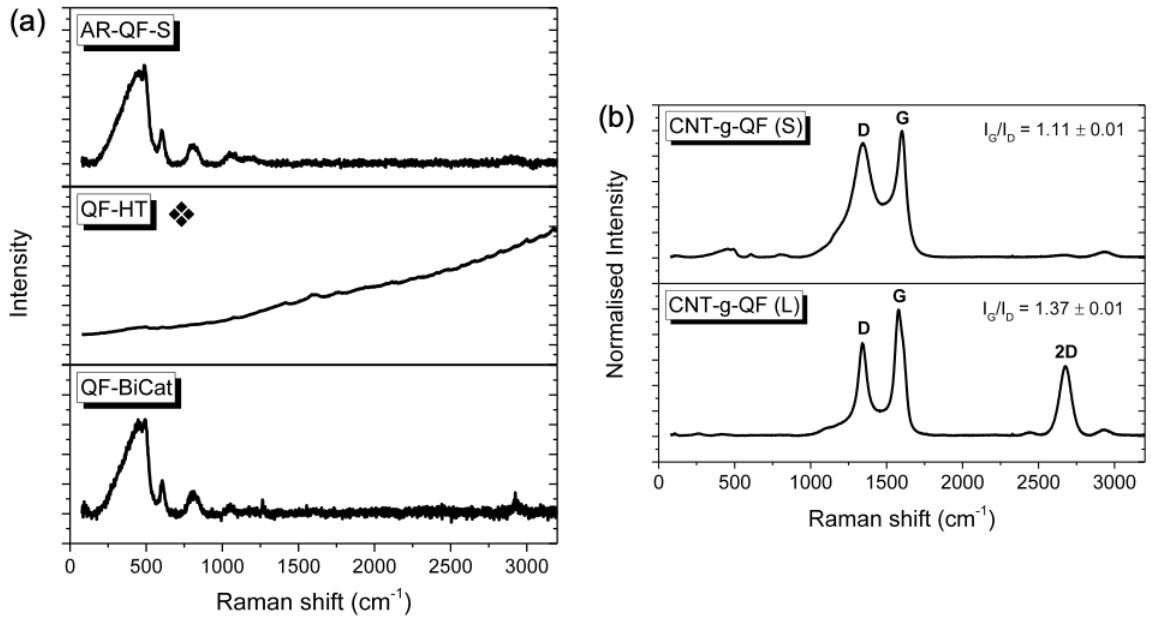


Fig. 4.7 Raman spectra for (a) as-received sized, heat-treated (thermally desized) and bi-catalyst decorated quartz fibres. ❖ Baseline for QF-HT was not subtracted due to the absence of modes resulting in significant noise. Raman spectra normalised to the G-peak for (b) CNT-g-QF (S) and CNT-g-QF (L), corresponding to a residence time in the furnace hot-zone of 15 min and 30 min, respectively. 2D-mode (2700 cm^{-1}), G-mode (1582 cm^{-1}) and D-mode (1350 cm^{-1}) and corresponding I_G to I_D ratio are included.

4.2.3. Single fibre mechanical and interfacial properties

The mechanical properties of composites depend both on the intrinsic tensile properties of the reinforcing fibres, and the fibre/matrix interface. The ability to transfer stress from the matrix to the parent fibres is characterised by the interfacial shear strength (IFSS), a measure of adhesion. QFs are typically coated with a polymeric sizing and/or silanised layer which enhances compatibility and promotes adhesion to epoxy [236]. IFSS can be measured by a variety of micromechanical approaches or inferred from larger coupon tests [71, 117]. Single fibre pull-out tests, performed here, provide a full load-displacement curve for the interfacial failure as a fibre is removed from a resin block. The IFSS presented here have an interaction area determined from the fracture surface for each fibre.

For the baseline QFs, an initially elastic regime was followed by plastic yielding of the resin; after an abrupt drop, associated with complete debonding, there was a region of lower frictional force, linearly decreasing until the fibre was fully extracted. In contrast, the pull-out curves for CNT-g-QF (S) (**Fig. 4.8**, bottom) exhibited a stick-slip response in the extraction region (blue area) as a result of the presence of CNTs. The difference may be explained by the surface roughening of the quartz fibres and the introduction of a mechanical interlocking effect between the CNTs and epoxy.

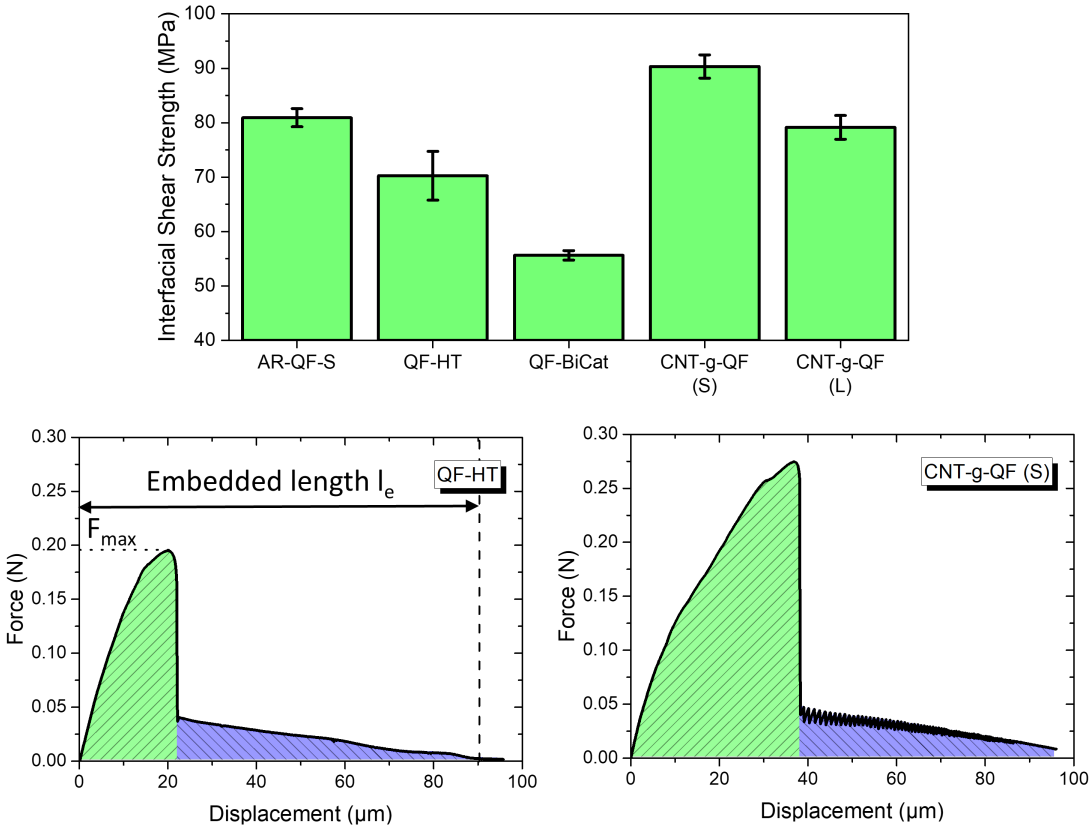


Fig. 4.8 Apparent interfacial shear strength obtained from single fibre pull-out tests (top) and typical single fibre pull-out test curves for heat-treated and short CNT-grafted quartz fibres (bottom). The green area corresponds to the debonding region where the fibre/epoxy interface has not yet failed; the blue area highlights the extraction region.

The apparent interfacial shear strength (IFSS, τ_{app}) was calculated using Eq. 3.4, the average IFSS was obtained from a linear fit fixed at the origin of the population when pull-out peak force (F_{max}) is plotted as a function of embedded fibre area (A_e) (**Fig. 4.9**).

Table 4.1 Single fibre pull-out test results with interfacial shear strength (IFSS) determined using fibre diameter after pull-out with standard error associated. Embedded area shown in **Fig. 4.9**.

	IFSS (MPa)	Fibre diameter after pull-out (μm)	# of spec.
AR-QF-S	81 ± 2	13.0 ± 0.2	16
QF-HT	70 ± 5	13.1 ± 0.1	14
QF-BiCat	55 ± 1	13.2 ± 0.1	22
CNT-g-QF (S)	90 ± 2	13.0 ± 0.1	16
CNT-g-QF (L)	79 ± 2	13.2 ± 0.2	17

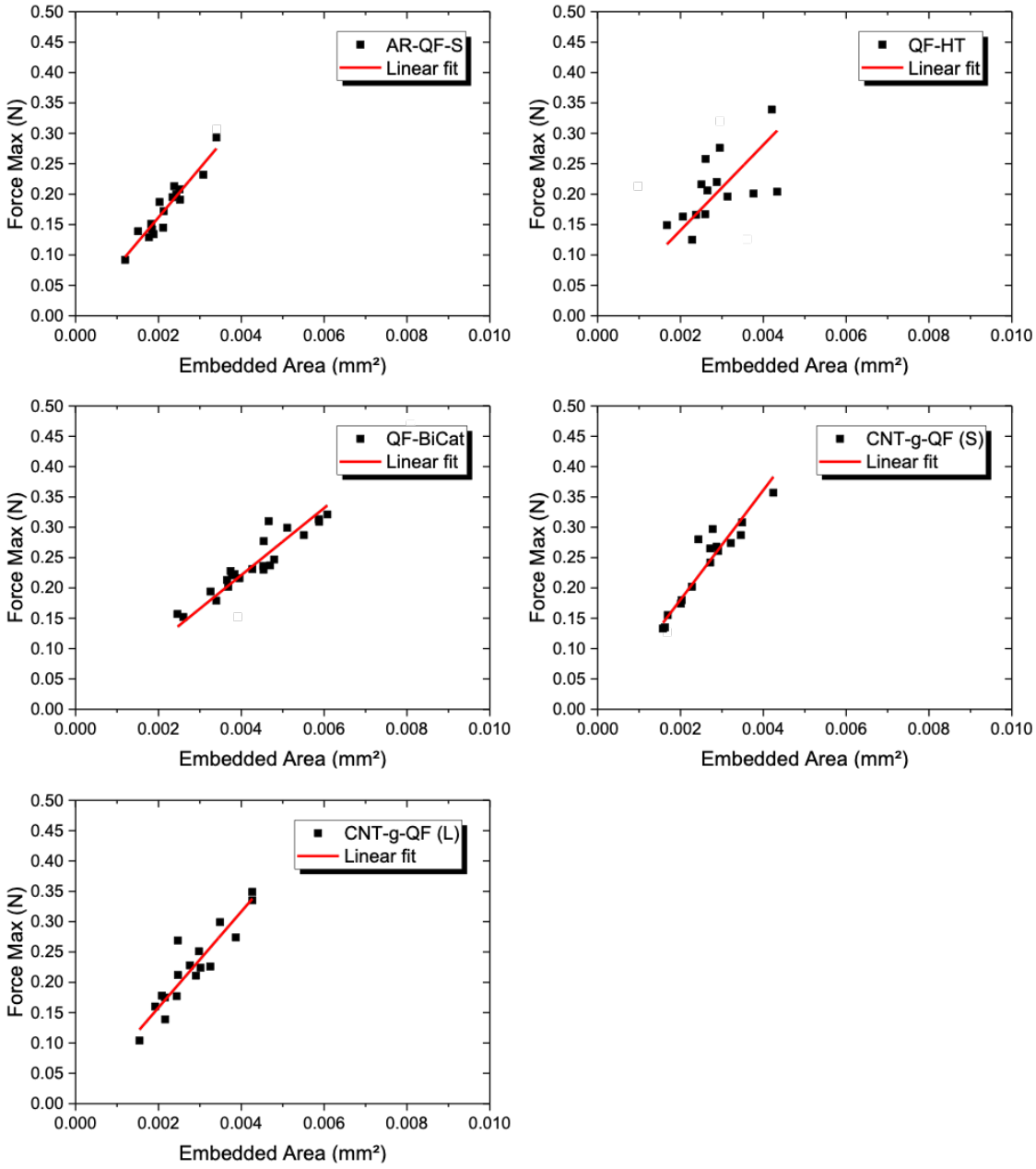


Fig. 4.9 Collated single fibre pull-out data including linear fits. The slope of the fits corresponds to the apparent IFSS tabulated in **Table 4.1**.

The collated IFSS data (**Fig. 4.8**, top) showed that the partial removal of the sizing from as-received QFs, both thermally (QF-HT) and chemically (QF-BiCat), greatly impaired performance, with decreases of 13 % (70 ± 5 MPa) and 31% (55 ± 1 MPa), respectively, compared to the original commercially sized QFs (AR-QF-S). The relatively large scatter associated with QF-HT IFSS measurements is consistent with incomplete sizing removal, in agreement with the TGA results (**Fig. 4.6**). QFs, nanoengineered with a short and uniform CNT coverage (CNT-g-QF (S)) had the highest IFSS of 90 ± 2 MPa, a 12 % increase over the baseline sized fibres. CNT-g-QF (L), however, did not show any statistically significant difference when compared to AR-QF-S with an IFSS of 79 ± 2 MPa, possibly due to the asymmetric CNT

coverage creating a complex stress state at the interface, leading to a premature failure. The fracture surface of CNT-g-QF (S) (**Fig. 4.10**a) was visibly rough due to the presence of epoxy residues. Moreover, the partially textured fibre surface indicated the presence of CNTs which would suggest a cohesive failure in the CNT/epoxy interphase close to the parent fibre, in agreement with the high IFSS measured. The CNT-g-QF (L) fracture surface (**Fig. 4.10**c), on the other hand, appeared cleaner with only limited matrix residue remaining on the fibres. CNTs can be seen to have bridged from the epoxy wetting cone (or "meniscus region"), aligned with the pull-out shear stresses generated during the test. Raman spectra collected from the fracture surfaces after pull-out of both CNT-g-QFs (**Fig. 4.10**b, d) and away from the fracture region (**Fig. 4.11**a, b) exhibited strong D- and G-modes, further confirming the presence of CNTs on QF after fracture, and hence a cohesive failure for both CNT configurations. The enhancement of the adhesion is likely the result of mechanisms acting at different length scales: matrix cracking, CNT debonding, CNT detachment and CNT breakage may all contribute to various extents. Experimentally, given the complexity of the system, it is difficult to identify which of these competing mechanisms was predominant. CNT strength and CNT/epoxy interfacial adhesion, however, have been suggested to play an important role in the onset of these different failure modes [85].

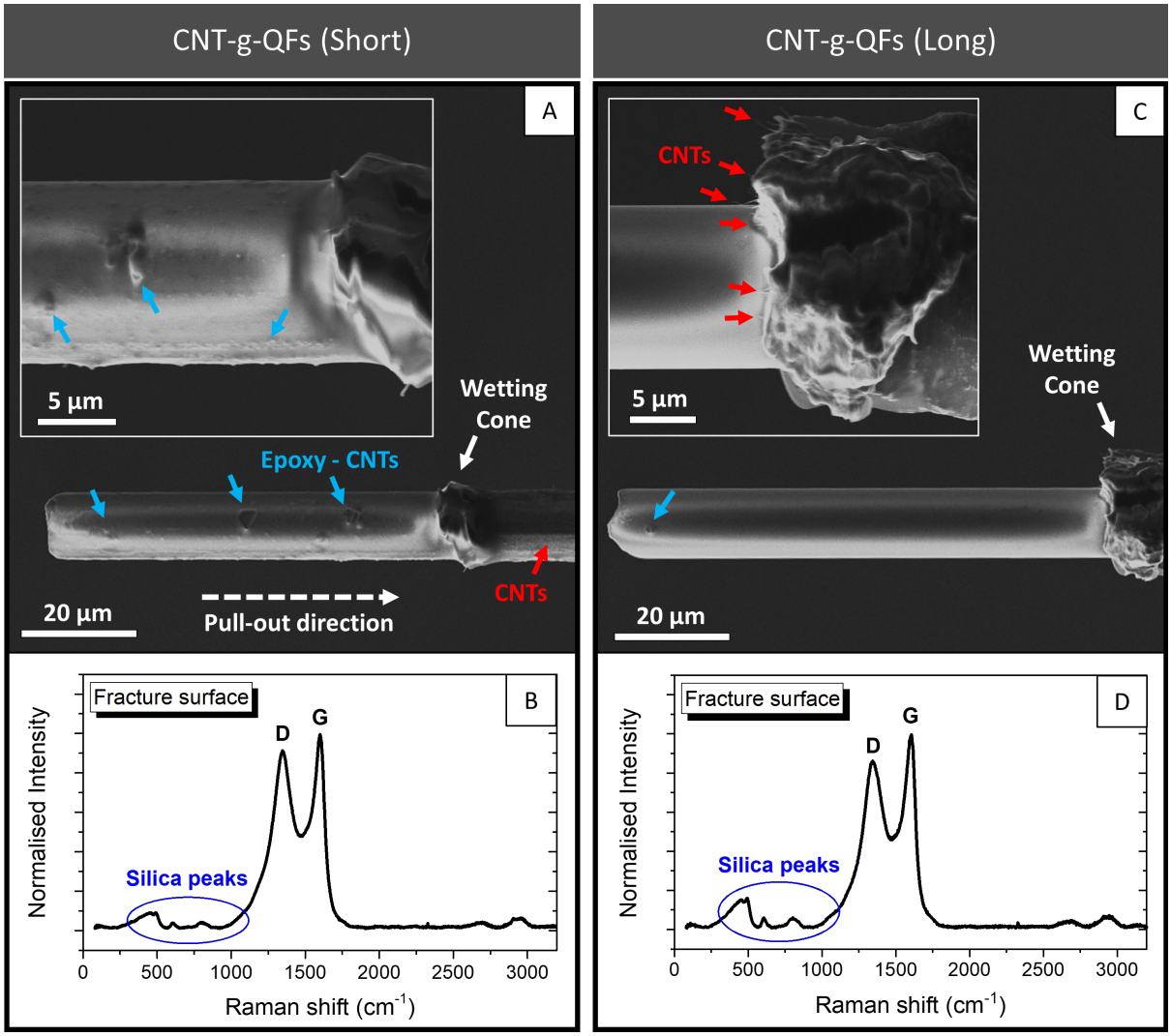


Fig. 4.10 SEM micrographs of fracture surfaces after pull-out from cured epoxy droplets with corresponding Raman spectra normalised to the G-peak for (a, b) CNT-g-QF (S) and (c, d) CNT-g-QF (L), respectively. Red arrows indicate the location of CNTs whilst blue arrows show epoxy-CNTs agglomerates.

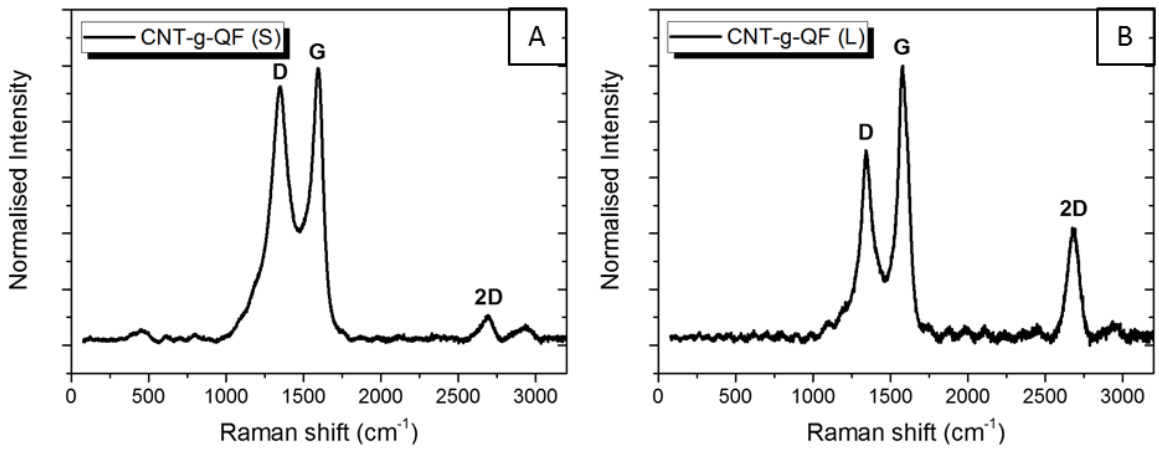


Fig. 4.11 Raman spectra normalised to the G-peak of (a) CNT-g-QF (S) and (b) CNT-g-QF (L) after single fibre pull-out, away from the fracture surfaces with D-mode (1350 cm^{-1}), G-mode (1582 cm^{-1}) and 2D-mode (2700 cm^{-1}).

The intrinsic tensile properties of the fibres were also evaluated at the single fibre level, after each treatment (**Fig. 4.12**). The modulus of all the fibres remained effectively unchanged, as the fibre core retained its properties. However, handling at high temperature halved the tensile strength, for both the CNT-grafted fibres, namely CNT-g-QF (S) and CNT-g-QF (L), and the thermally treated control (QF-HT); the initial loading of catalyst had no effect. High temperature treatment is known to damage glass fibres; surface defects may be created due to steam etching by adventitious moisture or simple mechanical damage after stripping the protective sizing [258]. At a commercial scale, such detrimental effects could likely be avoided.

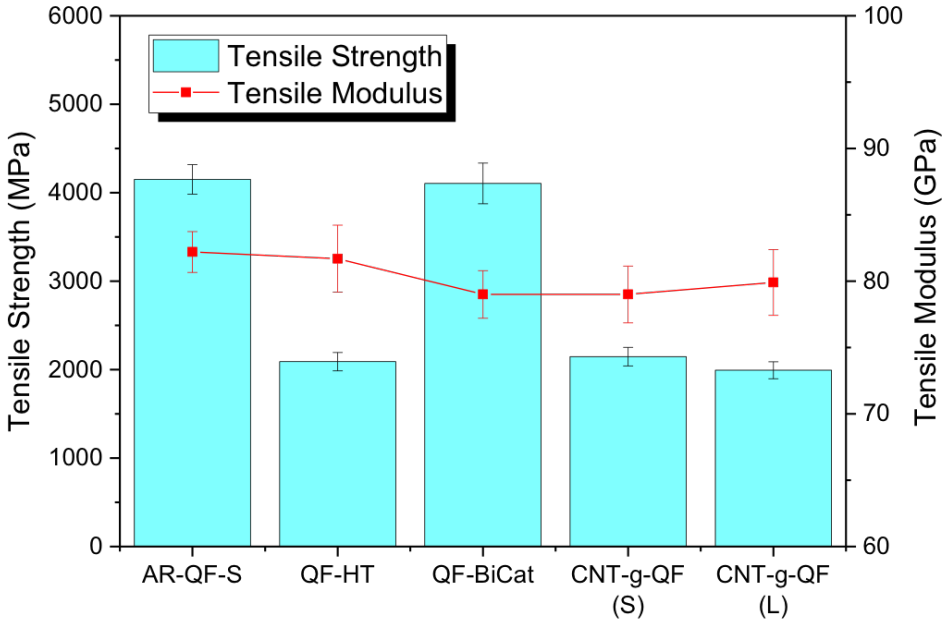


Fig. 4.12 Tensile properties of as-received quartz fibres before and after all thermal and/or chemical treatments, measured through single fibre tensile tests with a gauge length of 25 mm. Error bars correspond to standard error. A minimum of 13 specimens were tested per data set.

4.3. Characterisation of CNT-grafted quartz fibres unidirectional composites

Having established an effective continuous grafting process yielding improved absolute interfacial performance at the single fibre level, the next step was to study larger scale composites. As an attempt to both investigate the overall mechanical performance in the primary loading direction and to explore the electrical response introduced with the conductive filler, unidirectional bundle composites were manufactured (see Section **3.3.7**, pp. 89). The potential of the conductive, nanostructured, interfacial region for stain-sensing capability, namely through a piezoresistive response was investigated *in-situ* through macroscopic electric conductivity measurements.

4.3.1. Piezoresistive response of unidirectional hierarchical composites

The normalised tow composite tensile strengths and Young's moduli (**Table 4.2**) show qualitative trends in tensile performance consistent with those obtained from the single fibre tests: the stiffness, which relates to the bulk fibre properties remained unchanged, whilst the strength was reduced as a result of surface damage introduced during processing. As noted in the method section, the absolute fibre volume fractions (comprised between 29 and 38 vol.% for all specimens) are relatively low compared to practical structural composites. Yet, at these lower volume fractions, as specified by the ASTM D4018 standard, both long and short CNTs can be fully accommodated whilst at higher volume fractions typically found in structural composites, the longer CNTs would likely no longer fit. In fact, assuming an idealized hexagonal close packing, a CNT length superior to 3 μm would likely hinder the primary fibre volume fraction (approximately d/4.4, see Section **2.3.3**, pp. 48). The bundle test is therefore an adequate technique for long CNT-g-QFs.

Table 4.2 Mechanical and *in-situ* electrical properties of the unidirectional bundle composites measured in tension with standard error provided. Tensile properties were normalised to a nominal fibre mass fraction of 65 wt.% following ASTM D4018 standard, which corresponds to a Quartzel® fibre volume fraction of 49 vol.%.

Sample	Composite strength (MPa)	Composite Young's modulus (GPa)	Initial resistance [R_0] (Ω)	Strain gauge sensitivity†
AR-QF-S	1387 ± 52	38.9 ± 0.7	N/A	N/A
QF-HT	1003 ± 10	38.7 ± 0.5	N/A	N/A
QF-BiCat	1480 ± 53	38.8 ± 0.3	N/A	N/A
CNT-g-QF (S)	852 ± 18	38.8 ± 0.3	$4.1 \pm 0.5 \times 10^4$	3.64 ± 0.43
CNT-g-QF (L)	854 ± 16	39.7 ± 0.54	$1.4 \pm 0.1 \times 10^4$	2.79 ± 0.16

† Calculated between 0.5 and 2.0 % strain, Eq. 4.2.

The presence of the grafted CNT layer provided a measurable electrically conductive path parallel to the fibres. The initial electrical conductivity increased from 2.7 ± 0.3 $S.m^{-1}$ for the shorter CNT-g-QF (S) to around 7.4 ± 0.3 $S.m^{-1}$ for the longer CNT-g-QF (L) (**Fig. 4.13**c), consistent with the higher carbon loading in the latter case (CNT loading of 0.3 and 0.8 wt.% for composites containing CNT-g-QF (S) and CNT-g-QF (L), respectively, as determined from TGA). For comparison, the absolute electrical conductivities of CNT/epoxy systems found in the literature typically range from 1 x 10^{-5} to 2 $S.m^{-1}$ at CNT loadings suitable for conventional composite processing (i.e. ≤ 1 wt.%) [194]. Whilst the random nature of the percolated network commonly leads to electrically isotropic nanocomposites; the combination of CNT/epoxy with glass fibres (GF) generates anisotropic composites as in-plane conductive pathways form more easily along the fibre direction [199, 200]. The absolute in-plane electrical conductivity of CNT-dispersed GF/epoxy composites ranges from 5 x 10^{-7} to 1 x 10^{-2} $S.m^{-1}$ [106, 200, 265-267] and from 1 x 10^{-3} to 5 $S.m^{-1}$ for CNT-grafted GF/epoxy composites [194, 200, 206, 209, 210]. One recent study stands out as it reports an in-plane conductivity for CNT-grafted GF/epoxy of up to 100 $S.m^{-1}$ [203]; however, the composite's mechanical performance was drastically lowered, mainly because an excessive CNT length of 5.3 μm reduced the GF volume fraction. Thus, the bundle composites produced in this work exhibit one of the highest in-plane electrical conductivities for epoxy-based nanocomposites (**Fig. 4.13**b), with modest CNT loadings (< 1 wt.%).

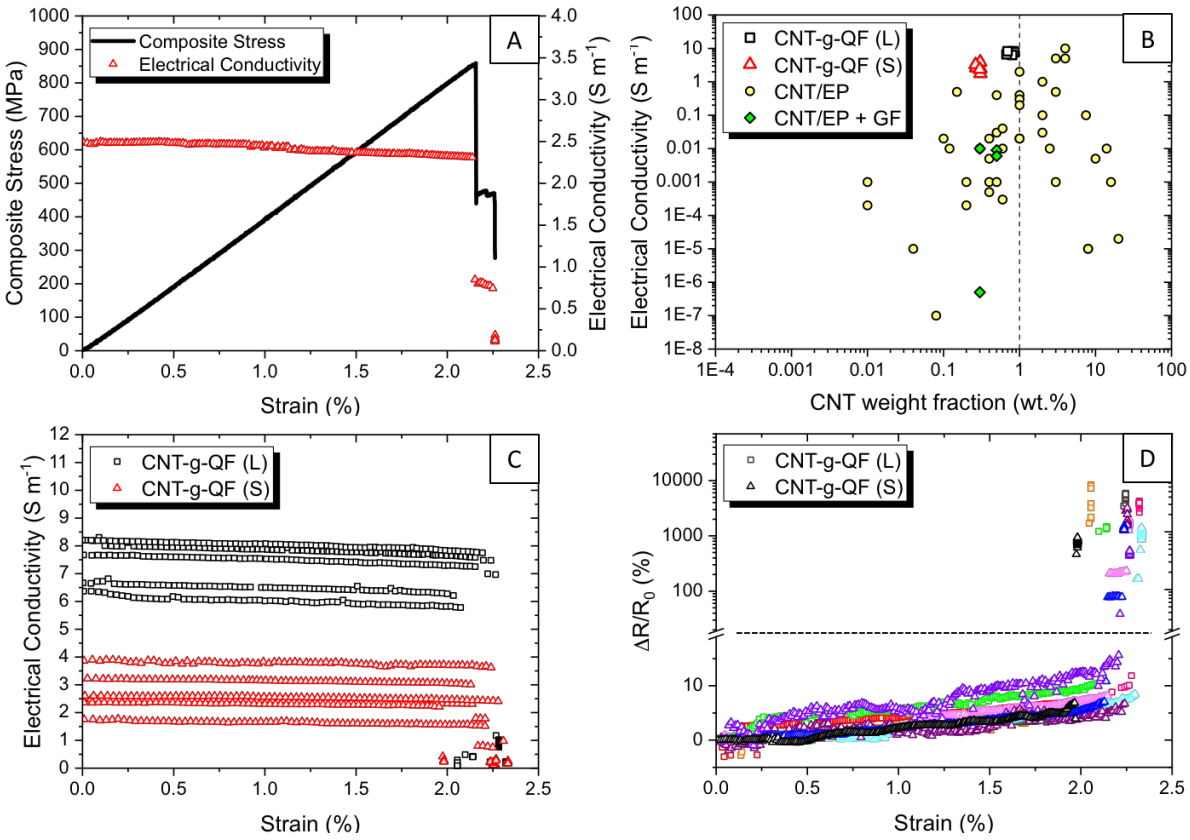


Fig. 4.13 (a) Representative stress-strain curve with real-time electrical conductivity measurements for CNT-g-QF (S). (b) Influence of CNT loading in composites on electrical conductivity for CNT-g-QF (S) (open squares) and CNT-g-QF (L) (open triangles) bundles both in the fibre direction (longitudinal). For comparison, various CNT/epoxy systems (filled circle) [98] and CNT/epoxy glass fibre composites (filled diamond) [106, 200, 265-267]. The typical CNT weight fraction upper limit for CNT/epoxy viable incorporation in composites (dashed vertical line) is included for reference. (c) Collated electrical conductivity for all CNT-g-QF (S) and CNT-g-QF (L) bundles. (d) Resistance variation $\Delta R/R_0$ for all hierarchical bundle composites; (dashed horizontal line) corresponds to a break in the ordinate with the upper part plotted on a logarithmic scale, for clarity.

The high electrical conductivity measured for these relatively low CNT loadings is the result of an efficient CNT network formation at the fibre/matrix interface. For the short and uniform CNT coverage (i.e. CNT-g-QF (S)), the CNT volume fraction in the interphase region can be estimated as follows (Eq. 4.1). First, assuming a MWCNT density of 1.8 g.cm^{-3} [268] and a quartz fibre density of 2.2 g.cm^{-3} [236], we obtain a CNT volume fraction for CNT-g-QF (S) of ca. 0.74 vol.%, from:

$$v_{CNT\ (interphase)} = \frac{V_{CNT}}{V_{Interphase}} = \frac{0.0074 \times \pi R^2 \times 1\ u.l.}{\pi(R^2 - r^2) \times 1\ u.l.}, \quad \text{Eq. 4.1}$$

where R is the radius of the CNT-g-QF (S), including the contribution from the 200 nm thick CNT layer, r the radius of the as-received QFs and u.l. corresponds to a unit length (**Fig. 4.15**). The geometric calculations suggest a CNT volume fraction of 12.6 vol.% within the interphase, consistent with aligned

arrays of CNTs grown over large areas [269]. The CNT loading in the interphase region is well above the local percolation threshold, but macroscopic conductivity requires percolation, at a longer scale, between these regions. Analogous selective localisation of CNTs has been found to be efficient in co-continuous polymer blends and double percolated structures [195]; the use of continuous fibres to structure the network is particularly effective in the fibre direction. However, both CNT-g-QF bundle composites exhibited an anisotropic behaviour with a transverse electrical conductivity an order of magnitude lower than its longitudinal conductivity (**Fig. 4.14**). For the longer CNTs (i.e. CNT-g-QF (L)), the local density in the interphase region is expected to be similar to that of the shorter, non-aligned CNTs (CNT-g-QF (S)). However, the CNT splayed "Mohawk" morphology, which leads to an apparently uneven CNT length along the tow, makes it difficult to estimate the CNT volume fraction more accurately.

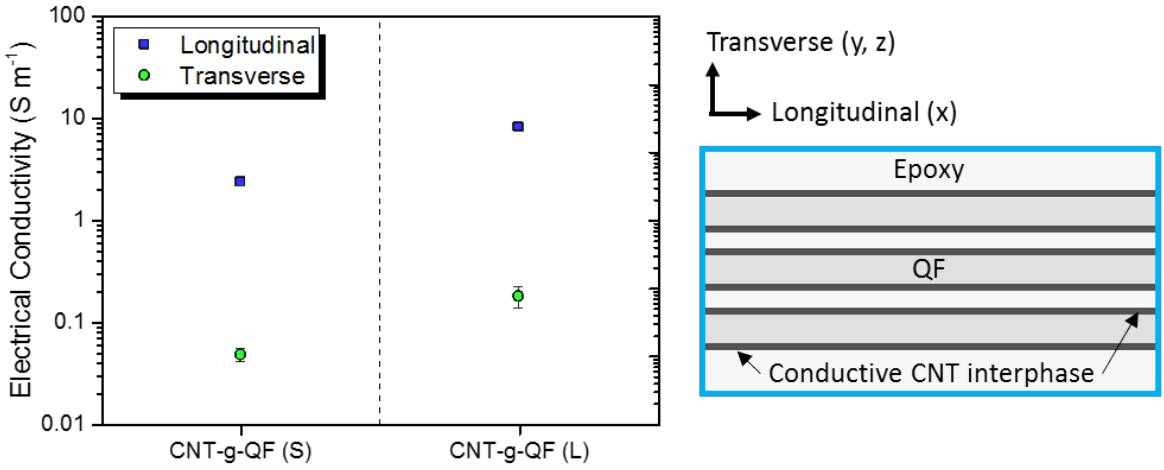


Fig. 4.14 *Ex-situ* electrical conductivity of the UD hierarchical bundle composites (longitudinal and transverse directions in relation to the loading direction) with standard error associated.

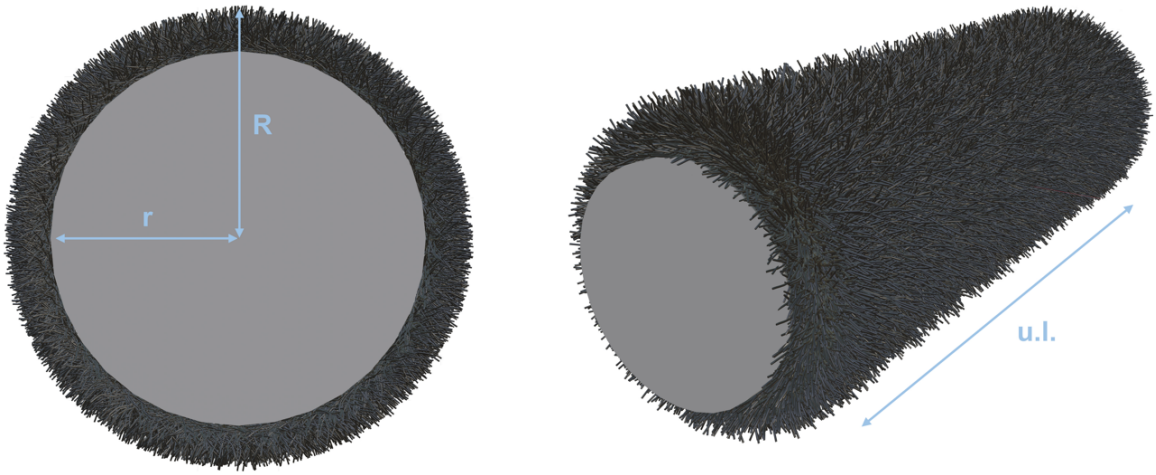


Fig. 4.15 A 3D model of a quartz fibre with a homogeneous coverage of short CNTs

Having established the *ex-situ* electrical conductivity of short and long CNT-g-QFs, we can now assess their piezo-resistive response in tension. With increasing load, the conductivity fell gently, until the sample approached its failure strain of ca. 2.1 %, at which point the conductivity dropped to zero, in one or more abrupt steps (**Fig. 4.13**a). Over the linear elastic mechanical range, the variation of the electrical resistance was also linear (**Fig. 4.13**d). Thus, the strain sensitivity can be calculated from the following Equation:

$$Sensitivity = \frac{\Delta\left(\frac{\Delta R}{R_0}\right)}{\Delta\varepsilon}, \qquad \text{Eq. 4.2}$$

where R_0 is the initial electrical resistance, ΔR is electrical resistance variation between 0.5 - 2.0% strain, and $\Delta\varepsilon$ = 1.5 % strain. The strain sensitivity of the shorter CNT-g-QF (S) sample (3.64 ± 0.43) was greater than that of the CNT-g-QF (L) sample decorated with longer CNTs (2.79 ± 0.16). A lower concentration of short CNTs is closer to the critical percolation network and, therefore, more sensitive to changes in network geometry as commonly observed in CNT/polymer systems [190]. The CNT-g-QF (S) bundle composites already show a two-fold increase in sensitivity over traditional resistance-type strain gauges [196], which might be improved further by optimising the CNT network architecture further towards criticality. In addition, the sensing network is embedded within the composite, intrinsically where the load is carried, rather than bonded to the surface; the arrangement of the conductive path along the primary reinforcing fibres provides a measure of strain in the load bearing direction. On approaching failure, the conductivity should correlate to the onset of fibre fragmentation, as observed in carbon fibre composites where the carbon fibres are used both as electrically conductive pathways and load bearing elements [270]. At higher strains, there is a non-linear region in the resistance change-strain curve; the gentle increase (**Fig. 4.13**d) could result

from plastic deformation of the CNT network at the interphase [206], fibre fragmentation/debonding [192] or a combination thereof. The absence of abrupt changes in $\Delta R/R_0$ below ~ 1.8 % strain (**Fig. 4.13**d) suggests that the electrical conductivity is not sensitive to isolated fibre breaks as the continuity of the network is retained [192], likely due to contacts amongst the large number of fibres (ca. 6000) in these bundle composites. Moreover, the change in conductivity associated with the onset of fibre fragmentation should depend on the subsequent locus of debonding. A failure at the CNT-fibre interface would leave the conductive network unchanged; however, the single fibre pull-out fracture surfaces (**Fig. 4.10**) suggest a cohesive failure, disconnecting the conductive sheath from neighbouring fibres. Thus, the larger jumps in $\Delta R/R_0$ at higher strains (**Fig. 4.13**d) were provisionally attributed to extended fibre debonding following fibre fracture.

4.3.2. Mechanistic study using correlated acoustic emission data

To confirm the origin of the $\Delta R/R_0$ steps, the electrical data was correlated with simultaneous acoustic emission (AE) data: AE has been extensively used in the field of composite materials as a non-invasive/non-destructive method to monitor the onset of damage and identify failure events associated with single or fibre cluster fracture [271]. A range of time-dependent parameters have been extracted from the AE signal as possible indicators of specific mechanisms. Simple AE amplitude is used most commonly; however, its strong dependence on testing type, material composition and configuration has led to contradictory failure mode classifications [272]. In addition, the amplitude is greatly influenced by the distance between the sensor and the internal failure event. While this phenomenon can allow for the location of events using a network of receivers, amplitude dampening limits failure mode identification. Recent work suggests that peak frequency may be the most reliable parameter to differentiate between failure mechanisms in composites materials [272].

Here, both the signal amplitude and the peak frequency were recorded as a function of strain (**Fig. 4.16**). The amplitude signal indicates the onset of damage and its evolution throughout the test, but fails to aid differentiate between failure modes. The peak frequency, however, exhibits discrete levels which (in ascending order of frequency) are attributed to matrix cracking, fibre/matrix debonding, fibre breakage and fibre pull-out [272]. Commercially sized quartz fibres, AR-QF-S, show predominantly matrix cracking, with only limited interfacial failure, as their interface is optimised for epoxy systems. Both QF-HT and QF-BiCat, on the other hand, show more fibre/matrix debonding than matrix cracking events, consistent with their poor compatibility with the epoxy system and, therefore, poor stress transfer capabilities. CNT-g-QFs, similarly to AR-QF-S, both show more matrix cracking than interfacial failure as expected based on the good interfacial performance observed in single fibre pull-out. Fibre/matrix debonding was delayed for the CNT grafted fibres, beginning at 0.8 - 1.0% strain,

rather than 0.4 - 0.5% strain for the various control fibres, consistent with an improved interfacial strength. The resistance-change increased linearly with the strain until the damage reached a threshold associated with a high amplitude event (**Fig. 4.16**, left). The peak frequency (**Fig. 4.16**, right), and especially the range from 400 to 500 kHz assigned to fibre breaks, indicated fibre fragmentation between 1.0 and 2.0 % strain, without any noticeable deviation from linearity of the $\Delta R/R_0$. The steady increase in $\Delta R/R_0$ up to 2.0 % strain did not correlate with specific composite damage mechanisms; the linear piezoresistive response can, therefore, be related to deformation of the CNT network conductive path [189], changes in the intertube tunnelling resistance [190], and/or the inherent piezoresistivity of CNTs [191]. Upon reaching ca. 2.1 % strain, the broken fibres began to debond, as evidenced by lower frequency events between 200 and 300 kHz, disconnecting the CNT coating on those fibres from the network; at this point, $\Delta R/R_0$ exhibited one or more sharp increases, before the final complete failure of the bundle and loss of the in-plane electrically conductive path. The conductivity along the CNT coatings provides a measure of strain across the load range and a warning of imminent failure as damage reaches a critical level.

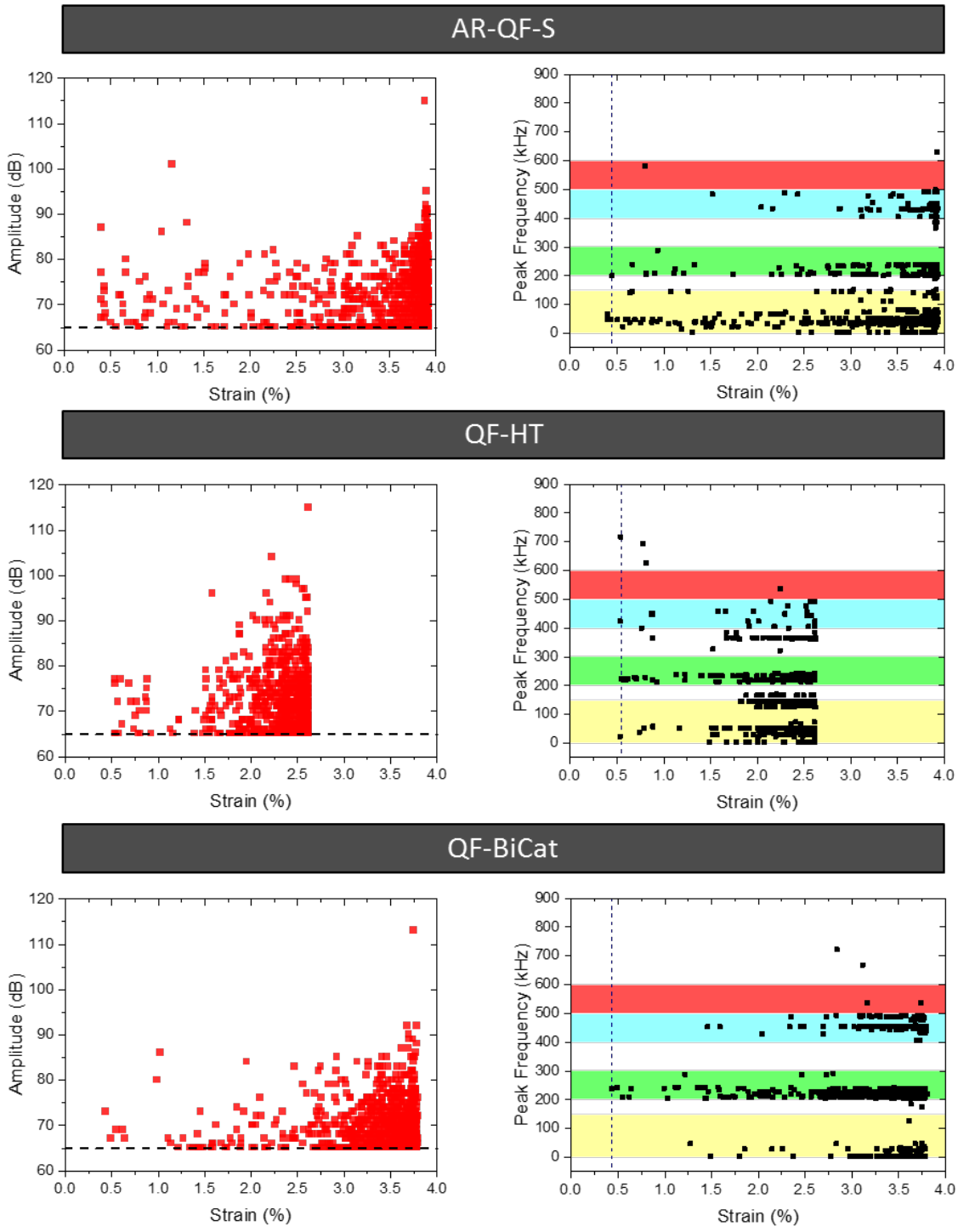


Fig. 4.16 Signal amplitude (left column) and peak frequency (right column) from acoustic emission events measured for all bundle composites (AR-QF-S, QF-HT, QF-BiCat, CNT-g-QF (S) and CNT-g-QF (L)) during tensile testing, and associated resistance-change ($\Delta R/R_0$) for UD hierarchical bundles. Vertical and horizontal dashed line correspond to 65 dB threshold and the onset of fibre/matrix debonding, respectively. Coloured peak frequency ranges were obtained from [272]. 0 – 150 kHz (yellow): matrix cracking; 200 – 300 kHz (green): fibre/matrix debonding; 400 – 500 kHz (blue): fibre failure; 500 – 600 kHz (red): fibre pull-out.

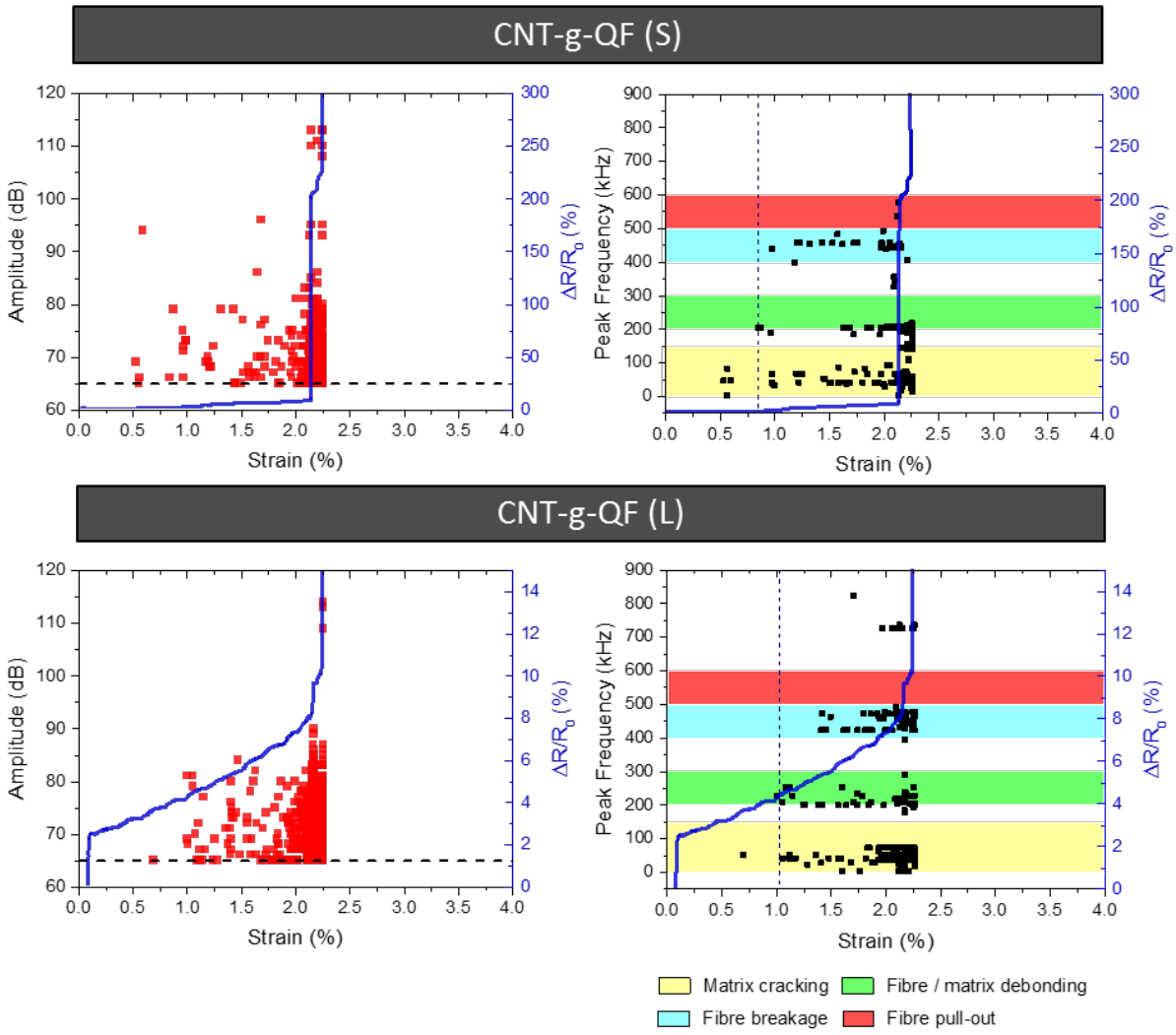


Fig. 4.16 (Continued).

4.4. Summary

A continuous process has been developed to graft CNTs onto quartz fibres, *via in-situ* CVD, to create homogeneous, "fuzzy" fibre reinforcements, throughout whole tows. The resulting hierarchical system combines features spanning many length scales: tow length (~ 20 m), tow diameter (~ 1 mm), fibre diameter (13 µm), CNT length (200 nm - 30 µm), CNT diameter (~ 10 nm). The grafted layer effectively improves the absolute interfacial shear strength between QF and epoxy by 12 % (90 ± 2 MPa) compared to the commercially sized QF control; fractographic observations indicate a cohesive failure in the CNT/epoxy interphase close to the parent fibre. Grafting shorter CNTs (~ 200 nm) to QF was more uniform/symmetric, and improved the interface more efficiently, even at low absolute CNT loading in the composite (ca. 0.3 wt.%). At the macroscale, AE confirmed the improved fibre/matrix interaction through a delayed onset of fibre/matrix debonding and a greater proportion of matrix microcracking to fibre debonding. Both single fibre and macroscopic tow composite tensile tests consistently showed that the primary fibre modulus was preserved, though a reduction in tensile strength demonstrated a need for improvements in process control and/or fibre handling.

More interestingly, despite the low loading, the organised CNT coatings provided an electrically conductive path through the otherwise insulating QF composites. The loading fractions, expected to be near percolation, combined with the distribution parallel to the primary fibres, provided a means to monitor strain in the fibre direction and the onset of fibre breakage. Fibres grafted with shorter CNTs, likely closer to the critical percolation threshold, had a particularly high strain sensitivity of 3.64 ± 0.43, a two-fold increase over traditional resistance strain gauges. In addition, the in-plane electrical conductivity was found to be significantly higher than conventional CNT/epoxy percolated networks and CNT-dispersed GF/epoxy composites. The relatively high conductivity (reaching 2.7 ± 0.3 $S.m^{-1}$ for shorter CNTs (0.3 wt.%)) is particularly useful for electrically-monitored damage detection, and other applications, such as static dissipation in composite radomes [19].

The continuous CNT-synthesis process presented here demonstrates a practical and scalable route to produce hierarchical quartz fibre reinforcements in large quantities. The very short grafted CNTs provide the best mechanical interfacial enhancement and the best strain sensing ability, without disrupting the primary fibre composite volume fraction. In addition, short CNTs do not activate nanotoxicological mechanisms (specifically frustrated phagocytosis) that have caused concerns about straight multiwalled-CNTs longer than around ten microns [273]. The continuous preparation of hierarchical fibrous reinforcements, suitable for implementation on carbon/glass fibres production lines, provides a route towards the manufacture of large multifunctional composite specimens. The growth of short CNT layers is a crucial requirement for practical structural composites, in which

primary volume fraction is such a key factor, but is often over-looked in the literature since longer CNTs are typically easier to grow and study. In principle, the mechanically keyed CNT-rich interphase could provide enhancements in a range of matrices, including more challenging thermoplastic systems [7], and may be less water sensitive than conventional glass fibre sizings [274].

Chapter 5 : Continuous synthesis of CNTs on carbon fibres - A parametric study

Whilst the growth of CNTs on quartz fibres is fairly straightforward, growth on carbon fibres can be challenging, since catalysts used for CVD growth typically etch carbon fibres. A new electric-field modulated CVD process promises high throughput production as a continuous process, with minimal fibre damage. This chapter describes a thorough investigation of process variables, offering both microstructural control and insights on growth mechanisms. The influences of both chemical and physical parameters on key CNT characteristics (length, density, etc.) were studied and adapted for application in CFRPs. CVD parametric studies are typically slow and daunting, due to experimental variability, especially when conducted on small batch systems. On the other hand, the continuous CVD technique offers a more efficient and reliable approach, providing better control of processing parameters and allowing real-time adjustments. Whilst previous work on batch CVD only produced limited quantities of CNT-grafted carbon fibres for microscale mechanical characterisation, the development of continuous processes allowed for more comprehensive mechanical evaluation of composites at the macroscale (refer to **Chapter 6**). Continuous CVD is key to the development of nanoengineered composites and could be readily adapted to the manufacture of carbon fibres for large scale production of materials.

5.1. In-line continuous deposition of catalyst precursor on carbon fibres

The deposition of catalyst precursors is critical in synthesising a homogenous coverage of CNTs on carbon fibre surfaces. However, depositing catalyst particles on thousands of closely packed micron-scale fibres can be challenging. The selection of catalyst precursors, concentrations, and substrate surface chemistry, all play an important role in the growth kinetics of CNTs. This section presents the development made towards scaling up an existing batch deposition system, including the selection of a scalable deposition technique, catalyst composition, and carbon fibre pre-treatment.

5.1.1. Morphology of the carbon fibres

As-received carbon fibres

Continuous tow of commercially-sized (AS4C-GP, 12K, 6.9 µm diameter, Hexcel, GB) and unsized (AS4, 12K, 7.1 diameter, Hexcel, GB) PAN-based carbon fibres were both used. Because these high-strength, high-strain carbon fibres have been commercially available for over a decade, they no longer stand as the highest performing carbon fibres available on the market. Nonetheless, they remain extensively used in the aerospace sector for structural applications owing to their compelling cost-performance ratio [61]. In addition, having been extensively used in both academic research and industry, a wide range of fibre properties are well established, including complete wetting/interfacial studies with and without plasma oxidation [247, 275]. Previous CNT synthesis on small numbers of individual AS4 sized carbon fibres offers valuable insight on the behaviour of these fibres as a substrate. Whilst carbon fibres tows generally contain between 1 to 24 k filaments, with some applications requiring the use of bobbins with a filament count as high as 600 k, tows containing 12 k filaments were chosen as a compromise between quantity, ease of processing and availability. For simplicity, the sized and unsized carbon fibres are referred to as AS4-S and AS4-US fibres, respectively. Both types of carbon fibre tows are formed of 12,000 filaments with a near circular cross-section. AS4-S fibres are generally preferred due to their ease of handling; the sizing acts as a protective coating as well as a binder, preventing fibre damage, and promoting adhesion to the matrix, respectively. SEM micrographs of AS4-S fibres (**Fig. 5.1**, left) show a smooth fibre surface due to the presence of polymeric sizing [67] along with some darker areas and bubble-like features indicative of coating inhomogeneity. On the other hand, AS4-US fibres exhibit a more textured surface with a more consistent topography, including pronounced longitudinal striations/crenulations (**Fig. 5.1**, right). Although AS4-US fibres are prone to damage during handling, the incorporation of a CNT growth step in existing fibre production lines would most likely occur prior to polymeric sizing deposition and potentially even earlier in the manufacturing of the carbon fibres before graphitisation temperatures are achieved, making unsized

fibres a more logical candidate for continuous CNT-g-CF CVD development. In any case, the sizing will be thermally decomposed during CNT growth, potentially leaving an unwanted residue.

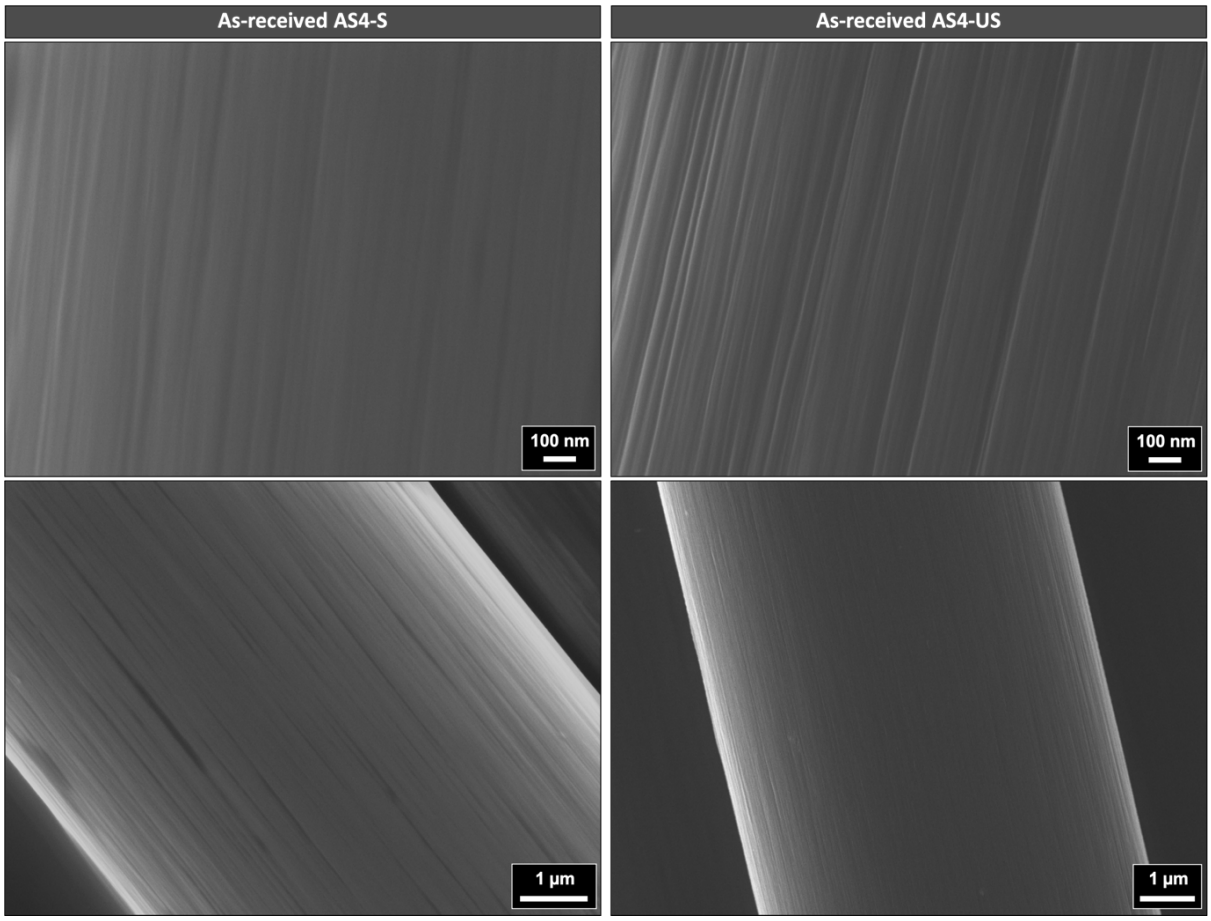


Fig. 5.1 SEM micrographs of as-received (left) sized and (right) unsized AS4 carbon fibres.

Plasma treated carbon fibres

Unsized commercial carbon fibres typically exhibit an inert, generally non-polar and smooth surface, leading to poor wetting properties, particularly with metallic catalyst precursors. Commercially produced carbon fibres generally undergo an electro-oxidative process to improve adhesion to common composite matrices (such as epoxy); however, the degree of oxidation is not sufficient for effective wetting by highly polar catalyst precursors. Additional oxidative treatments, for example using atmospheric-pressure plasma, introduce oxygen-containing groups and topographical features onto the surface of carbon fibres that promote the formation of micropores and adsorbent sites [65]. In addition, plasma treatment is expected to form a more homogeneous carbon fibre surface chemistry, removing contaminants [63]. The surface of AS4-US fibres was plasma treated prior to catalyst precursor deposition (referred to as P-AS4-US fibres), using both oxygen and compressed air as plasma feed gases. The plasma treatment conditions were set to maximise surface oxides

homogeneity and avoid damage to the parent fibres, as reported in previous literature [275]. The latter study, by Erden *et al.,* was performed on unsized, industrially oxidised AS4 fibres, evidencing improvement in carbon fibre wetting properties while retaining their mechanical properties. An extensive study of the surface properties of P-AS4-US fibres was not pursued, as XRD and BET data were already available [275]. However, for confirmation and quality control, the wetting and mechanical properties of P-AS4-US fibres were assessed using the Wilhelmy method (refer to **Chapter 3**) and unidirectional bundle composites tests (refer to **Chapter 6**), respectively.

The atmospheric plasma oxidation (APO) treatment of the carbon fibres resulted in a decrease in the receding contact angle, namely, from 43.9° to 25.1°, and from 43.9° to 40.8°, using oxygen and compressed air as gas-feed, respectively, as compared to untreated AS4-US fibres (**Table 5.1**), consistent with values previously reported [275]. The reduction in the water contact angle is characteristic of an increase in hydrophilicity, as well as an increase in the overall fibre surface tension. Even though the use of oxygen as gas-feed (33 $L.min^{-1}$) led to the production of P-AS4-US with superior hydrophilicity, compressed air was selected as a more cost-effective alternative.

Table 5.1 Contact angle measurements of carbon fibres in water, before and after APO treatment.

Fibres	θ_a (°)	θ_r (°)	$\Delta\theta$ (°)
AS4-US	59.5 ± 0.9	43.9 ± 0.7	15.6 ± 0.5
P-AS4-US (Air)	64.6 ± 1.0	40.8 ± 0.6	23.8 ± 0.7
P-AS4-US (O_2)	65.1 ± 1.0	25.1 ± 0.4	40.0 ± 1.3

θ_a = Advancing contact angle; θ_r = Receding contact angle; $\Delta\theta$ = Water contact angle hysteresis.

5.1.2. Bi-catalyst precursors deposition on carbon fibres

Both plasma-treated (P-AS4-US) and untreated (AS4-S) carbon fibres were investigated as substrates for the deposition of bi-catalyst precursors; the latter was used as control for comparison with previous studies carried out by Anthony [3, 245]. The deposition of catalyst particles on the surface of AS4-S fibres was challenging due to the presence of polymeric sizing. When introducing the fibres into the bi-catalyst precursor solution consisting of a mixture of iron (III) nitrate nonahydrate and nickel (II) acetylacetonate in ethanol, the sizing only partially dissolved, as evidenced previously by Anthony with TGA [8]. Hence, small aggregates formed on the surface of the fibres (**Fig. 5.2**), as a result of the metal salts and residual polymer mixing. Furthermore, sized carbon fibres were found to stick together, generating drying artefacts and an uneven distribution of catalyst particles (**Fig. 5.2**, right). The presence of residual polymer after deposition is a source of variability for the growth of CNTs as the coating can locally alter the fibre surface composition in oxygen, carbon and hydrogen; the ternary surface composition is critical for the synthesis of CNTs (see Section **2.1.4**, pp. 29), and can potentially

lead to spatial inhomogeneity (**Fig. 5.3**). However, AS4-S fibres was investigated as a potential substrate owing to promising initial results in growing uniform CNT in batch conditions [245].

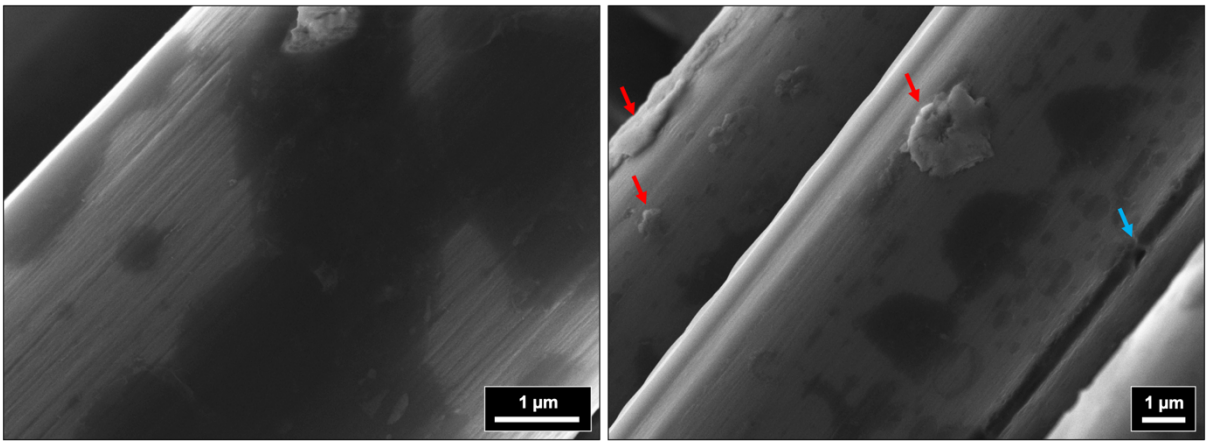


Fig. 5.2 SEM micrographs of bi-catalyst deposited AS4-S fibres. Red arrows indicate the presence of catalyst precursor-polymer aggregates, while the blue arrow shows a typical agglomeration between two adjacent carbon fibres.

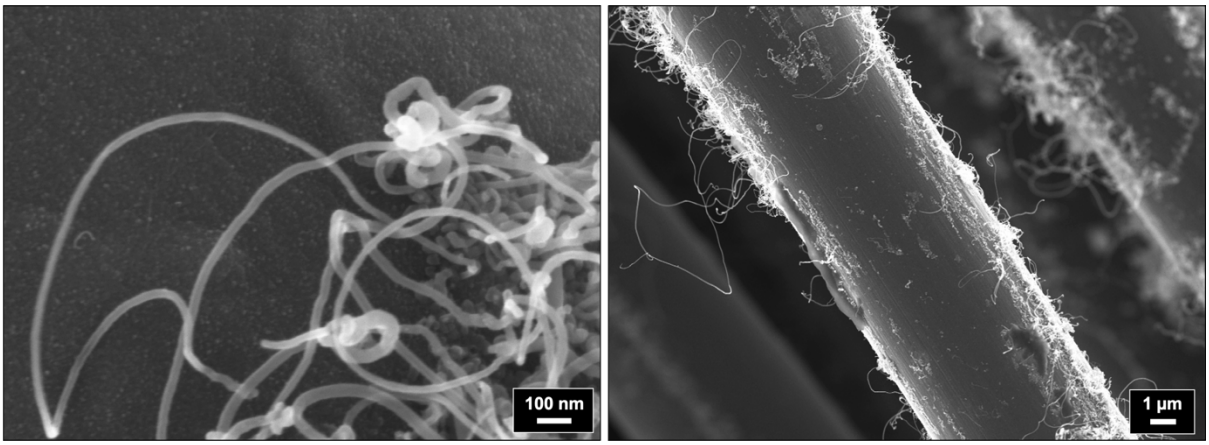


Fig. 5.3 SEM micrographs of CNT growth on bi-catalyst deposited AS4-S fibres produced with CVD_H synthesis conditions (refer to **Table 5.4** for details on CVD_H growth conditions).

Whilst the deposition of bi-catalyst precursors was more successful (no drying artefact) on AS4-US fibres as compared to AS4-S fibres, the deposition on the plasma-treated P-AS4-US fibres improved the density of CNT nucleation sites and homogeneity across the tow (**Fig. 5.4**). Fibres were selected at random locations across and along the tow, to examine each sample fairly. By investigating over 100 individual CNT-grafted carbon fibres, the percentage of carbon fibres yielding a satisfying CNT growth, was estimated to be around 60 and 90 % for AS4-US and P-AS4-US fibres, respectively.

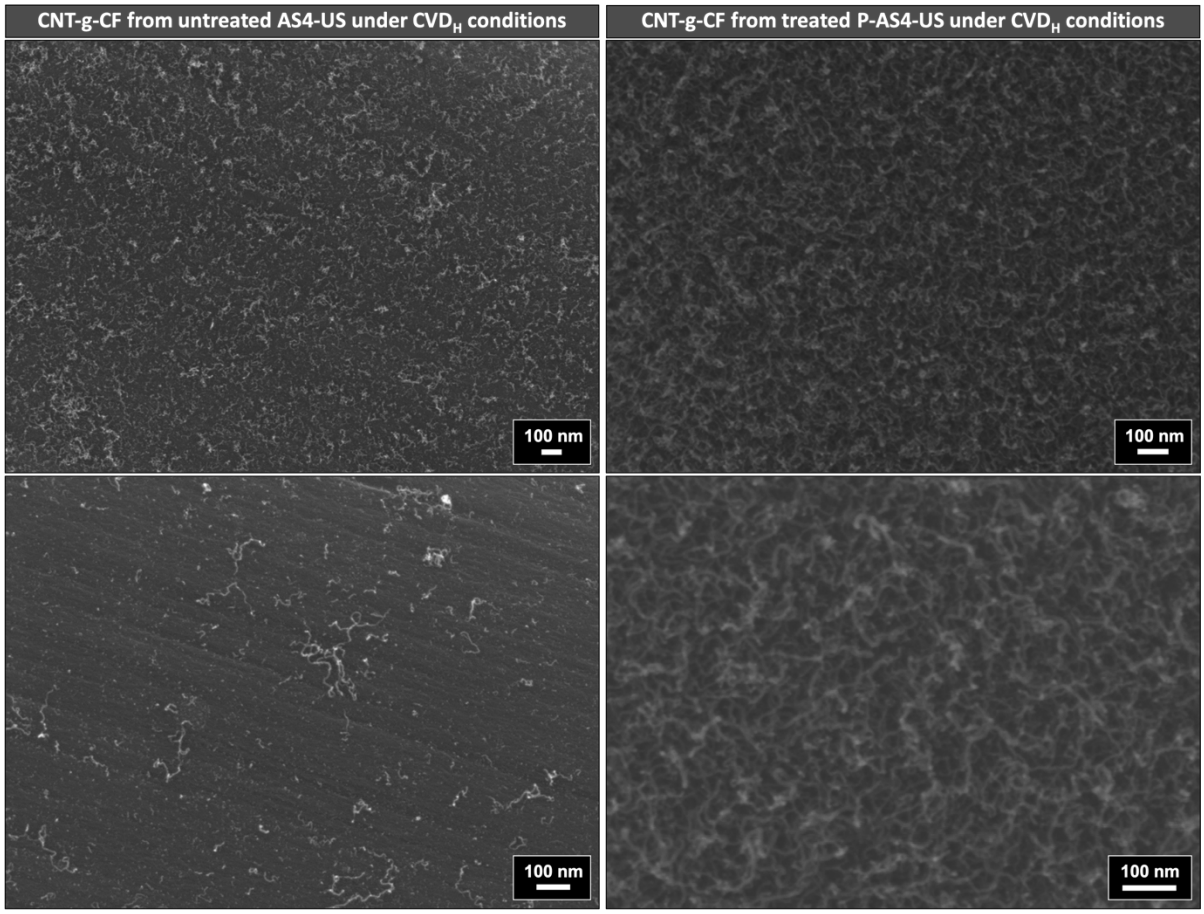


Fig. 5.4 SEM micrographs of CNT growth on bi-catalyst deposited untreated AS4-US fibres (left) and plasma treated P-AS4-US fibres (right) under CVD_H synthesis conditions.

5.1.3. Effect of bi-catalyst precursors composition on CNT synthesis

As discussed in Section **2.1.4**, Binary catalysts, including those based on Ni-Fe alloy, have often been reported to be efficient for CVD growth [276]; however, the variations in substrate, feedstock, and other species, such as water and CO_2, makes comparisons difficult. Moreover, the use of carbon fibres as substrates make correlations even more challenging as different levels of graphitisation (sp^2:sp^3 hybridisation ratio) have been found to strongly affect the CNT yield; while sp^3 rich carbon leads to a poor catalyst-support interaction and low CNT yield, sp^2 rich carbon promotes controlled growth of dense CNT forests [37].

An optimal Ni:Fe composition for AS4 carbon fibres was determined using binary Ni:Fe ratios (1:0.33, 1:0.5, 1:0.64, 1:1, 1:2 mol.%) under previously studied CVD conditions (CVD_H, **Table 5.4**). When combined, Ni and Fe generate CNTs of varying morphologies, depending on the bi-catalyst composition, with a combination of stubby (> 20 nm) and slender (~ 10 nm) CNTs when Ni is use in excess (**Fig. 5.5**a). Similarly, when Fe is predominantly used, a combination of stubby and slender CNTs with low quality are observed (**Fig. 5.5**e). The difference in growth characteristics can be attributed to contrasting wetting behaviour between the two metals with the carbon fibres, leading to the formation of smaller catalyst particles for Fe and larger particles for Ni producing CNTs with different diameters, as previously reported [44]. Generally, an increase in CNT yield can be achieved with bi-catalyst systems as compared to single system even though most stoichiometries leads to a relatively scarce and inhomogeneous growth coverage, with an optimal yield obtained for a ratio of 1:0.64 mol.% (Ni:Fe) (**Fig. 5.5**c). Despite Ni being the predominant catalyst in the optimal mixture composition, the synthesised CNTs morphology show some similarities with those typically obtained from single Fe systems [44]; “slender” CNTs with diameter of about 10 nm and length (perpendicular to the carbon fibre surface) of about 200 nm were produced.

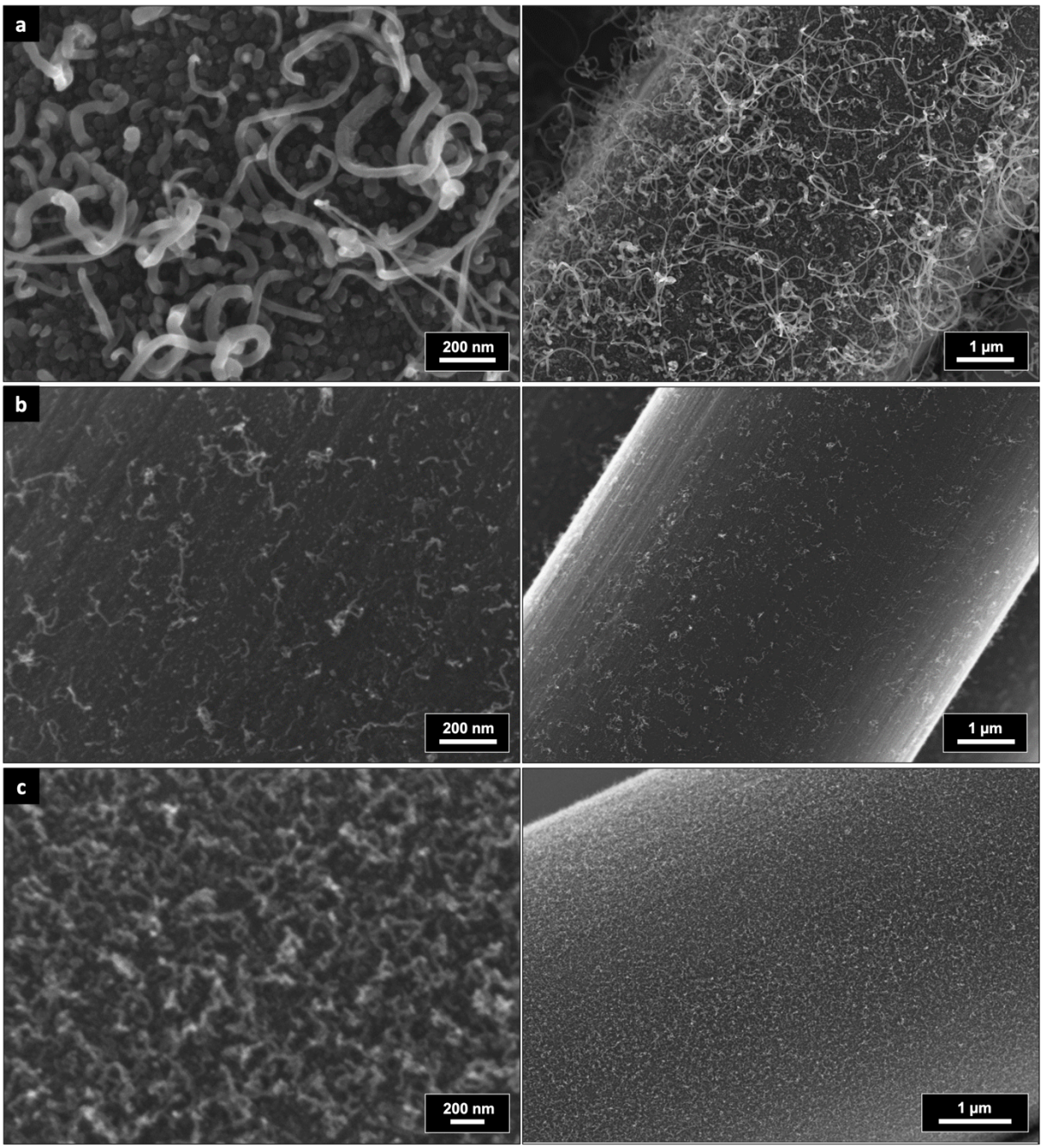


Fig. 5.5 SEM micrographs of CNT growth on carbon fibres using varying bi-catalyst stoichiometries: (a) 1:0.33, (b) 1:0.5, (c) 1:0.64, (d) 1:1 and (e) 1:2 mol.% Ni:Fe. The deposition was performed in batch conditions on untreated AS4-S fibres with a EtOH concentration of 1 wt.% $Ni(acac)_2$ + $Fe(NO_3)_3$. The growth was performed using CVD_H synthesis conditions.

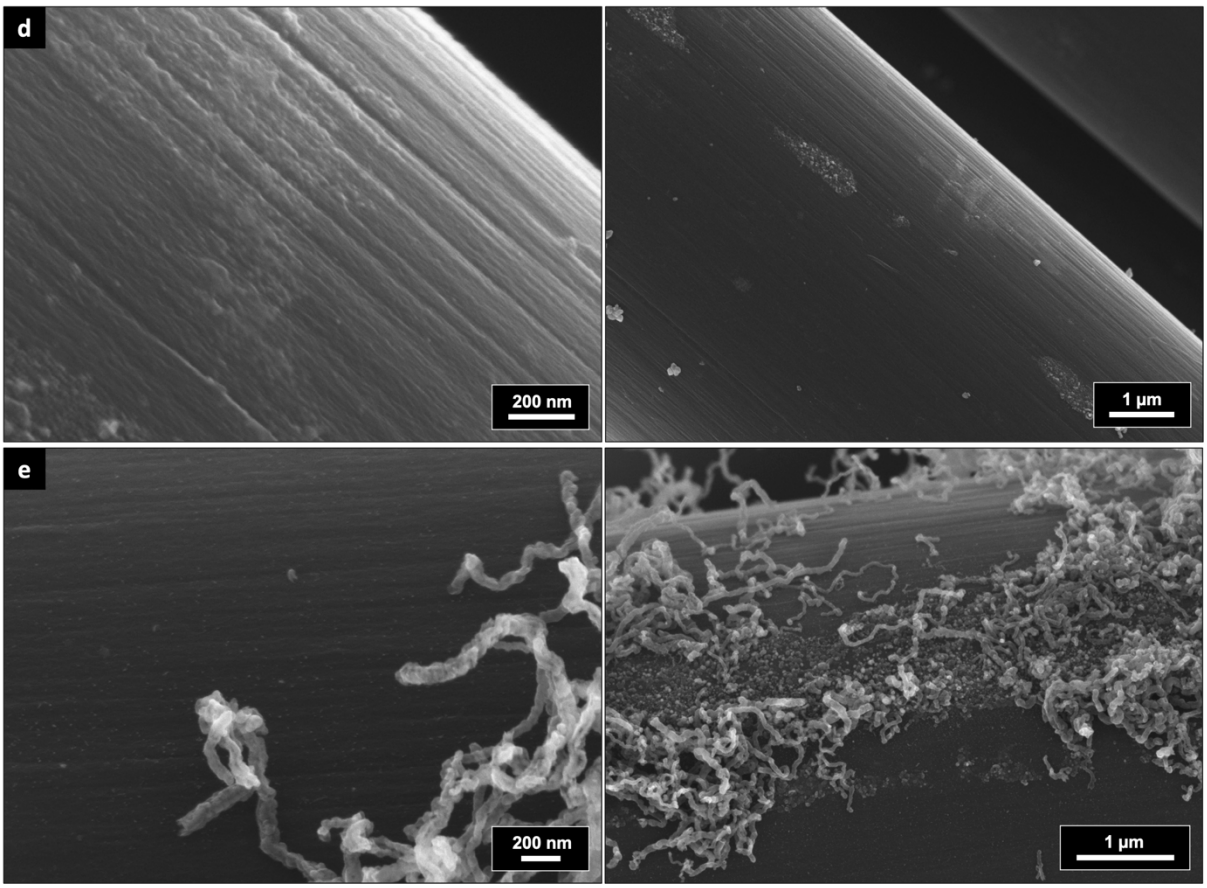


Fig. 5.5 (Continued)

5.1.4. Effect of bi-catalyst precursors concentration on CNT synthesis

Having established a suitable Ni-Fe alloy stoichiometry promoting the growth of CNTs on AS4 carbon fibres, the process needed further optimisation to achieve uniform and dense coverage. Adjusting the concentration of bi-catalyst precursors in solution was attempted to address uniformity and density concerns. An insufficient catalyst precursor concentration typically produces a scarce but homogeneous coverage of catalyst (assuming adequate carbon fibre surface treatment); an excess of catalyst in solution leads to the formation of aggregates generating heterogeneous CNT growth. Previous work by Qian used oxidised unsized carbon fibres as substrates, on which pure Fe catalyst systems were deposited with a concentration in solution of 5 wt.%; however, an additional washing step in water led to an apparent catalyst content on carbon fibres of approximately 0.4 wt.% [144]. More recent work by Anthony, focused on untreated sized carbon fibres using a Ni-Fe catalyst system [3], which confirmed that a concentration of 4 wt.% was excessive and similarly required a washing step in water, leading to poor repeatability in the deposition process. Given the larger deposition scale deployed in this work, an initial bi-catalyst concentration of 5 wt.% was selected. However, this concentration was found to saturate the solution with the formation of a slurry after few hours of mechanical stirring at larger scales, leading to local variation in Ni-Fe stoichiometry and the presence

of aggregates on the fibres. Diluted solutions were investigated, across two orders of magnitudes in concentration, namely, 0.1, 0.5 and 1 wt.% in EtOH to achieve a suitable catalyst precursor solution for large scale continuous deposition without an explicit washing step. Given the difficulty in assessing the quality of the catalyst precursor deposition prior to catalyst reduction, and maintaining the alloy stoichiometry, each sample set was simply exposed to CVD synthesis conditions CVD_{α} (**Table 5.8**). All precursor solution concentrations (0.1, 0.5 and 1 wt.%) produced uniform coverage of nucleation sites (**Fig. 5.6**), with the lowest concentration leading to a sparse coating (**Fig. 5.6**a). The 1 wt.% bi-catalyst solution allowed for a high density of nucleation sites, promoting the formation of a dense CNT coating (**Fig. 5.6**). This concentration was then used for the majority of studies when CVD variables were investigated. The bi-catalyst precursors deposition parameters used throughout the CVD parametric study were therefore selected as described in **Table 5.2**:

Table 5.2 Final bi-catalyst precursors deposition parameters

Fibre substrate		Line speed	Bath composition	Bath residency time
Type	Surface condition	($m.h^{-1}$)		(min)
CF (AS4)	Unsized, plasma treated	20	1 wt.% $Ni(acac)_2$ + $Fe(NO_3)_3$ in EtOH (1:0.64 mol.%)	1

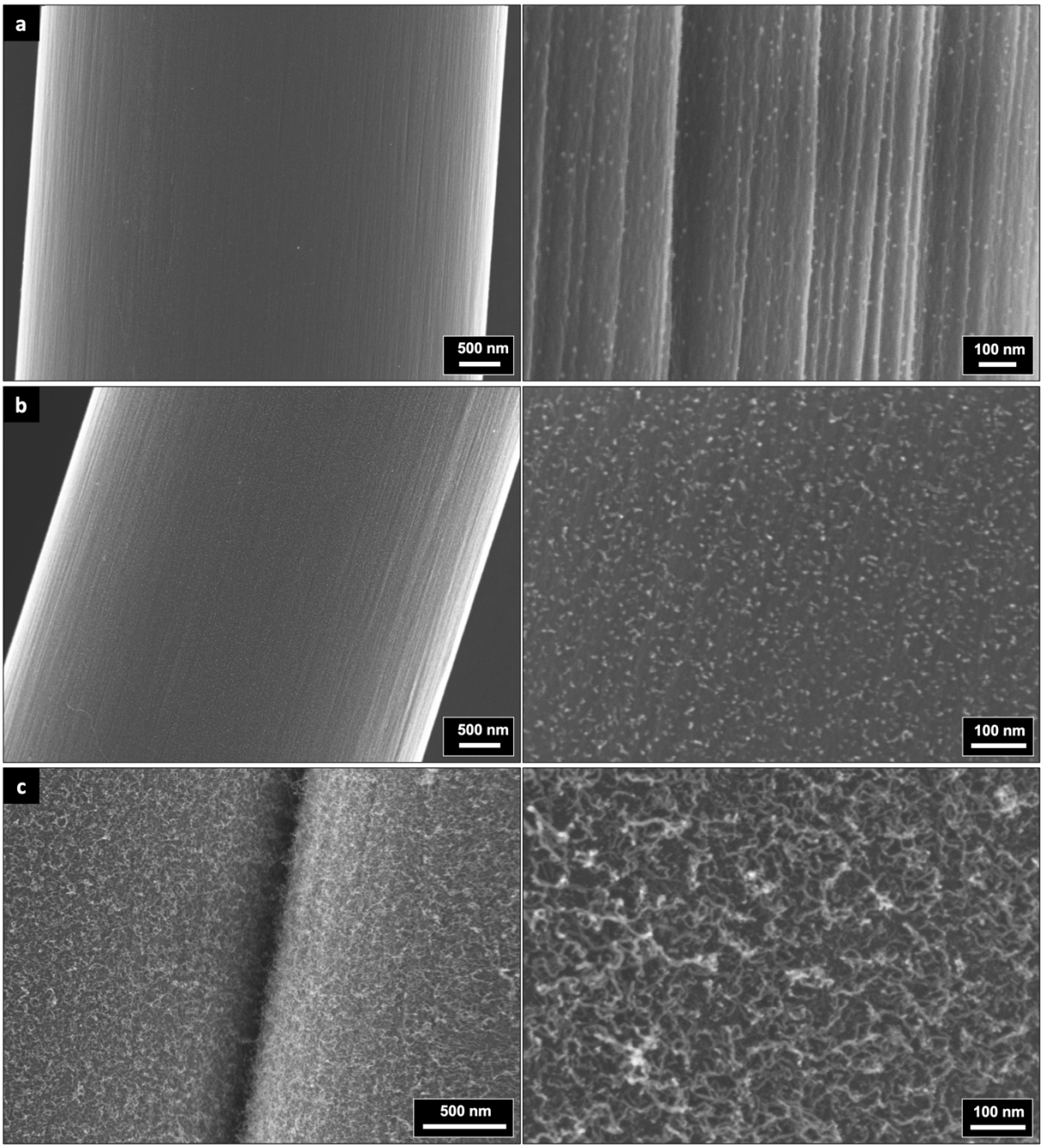


Fig. 5.6 SEM micrographs of CNT-grafted carbon fibres produced from deposition in (a) 0.1 wt.%, (b) 0.5 wt.% and (c) 1.0 wt.% bi-catalyst (Ni:Fe, 1:0.64 mol.%) solutions.

5.2. In-line CNT-synthesis via chemical vapour deposition

Following the development and scale-up of a suitable catalyst deposition route on carbon fibre tows, and the identification of an efficient bi-catalyst precursor system, both in terms of composition and concentration, the subsequent growth of CNTs on carbon fibres was investigated.

5.2.1. Continuous CVD parameter space

The temperature, active gas composition, reduction and growth duration are well-known to strongly influence CNT growth characteristics [46]. Hence, the ability to control these parameters and fine tune them is critical. Due to the continuous nature of the process, the synthesis duration, and more specifically the reduction and growth durations, are determined by the choice of line speed and internal quartz tubing arrangement. However, only the latter allows for independent adjustments of both the reduction and growth time. The ratio of active gases (i.e. [C_2H_2:H_2]) were controlled by fine-tuning of individual gas flow (H_2 and C_2H_2) using the MFCs. A list of all process variables is provided in **Table 5.3,** including potential difference which was generated from a power supply connected to a voltage amplifier, forming a capacitor-like circuit with the graphite foil and the carbon fibres (**Fig. 3.5**). For comparative purposes, the initial synthesis conditions were chosen from Anthony's prior work [8], these (historically used) CVD conditions are referred to as "CVD_H" and are presented in **Table 5.4**.

Table 5.3 CVD line equipment list and associated process variables.

Equipment	Variable	Unit	Range
Furnace	Temperature	°C	[650 – 950]
Motorised collection creel (pulley system, electrical motor, power supply)	Line-speed	m/h	[0.6 – 10]
Mass-flow controllers	Gas-flow	sccm	[7500 – 12000] N_2 [3400 – 6800] H_2 in N_2 [162 – 650] C_2H_2 in N_2
Capacitor-like circuit (Graphite foil, carbon fibre tow, power supply, voltage amplifier)	Potential difference	V	[0 – 1500]
Internal quartz tubing arrangement (altered displacement)	Reduction time Growth time	min	[0.72 – 10] [3.1 – 50]

Table 5.4 CVD_H synthesis conditions.

Temperature (°C)	Line speed ($m \cdot h^{-1}$)	Reduction time (min)	Growth time (min)	N_2 flow (sccm)	H_2 flow (sccm)	C_2H_2 flow (sccm)	C_2H_2:H_2 ratio	Potential difference (V)
770	1.2	10	30	7500	3400	325	1:19.3	300

5.3. Refining the CVD parameter space for enhanced CNT synthesis

Having defined all major process variables in the previous section (**Table 5.3**), a parametric study was carried out starting from the previously established CVD synthesis conditions (CVD_H). The effect of potential difference was first investigated, as it was previously shown to promote CNT growth and avoid damage to the carbon fibres. The growth temperature, active gases composition, reduction and growth time parameters were studied subsequently.

5.3.1. Effect of applied potential difference on CNT synthesis

The use of a modest potential difference of 300 V was previously shown by Anthony [8] to enhance the CNT growth and hinder detrimental effects to the carbon fibres such as catalyst pitting (**Fig. 5.7**b). However, a further increase in the potential difference to 1000 V did not provide significant improvement in growth characteristics (**Fig. 5.7**c). On the other hand, in the absence of a potential difference, the growth of carbon nanotube was extremely sporadic, with pitting on the carbon fibres surface clearly visible (**Fig. 5.7**a), in good agreement with previous findings.

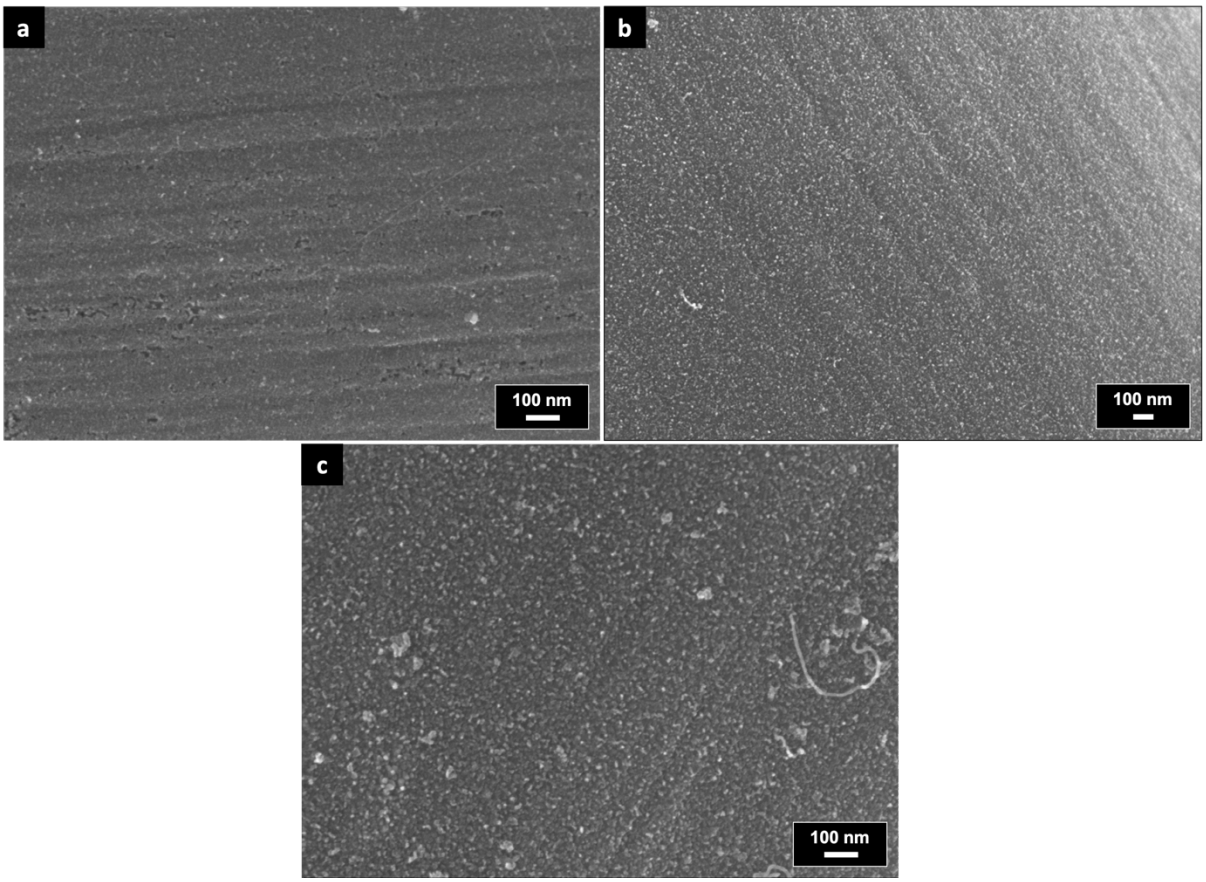


Fig. 5.7 SEM micrographs of CNT-g-CF from CVD_H conditions using a potential difference of (a) 0 V, (b) 300 V, and (c) 1000 V.

Smaller variations of the potential difference with 50 V increments between 0 and 200 V exhibited an on/off response with potential difference below 100 V unable to promote the growth of CNTs (**Fig. 5.8**). For potential difference of 100 and 150 V, sporadic CNT growth could be observed whilst a further increase to 200 V led to a homogeneous and dense coverage of CNTs similar to that of an applied potential difference of 300 V (**Fig. 5.7**b). Given that increasing the potential difference further did not lead to further improvement in the CNT synthesis, 300 V was chosen as the applied potential difference throughout the parametric study.

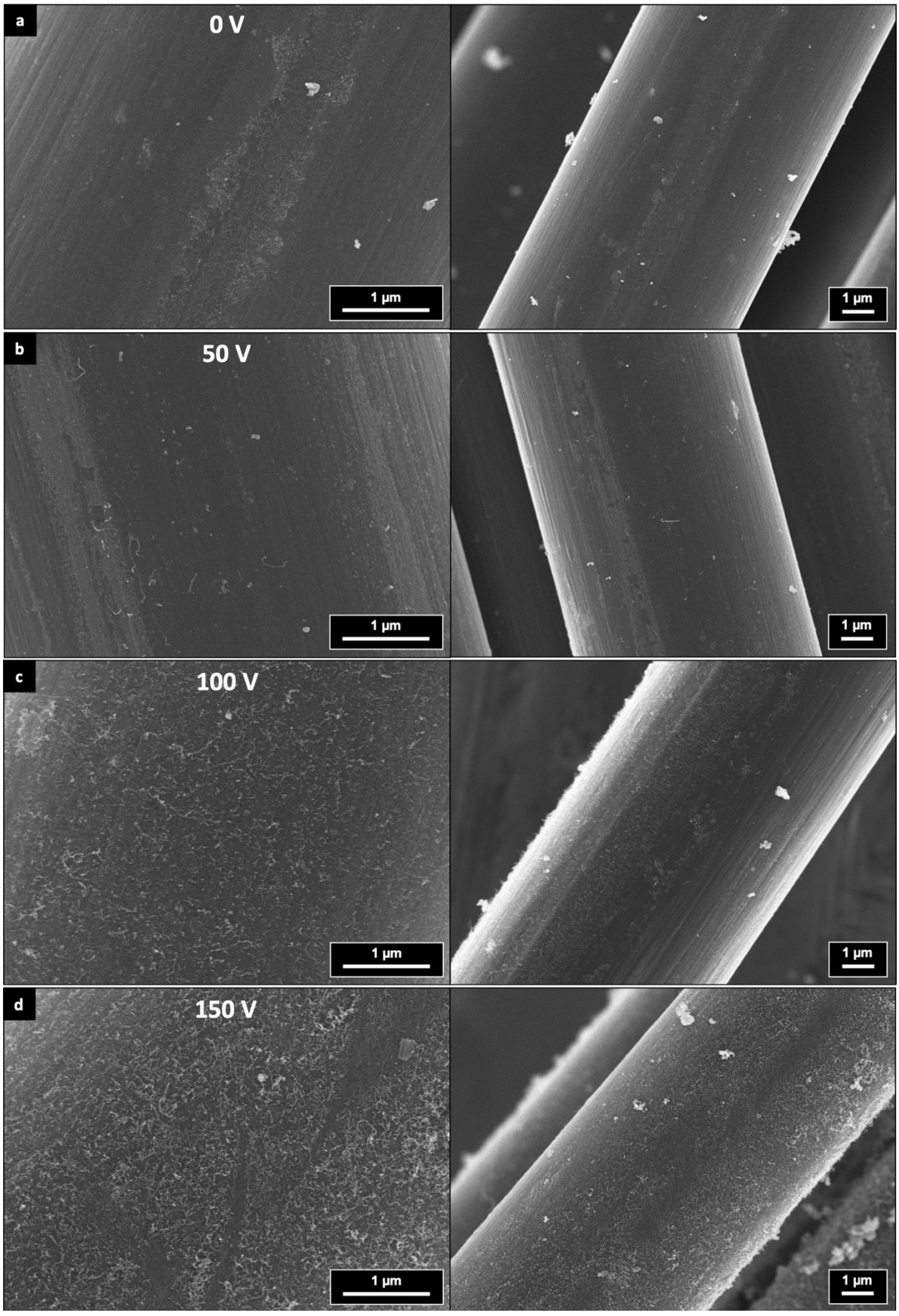


Fig. 5.8 SEM micrographs of CNT-g-CF from CVD_H conditions with sequentially increased potential difference starting from 0 V.

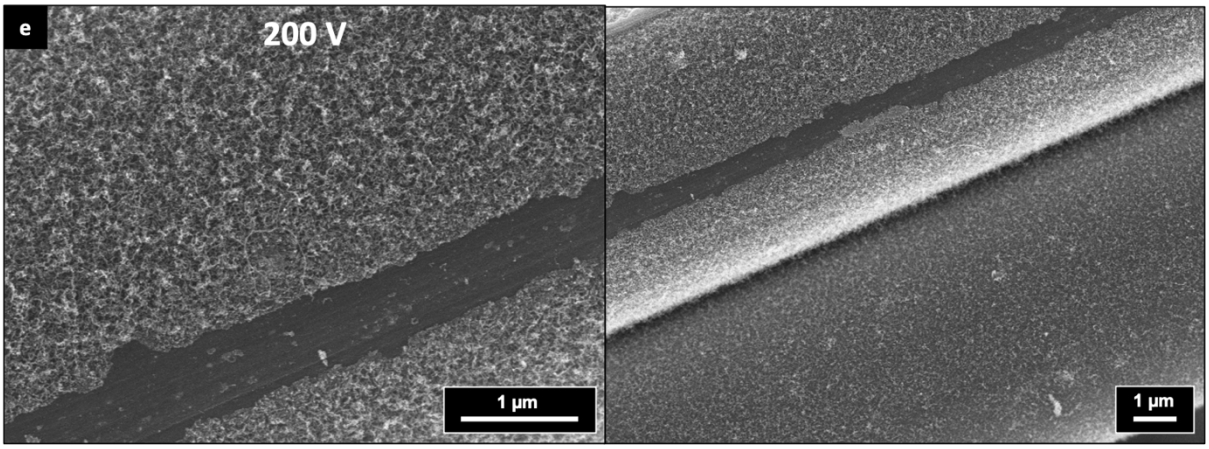


Fig. 5.8 (Continued)

5.3.2. Effect of the furnace temperature

High synthesis temperature offers both an improved CNT yield due to an increase in carbon solubility in the catalyst metals and a higher degree of CNT crystallinity. Whilst lower synthesis temperature typically offers lower CNT quality, they are generally preferred as to reduce both carbon fibre damage and the system energy requirements. Some compromise between CNT yield/quality and carbon fibre structural integrity may be inevitable. A wide range of growth temperatures, from 670 to 970 °C, were initially investigated with all others process variables kept constant (CVD_{α} conditions) (**Table 5.8**). Finer variations in the growth temperature were then undertaken (**Fig. 5.10**). The lower end of the temperature (< 720 °C) did not allow for the growth of CNTs on carbon fibres surfaces; SEM micrographs revealed an even coverage of catalyst particles on the surface of the fibres, which did not nucleate any extended growth, though they are likely encapsulated by carbon (**Fig. 5.9**a). Increasing the growth temperature to 720 °C generated a sparse coverage of CNTs (**Fig. 5.9**b), while further increase to 770 °C allowed for a dense and even coverage of slender (~ 10 nm) CNTs (**Fig. 5.9**c). Surprisingly, and in contradiction to previous findings, a further increase in temperature (> 770 °C) appeared detrimental to the synthesis of CNTs, with only some sporadic CNTs produced at a temperature of 870 °C (**Fig. 5.9**e). Interestingly, by increasing the growth temperature from 870 to 970 °C, the size of the catalyst particles seemed altered, with larger particles obtained at higher temperatures. In fact, a direct comparison between the catalyst particles formed at 670 °C and 970 °C show a significant variation in catalyst particle sizes, suggesting that temperature have an impact on the formation of catalyst particles. Finer temperature variations around 770 °C, by increments of 10 °C, suggests that the temperature window for optimal CNT growth is relatively small (**Fig. 5.10**). The CNT configuration obtained at 770 °C (**Fig. 5.9**c and **Fig. 5.10**c) is attractive, offering higher CNT aspect ratio and density, and was therefore selected as synthesis temperature for the remainder of the parametric study.

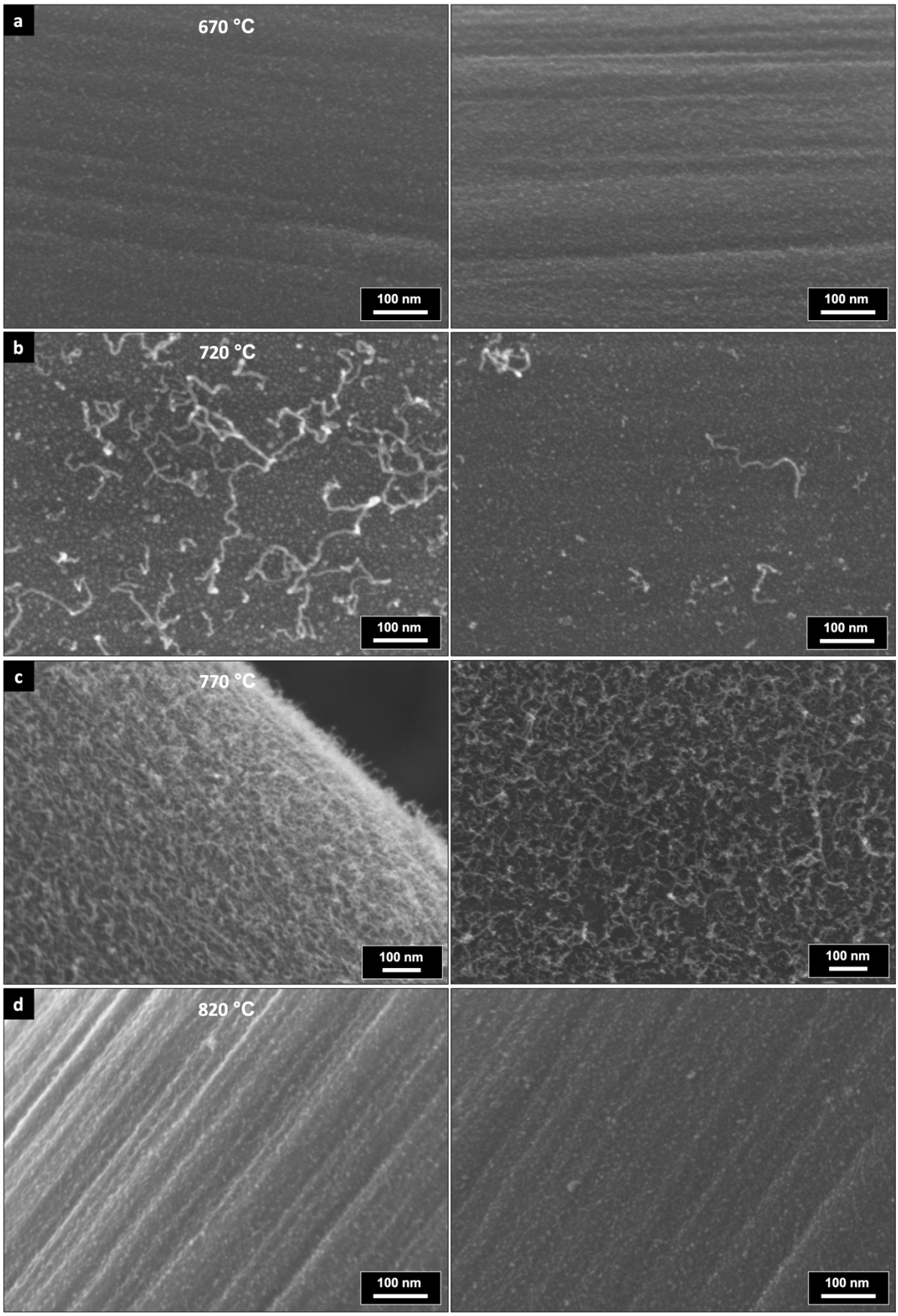


Fig. 5.9 SEM micrographs of CNT-g-CFs synthesised for a growth temperature of (a) 670, (b) 720, (c) 770, (d) 820, (e) 870, (f) 920, and (g) 970 °C.

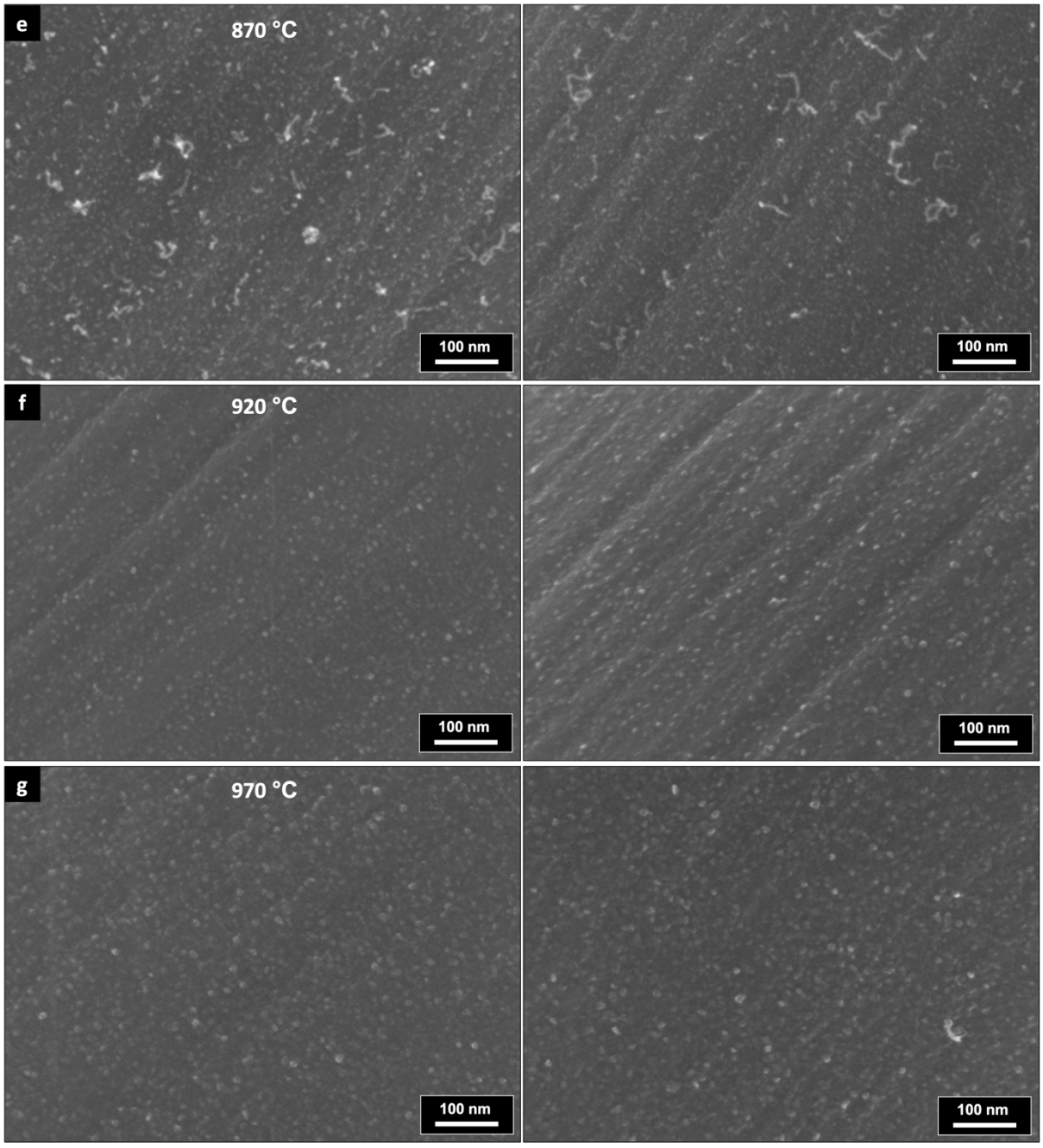


Fig. 5.9 (Continued)

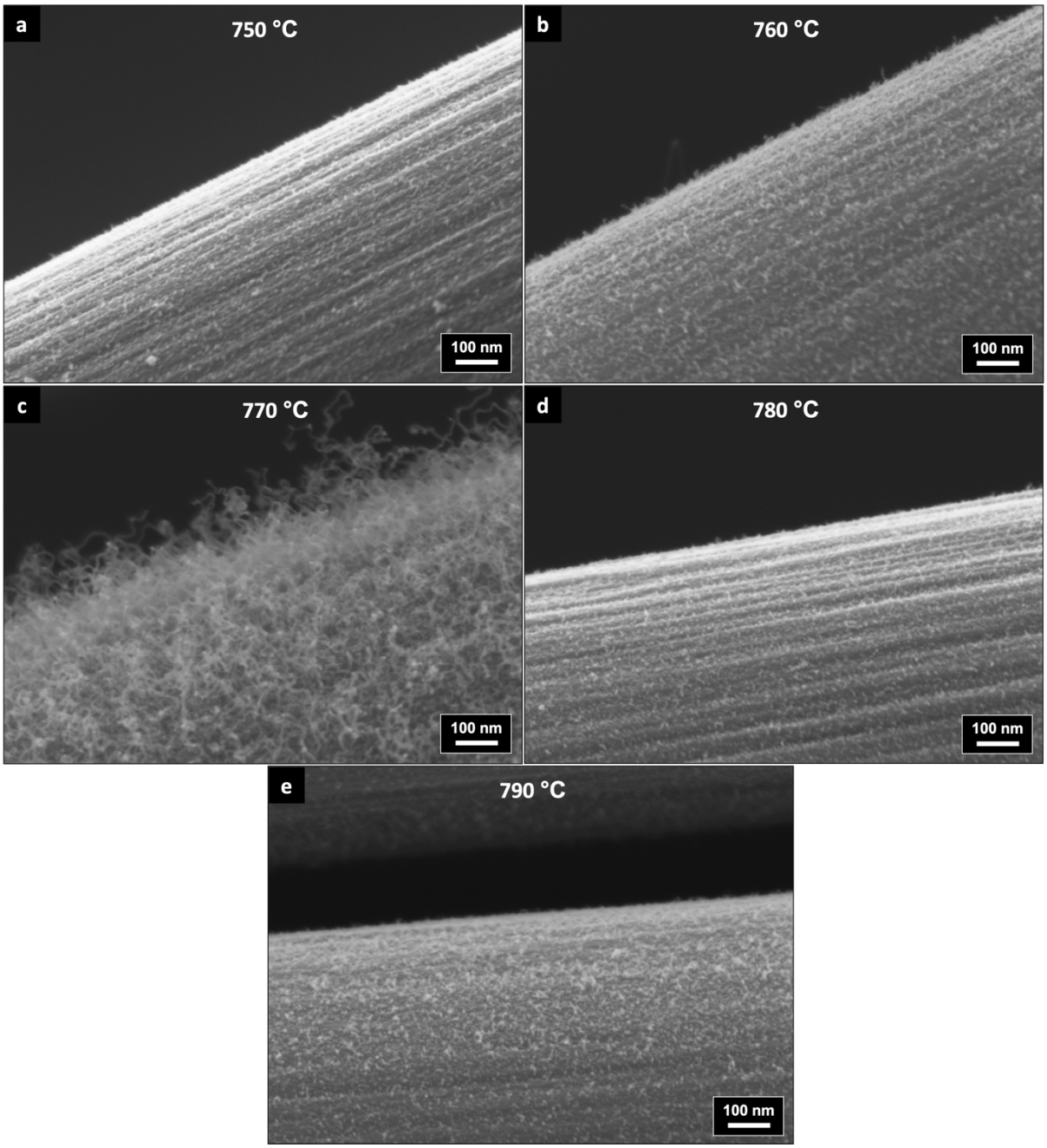


Fig. 5.10 SEM micrographs of CNT-g-CFs with fine temperature variation around the control temperature: (a) 750, (b) 760, (c) 770, (d) 780, and (e) 790 °C.

5.3.3. Effect of active gases composition and flow rate

Reductive gases (hydrogen) and carbon feedstock (acetylene) ratios were altered with a relatively broad range of composition ratios assessed, 1:10 to 1:80. This range includes most experimental conditions presented in literature, including control/historical (CVD_H) conditions (1:20). Large variations in ratio were selected to mitigate the effect of uncertainties associated with gas flow readings. Altering the acetylene to hydrogen ratios to the extremities of the range did not lead to the nucleation of CNTs (**Fig. 5.11**), while conditions close to those historically used in the system showed

similar growth as previously described by Anthony (**Fig. 5.11**b). Whilst large adjustments in gas composition ratio completely inhibited the growth of CNTs, investigating gas ratio closer to the control conditions could be of interest in the future. On the other hand, any systematic variation in hydrogen and acetylene flow rates (at fixed 1:20 ratio), did not show any significant impact on the growth characteristics of CNTs. In addition, altering the flow rates did not change the measured temperature (*in situ*) in the centre of the continuous CVD rig.

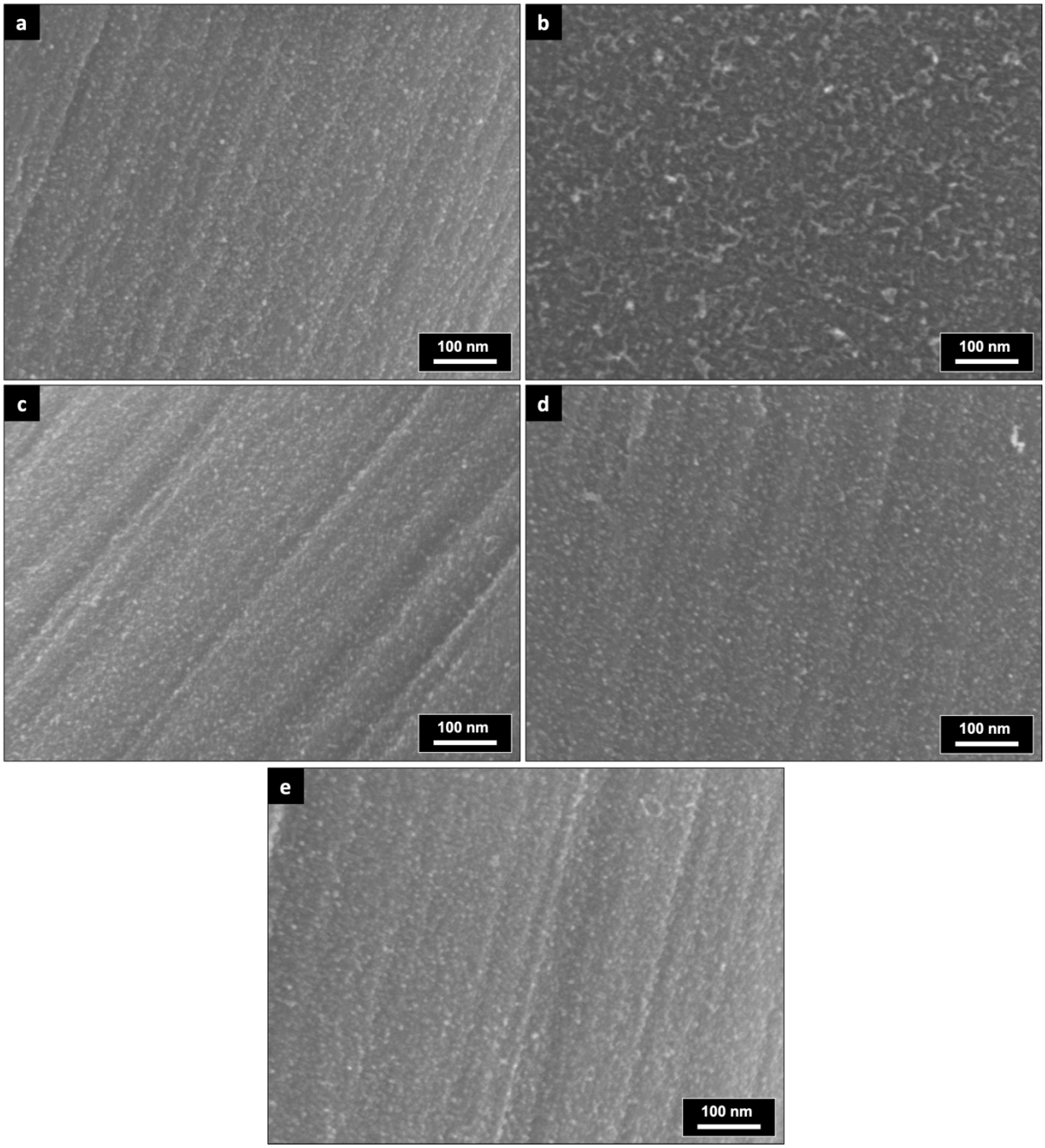


Fig. 5.11 SEM micrographs of CNT-g-CFs synthesised with a C_2H_2:H_2 ratio of (a) 1:10, (b) 1:19.3, (c) 1:30, (d) 1:40, and (e) 1:80.

Table 5.5 Ratio of acetylene to hydrogen with associated gas flow.

C_2H_2:H_2 ratio	N_2 flow‡ (sccm)	H_2 in N_2 flow (sccm)	C_2H_2 in N_2 flow (sccm)	CNT Growth
1:10	9680	3400	650	No
1:19.3	10000	3400	325	Yes
1:30	8340	5100	325	No
1:40	6682	6800	325	No
1:80	6842	6800	162	No

‡ *The nitrogen flow was adjusted to maintain the same proportion of nitrogen within the furnace for all C_2H_2:H_2 ratios.*

5.3.4. Effect of reduction and growth durations

The process involves two direct reactions in different gas atmospheres: first the reduction of the catalyst precursor to form active metal nanoparticles, and subsequently the growth of the CNT from hydrocarbon feedstock. Increasing the duration of the reduction may lead to catalyst coarsening, particle encapsulation and therefore prevent the CNT synthesis [46]. Hence, reduction conditions must be controlled and linked to a suitable growth duration for successful CNT synthesis.

The continuous CVD rig allows for the synthesis duration and reduction conditions to be altered through line-speed and adjustment of the internal arrangement of quartz tubes. Three nested quartz tubes B, C_1 and C_2 shown in **Fig. 5.12** allows for an independent control of the reduction and growth region lengths. Altering the line-speed simultaneously alters the reduction and growth durations at fixed quartz tube arrangements. The change of the line-speed also affects how the tow enters the furnace changing the heating rate of the fibres to synthesis temperatures. Similarly, modifying the length of the quartz tube B adjusts both the length of the reduction and growth regions, yet changes the growth-to-reduction duration ratio. The length of the quartz tube C_1, on the other hand, offers an independent control of the reduction duration; located at the edge of the stable hot zone, modifying its length alters the temperature at which the catalyst particles are exposed to the reductive gas sleeve. Increasing the length of the tube C_1, which decreases the duration of the reduction step, shifts the reduction region further into the furnace leading to similar reduction and growth temperatures ($T_R = T_G$). Contrarily, increasing the duration of the reduction step (shortening tube C_1) shifts the onset of the reduction further to the left, away from the stable hot zone, such as $T_R < T_G$ (**Fig. 5.12**). Finally, the sheathed quartz tube C_2 controls both the growth duration and the location of the graphite foil counter electrode within the furnace.

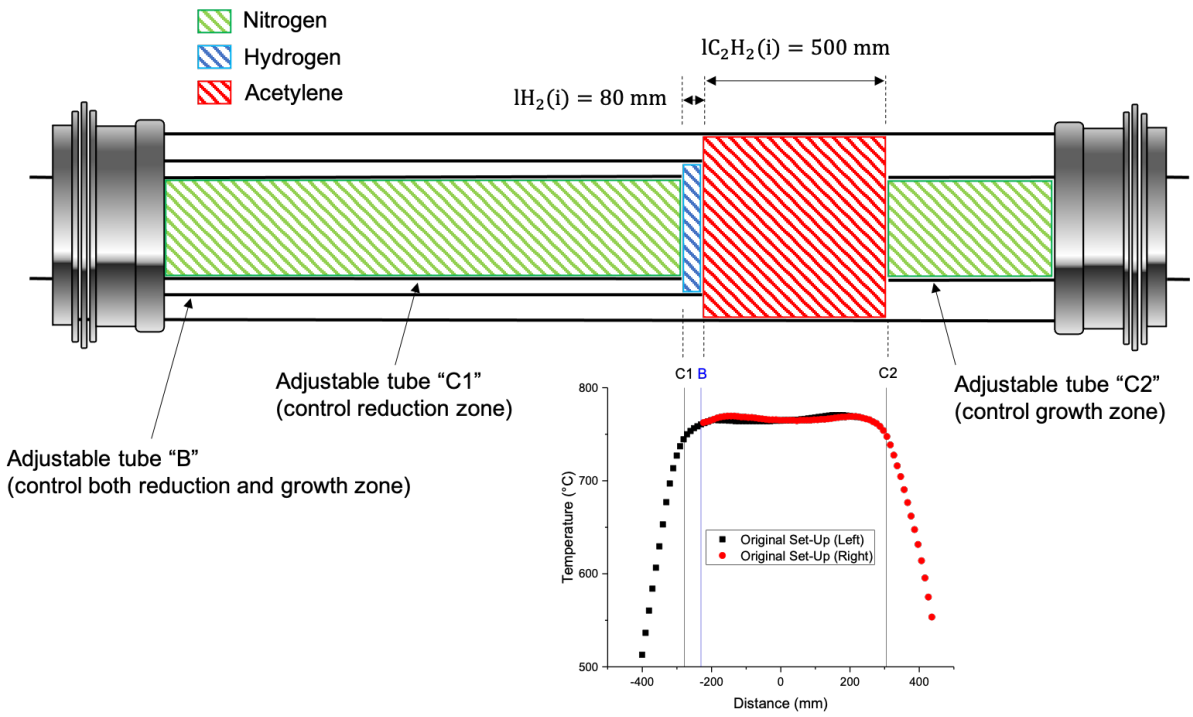


Fig. 5.12 Schematic representation of the quartz tube arrangement along with the furnace temperature profile in the stable hot-zone.

Line-speed

Matching the operating speed of conventional carbon fibres production lines, about 10 m.h^{-1}, will be important for incorporation and future uptake. Whilst it is commonly accepted that a longer dwell time can generates longer CNTs, a premature termination of the growth can also occur dependent on the nature of the catalyst and the growth conditions. A relatively large range of line speed was investigated, from 0.6 to 6.7 m.h^{-1}. Surprisingly, the perpendicular CNT length (from the carbon fibre surface) was found to increase with faster line-speed up to 4.8 m.h^{-1}. Whilst the slowest line-speed did not produce any significant growth, indicating catalyst poisoning (**Fig. 5.13**a, b), increasing the speed to 2.4 m.h^{-1} led to the formation of a uniform CNT coating with a thickness of about 200 nm (**Fig. 5.13**c). An increase to 4.8 m.h^{-1} generated an even thicker coating, with a length of about 400 nm (**Fig. 5.13**d). Any further increase led to a decline in both the thickness and the homogeneity of the coating (**Fig. 5.13**e), potentially a result of an unfinished reduction step. Even though the thickest CNT coating was obtained at a line speed of 4.8 m.h^{-1}, a line-speed of 2.4 m.h^{-1} was found to be the best compromise between CNT length, coverage homogeneity and synthesis repeatability. An increase in line-speed leading to longer synthesized CNTs could be explained by a change in the substrate heating rate and a lower temperature reduction onset. These factors potentially affect the size of the metal catalyst particles. A second hypothesis relies on the fact that the carbon fibre tow could enter quickly a region with specific gas conditions when entering the furnace at a fast pace, avoiding premature

deactivation of the catalyst precursors by over exposure to a reductive environment. Whilst in theory the gas sleeves allow for well-defined gas regions, there is clearly a local composition variation at the boundaries; traversing the transition more rapidly may be an advantage given the sensitivity to growth gas composition (see Section **5.3.3** above).

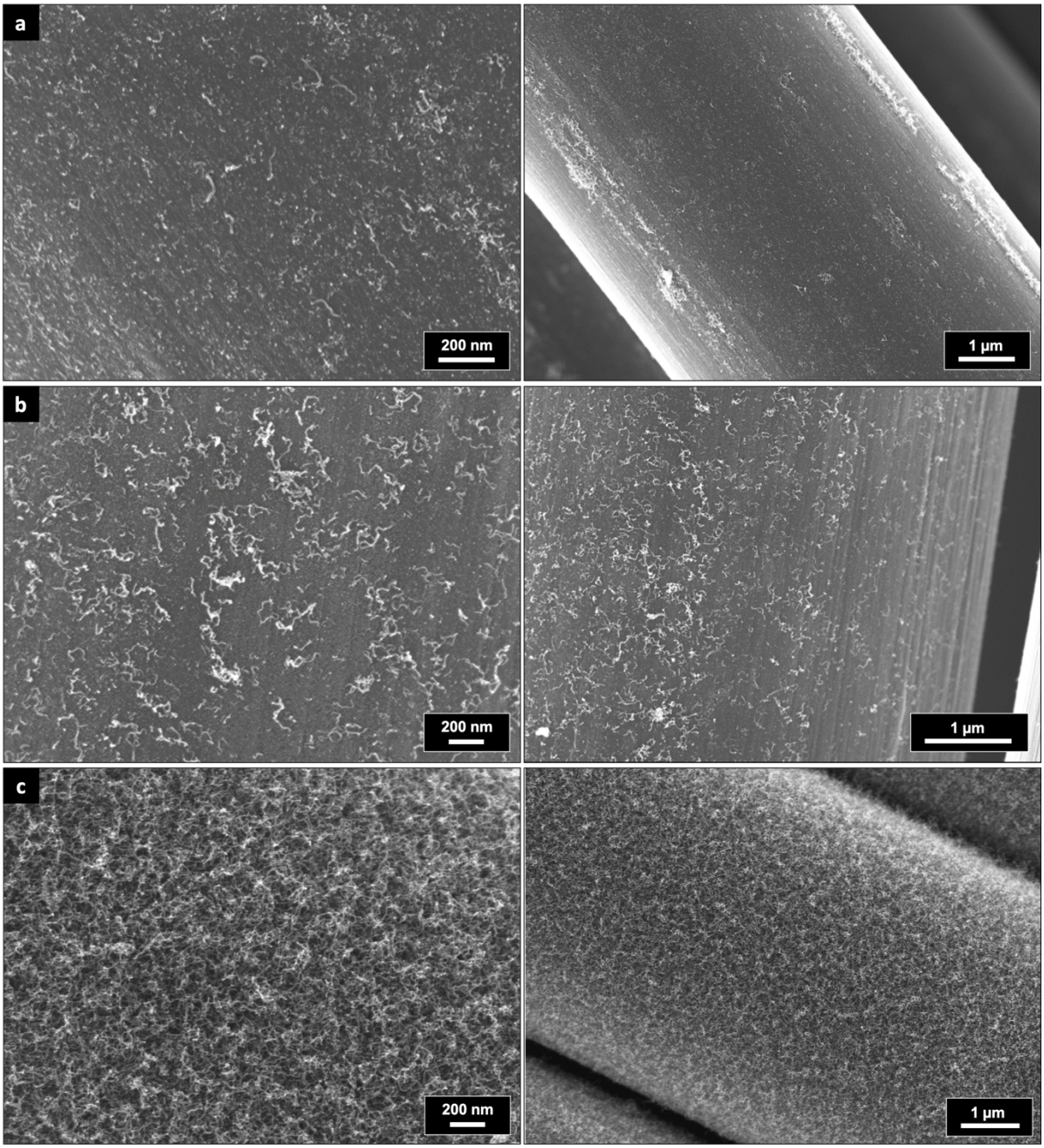


Fig. 5.13 SEM micrographs of CNT-g-CFs synthesised at a line speed of (a) 0.6, (b) 1.2, (c) 2.4, (d) 4.8, and (e) 6.7 $m.h^{-1}$.

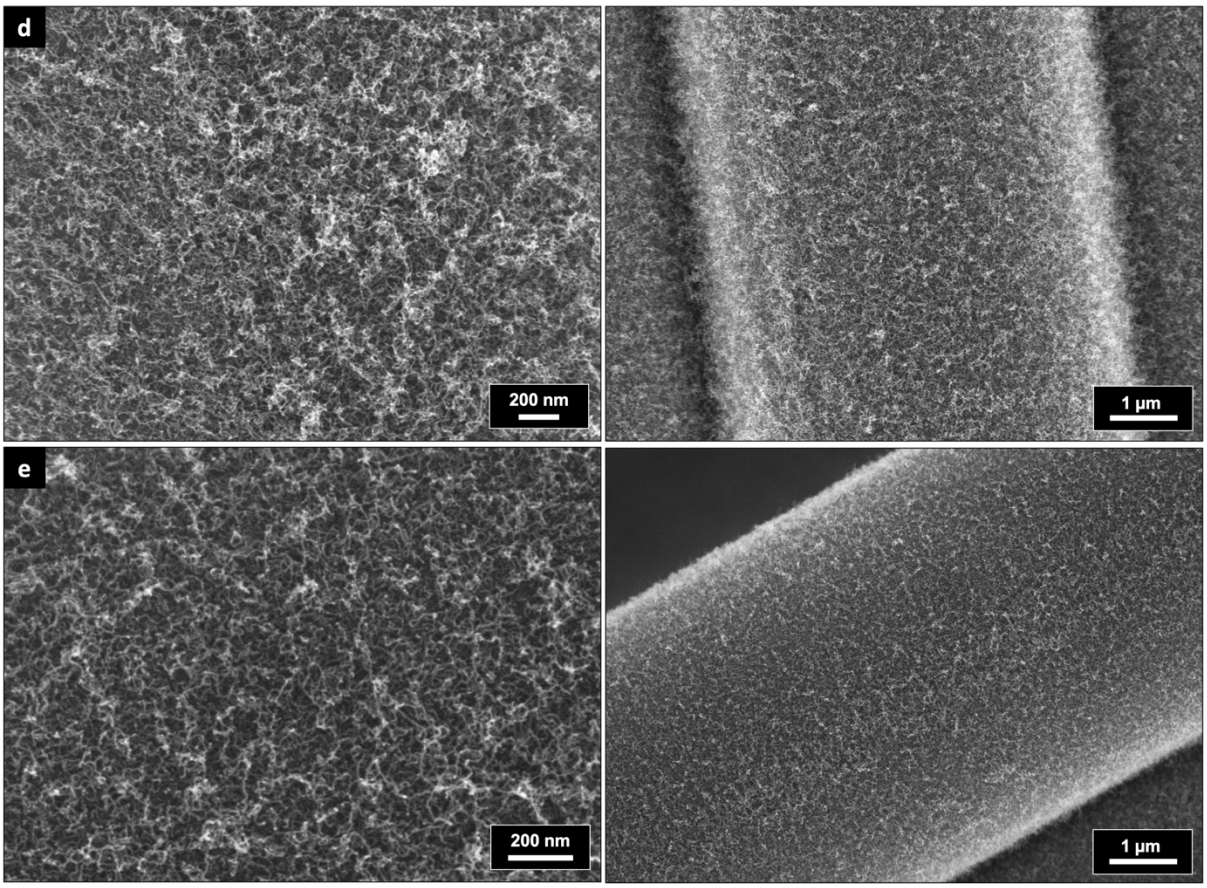


Fig. 5.13 (Continued)

Independent modification of the reduction zone

Even though the effect of the reduction temperature on the growth of CNTs has not been investigated, it can be assumed that the CNT synthesis is reduction/nucleation driven. The quartz tubes B and C_1 were therefore adjusted to shift the location of the reduction zone with regard to the furnace stable hot-zone (**Fig. 5.12**); the length of the reduction zone was kept constant (about 80 mm, **Table 5.6**, configuration 1 - 3). Subsequently, arrangements with a reduction region length halved (configuration 4) as well as doubled (configuration 5) were investigated. These different set-ups, including the dimensions of the quartz tubes, line-speeds and associated process variables, are described in **Table 5.6**. Interestingly, by shifting the reduction zone further inside the furnace (configuration 2), such as $T_R = T_G = 770$ °C, an increase in the onset reduction temperature of approximately 30 °C as compared to the control arrangement, whilst retaining the same reduction duration, prohibited the growth of CNTs regardless of the line-speeds (**Fig. 5.14**b). On the other hand, shifting the reduction zone to the outside of the furnace (configuration 3), into a colder environment (i.e. $T_R = 700$ °C < T_G), enabled significant CNT growth, similar to that obtained from the control conditions (**Fig. 5.14**c). Reducing the onset reduction temperature even further to $T_R = 620$ °C, whilst simultaneously doubling the length of the reduction region (configuration 5), only marginally promoted the growth of CNTs at a line-speed

of 4.8 m.h^{-1} (**Fig. 5.14**g). Yet, at a lower line speed of 2.4 m.h^{-1}, an inhomogeneous and sparse coverage of large CNTs was observed (**Fig. 5.14**f); shorter reduction duration (i.e. 2 min) led to slender (~ 10 nm) CNTs similar to those produced from control conditions, with a premature termination of the growth generating inactivate catalyst particles. Finally, by positioning the onset reduction temperature in the stable hot-zone, such as $T_R = T_G = 770$ °C, and halving the length of the reduction region (configuration 4), only deactivated catalyst particles were observed regardless of the line speed (**Fig. 5.14**d, e). These results suggest that an optimum temperature exist for the onset reduction, such as 700 °C < T_R < T_G and t_R = 2 min. Yet, once again large adjustments in variables tend to rapidly inhibit the process, suggesting that fine adjustments in both the onset temperature and reduction region lengths should be tailored carefully once justified by sufficient process control.

Table 5.6 Quartz tubes (B and C_1) arrangements of the reduction zone with associated process variables.

Label	Quartz tubes		Line speed	Reduction duration	Reduction temperature	Growth duration	Growth temperature
	B (mm) [Δ]†	C_1 (mm) [Δ]†	s (m.h^{-1})	t_R (min)	T_R (°C)	t_G (min)	T_G (°C)
Config. 1 (Control)	600 [+0]	680 [+0]	1.2	4	740	25	770
			2.4	2		12.5	
			4.8	1		6.25	
Config. 2 (T_R +)	680 [+80]	760 [+80]	1.2	4	770	21	770
			2.4	2		10.5	
			4.8	1		5.25	
Config. 3 (T_R -)	560 [-40]	640 [-40]	1.2	4	700	27	770
			2.4	2		13.5	
			4.8	1		6.75	
Config. 4 (T_R + and t_R -)	600 [+0]	720 [+40]	1.2	2	770	25	770
			2.4	1		12.5	
Config. 5 (T_R - and t_R +)	600 [+0]	600 [-80]	2.4	4	620	12.5	770
			4.8	2		6.25	

† *= difference in tube length when compared to control arrangement. Note that despite being shorter, tube B extends further inside the furnace when compared to tube C_1 due to its left hand-side position relative to tube C_1, with an offset of +160 mm (**Fig. 5.12**).*

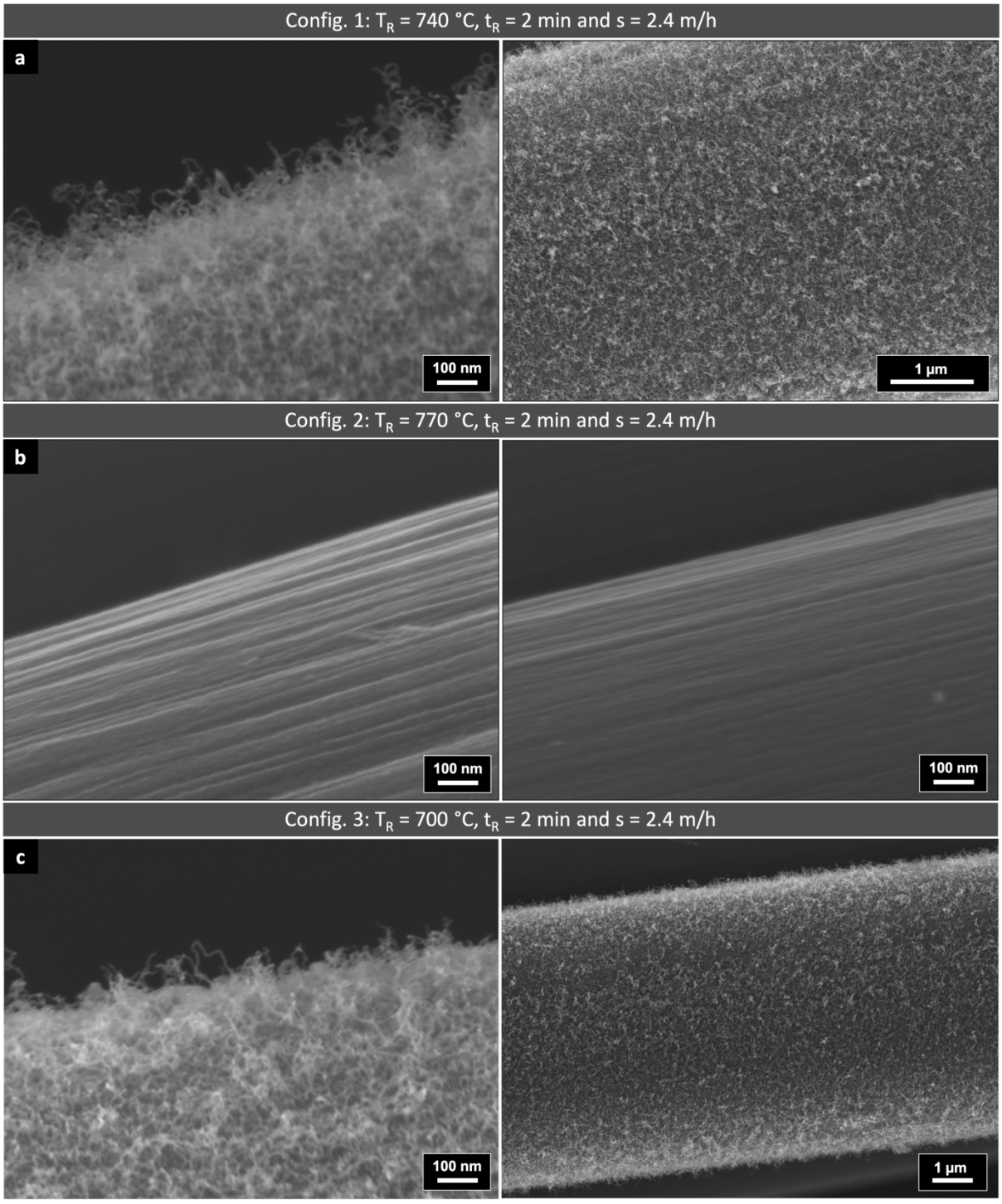


Fig. 5.14 SEM micrographs of CNT-g-CFs produced at different line-speed using (a) configuration 1, (b) configuration 2, (c) configuration 3, (d, e) configuration 4, and (f, g) configuration 5.

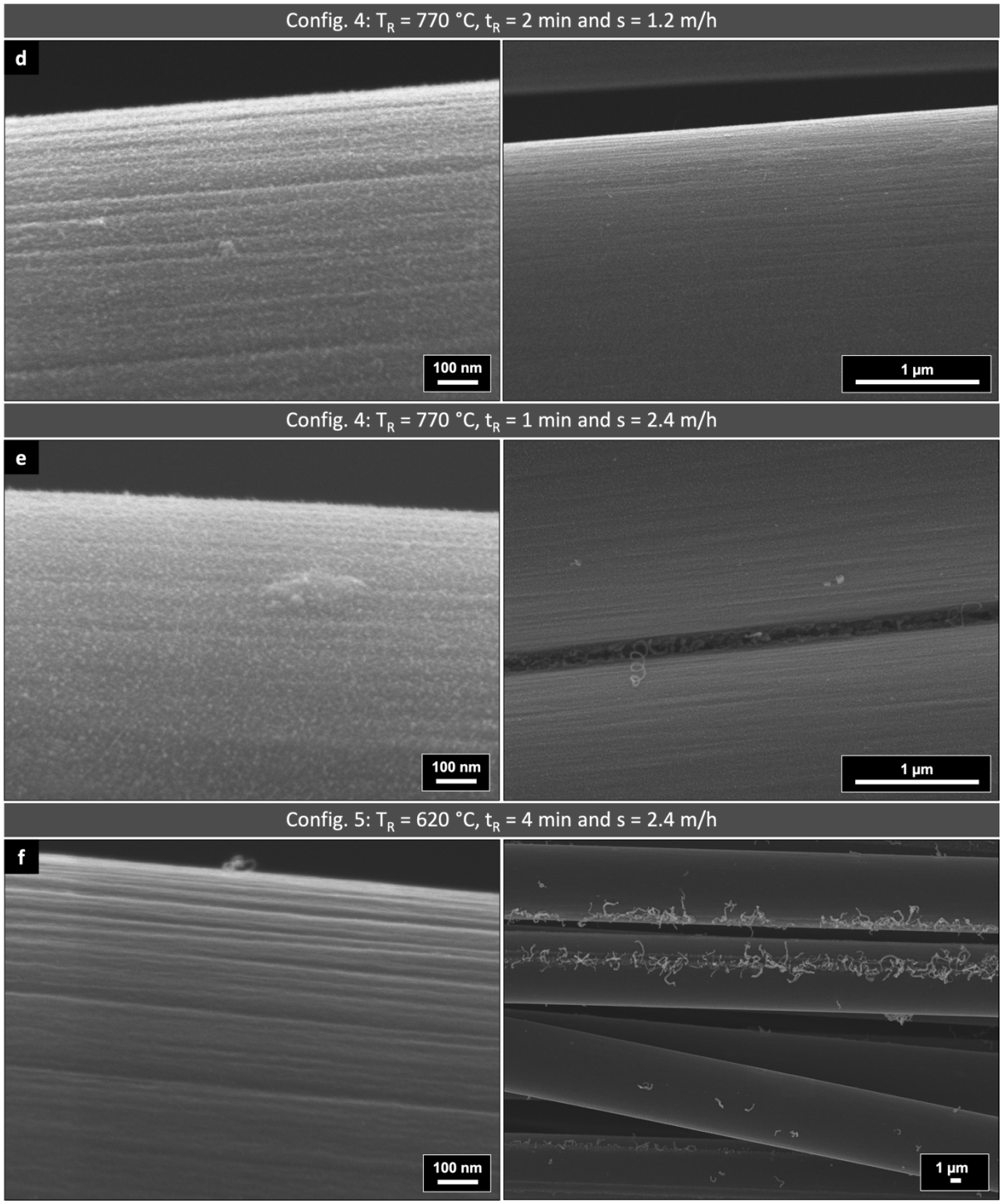


Fig. 5.14 (Continued)

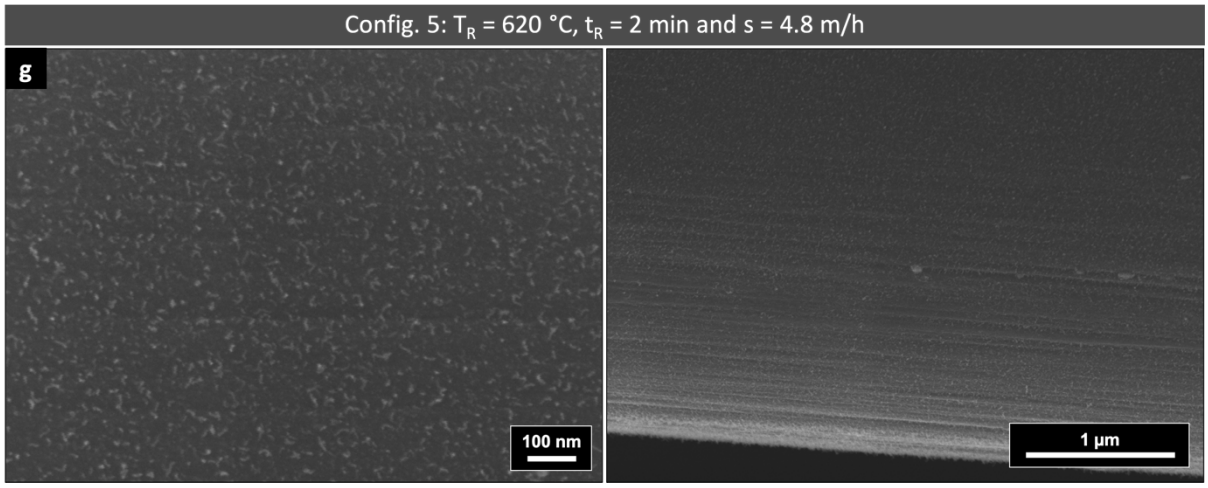


Fig. 5.14 (Continued)

Independent modification of the growth zone

The overall length/duration of the synthesis region can also be altered by changing the nested tubes for different lengths instead of simply rearranging them. A bespoke sheathed tube (C_2) which encases the rolled graphite foil counter electrode that extends further inside the furnace stable hot-zone was inserted to reduce the length of the growth zone to half of that of the control arrangement. These two set-ups and associated process variables are presented in **Table 5.7**. The reduction of the growth duration appeared to have some effect on the growth characteristics of CNTs. Indeed, whilst both set-ups promoted the growth of CNTs (**Fig. 5.15**a, c), configuration 2 exhibited an early onset of CNT termination with the catalyst particles having only partially nucleated (**Fig. 5.15**c). Once again, slower line-speed of 1.2 $m.h^{-1}$ hindered the growth of CNTs drastically (**Fig. 5.15**b). Such a minimal difference in growth characteristics for a line-speed of 2.4 $m.h^{-1}$ suggests that the synthesis is predominantly nucleation/reduction dependent.

Table 5.7 Quartz tube (C_2) dimension and associated process variables including line speed, reduction and growth duration within the growth zone

Label	Quartz tube C_2 (mm)	Line speed ($m \cdot h^{-1}$)	Reduction duration t_R (min)	Growth duration t_G (min)	CNT growth
Configuration 1 (control)	650 [+0]	2.4	2	12.5	Yes
Configuration 2 (t_G -)	900 [+250]	1.2 2.4	4 2	12.5 6.25	Sporadic (-) Sporadic (+)

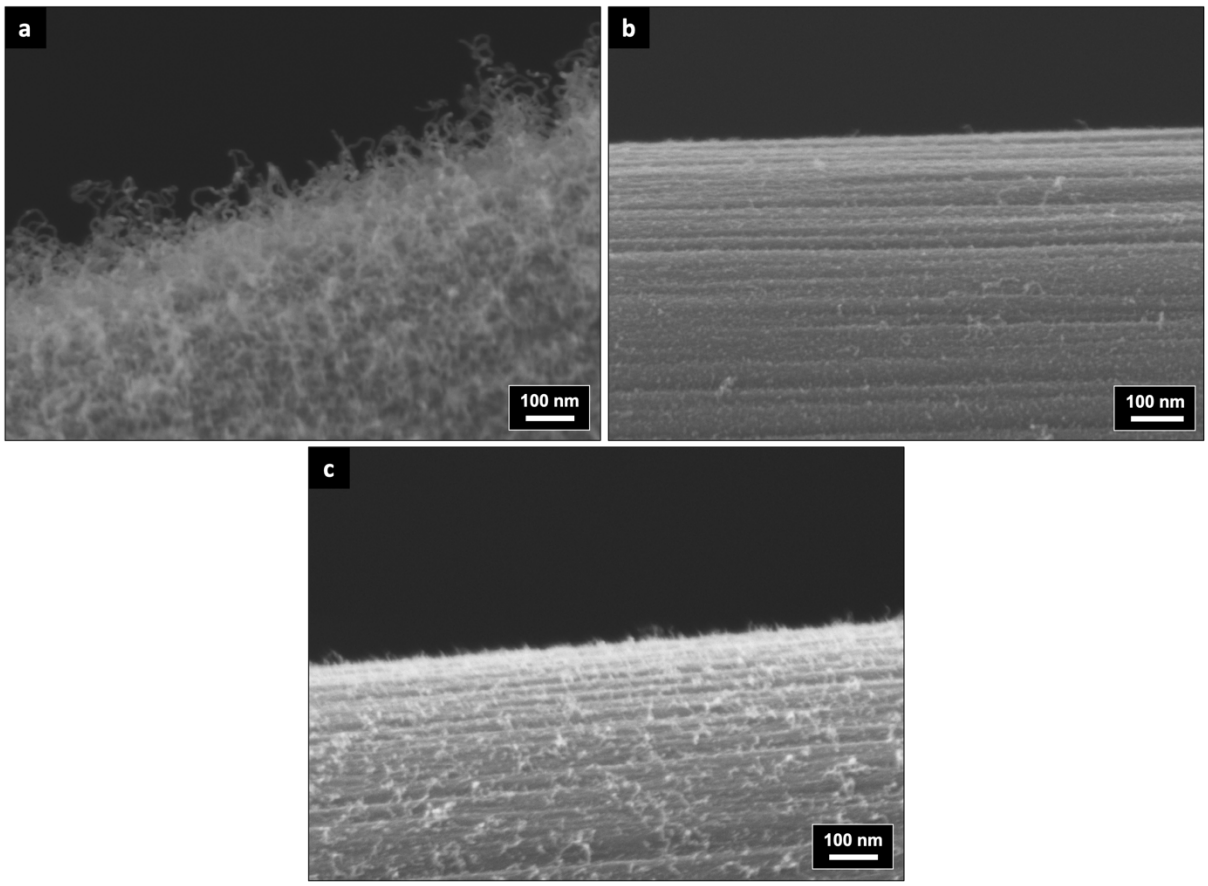


Fig. 5.15 SEM micrographs of CNT-g-CFs produced at 2.4 $m.h^{-1}$ using (a) the control configuration 1 and (b) configuration 2 with a halved growth duration.

5.4. Refined CVD conditions and repeatability

CVD systems are known to operate erratically, frustrating many researchers and hindering uptake by end-users. In fact, some have reported that their system was not able to synthesise CNTs for months on end after dismantling it for cleaning purposes. This section aims to assess the robustness of the developed CVD process, an absolute requirement for its future implementation in a pilot plant. The continuous CVD system was investigated within a one-year timeframe, following multiple break-up and cleaning procedures. The refined CVD conditions selected from the parametric study were as follow:

Table 5.8 CVD_{α} synthesis conditions.

Temperature (°C)	Line speed ($m{\cdot}h^{-1}$)	Reduction time (min)	Growth time (min)	N_2 flow (sccm)	H_2 flow (sccm)	C_2H_2 flow (sccm)	C_2H_2:H_2 ratio	Potential difference (V)
770	2.4	2	12.5	10000	3400	325	1:19.3	300

*NB: Configuration 1 (control) was selected for the quartz tube arrangement (**Table 5.6**).*

5.4.1. Morphology of the CNT-grafted carbon fibres

Perhaps surprisingly, dismantling the CVD system four times over the course of a year, for both cleaning and altering the arrangement of quartz tubes, did not disrupt the system for any period of time. Even the replacement of quartz tubes after breakage, often source of issues for many researchers due to an altered surface chemistry, as a result of aging, did not lead to any downtime. The overview provided below (**Fig. 5.16**) demonstrates the reproducibility and robustness of the continuous CVD process with all CNT-grafted carbon fibres (CNT-g-CF) exhibiting a homogeneous and dense coverage of sub-200 nm long CNTs. An overview of the different processing variables and associated CNT yield can be found in the **Annex 4**.

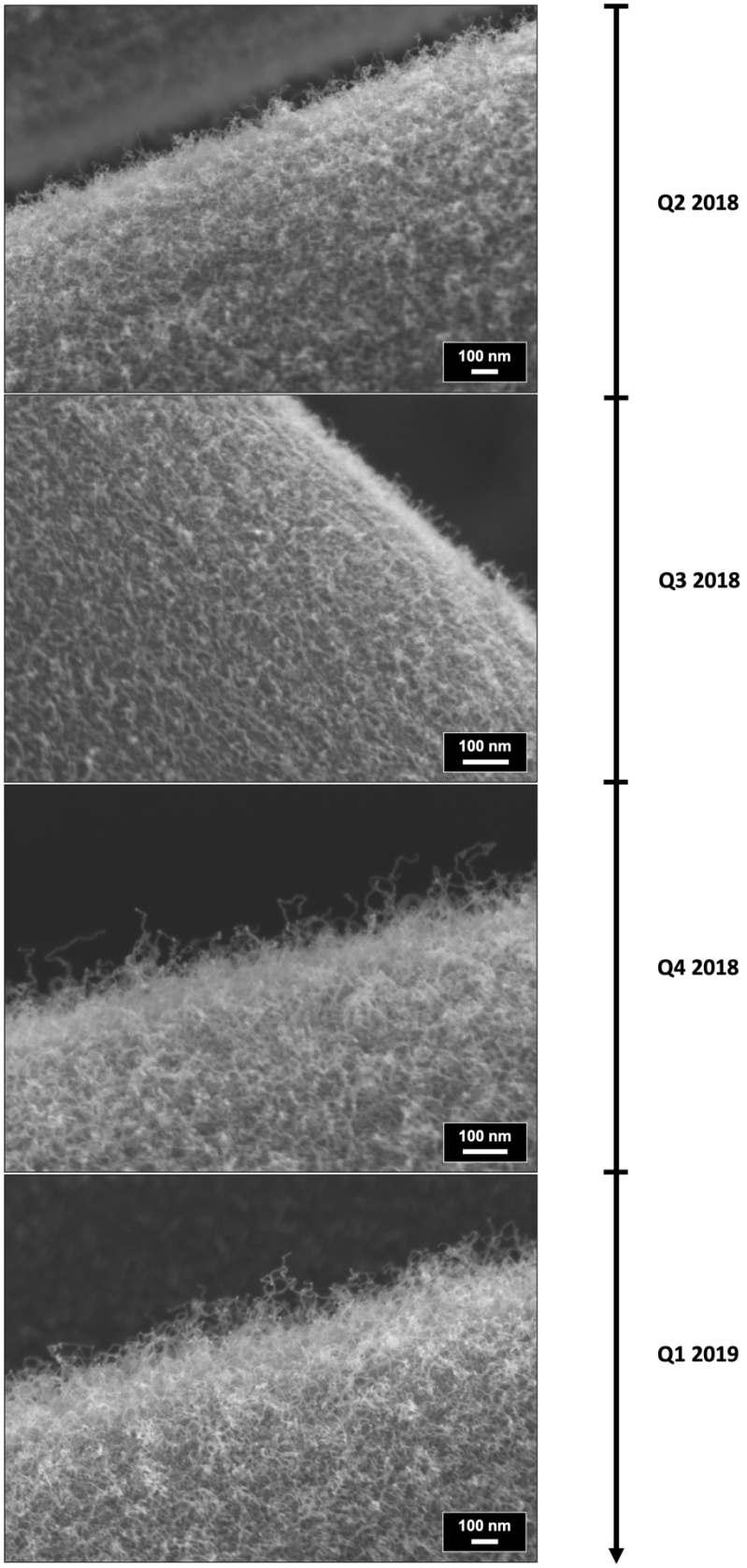


Fig. 5.16 Repeatability and robustness of the CVD system after dismantling and cleaning procedures over four quarters (CVD system was dismantled at least once per quarter). CNT-g-CFs were synthesised using CVD_{α} conditions.

5.5. Summary

A continuous deposition process including an in-line plasma treatment was successfully developed, allowing for the production of over 300 meters of bi-catalyst precursors deposited carbon fibres in a day. The continuous CVD system used in combination enabled a full investigation of the effects of different CVD growth conditions, such as the reactive gas composition, catalyst reduction and growth duration, as well as the growth temperature and line speed on the morphology of CNTs. The thickness of the grafted CNT layer was successfully controlled from a few tens of nanometres to about 500 nm, adjusting the speed of the line. On the other hand, other process variables, including the active gas composition and growth temperature, were found to only operate within a narrow window for successful CNT growth. The use of a potential difference (+ 300 V) was deemed to be an absolute necessity to avoid carbon fibre surface pitting. The CNT synthesis appeared to be strongly dependent on the reduction process, with the onset reduction temperature being critical for the success of the CNT growth. Over 50 meters of CNT-g-CFs can be produced in one day, allowing for a more comprehensive mechanical evaluation of composite materials to take place, including micro- and macro-mechanical tests, as discussed in the next chapter. The developed continuous CVD process offers a robust route to producing nanoengineered carbon fibres with a dense and uniform layer of CNTs.

Chapter 6 : CNT-reinforced carbon fibre composites - A micro/macro-scale approach

This chapter focuses on the mechanical evaluation of the CNT-grafted carbon fibres, both at the micro and macroscale, providing a general understanding of the failure mechanisms at play. The effect of the CNT coating on the mechanical performance and failure of the fibre/matrix interface was investigated at the single fibre level, initially for unreactive polyolefin matrices, namely polypropylene (PP), where wetting is particularly challenging and for both as-received aerospace grade epoxy and SWCNT-reinforced epoxy systems. Unidirectional hierarchical bundle composites were manufactured and tested in tension. A methodology for the production of short beam shear coupons with practical primary fibre volume fraction was developed and allowed for the measurement of composite interlaminar shear strength.

6.1. Characterisation of carbon fibre/matrix interface

Having established a robust CVD synthesis process allowing for the production of a short (~ 200 nm) and homogeneous coverage of CNTs on large quantities of CFs (**Fig. 5.16**), we can now evaluate the mechanical performance of these hierarchical reinforcements across multiple lengthscales. Initially, at the microscale with techniques including microdroplet debonding and single fibre pull-out, subsequently on larger specimens such as unidirectional bundle composites and short beam shear (SBS) coupons.

6.1.1. Interfacial shear strength of single fibre model composites

As discussed, fibre-matrix interfaces are pivotal for the integrity and performance of composite materials. As a first step, performance was evaluated at the microscale, for both thermoplastics and thermosets.

Polypropylene resin

Polypropylene (PP) is an archetypical thermoplastic, low cost and inert, though with relatively modest properties; as a composite it is used commercially, in PP/PP systems, but is notoriously challenging to use with more structural fibres, due to the weak adhesion. Since the polymer is chemically inert, mechanical keying with a nanostructured interface may be appealing. The wetting and interfacial properties between the CNT-g-CFs and PP were investigated by David Seveno's group in KU Leuven, using Wilhelmy wetting and the microdroplet dedonding test, respectively [277]. For these tests, CNT-g-CFs grown under the historical CVD conditions (described in **Table 5.4**) were selected, as the work was carried out as a proof of concept prior to the in-depth parametric studies. The wetting measurements were carried out using diiodomethane (DIM), an exclusively dispersive liquid, considered a model for PP, as test liquid. CNT-g-CF showed a reduced contact angle in DIM, when compared to as-received CFs consistent with the improvement in interfacial shear strength (IFSS) observed with PP (**Fig. 6.1**f). The IFSS of the CNT-g-CF/PP system (11.2 ± 0.3 MPa) increased by 39 %, 40 % and 53 % compared to that of sized, heated/reduced bi-catalyst coated (HRBC) and unsized CFs, respectively, characteristic of an improved adhesion (**Fig. 6.1**f). Whilst unsized, sized, and HRBC-CFs all showed rather clean fracture surfaces distinctive of an adhesive failure (**Fig. 6.1**a, b, c), the rougher fracture surface observed for CNT-g-CF (**Fig. 6.1**fd, e) suggests an intermediate cohesive failure closer to the ends of the CNTs-matrix region. These results suggest that keying (also referred to as *mechanical interlocking*) is useful especially in low adhesion systems, the CNT-grafting can address even the most challenging wetting/adhesion problems, as illustrated by PP.

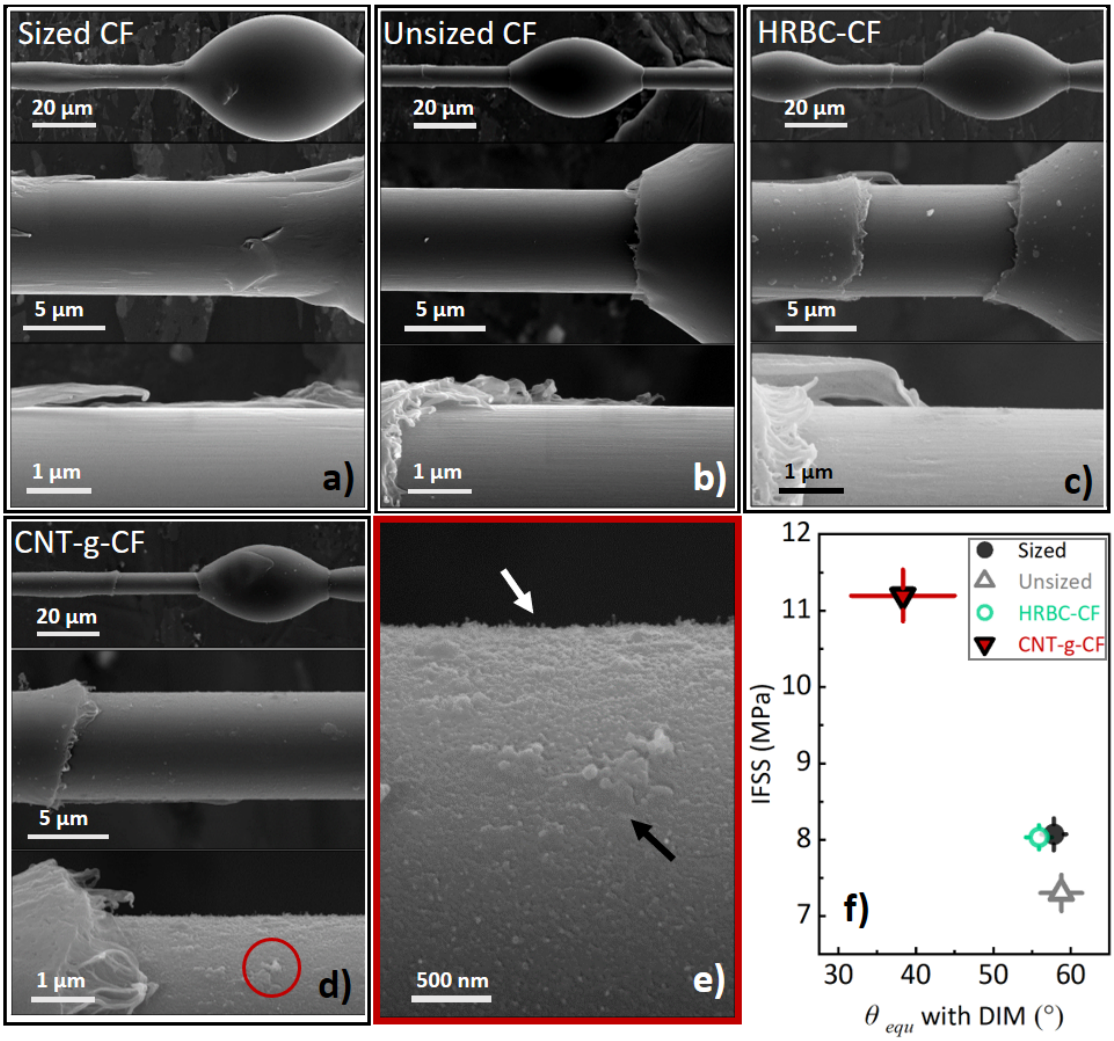


Fig. 6.1 Fractography micrographs of microdroplet fibre-polypropylene model composites, a) sized CF, b) unsized CF, c) HRBC-CF, d) CNT-g-CF, e) CNT-g-CF high magnification of fracture surface circled in d), with residual PP indicated with a black arrow and fractured CNTs indicated by the white arrow. f) Relationship between the equilibrium contact angle of CFs in diiodomethane (DIM) and the IFSS results from microdroplet PP single fibre composites. Reproduced from [277].

Aerospace grade epoxy resin

A classic bisphenol-A type epoxy was selected as an archetypal example of more widely employed thermoset composite resin. The effect of CNT-grafting on the interfacial performance was investigated using an as-received aerospace grade epoxy system (L20:EPH161, R&G Faserverbundwerkstoffe GmbH) denoted hereafter as “neat epoxy”. In addition, nano-reinforced matrix variants, containing 0.1 and 1.0 wt.% single-walled carbon nanotubes (SWCNTs), were prepared to search for synergistic reinforcement effects. The apparent IFSS was determined by single fibre pull-out tests (refer to Section **3.3.6**, pp. 87). For these tests, and throughout the remainder of the mechanical study, the CNT-g-CFs were grown from improved CVD conditions (**Table 5.8**).

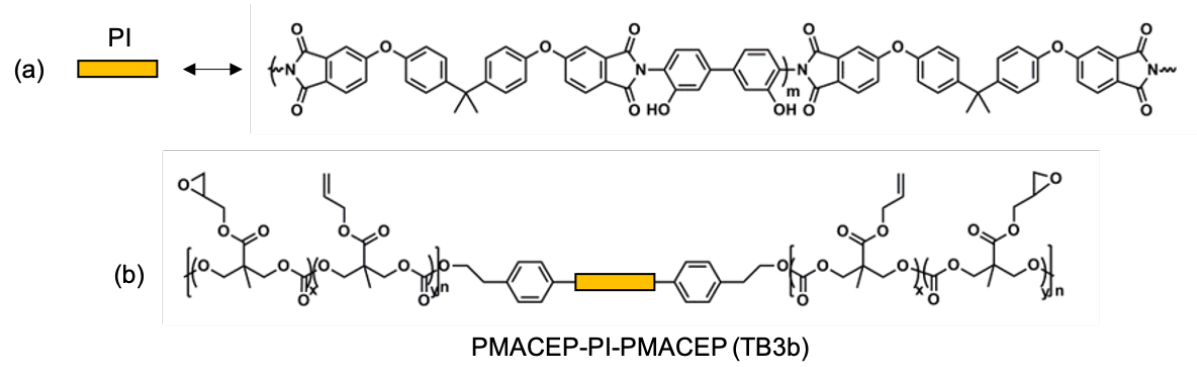


Fig. 6.2 (a) Polyimide (PI) linker and (b) triblock copolymer PMACEP-PI-PMACEP (TB3b). Adapted from [4].

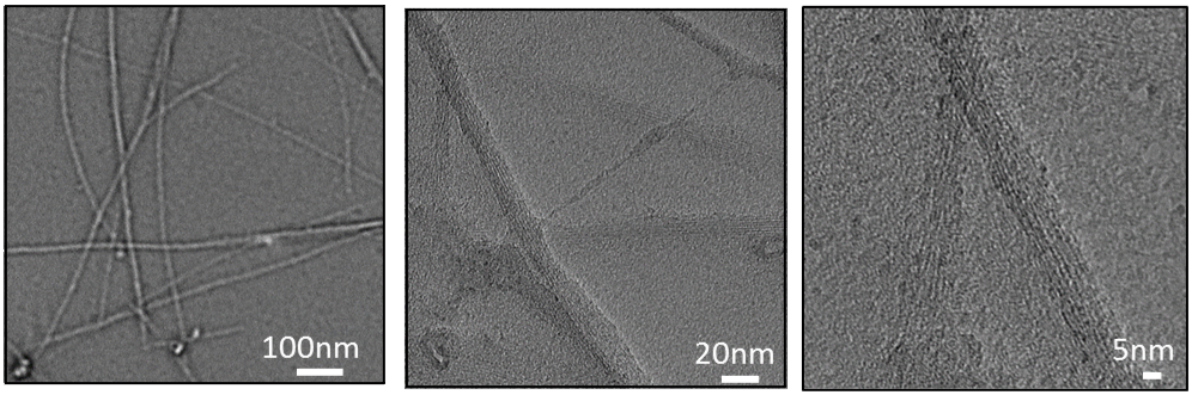


Fig. 6.3 TEM micrographs of dispersed SWNTs with TB3b at different magnifications. Adapted from [4].

A triblock copolymer, based on polyimides (PI) and an epoxidized derivative of poly(2-methyl-2-(allyloxycarbonyl)propylene carbonate) (PMACEP), was synthesised by Prof Mary Chan's group in Nanyang Technological University (Singapore) following their reported procedure [4] and used as a dispersing agent for SWCNTs in THF. The triblock copolymer TB3b (**Fig. 6.2**) was initially dissolved in THF prior to adding the SWCNTs at a weight ratio between (2:1) and (1:1). The suspension (< 20 mL) was then tip-sonicated (flat tip, 750 W, 20 %, pulsed 1 s/1 s) and centrifuged (6000 G, 10 min). The supernatant was subsequently collected and evaluated by UV-Vis-NIR absorption spectroscopy. TB3b appeared to disperse SWCNTs in THF well, with the absence of aggregates as observed from TEM (**Fig. 6.3**). In order to measure the concentration of SWCNTs in THF, SWCNT solutions with known concentrations were prepared (0, 0.02, 0.04, 0.1, and 0.15 mg.mL^{-1}) for which the absorbance at 700 nm was measured (**Fig. 6.4**a). The slope of the absorbance at 700 nm versus SWCNT concentration in THF (**Fig. 6.4**b) was used to determine the extinction coefficient (ε = 22.5 mL.mg^{-1}.cm^{-1}), which was used to calculate the concentrations of the SWCNT dispersion. Epoxy was then added to the SWCNT dispersion and thoroughly mixed using bath sonication, before evaporating the solvent. Finally, the

hardener was added and stirred to initiate the curing of the epoxy (curing conditions as given in **Table 3.2**).

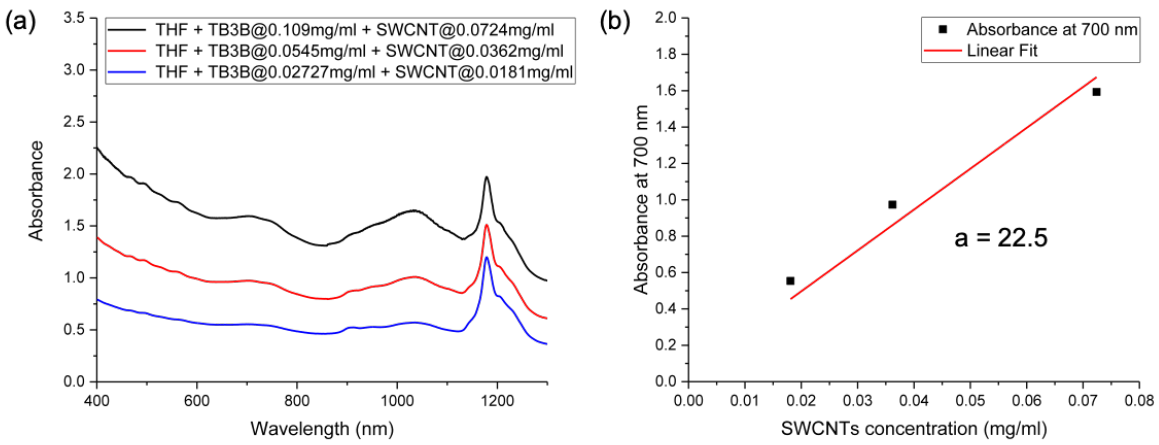


Fig. 6.4 (a) UV-Vis-NIR absorption spectra of SWCNTs/TB3b dispersant at different SWCNT concentrations. (b) Absorbance of the different dispersions at 700 nm fitted with a linear least square fit (slope a).

After embedding, each test fibre was pulled out of a cured epoxy droplet. Upon displacement of the piezo-translator along the axial direction of the fibre, the load increases linearly in the elastic regime until one of the three following events occurs. For excessive fibre embedded lengths, the load required to initiate fibre debonding may exceed the fibre tensile strength leading to fibre failure. For non-ductile/compliant matrices, the fibre can prematurely debond at high local stress region of the interface, leading to a sudden load drop (brittle failure). Finally, for ductile matrices, plastic yielding of the resin can lead to shear stress redistribution along the fibre length (ductile failure), causing the load to progressively level off until complete debonding. In this study, the latter case was observed for all resin systems, emphasised by the linear relationship between the apparent shear strength and the fibre embedded length (**Fig. 6.5**).

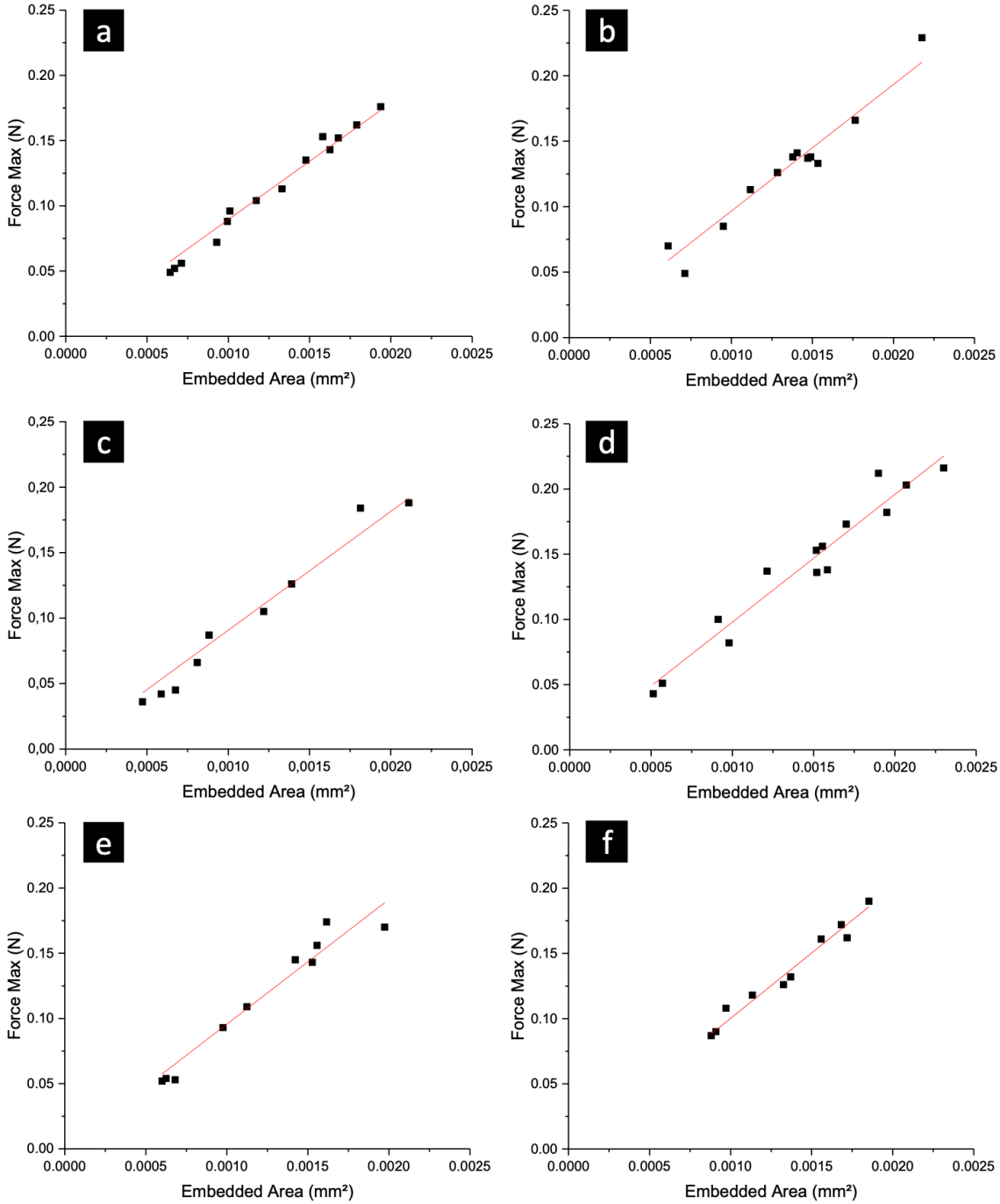


Fig. 6.5 Maximum force as a function of fibre embedded area for (a) unsized carbon fibres and (b) CNT-g-CFs in neat epoxy, (c) unsized carbon fibres and (d) CNT-g-CFs in TB3b-dispersed SWCNTs (0.1 wt.%) reinforced epoxy, (e) unsized carbon fibres and (f) CNT-g-CFs in TB3b dispersed SWCNTs (1.0 wt.%) reinforced epoxy. Average apparent interfacial shear strength is calculated from the linear fit (red line).

Consistent with previous measurements [3], the nano-structured interphase increased the IFSS by 8 % (97 ± 2 MPa) as compared to as-received unsized carbon fibres (89 ± 1 MPa) in neat epoxy (**Fig. 6.6**). For the unmodified carbon fibres, introducing SWCNTs into the epoxy matrix, at 1.0 wt.% measurably

increased the apparent IFSS by 7 % (96 ± 3 MPa; **Fig. 6.6**, fifth column) as compared to neat epoxy (89 ± 1 MPa). The apparent IFSS increased further when embedding CNT-g-CFs in a SWCNT/TB3b-reinforced epoxy resin matrix, by 11 % (100 ± 1 MPa) as compared to the baseline.

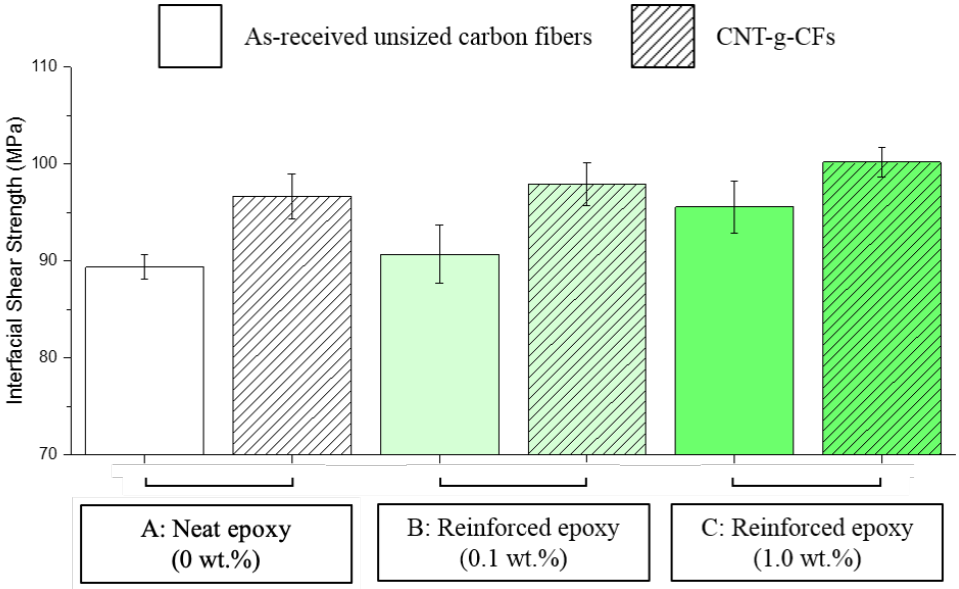


Fig. 6.6 Single fibre pull-out test results for carbon fibres without (plain)) and with CNTs grafted (hatched) on their surface, embedded in (A) neat epoxy, (B) 0.1 wt.% TB3b dispersed SWNT-reinforced epoxy, and (C) 1.0 wt.% TB3b-dispersed SWNT-reinforced epoxy. Error bars represent standard errors.

The fibre surfaces of the as-received unsized carbon fibres observed after pull-out (**Fig. 6.7**) from the neat epoxy were relatively clean; no epoxy residue was observed. The CNT-g-CF samples, on the other hand, exhibited rougher surfaces when pulled-out from neat epoxy, consistent with the increased IFSS, and deflection of the crack path along the CNT/epoxy interface. However, for embedded CNT-g-CFs in epoxy matrix reinforced with 1.0 wt.% SWCNTs, the interface reveals a different failure mechanism (**Fig. 6.7**); the absence of epoxy residue on the surface of the fibres after pull-out suggests that the failure occurs at the CNT/carbon fibre interface. The epoxy system reinforced with 1.0 wt.% SWNTs promotes the fracture of the grafted CNTs at the carbon fibre surface, rather than that of the grafted CNT/matrix interface. Failure of the grafted CNT/matrix interface was only observed for unreinforced epoxy, suggesting a synergistic interaction between the nano-engineered epoxy and the CNT-grafted carbon fibres. In other words, reinforcing the interface pushing the failure out into the virgin epoxy; reinforcing the matrix supresses this displaced failure, and ensures that the maximum benefit is obtained from the interfacial reinforcement of the grafted CNT layer.

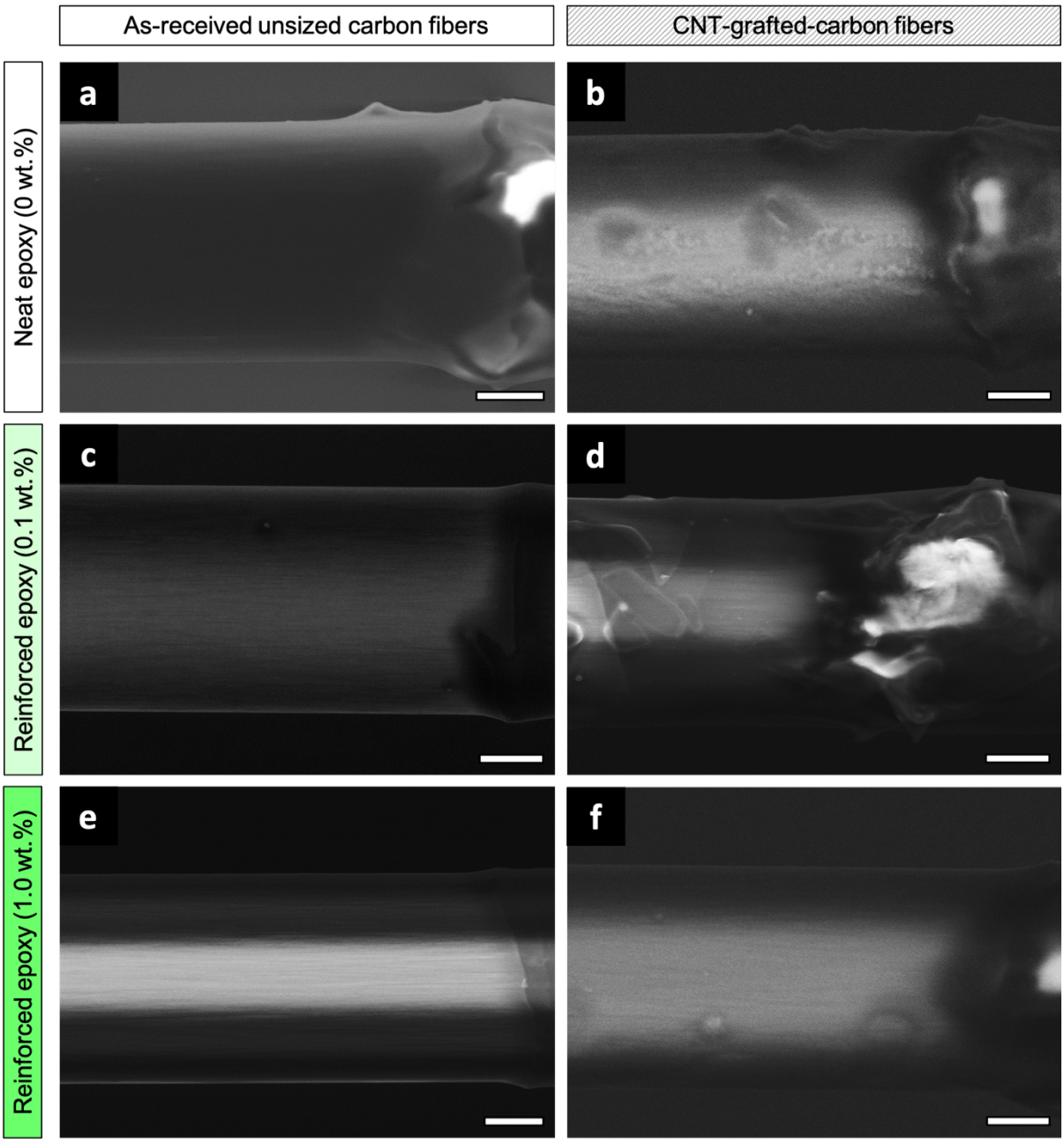


Fig. 6.7 Fibre surfaces after single fibre pull-out tests for (a) unsized carbon fibre and (b) CNT-g-CF in neat epoxy, (c) unsized carbon fibre and (d) CNT-g-CF in TB3b-dispersed SWCNT (0.1 wt.%) reinforced epoxy, (e) unsized carbon fibre and (f) CNT-g-CF in TB3b-dispersed SWCNT (1.0 wt.%) reinforced epoxy - scale bars = 2 µm.

6.2. Mechanical performance of carbon fibres

6.2.1. Tensile properties of unidirectional bundle composites

As a first attempt to fabricate practical, unidirectional carbon fibre reinforced polymer (CFRP) composites, whole fibre bundles / tows were simply infused with resin. This approach allowed the tensile properties, including strength and modulus, to be measured for both bi-catalyst deposited P-AS4-US (AS4-BiCat) and CNT-g-CFs (CNT-g-AS4), and compared to those of as received carbon fibres (AR-AS4-US) used as controls. Note that the acronyms "CF" and "AS4" were used interchangeably given that AS4 carbon fibres were the only type of carbon fibre investigated in this study. The unidirectional bundle manufacturing process (described in detail in Section **3.3.7**) was designed in theory for a fibre volume fraction of approximately 40 %. However, during the manufacturing process, only a limited pressure was applied, as a precaution against damaging the fibres or their coatings; as a result, the cross-sections of the final bundle composites were slightly greater than intended, leading to slightly lower fibre volume fractions in the range 20 and 30 %. This range is still consistent with the ASTM standard used, yet is lower than most practical continuous fibre composites; it may therefore be a better test of fibre properties as it reduces the effects of fibre-fibre interactions. To directly compare fibre performance within the context of a composite, the effective fibre stress was calculated by dividing the applied load by the total cross-sectional area of the fibres (Eq. 6.1), effectively normalising to fibre volume fraction:

$$\sigma_{effective,\ single\ fibre} = \frac{F}{n\pi r^2}, \qquad \text{Eq. 6.1}$$

where F is the applied tension load, n the number of carbon fibres and r the fibre radius. Stress-strain plots were normalised to the single fibre effective stress for both unidirectional AR-AS4-US and CNT-g-AS4 bundle composites (**Fig. 6.8**), showing good agreement with previously acquired single fibre tensile data [3]. AR-AS4-US exhibited a tensile strength and modulus of 3900 ± 183 MPa and 249.3 ± 1.5 GPa, respectively, and a strain to failure of approximately 1.48 ± 0.07 %, similar to the data provided by the carbon fibre manufacturer [235].

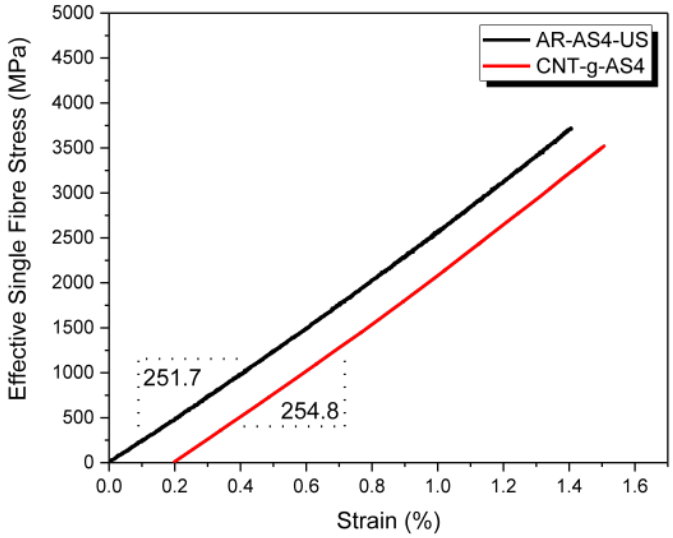


Fig. 6.8 Effective single fibre stress-strain curve under tension for AR-AS4-US (black) and CNT-g-AS4 (red). CNT-g-AS4 data were offset by 0.2 % strain for clarity.

Bi-catalyst deposited carbon fibres showed no degradation in their tensile properties, with a tensile strength of 3973 ± 98 MPa (**Fig. 6.9**), suggesting that the continuous deposition process, including in-line plasma oxidation, caused negligible carbon fibre damage. On the other hand, exposing the bi-catalyst deposited carbon fibres to the CVD treatment led to a minor decrease in tensile strength by 13 % (3361 ± 78 MPa), when compared to as-received carbon fibres. This small decrease is consistent with minimal intrinsic catalyst damage. The tensile modulus of all the fibres remained effectively unchanged, as the fibre core retained its properties. Despite some slight reductions in tensile strength, the CNT-g-CFs are expected to improve composite properties as a whole, with CNTs promoting crack bridging and dissipating energy through CNT pull-out/fracture.

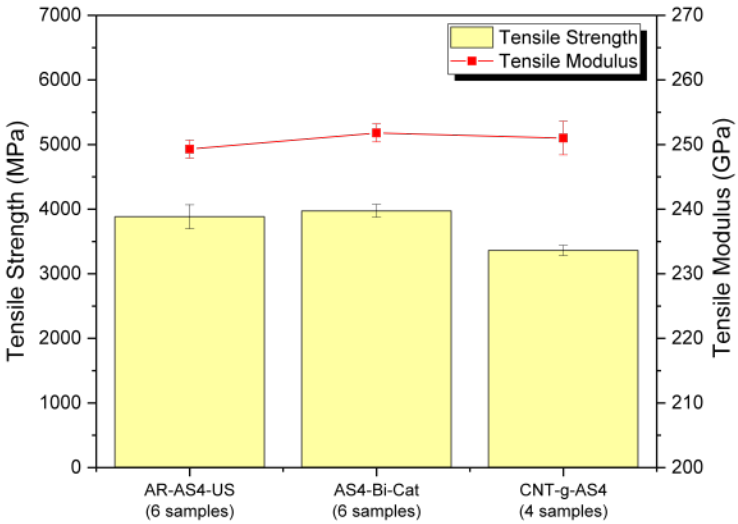


Fig. 6.9 Tensile strength and modulus of unidirectional CFRP bundle composites made of as-received AS4-US, AS4-BiCat and CNT-g-AS4. Error bars correspond to standard errors.

6.3. Characterisation of nano-reinforcements at the macroscale

6.3.1. Processing nano-reinforced short beam shear composites

Whilst the interfacial shear strength measurements provide indications of the potential macroscale improvements of the nano-reinforced composite, a more complete mechanical evaluation accounting for macroscale deformation mechanisms that appear in structural composites (void, fibre bridging, etc.) requires the manufacture of composite coupons. Previously not conceivable, the scaled-up production of CNT-g-CFs made the task of producing larger composite specimens feasible. However, even with the continuous process, the quantities of CNT-g-CFs that can be produced in the lab are limited; therefore, a new composite coupon preparation methodology had to be developed. The short beam shear (SBS) test was selected as a practical means to evaluate interfacial properties for a whole composite, using a small sample. Deliberately misaligning the fibres by a small degree in the top and bottom half of the specimen was intended to drive the failure at the middle plane to create a valid shear failure.

A process was developed to allow for the production of short beam shear (SBS) coupons from continuous tow production, following requirements specified in the ASTM D2344 standard [257]. The first generation design consisted in wrapping the carbon fibre tow around stainless steel pins (Ø 2 mm) fixed on a stainless steel mould (itself wrapped in PTFE film and peel ply). The pins ensured an angle of approximately 3.0° (± 1.5°) between two successive layers (**Fig. 6.10**a, b) as an attempt to alleviate fibre bridging. The tow was wrapped until a minimum of 4 plies was reached to obtain sufficient fibre volume fraction. Stainless steel inserts were then added on each side of the mould to contain the epoxy which was subsequently and partially poured from one edge of the mould. An initial degassing cycle was then performed in a vacuum oven before adding the rest of the epoxy mixture to facilitate evacuation of the air trapped from the initial pour. Several degassing cycles was performed after pouring the rest of the resin, prior to the insertion of the lid. Once the lid was slowly inserted, sitting flush with the lateral inserts to ensure a final composite thickness of 2 millimetres (**Fig. 6.10**c), a final degassing cycle was conducted, making sure that the total duration of the degassing step didn't exceed the pot life of the epoxy. The composite was then left to cure at atmospheric pressure following the manufacturer's recommendation. After curing, the composite panel was removed from the mould and cut using a computer numerical control (CNC) machine. Interestingly, discrete regions were observed on the transverse side of the SBS specimens, with the naked eye, suggesting nonoptimal/heterogenous distribution of the carbon fibres (**Fig. 6.10**d).

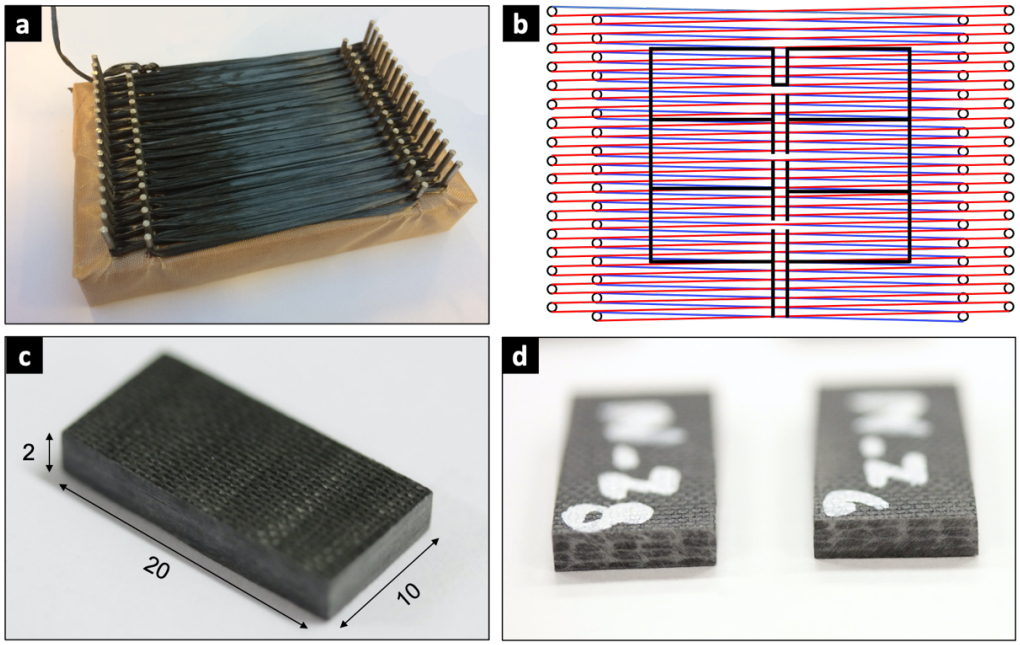


Fig. 6.10 (a) photograph of the first generation short beam shear stainless steel mould. (b) Schematic representation of the winding process ensuring an angle of 3.0° (± 1.5°) between two successive plies; specimen locations indicated by cutting marks (black lines). (c, d) Photographs of the SBS specimens after curing and cutting (dimensions in mm).

Reducing the diameter of the pins appeared necessary to avoid the heterogenous distribution of the tows and potential intralaminar failure; cracks are prone to propagate within resin-rich regions between layers. However, a reduction of the pin diameter led to high local curvature, and therefore high transverse stresses in carbon fibres during wrapping, producing fibre breakage. Hence, a second generation design was developed to minimise bending of the carbon fibre tow. The approach, compatible with in-line processes, involved using two moulds with a similar design to that of the first generation as well as smaller pins diameter (Ø 1.5 mm). The tow was wrapped up around both moulds, effectively producing two sets of SBS specimens at once (**Fig. 6.11**b). The moulds were assembled together onto a stainless steel rod and allowed to rotate freely to facilitate fibre winding (refer to the **Annex 5 and 6** for mould technical drawings and winding instructions). The tow was then wrapped up around the assembly until 4 layers were achieved on both sides. The small pin diameter, which dictates spacing between tows, allowed for a fibre volume fraction between 50 and 69 vol.% in the final composites. Once the winding was completed, four inserts were added on each side to secure the fibres in position (**Fig. 6.11**e). The carbon fibre tows were then cut with a scalpel blade at the junction between the two moulds to allow for their separation. The rest of the procedure was similar to that of the first generation design, including degassing, curing and cutting of the SBS specimens with the only difference being the use of a G-clamp to maintain pressure on the lid during the cure to ensure a specimen thickness of 2 mm (**Fig. 6.11**h), and the addition of Tacky Tape to limit flow over specific mould regions.

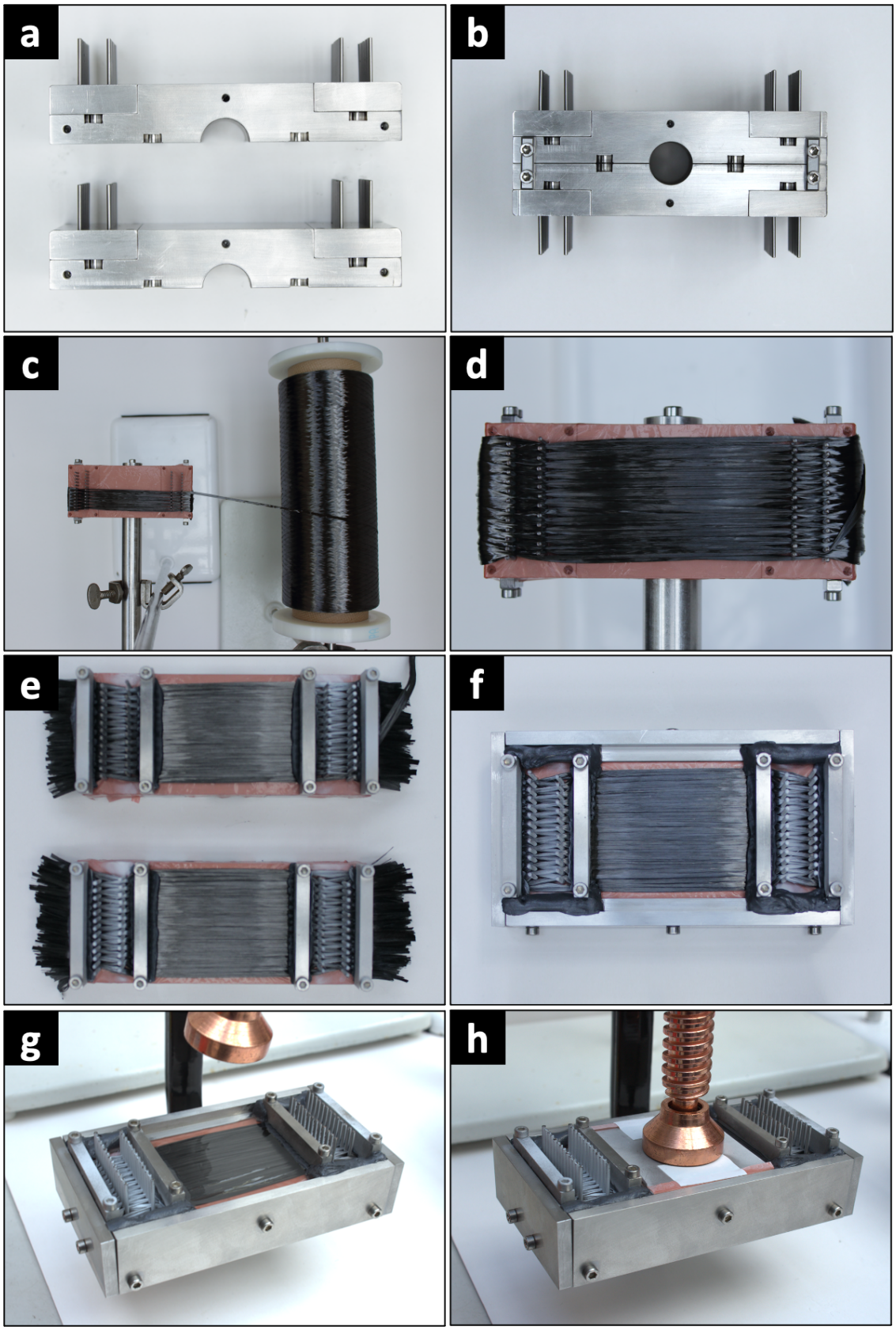


Fig. 6.11 Photographs of the second generation short beam shear stainless steel mould (a) with the different fabrication steps including, (b) moulds assembly, (c, d) fibre winding, (e) top inserts for securing the tows, cutting and separation of the moulds, (f) introduction of the mould lateral inserts and tacky tape for (g) pouring epoxy and (h) addition of the mould lid.

Both mould designs showed difficulties with resin infiltration, with dry areas often present at the bottom of the composite panels despite the addition of a flow medium placed between the PTFE film and the peel ply wrapped on the mould (**Fig. 6.12**). The second generation design, allowing for the production of over twice the amount of SBS specimens, required to comply with the ASTM D2344 standard. The interlaminar shear strength of CNT-g-CFs was investigated for two different aerospace grade epoxies, namely 20ULV and L20:EPH161. Whilst the former helps significantly with issues related to resin infusion (i.e. void content), due to its ultra-low viscosity, the latter is stiffer and more ductile (**Table 6.1**), potentially promoting better stress transfer through the critical CNT-g-CF/epoxy interface. The synergistic nano-reinforced epoxy (described in Section **6.1.1**) was also briefly attempted, however, its increased viscosity limited degassing, leading to inconclusive interlaminar shear strength (ILSS) measurements. However, improvements in the infusion process may in the future allow for such nano-reinforced system to be used with CNT-g-CFs.

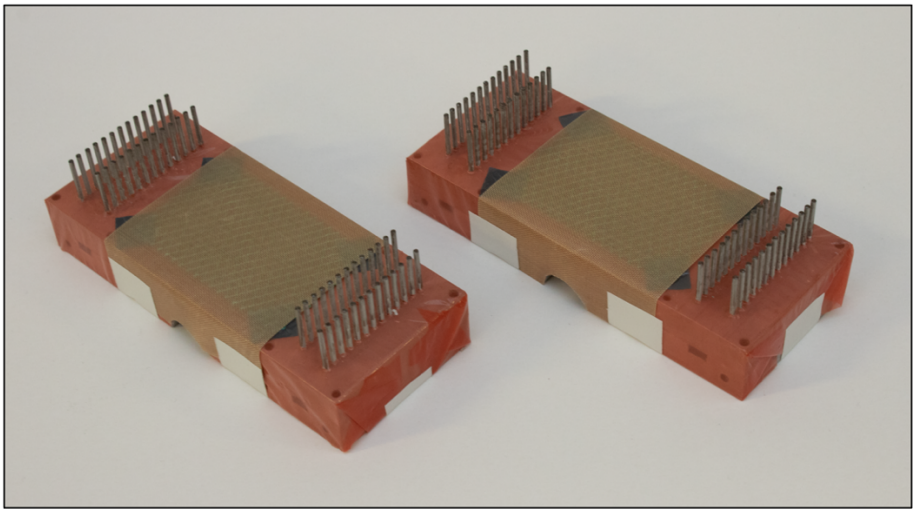


Fig. 6.12 Second generation mould with flow media intercalated between the PTFE release film and the peel ply.

Table 6.1 Mechanical properties of the epoxy systems.

Epoxy system	Tensile properties		Strain to failure (%)	Interlaminar shear strength ILSS (MPa)	Reference[†]
	Strength (MPa)	Modulus (GPa)			
L20:EPH161	70.2	3.4	9.5	54.0	[239]
20ULV	71.2	2.9	6.3	48.4	[238]

[†] *data collated from manufacturer's datasheet.*

6.3.2. Interlaminar shear strength of nano-reinforced short beam shear composites

First generation design

Short beam shear tests carried out on specimens produced from the first generation mould design showed a reproducible response, but a potentially inconsistent failure mode. The implied shear stress in short beam shear tests should increase linearly until plastic deformation occurs; after yielding and reaching a maximum load characterised by the onset of delamination, the shear stress should then decrease as the interlaminar failure progresses. If an excessive load is applied, the specimen may experience crushing characterised by the load increasing again. Both AR-AS4-US and CNT-g-CF showed a mild inflection point with theoretical ILSS of 58.49 ± 1.50 and 56.22 ± 0.57 MPa (**Fig. 6.13**), respectively, in agreement with the ILSS provided by the L20:EPH161 epoxy manufacturer (**Table 6.1**). However, in both cases, the shear stress continued to increase after delamination until a plateau was reached, which is likely to be the result of compressive contributions due to a low fibre volume fraction, as suggested from the discrete tow distributions previously discussed (**Fig. 6.10**d). However, CNT-g-CF exhibited a more brittle response, with shear stress levelling off for large displacement characteristic of a mix-mode failure.

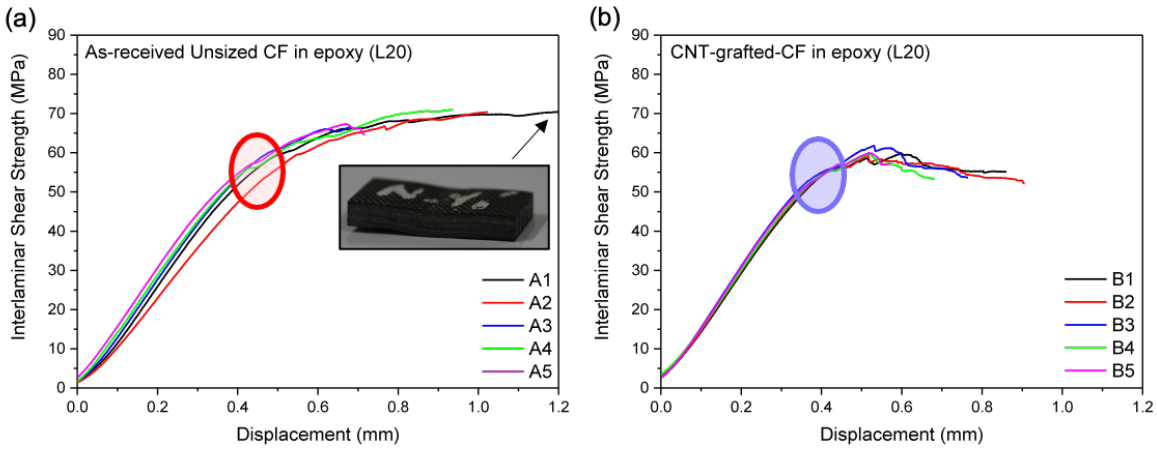


Fig. 6.13 Interlaminar shear strength measurements for both (a) AR-AS4-US and (b) CNT-g-CF in neat epoxy (L20:EPH161) from SBS specimen produced with the first-generation mould design. Ellipses highlight the onset of interlaminar failure.

Second generation design

SBS specimens produced from the second generation mould showed a more consistent ILSS-displacement plot (**Fig. 6.14**). AR-AS4-S ILSS characteristics appeared marginally better than its unsized counterpart, owing to better wetting properties due to the presence of polymeric sizing thus improving the resin infusion process. Whilst the ultra-low viscosity epoxy (20ULV) could infuse AR-AS4-S and AR-AS4-US relatively well, as evidenced by the ILSS plot characteristics (**Fig. 6.14**a-d).

SBS test results for CNT-g-CF in 20ULV exhibited multiple abrupt drops after initial failure (**Fig. 6.14**e), potentially the result of poor resin infusion with partial epoxy adhesion leading to cracks jumping from one unbonded region to another. In addition, CNT-g-CF SBS specimens couldn't be manufactured using the tougher (L20) epoxy system, due to an increased viscosity leaving one side of the composite panel dry. Although CNT-g-CF in 20ULV show a decrease in ILSS by 8.3 % (62.0 ± 0.4) when compared to AR-AS4-S in 20ULV (67.6 ± 0.6) **Table 6.2**, it is hard to draw any conclusion on the potential macroscopic interlaminar improvement, due to limitations of the infusion process. Whilst in principle, the grafted CNT morphology is compatible with conventional resin processing, the nanoscale channels may slow the infusion process. More development is needed, for example to use an appropriate vacuum infusion technique.

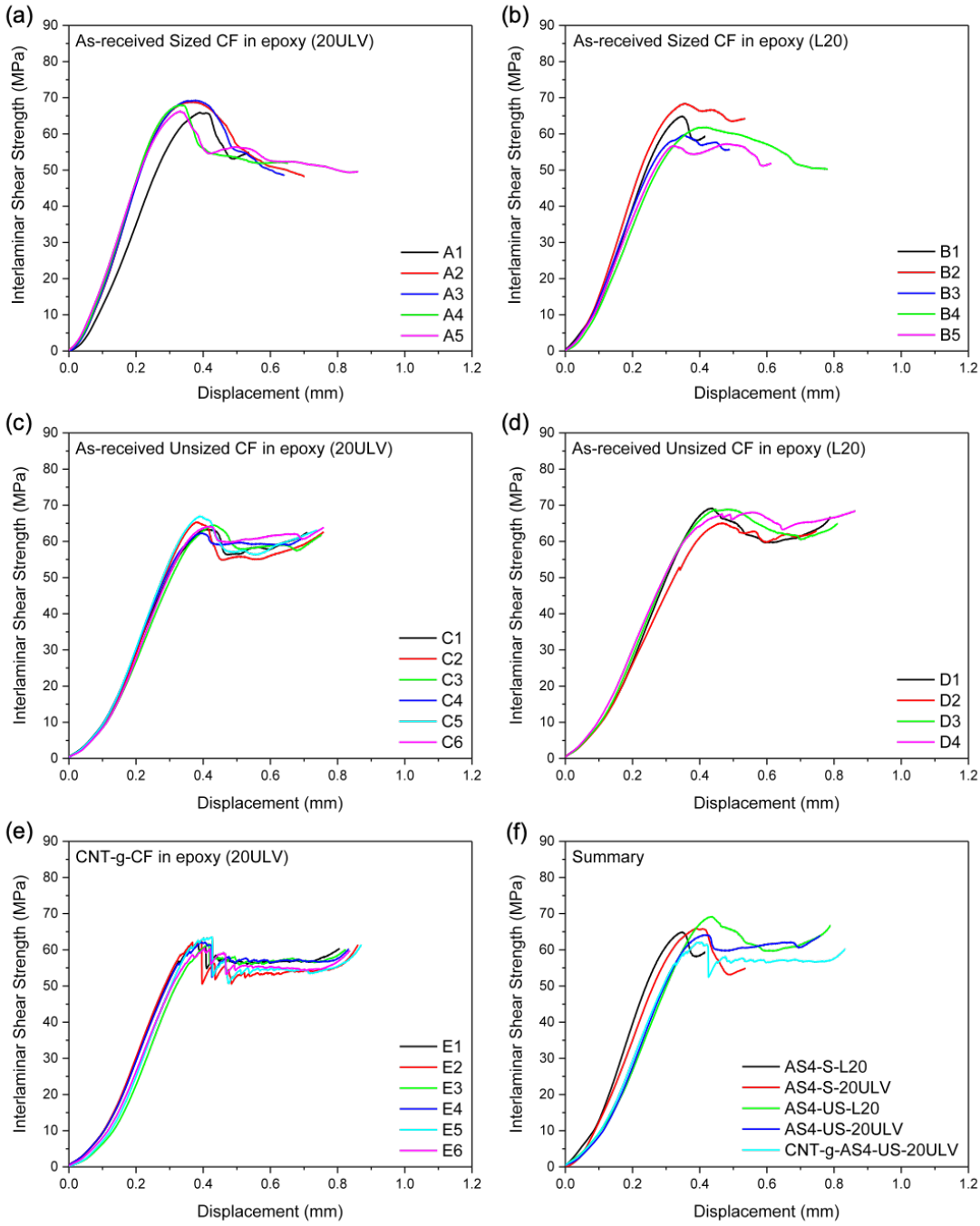


Fig. 6.14 Interlaminar shear strength measurements for AR-AS4-S with (a) 20ULV and (b) L20:EPH161 epoxy resins and for AR-AS4-US with (c) 20ULV and (d) L20:EPH161 epoxy resins.

Table 6.2 Collated ILSS data for AR-AS4-US and AR-AS4-S with 20ULV and L20:EPH161 epoxy resins.

Fibres	Epoxy	V_f (%)	ILSS (MPa)
AR-AS4-S	20ULV	63 - 74	67.6 ± 0.6
AR-AS4-S	L20:EPH161	56 - 69	62.2 ± 1.8
AR-AS4-US	20ULV	50 - 60	64.4 ± 0.6
AR-AS4-US	L20:EPH161	49 - 58	69.4 ± 1.3
CNT-g-CF	20ULV	49 - 57	62.0 ± 0.4

6.4. Summary

At the microscale, CNT-g-CFs exhibited particularly attractive interfacial properties with both unreactive thermoplastic matrices, where wetting and adhesion typically limit composite performance, and reactive structural epoxy systems. In the thermoplastic, the failure mode changed from a simple interfacial de-adhesion to a cohesive fracture of the CNT-reinforced interphase. Furthermore, the first evidence for a synergistic enhancement in interfacial properties when combining CNT-g-CFs with a SWCNT-reinforced epoxy resin emerged. At the macroscale, simple tensile tests of unidirectional bundle composites showed only a modest decrease in tensile strength of approximately 13 % for CNT-g-CF when compared to its as-received counterpart; the tensile modulus, a core property, was fully retained. A process for the production of CNT-g-CF SBS specimens was developed, although infusion related issues still did not allow for the improvement in the interlaminar properties to be confirmed at the macroscopic scale. Further developments, either with vacuum infusion, or direct filament winding, using a sizing bath at the end of the CVD line may resolve these problems in the future.

Chapter 7 : Conclusions and outlook

7.1. Summary of findings

This thesis reports the development and optimisation of a continuous, catalytic CVD process for growing CNTs on structural reinforcing fibres.

Continuous bi-catalyst precursor deposition

A scalable, in-line catalyst precursor deposition system was developed, including an atmospheric oxidative plasma treatment step. Oxidative treatment of the carbon fibres (CFs) was a requirement for adequate, homogeneous distribution of the hydrophilic catalyst precursors. Fine tuning of the bi-catalyst (Ni:Fe) precursor stoichiometry and concentration in solution both enhanced the CNT growth and ensured an optimum coverage of nucleation sites. The optimum metal catalyst precursor solution concentration (1.0 wt.%), for both silica and carbon fibres, provided sufficient metal for a dense catalyst covering, whilst avoiding the inhomogeneous precipitation of large crystals. The optimum (Ni:Fe) metal stoichiometry was also similar for both systems, consistent with previous bimetallic catalysts in the literature, but slightly more Fe-rich on quartz (1:0.5 mol.%) than carbon (1:0.69 mol.%) fibres. The catalyst precursor deposition was performed on whole tows, allowing for the production of 300 meters of bi-catalyst precursor deposited fibres in a day. This production rate was crucial for finally enabling largescale parametric studies and the subsequent manufacture of composite coupons.

Continuous CNT growth on quartz fibres

The continuous synthesis of CNTs on quartz fibres demonstrated the potential of continuous CVD for grafting CNTs in a practical and scalable manner. Adjustments of the CVD line speed led to the formation of distinctive CNT morphologies. Whilst a slower line speed of 1.2 $m.h^{-1}$ (dwell time of 30 min) led to longer CNTs (> 5 µm) with a splayed “Mohawk” configuration, an increased line speed of 2.4 $m.h^{-1}$ (dwell time of 15 min) promoted the growth of a short and highly entangled layer of CNTs. The resulting uniform coverage of 200 nm long CNTs increased the interfacial shear strength with epoxy (90.3 ± 2.1 MPa) by 12% compared to the commercially-sized reference. In addition, the grafted CNTs formed a conductive path, predominantly parallel to the fibres reaching a longitudinal electrical conductivity of 2.7 ± 0.3 $S.m^{-1}$, particularly useful for electrically-monitored damage detection. The baseline resistivity parallel to the fibres ($\rho_0 = 3.9 \pm 0.4 \times 10^{-1}\ \Omega.m$) displayed a linear piezoresistive response (K = 3.64), also referred to as "gauge factor”, a two-fold improvement over traditional resistance strain gauges. The simultaneous analysis of electrical conductivity, stress-strain performance, and acoustic emission allowed the sensitivity to specific composite failure modes to be

determined. The very short grafted CNTs provided the best mechanical interfacial enhancement and the best strain sensing ability, without disrupting the primary fibre composite volume fraction, a crucial requirement for practical design of structural composites, in which primary volume fraction is such a key factor. However, simple interfacial strength may not be the key parameter for quartz fibres, as glass fibre composites are governed by hydrolysis at the interface due to the water sensitivity of the conventional silane coating. The hydrophobic, mechanically-keyed CNT coating may be particularly beneficial from this perspective, though further studies are needed. In any case, the multifunctional enhancement is very encouraging, both improving the mechanical response and embedding a structural health monitoring capability. Many structural health monitoring strategies, particularly that monitor fibre damage, as opposed to matrix cracking, disrupt the primary structure. The CNT grafted strategy avoids these problems and may be readily implemented to provide in situ fibre strain and damage data.

Continuous CNT growth on carbon fibres

Extensive CVD parametric studies carried out on bi-catalyst precursor deposited carbon fibres highlighted the key dependencies of the continuous CVD system. Both growth temperature and reactive gas composition exhibited extremely narrow operating windows with any large variations shutting down the system entirely. On the other hand, adjustments of the line speed allowed for some control on the thickness of the grafted CNT layer, with variations from 1.2 $m.h^{-1}$ to 4.8 $m.h^{-1}$ promoting CNT coatings from tens of nanometres to sub-500 nm, respectively. As previously established by Anthony *et al.* [3], the use of a potential difference (300 V) was an absolute necessity to promote the CNT growth and avoid carbon fibre surface pitting. Whilst alteration to the reaction duration affected the CNT growth marginally, any change in the onset reduction temperature had a strong effect suggesting the CNT synthesis is mainly controlled by the catalyst reduction step. Over 50 meters of CNT-g-CFs were finally produced consistently per day. Importantly, the results were proved to be highly reproducible over the course of over a year, with multiple system re-builds. The continuous CVD process developed here offers a robust route to nanoengineer carbon fibres with a dense and uniform layer of CNTs.

Microscale investigations of the interfacial properties showed that CNT-g-CFs were an excellent candidate as microscale reinforcement both when combined with epoxy and unreactive polypropylene resins. Whilst thermoplastics typically exhibit poor wetting and adhesion with carbon fibre surfaces, the presence of a nanostructured dense layer of short (~200 nm) and small diameter (~10 nm) CNTs improved the wetting properties and introduced a mechanical interlocking effect between the polymer and the CNT network. The resulting interfacial shear strength (IFSS) was

increased by up to 52 % compared to the appropriate control samples. Similarly, CNT-g-CF exhibited an improved IFSS with aerospace-grade epoxy (up to +7.5%) compared to the control unsized carbon fibres. A large increase (+10.8 %) was obtained when the epoxy was reinforced with SWCNTs, demonstrating the first evidence for a synergistic enhancement in interfacial properties. Quantitatively, the IFSS measured is slightly higher than that commonly reported in the literature (**Fig. 2.22**). This result is particularly promising as literature studies often overestimate IFSS by not accounting for the CNT contribution to the overall fibre diameter.

At the macroscale, tensile testing of unidirectional CF bundle composites showed mild degradation (13 %) of the tensile strength but a retained tensile modulus. A process for the manufacture of short beam shear specimens from continuous tow was developed. Unfortunately, due to resin infusion issues, an improvement in interlaminar properties could not yet be confirmed. Short beam shear test results in the literature have shown very large dispersion and variability, which make comparison complicated due to composite processing discrepancies (**Table 2.5**). However, degradation in the interlaminar properties and reports of intralaminar failure due to an inability to grow CNTs within woven CF fabric [214] emphasise the advantage of growing CNTs directly on continuous tows potentially providing both an intralaminar and interlaminar reinforcement.

7.2. Outlook

Hierarchical manmade composites remain a focus of worldwide research, as the challenge of bringing them closer to reality remains. Moving beyond batch syntheses, the continuous CVD process has been shown to improve reproducibility and consistency, a major issue in largescale applications. The subsequent systematic study of the process variables evidences the possibility of making a pilot line, sufficient to generate materials for standardised tests. Continuous tow processing represents the next step forward in the field towards implementation of hierarchical composites, generating complex architectures in a scalable manner.

7.3. Future work

The promising results obtained in this thesis pave the way for a range of future developments. Firstly, there are a number of potential modifications to the CVD line:

- The development of an in-line sizing procedure post CNT growth should avoid potential fibre damage through handling, alleviate issues with resin infiltration, improve interfacial properties further and address safety concerns associated with dry nano-/micro- scale materials collection.
- The custom-made tensioning unit could be replaced by a close-circuit tension measurement and control unit (similar to that of the deposition line) to have a better control on the tension applied during synthesis.
- An untwisting unit (ideally prior to the deposition) should minimize mechanical performance variations in the final composite coupons.
- A portable Raman system could be introduced at the exit point of the furnace, to assess the success and quality of the CNT growth in real-time.
- An automated collection process (similar to filament winding) could facilitate the production of composite coupons (currently performed manually – see SBS production **Chapter 6**)

More fundamental developments of the deposition/synthesis procedure could include the following questions/issues:

- Analyse the SBS specimens fratographically to confirm the resin infusion issue and understand the failure mechanisms fully.
- Pinpoint where in the carbon fibre production process the CVD line should be implemented by using PAN-based carbon fibres at different stages of the carbonisation process for deposition, followed by CVD CNT synthesis and graphitisation under tension. In principle, the CNTs may be better integrated with the primary fibre if grown before the graphitisation, leading to improved interfacial performance. This approach may also remove even the modest degradation in tensile strength observed in the current data.
- Explore intermittent bonding by modulating the potential difference hence generating regions of high and low shear strength (this strategy may require reducing the length of the CVD synthesis region).

- Manufacture sufficient materials for compression specimens. These larger specimens may require an increased line speed or overnight work authorization to produce enough material. Such specimens would be interesting given the potential for the radial CNT reinforcement to support the fibres against micro-buckling during longitudinal compression.
- Explore adaptability of the system to other continuous reinforcements, including continuous CNT fibres, of interest as the bi-catalyst precursor could penetrate the porous fibre structure and dramatically increase surface area.
- Assess whether the bi-catalyst particles diffuse in the carbon fibres during CVD growth through X-ray computed tomography [278] or through FIB-TEM.
- Study of the mechanisms driving successful CNT synthesis with the application of a potential difference.
- Investigate the nature of the CNTs formed at different temperatures to understand the change in growth mode, and whether there is a change in active metals or deposition of pyrocarbon on the catalyst surface (TEM imaging).
- Investigate the combination of CNT-g-CFs with a high CNT volume fraction epoxy (approximately 25 wt.%) through the use of the wet powder impregnation method developed in the group [97] to assess synergistic effects at large scales (**Fig. 7.1**).
- Explore the multifunctional benefits of grafting CNTs on quartz glass fibres, particularly the effects on water sorption and resistance to interfacial de-adhesion.
- Investigate the growth of CNTs at lower temperature on more challenging commercial glass fibres, to create a more widely relevant functional system.

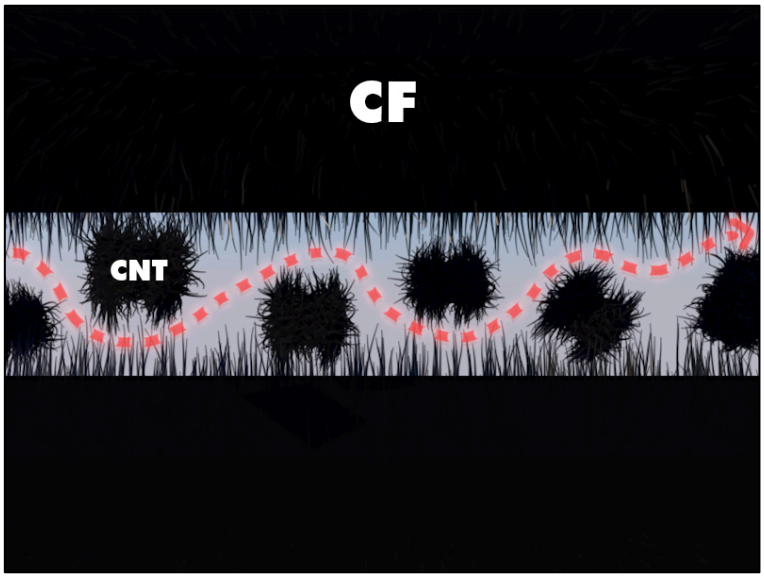


Fig. 7.1 3D illustration of the combination of CNT-g-CF with sub-micron scale CNT reinforcements in epoxy. Red line suggests the propagation of a crack in the epoxy rich regions (not to scale) with grafted CNTs pushing the crack away from the critical fibre-matrix interface.

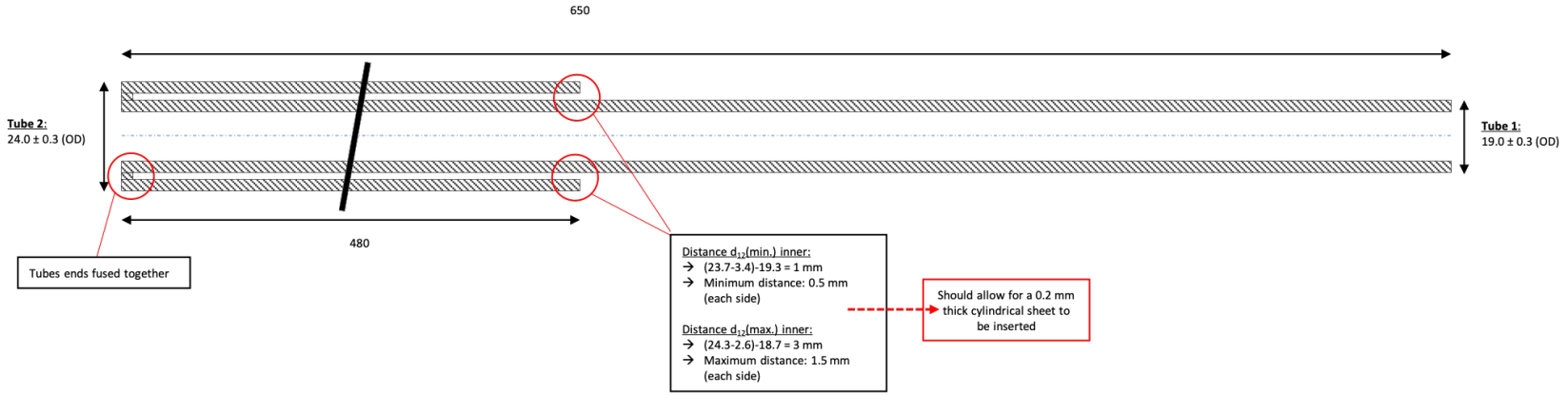
Annex 1: Technical drawings of the sheathed quartz tube "C_2"

Side View

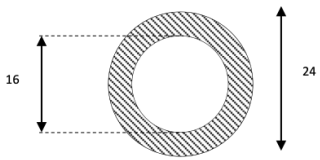
Custom quartz tubing Robson Scientific

Schematic not to scale

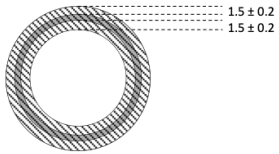
	Outer diameter (mm)	Wall thickness (mm)
Tube 1	19.0 ± 0.3	1.5 ± 0.2
Tube 2	24.0 ± 0.3	1.5 ± 0.2



Front View

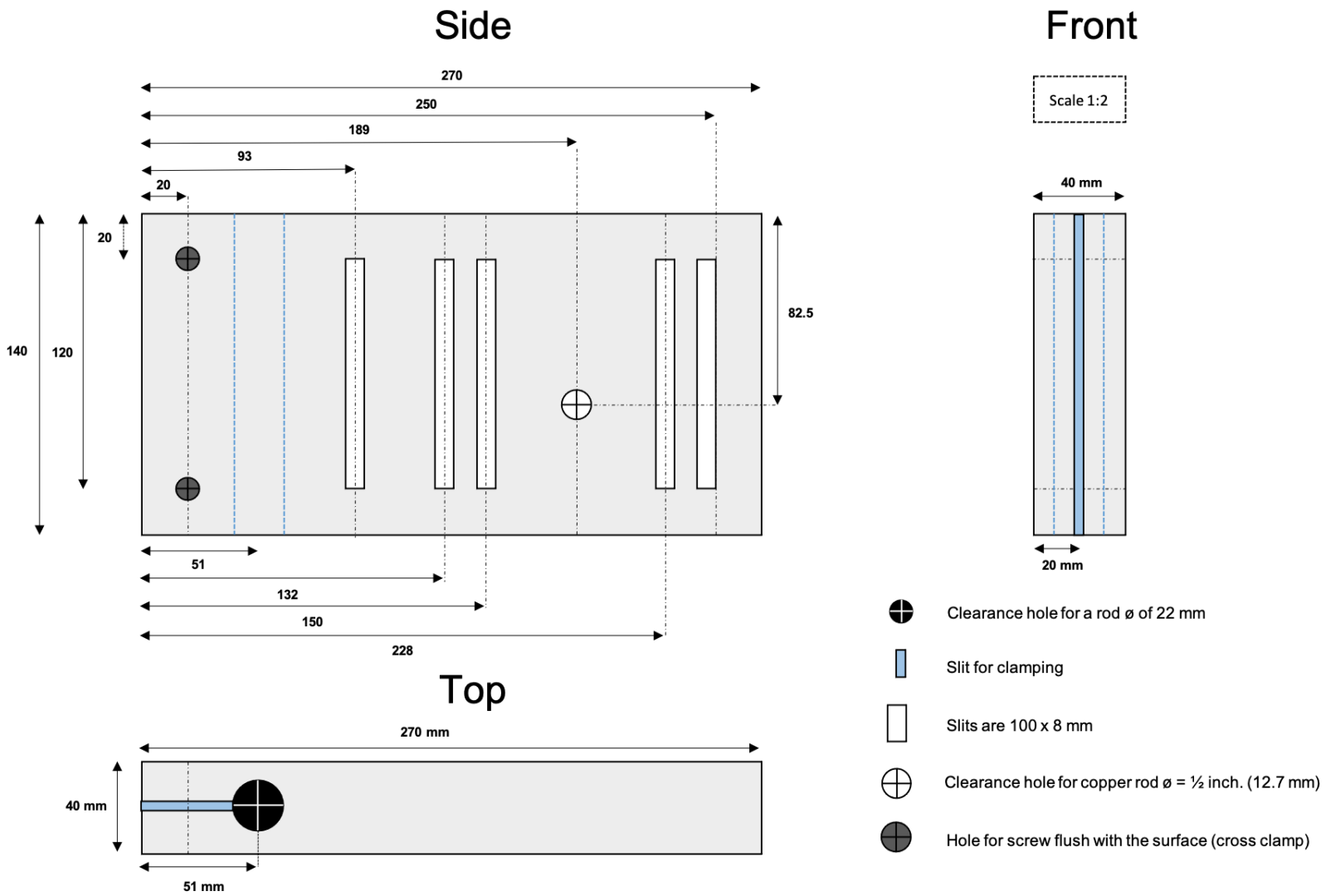


Back View

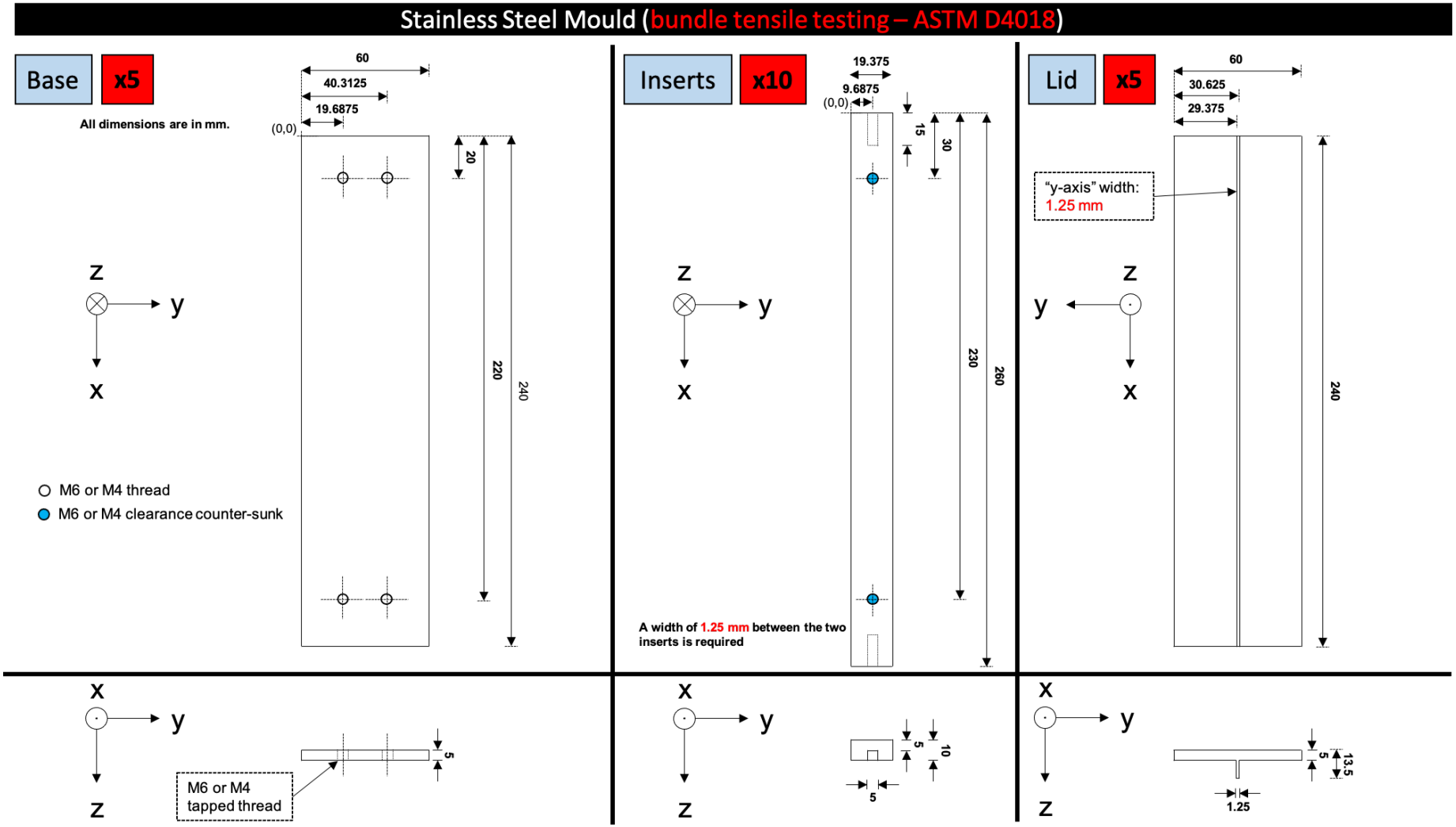


NB: Tube ends should be flame polished

Annex 2: Technical drawings of the CVD line tensioning unit with ball bearings



Annex 3: Technical drawings of the bundle composite stainless streel mould



Annex 4: CVD growth parameter space – List of experiments (part 1/3)

Experiment #	Carbon fibre			Catalayst precusors			Ni:Fe Molar ratio (mol.%)						Concentration wt.% (in ethanol)				Residency time in catalyst precurosr (min)		Deposition method		Deposition speed ($m\ h^{-1}$)	
	AS4-Sized	AS4-US	AS4-US PlasmaOx	$Fe(NO_3)_3$	$Fe(acac)_3$	$Ni(acac)_2$	1:0.33	1:0.5	1:0.64	1:0.73	1:1	1:2	0.1	0.5	1	4	1	2	Dipped	Cont. Line	10	20
EXP1	x			x		x					x					x		x	x			
EXP2	x			x		x					x					x		x	x			
EXP3	x			x		x					x					x		x	x			
EXP4	x			x		x					x					x		x	x			
EXP5	x				x	x				x			x					x	x			
EXP6	x				x	x				x					x			x	x			
EXP7	x			x		x			x				x					x	x			
EXP8	x			x		x			x						x			x	x			
EXP9	x			x		x			x						x			x	x			
EXP10	x			x		x	x								x			x	x			
EXP11	x			x		x		x							x			x	x			
EXP12	x			x		x			x						x			x	x			
EXP13	x			x		x						x			x			x	x			
EXP14	x			x		x			x						x			x		x	x	
EXP15	x			x		x			x						x			x		x	x	
EXP16		x		x		x			x						x			x		x	x	
EXP17		x		x		x			x						x			x		x	x	
EXP18		x		x		x			x						x			x		x	x	
EXP19		x		x		x			x						x			x		x	x	
EXP20		x		x		x			x						x			x		x	x	
EXP21		x		x		x			x						x			x		x	x	
EXP22		x		x		x			x						x			x		x	x	
EXP23		x		x		x			x						x			x		x	x	
EXP24		x		x		x			x						x			x		x	x	
EXP25			x	x		x			x					x			x			x		x
EXP26			x	x		x			x						x		x			x		x
EXP27			x	x		x			x						x		x			x		x
EXP28			x	x		x			x						x		x			x		x
EXP29			x	x		x			x						x		x			x		x
EXP30			x	x		x			x						x		x			x		x
EXP31			x	x		x			x						x		x			x		x
EXP32			x	x		x			x						x		x			x		x
EXP33			x	x		x			x						x		x			x		x
EXP34			x	x		x			x						x		x			x		x
EXP35			x	x		x			x						x		x			x		x
EXP36			x	x		x			x						x		x			x		x
EXP37			x	x		x			x						x		x			x		x
EXP38			x	x		x			x						x		x			x		x
EXP39			x	x		x			x						x		x			x		x
EXP40			x	x		x			x						x		x			x		x
EXP41			x	x		x			x						x		x			x		x
EXP42			x	x		x			x						x		x			x		x
EXP43			x	x		x			x						x		x			x		x
EXP44			x	x		x			x						x		x			x		x
EXP45			x	x		x			x						x		x			x		x
EXP46			x	x		x			x						x		x			x		x

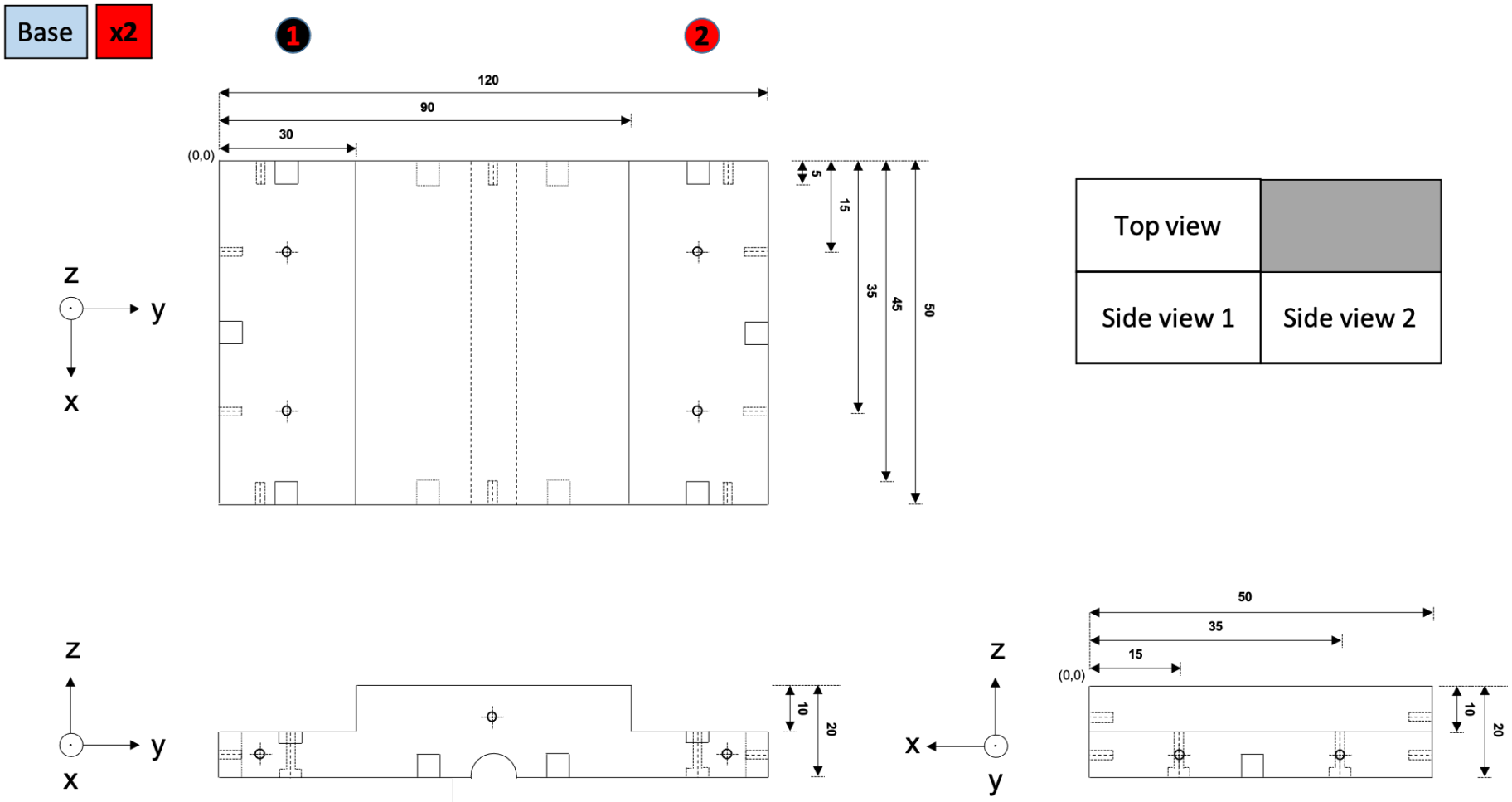
CVD growth parameter space – List of experiments (part 2/3)

Experiment #	Potential difference (V)					Carbon fibres			Counter electrode			Growth temperature (°C)			CVD Pull through speed (m h^{-1})					Reduction time (min)					
	100	150	200	300	1000	Hole (+ve)	Electron (-ve)	Earth	Hole (+ve)	Electron (-ve)	Earth	720	770	820	0.6	1.2	2.4	4.8	6.7	10	8	4	2	1	0.72
EXP1				x		x					x		x			x				x					
EXP2			x			x					x		x			x				x					
EXP3		x				x					x		x			x				x					
EXP4	x					x					x		x			x				x					
EXP5				x		x					x		x			x						x			
EXP6				x		x					x		x			x						x			
EXP7				x		x					x		x			x						x			
EXP8				x		x					x		x			x						x			
EXP9					x	x					x		x			x						x			
EXP10				x		x					x		x			x						x			
EXP11				x		x					x		x			x						x			
EXP12				x		x					x		x			x						x			
EXP13				x		x					x		x			x						x			
EXP14				x		x					x		x			x						x			
EXP15				x		x					x		x			x						x			
EXP16				x		x					x		x			x						x			
EXP17				x			x				x		x			x						x			
EXP18				x				x	x				x			x						x			
EXP19				x				x		x			x			x						x			
EXP20				x		x					x		x		x						x				
EXP21				x		x					x		x			x						x			
EXP22				x		x					x		x				x						x		
EXP23				x		x					x		x					x						x	
EXP24				x		x					x		x						x						x
EXP25				x		x					x		x			x						x			
EXP26				x		x					x		x			x						x			
EXP27				x		x					x		x				x						x		
EXP28				x		x					x		x			x							x		
EXP29				x		x					x		x				x							x	
EXP30				x		x					x		x					x						x	
EXP31				x		x					x		x				x						x		
EXP32				x		x					x	x					x						x		
EXP33				x		x					x		x				x						x		
EXP34				x		x					x			x			x						x		
EXP35				x		x					x		x				x						x		
EXP36				x		x					x		x				x						x		
EXP37				x		x					x		x				x						x		
EXP38				x		x					x		x				x						x		
EXP39				x		x					x		x				x						x		
EXP40				x		x					x	x					x						x		
EXP41				x		x					x		x				x						x		
EXP42				x		x					x			x			x						x		
EXP43				x		x					x		x			x						x			
EXP44				x		x					x		x				x						x		
EXP45				x		x					x		x			x						x			
EXP46				x		x					x		x				x						x		

CVD growth parameter space – List of experiments (part 3/3)

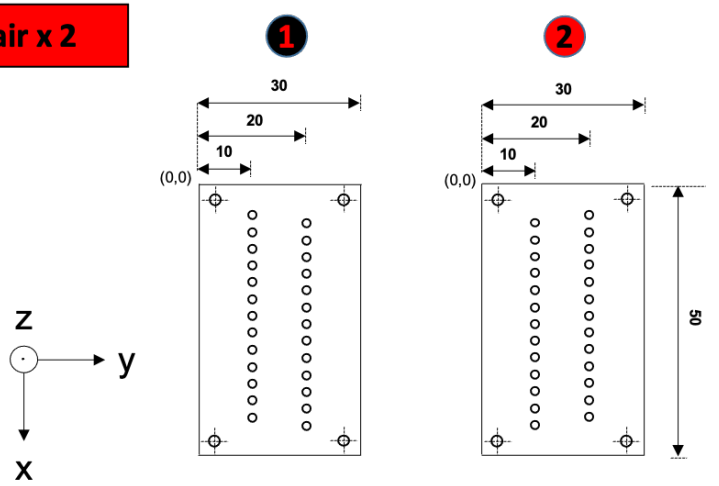
Experiment #	Growth time (min)							Nitrogen flow [100 vol.%] (sccm)						Hydrogen flow [2.4 vol.% in N_2] (sccm)			Acetylene flow [1.3 vol.% in N_2] (sccm)			C_2H_2:H_2 ratio				
	50	30	25	21	12.5	6.25	4.5	6682	6842	7500	8340	9680	10000	3400	5100	6800	162	325	650	1:10	1:19.3	1:30	1:40	1:80
EXP1		x								x				x				x			x			
EXP2		x								x				x				x			x			
EXP3		x								x				x				x			x			
EXP4		x								x				x				x			x			
EXP5			x							x				x				x			x			
EXP6			x							x				x				x			x			
EXP7			x							x				x				x			x			
EXP8			x							x				x				x			x			
EXP9			x							x				x				x			x			
EXP10			x							x				x				x			x			
EXP11			x							x				x				x			x			
EXP12			x							x				x				x			x			
EXP13			x							x				x				x			x			
EXP14			x							x				x				x			x			
EXP15			x							x				x				x			x			
EXP16			x							x				x				x			x			
EXP17			x							x				x				x			x			
EXP18			x							x				x				x			x			
EXP19			x							x				x				x			x			
EXP20	x									x				x				x			x			
EXP21			x							x				x				x			x			
EXP22					x					x				x				x			x			
EXP23						x				x				x				x			x			
EXP24							x			x				x				x			x			
EXP25			x										x	x				x			x			
EXP26			x										x	x				x			x			
EXP27					x								x	x				x			x			
EXP28			x										x	x				x			x			
EXP29					x								x	x				x			x			
EXP30						x							x	x				x			x			
EXP31					x								x	x				x			x			
EXP32					x								x	x				x			x			
EXP33					x								x	x				x			x			
EXP34					x								x	x				x			x			
EXP35					x							x		x					x	x				
EXP36					x								x	x				x			x			
EXP37					x						x				x			x				x		
EXP38					x			x								x		x					x	
EXP39					x				x							x	x							x
EXP40					x								x	x				x			x			
EXP41					x								x	x				x			x			
EXP42					x								x	x				x			x			
EXP43				x									x	x				x			x			
EXP44					x								x	x				x			x			
EXP45					x								x	x				x			x			
EXP46						x							x	x				x			x			

Annex 5: Technical drawings of the second generation SBS mould (part 1/6)

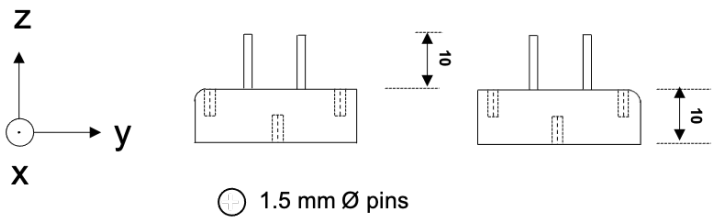


Technical drawings of the second generation SBS mould (part 2/6)

Inserts | Pair x 2



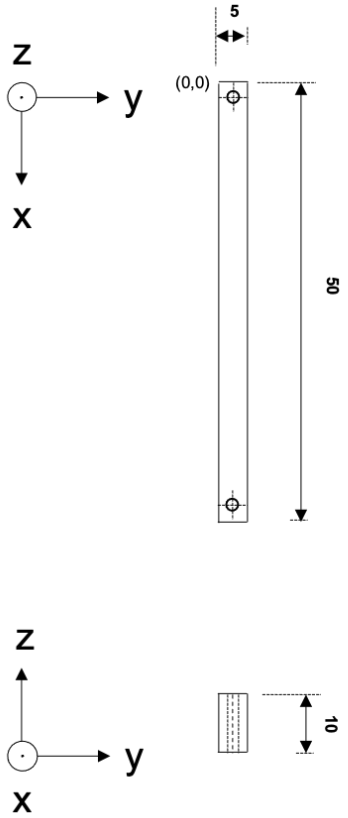
Top view	
Side view 1	



13 pins per row
Spacing between pin = pin diameter

Technical drawings of the second generation SBS mould (part 3/6)

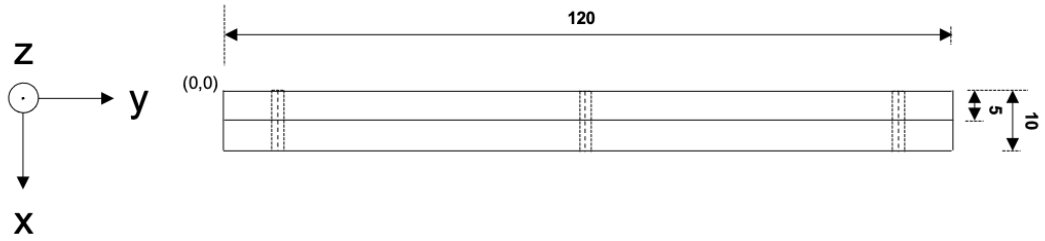
Top insert **1** **x8**



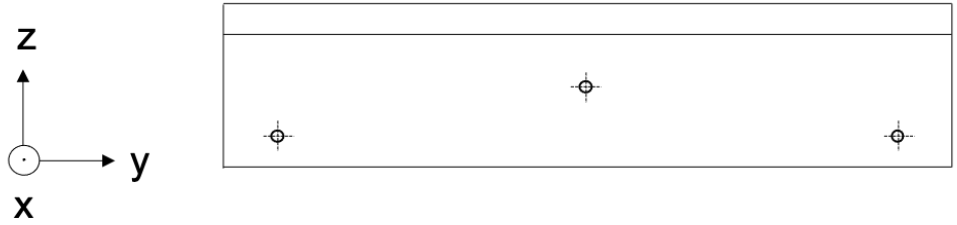
Top view	
Side view 1	

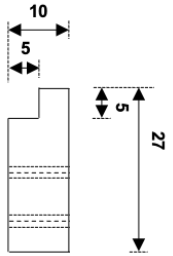
Technical drawings of the second generation SBS mould (part 4/6)

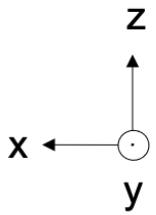
Outline insert **1** **x4**



Top view	
Side view 1	Side view 2

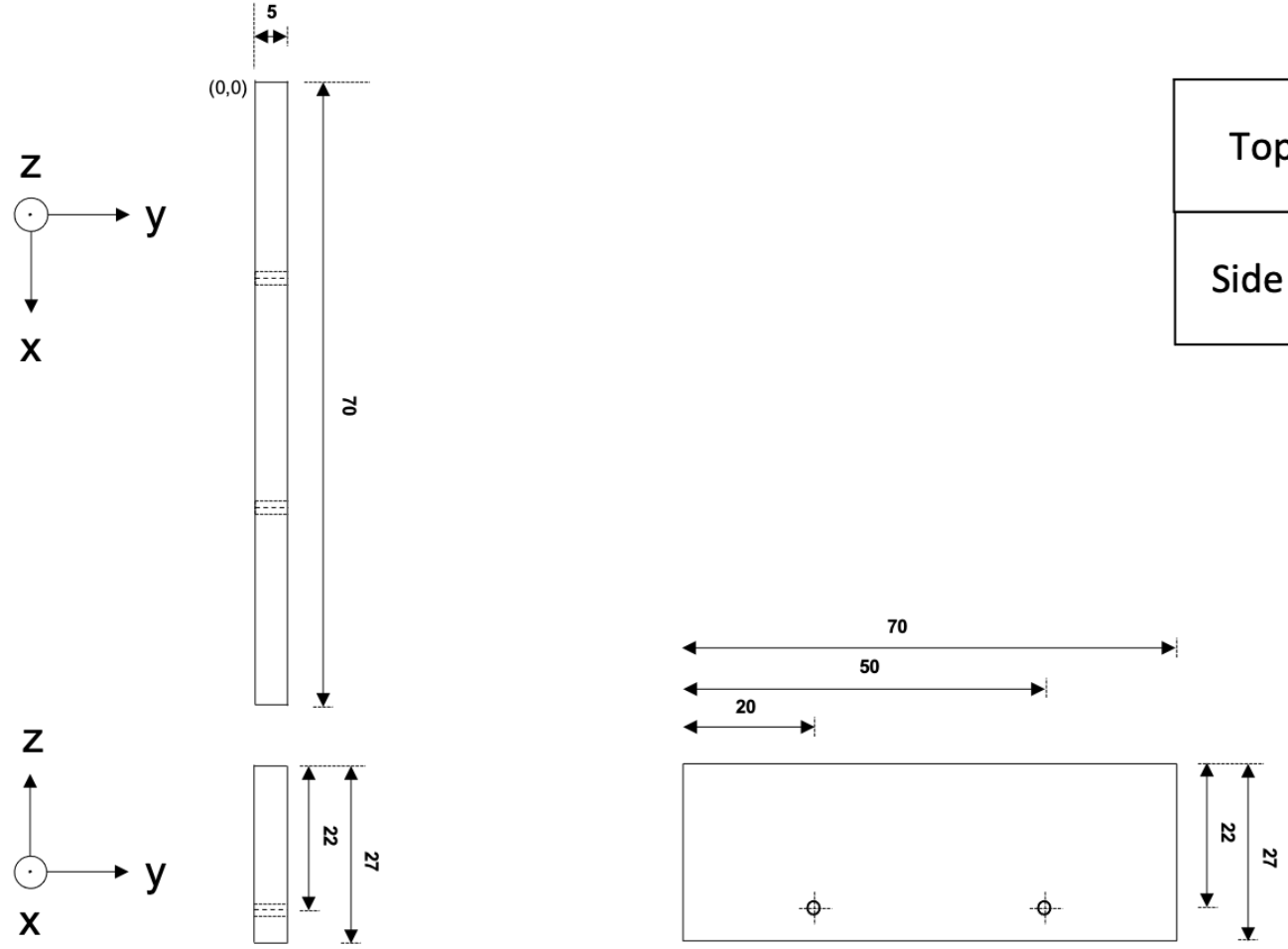






Technical drawings of the second generation SBS mould (part 5/6)

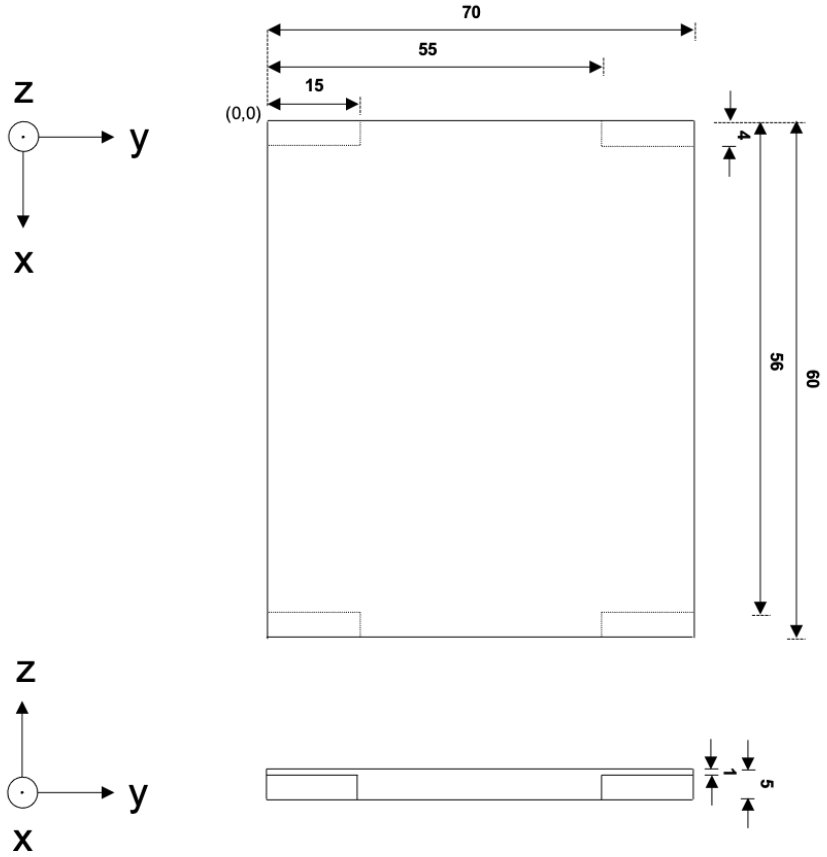
Outline insert **2** **x4**



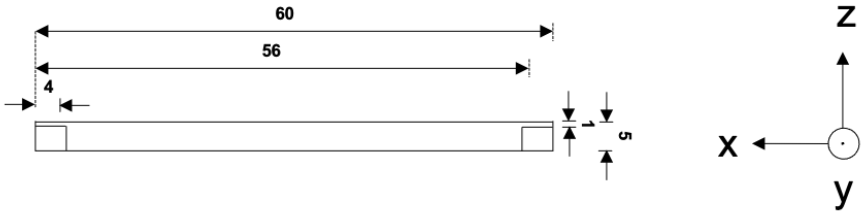
Top view	
Side view 1	Side view 2

Technical drawings of the second generation SBS mould (part 6/6)

Top of the mould **x2**



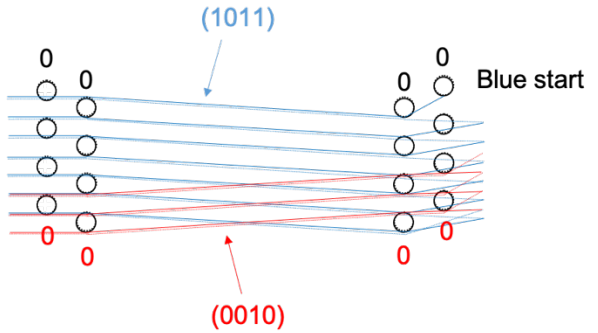
Top view	
Side view 1	Side view 2



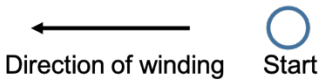
Annex 6: Fibre winding instructions for the second generation SBS mould

Layer 3			Layer 1		
1	0	1	1		
1	1	1	2		
2	1	2	2		
2	2	2	3		
3	2	3	3		
3	3	3	4		
4	3	4	4		
4	4	4	5		
5	4	5	5		
5	5	5	6		
6	5	6	6		
6	6	6	7		
7	6	7	7		
7	7	7	8		
5	6	5	5		
5	5	5	4		
4	5	4	4		
4	4	4	3		
3	4	3	3		
3	3	3	2		
2	3	2	2		
2	2	2	1		
1	2	1	1		
1	1	1	0		

Layer 4			Layer 2		
0	1	1	1		
1	1	2	1		
1	2	2	2		
2	2	3	2		
2	3	3	3		
3	3	4	3		
3	4	4	4		
4	4	5	4		
4	5	5	5		
5	5	6	5		
5	6	6	6		
6	6	7	6		
6	7	7	7		
7	7	8	7		
6	5	5	5		
5	5	4	5		
5	4	4	4		
4	4	3	4		
4	3	3	3		
3	3	2	3		
3	2	2	2		
2	2	1	2		
2	1	1	1		
1	1	0	1		



Black/blue numbering starts from the top row downward.
Red numbering starts from the bottom row upward.



Annex 7: Prediction of unidirectional bundle composites longitudinal tensile strength

Assuming both fibres and matrix behave elastically, fail in a brittle manner and that the matrix has a strain to failure superior to that of the fibres ($\varepsilon_{fu} < \varepsilon_{mu}$). The ultimate strength σ_{1u} of a unidirectional lamina with an applied tensile stress parallel to the fibres can be determined with the following equation [56]:

$$\sigma_{1u} = \sigma_{fu} V_f + \sigma_{mfu}(1 - V_f)$$

where σ_{mfu} is the matrix stress at the onset of fibre cracking ($\varepsilon_1 = \varepsilon_{fu}$) with $\frac{\sigma_{mu} - \sigma_{mfu}}{\varepsilon_{mu} - \varepsilon_{fu}} = \frac{\sigma_{mu}}{\varepsilon_{mu}}$.

When the matrix has a strain to failure inferior to that of the fibres ($\varepsilon_{fu} > \varepsilon_{mu}$), the ultimate strength σ_{1u} is obtained by setting the following equation:

$$\sigma_{1u} = \sigma_{fmu} V_f + \sigma_{mu}(1 - V_f)$$

where σ_{fmu} is the fibre stress at the onset of matrix cracking ($\varepsilon_1 = \varepsilon_{mu}$) with $\frac{\sigma_{fu} - \sigma_{fmu}}{\varepsilon_{fu} - \varepsilon_{mu}} = \frac{\sigma_{fu}}{\varepsilon_{fu}}$.

NB: σ_{fu} and σ_{mu} are the tensile strength of the fibres and the matrix, respectively.

Composite system	Tensile Strength (MPa)		Strain to failure (%)	Fibre volume fraction V_f[‡] (%)	σ_{mfu} (MPa)	σ_{fmu} (MPa)	Predicted composite tensile strength σ_{1u} (MPa)
	From Manufacturer	Measured with SFTT[†]					
AS4	4447	3861 ± 157	1.7	55	19.3	-	2132.2
20ULV	71.2	-	6.3	-			
Quartzel	6000	4151 ± 166	7.7	49	-	3396	1700
20ULV	71.2	-	6.3	-			

[†]SFFT: Single fibre tensile test, measured for a gauge length of 25 mm. [‡]Maximum fibre volume fraction suggested by the ASTM D3039 standard [255].

References

[1] L. Gorbatikh, et al., Hierarchical Lightweight Composite Materials for Structural Applications, MRS Bulletin 41(09) (2016) 672-677. https://doi.org/10.1557/mrs.2016.170

[2] T.M. Herceg, et al., Thermosetting Hierarchical Composites with High Carbon Nanotube Loadings: En Route to High Performance, Compos Sci Technol (2016). https://doi.org/10.1016/j.compscitech.2016.02.015

[3] D.B. Anthony, et al., Continuous Carbon Nanotube Synthesis on Charged Carbon Fibers, Composites Part A: Applied Science and Manufacturing 112 (2018) 525-538. https://doi.org/10.1016/j.compositesa.2018.05.027

[4] B. Liu, et al., Synthesis of Epoxidized Poly(Ester Carbonate)-B-Polyimide-B-Poly(Ester Carbonate): Reactive Single-Walled Carbon Nanotube Dispersants Enable Synergistic Reinforcement around Multi-Walled Nanotube-Grafted Carbon Fibers, Polymer Chemistry 10(11) (2019) 1324-1334. https://doi.org/10.1039/c8py01465e

[5] R.J. Sager, et al., Effect of Carbon Nanotubes on the Interfacial Shear Strength of T650 Carbon Fiber in an Epoxy Matrix, Compos Sci Technol 69(7-8) (2009) 898-904. https://doi.org/10.1016/j.compscitech.2008.12.021

[6] H. Qian, et al., Carbon Nanotube Grafted Carbon Fibres: A Study of Wetting and Fibre Fragmentation, Composites Part A: Applied Science and Manufacturing 41(9) (2010) 1107-1114. https://doi.org/10.1016/j.compositesa.2010.04.004

[7] H. Qian, et al., Carbon Nanotube Grafted Silica Fibres: Characterising the Interface at the Single Fibre Level, Compos Sci Technol 70(2) (2010) 393-399. https://doi.org/10.1016/j.compscitech.2009.11.014

[8] D.B. Anthony, Improved Synthesis of Carbon Nanotube Grafted Carbon Fibre: Towards Continuous Production, Chemical engineering, Imperial College London, 2012.

[9] H.W. Kroto, et al., C60: Buckminsterfullerene, Nature 318(6042) (1985) 162-163. https://doi.org/10.1038/318162a0

[10] V.M.L. L.V. Radushkevich, O Strukture Ugleroda, Obrazujucegosja Pri Termiceskom Razlozenii Okisi Ugleroda Na Zeleznom Kontakte, Zurn Fisic Chim 26 (1952) 88-95.

[11] S. Iijima, Helical Microtubules of Graphitic Carbon, Nature 354(6348) (1991) 56-58. https://doi.org/10.1038/354056a0

[12] V. Popov, Carbon Nanotubes: Properties and Application, Materials Science and Engineering: R: Reports 43(3) (2004) 61-102. https://doi.org/10.1016/j.mser.2003.10.001

[13] J. Che, et al., Thermal Conductivity of Carbon Nanotubes, Nanotechnology 11(2) (2000) 65-69. https://doi.org/10.1088/0957-4484/11/2/305

[14] T.W. Ebbesen, et al., Electrical Conductivity of Individual Carbon Nanotubes, Nature 382(6586) (1996) 54-56. https://doi.org/10.1038/382054a0

[15] M.F. De Volder, et al., Carbon Nanotubes: Present and Future Commercial Applications, Science 339(6119) (2013) 535-9. https://doi.org/10.1126/science.1222453

[16] R.F. Gibson, A Review of Recent Research on Mechanics of Multifunctional Composite Materials and Structures, Composite Structures 92(12) (2010) 2793-2810. https://doi.org/10.1016/j.compstruct.2010.05.003

[17] G. Pandey, E.T. Thostenson, Carbon Nanotube-Based Multifunctional Polymer Nanocomposites, Polymer Reviews 52(3) (2012) 355-416. https://doi.org/10.1080/15583724.2012.703747

[18] T.-W. Chou, et al., An Assessment of the Science and Technology of Carbon Nanotube-Based Fibers and Composites, Compos Sci Technol 70(1) (2010) 1-19. https://doi.org/10.1016/j.compscitech.2009.10.004

[19] J. Sandler, et al., Development of a Dispersion Process for Carbon Nanotubes in an Epoxy Matrix and the Resulting Electrical Properties, Polymer 40(21) (1999) 5967-5971. https://doi.org/10.1016/s0032-3861(99)00166-4

[20] K.S. Novoselov, et al., Electric Field Effect in Atomically Thin Carbon Films, Science 306(5696) (2004) 666-9. https://doi.org/10.1126/science.1102896
[21] E.T. Thostenson, et al., Advances in the Science and Technology of Carbon Nanotubes and Their Composites: A Review, Compos Sci Technol 61(13) (2001) 1899-1912. https://doi.org/Doi 10.1016/S0266-3538(01)00094-X
[22] S.A. Hodge, et al., Unweaving the Rainbow: A Review of the Relationship between Single-Walled Carbon Nanotube Molecular Structures and Their Chemical Reactivity, Chem Soc Rev 41(12) (2012) 4409-29. https://doi.org/10.1039/c2cs15334c
[23] W. Cho, et al., Growth and Characterization of Vertically Aligned Centimeter Long Cnt Arrays, Carbon 72 (2014) 264-273. https://doi.org/10.1016/j.carbon.2014.01.074
[24] Q. Lu, B. Bhattacharya, Effect of Randomly Occurring Stone–Wales Defects on Mechanical Properties of Carbon Nanotubes Using Atomistic Simulation, Nanotechnology 16(4) (2005) 555-566. https://doi.org/10.1088/0957-4484/16/4/037
[25] O. Zhou, et al., Defects in Carbon Nanostructures, Science 263(5154) (1994) 1744-7. https://doi.org/10.1126/science.263.5154.1744
[26] S. Iijima, et al., Pentagons, Heptagons and Negative Curvature in Graphite Microtubule Growth, Nature 356(6372) (1992) 776-778. https://doi.org/10.1038/356776a0
[27] O.L. Min-Feng Yu, Mark J. Dyer, Katerina Moloni, Thomas F. Kelly, Rodney S. Ruoff, Strength and Breaking Mechanism of Multiwalled Carbon Nanotubes under Tensile Load, Science 287(5453) (2000) 637-640.
[28] R.S.R.a.D.C. Lorents, Mechanical and Thermal Properties of Carbon Nanotubes, Carbon 33(7) (1995) 925-930.
[29] R.S. Ruoff, et al., Mechanical Properties of Carbon Nanotubes: Theoretical Predictions and Experimental Measurements, Comptes Rendus Physique 4(9) (2003) 993-1008. https://doi.org/10.1016/j.crhy.2003.08.001
[30] M.F. Yu, et al., Tensile Loading of Ropes of Single Wall Carbon Nanotubes and Their Mechanical Properties, Phys Rev Lett 84(24) (2000) 5552-5. https://doi.org/10.1103/PhysRevLett.84.5552
[31] J. Kong, et al., Synthesis, Integration, and Electrical Properties of Individual Single-Walled Carbon Nanotubes, Applied Physics A: Materials Science & Processing 69(3) (1999) 305-308. https://doi.org/10.1007/s003390051005
[32] Z. Han, A. Fina, Thermal Conductivity of Carbon Nanotubes and Their Polymer Nanocomposites: A Review, Progress in Polymer Science 36(7) (2011) 914-944. https://doi.org/10.1016/j.progpolymsci.2010.11.004
[33] M.F. Yu, et al., Strength and Breaking Mechanism of Multiwalled Carbon Nanotubes under Tensile Load, Science 287(5453) (2000) 637-40. https://doi.org/10.1126/science.287.5453.637
[34] J.-P. Salvetat, et al., Elastic Modulus of Ordered and Disordered Multiwalled Carbon Nanotubes, Advanced Materials 11(2) (1999) 161-165. https://doi.org/10.1002/(sici)1521-4095(199902)11:2<161::Aid-adma161>3.0.Co;2-j
[35] M. Fujii, et al., Measuring the Thermal Conductivity of a Single Carbon Nanotube, Phys Rev Lett 95(6) (2005) 065502. https://doi.org/10.1103/PhysRevLett.95.065502
[36] C. Bower, et al., Plasma-Induced Alignment of Carbon Nanotubes, Applied Physics Letters 77(6) (2000) 830. https://doi.org/10.1063/1.1306658
[37] R.J. Cartwright, et al., The Role of the Sp2:Sp3 Substrate Content in Carbon Supported Nanotube Growth, Carbon 75 (2014) 327-334. https://doi.org/10.1016/j.carbon.2014.04.011
[38] M.A.B. R. T. K. Baker, P. S. Harris, F. S. Feates, and R. J. Waite, Nucleation and Growth of Carbon Deposits from the Nickel Catalyzed Decomposition of Acetylene Journal of Catalysis 26 (1972) 51-62.
[39] N. Yamamoto, et al., High-Yield Growth and Morphology Control of Aligned Carbon Nanotubes on Ceramic Fibers for Multifunctional Enhancement of Structural Composites, Carbon 47(3) (2009) 551-560. https://doi.org/10.1016/j.carbon.2008.10.030

[40] D.L.P. Eric R. Meshot, Sameh Tawfick, Yongyi Zhang, Eric A. Verploegen, A. John Hart, Engineerng Vertically Aligned Carbon Nanotube Growth by Decoupled Thermal Treatment of Precursor and Catalyst, ACS Nano 3(9) (2009) 2477-2486.
[41] A.G.N. Anna Moisala, Esko I Kauppinen, The Role of Metal Nanoparticles in the Catalytic Production of Single-Walled Carbon Nanotubes - a Review, Journal of Physics: Condensed Matter (2003).
[42] S.G.L.v. E.F. Kukovitsky, N.A. Sainov, V.A. Shustov, L.A. Chernozatonskii, Correlation between Metal Catalyst Particle Size and Carbon Nanotube Growth, Chemical Physics Letters 355(5-6) (2002) 497-503.
[43] C.T. Wirth, et al., Diffusion- and Reaction-Limited Growth of Carbon Nanotube Forests, ACS Nano 3(11) (2009) 3560-6. https://doi.org/10.1021/nn900613e
[44] S. Esconjauregui, et al., The Reasons Why Metals Catalyze the Nucleation and Growth of Carbon Nanotubes and Other Carbon Nanomorphologies, Carbon 47(3) (2009) 659-669. https://doi.org/10.1016/j.carbon.2008.10.047
[45] R.T.K. Baker, et al., A Comparison of the Catalytic Influence of Nickel, Iron and Nickel-Iron on the Gasification of Graphite in Various Gaseous Environments, Carbon 23(3) (1985) 245-254. https://doi.org/10.1016/0008-6223(85)90109-5
[46] V. Jourdain, C. Bichara, Current Understanding of the Growth of Carbon Nanotubes in Catalytic Chemical Vapour Deposition, Carbon 58 (2013) 2-39. https://doi.org/10.1016/j.carbon.2013.02.046
[47] R. Abbaschian, et al., Physical Metallurgy Principles Cengage Learning, Stamford, CT (2009).
[48] A. Dupuis, The Catalyst in the Ccvd of Carbon Nanotubes—a Review, Progress in Materials Science 50(8) (2005) 929-961. https://doi.org/10.1016/j.pmatsci.2005.04.003
[49] J. Gavillet, et al., Nucleation and Growth of Single-Walled Nanotubes: The Role of Metallic Catalysts, Journal of Nanoscience and Nanotechnology 4(4) (2004) 346-359. https://doi.org/10.1166/jnn.2004.068
[50] R. Li, et al., Low-Temperature Growth of Carbon Nanotubes Catalyzed by Sodium-Based Ingredients, Angew Chem Int Ed Engl 58(27) (2019) 9204-9209. https://doi.org/10.1002/anie.201902516
[51] M. Kumar, Y. Ando, Chemical Vapor Deposition of Carbon Nanotubes: A Review on Growth Mechanism and Mass Production, J Nanosci Nanotechnol 10(6) (2010) 3739-58. https://doi.org/10.1166/jnn.2010.2939
[52] A. Magrez, et al., Low-Temperature, Highly Efficient Growth of Carbon Nanotubes on Functional Materials by an Oxidative Dehydrogenation Reaction, Acs Nano 4(7) (2010) 3702-3708. https://doi.org/10.1021/nn100279j
[53] N. De Greef, et al., Direct Growth of Carbon Nanotubes on Carbon Fibers: Effect of the Cvd Parameters on the Degradation of Mechanical Properties of Carbon Fibers, Diamond and Related Materials 51 (2015) 39-48. https://doi.org/10.1016/j.diamond.2014.11.002
[54] T. Tomie, et al., Prospective Growth Region for Chemical Vapor Deposition Synthesis of Carbon Nanotube on C–H–O Ternary Diagram, Diamond and Related Materials 19(11) (2010) 1401-1404. https://doi.org/10.1016/j.diamond.2010.08.005
[55] Q. Zhang, et al., Hierarchical Composites of Carbon Nanotubes on Carbon Fiber: Influence of Growth Condition on Fiber Tensile Properties, Compos Sci Technol 69(5) (2009) 594-601. https://doi.org/10.1016/j.compscitech.2008.12.002
[56] D. Hull, T.W. Clyne, An Introduction to Composite Materials, 2nd ed., Cambridge University Press1981.
[57] D.B. Anthony, Continuous Synthesis of Carbon Nanotubes on Carbon Fibr, E-MRS Fall Meeting, Poland, 2014.
[58] P. Morgan, Carbon Fibers and Their Composites, 1st ed., Boca Raton, 2005.
[59] D.D.L. Chung, Carbon Fiber Composites, 1994.

[60] D.D. Edie, The Effect of Processing on the Structure and Properties of Carbon Fibers, Carbon 36(4) (1998) 345-362.
[61] H. Composites, Hextow® Carbon Fiber from Hexcel, 2018.
[62] M. Plastics, Pitch-Based Carbon Fiber, 2018.
[63] M. Sharma, et al., Carbon Fiber Surfaces and Composite Interphases, Compos Sci Technol 102 (2014) 35-50. https://doi.org/10.1016/j.compscitech.2014.07.005
[64] L.T. Drzal, et al., Adhesion of Graphite Fibers to Epoxy Matrices: I. The Role of Fiber Surface Treatment, The Journal of Adhesion 16(1) (2006) 1-30. https://doi.org/10.1080/00218468308074901
[65] F.R. Jones, Interphase in Fiber-Reinforced Composites, (2012). https://doi.org/10.1002/9781118097298.weoc116
[66] F.R. Jones, A Review of Interphase Formation and Design in Fibre-Reinforced Composites, Journal of Adhesion Science and Technology 24(1) (2010) 171-202. https://doi.org/10.1163/016942409x12579497420609
[67] L.T. Drzal, et al., Adhesion of Graphite Fibers to Epoxy Matrices: Ii. The Effect of Fiber Finish, The Journal of Adhesion 16(2) (1983) 133-152. https://doi.org/10.1080/00218468308074911
[68] F.T. Wallenberger, Commercial and Experimental Glass Fibers, (2010) 3-90. https://doi.org/10.1007/978-1-4419-0736-3_1
[69] Y.-W.M. Jang-Kyo Kim, Engineered Interfaces in Fiber Reinforced Composites, 1st ed., Elsevier1998.
[70] D.A. Jesson, J.F. Watts, The Interface and Interphase in Polymer Matrix Composites: Effect on Mechanical Properties and Methods for Identification, Polymer Reviews 52(3) (2012) 321-354. https://doi.org/10.1080/15583724.2012.710288
[71] P.J. Herrera-Franco, L.T. Drzal, Comparison of Methods for the Measurement of Fibre/Matrix Adhesion in Composites, Composites 23(1) (1992) 2-27. https://doi.org/10.1016/0010-4361(92)90282-y
[72] L.H. Sharpe, Some Thoughts About the Mechanical Response of Composites, The Journal of Adhesion 6(1-2) (1974) 15-21. https://doi.org/10.1080/00218467408072236
[73] S. Yumitori, et al., The Role of Sizing Resins in Carbon Fibre-Reinforced Polyethersulfone (Pes), Composites 25(7) (1994) 698-705. https://doi.org/10.1016/0010-4361(94)90204-6
[74] L.T. Drzal, M. Madhukar, Fibre-Matrix Adhesion and Its Relationship to Composite Mechanical Properties, Journal of Materials Science 28(3) (1993) 569-610. https://doi.org/10.1007/bf01151234
[75] V.S. Romanov, et al., Modelling Evidence of Stress Concentration Mitigation at the Micro-Scale in Polymer Composites by the Addition of Carbon Nanotubes, Carbon 82 (2015) 184-194. https://doi.org/10.1016/j.carbon.2014.10.061
[76] S. Pimenta, S.T. Pinho, Hierarchical Scaling Law for the Strength of Composite Fibre Bundles, Journal of the Mechanics and Physics of Solids 61(6) (2013) 1337-1356. https://doi.org/10.1016/j.jmps.2013.02.004
[77] S. Behzadi, et al., Improving the Prediction of Tensile Failure in Unidirectional Fibre Composites by Introducing Matrix Shear Yielding, Compos Sci Technol 69(14) (2009) 2421-2427. https://doi.org/10.1016/j.compscitech.2009.06.010
[78] A.J. Clancy, et al., Metal Mimics: Lightweight, Strong, and Tough Nanocomposites and Nanomaterial Assemblies, ACS Appl Mater Interfaces 12(14) (2020) 15955-15975. https://doi.org/10.1021/acsami.0c01304
[79] A.G. Atkins, Imparting Strength and Toughness to Brittle Composites, Nature 252(5479) (1974) 116-118. https://doi.org/10.1038/252116b0
[80] A.G. Atkins, Intermittent Bonding for High Toughness/ High Strength Composites, Journal of Materials Science 10(5) (1975) 819-832. https://doi.org/10.1007/bf01163077
[81] I. Greenfeld, et al., Intermittent Beading in Fiber Composites, Compos Sci Technol 160 (2018) 21-31. https://doi.org/10.1016/j.compscitech.2018.03.003

[82] J.J. Blaker, et al., Property and Shape Modulation of Carbon Fibers Using Lasers, ACS Appl Mater Interfaces 8(25) (2016) 16351-8. https://doi.org/10.1021/acsami.6b05228
[83] S. Weiner, H.D. Wagner, The Material Bone: Structure-Mechanical Function Relations, Annual Review of Materials Science 28(1) (1998) 271-298. https://doi.org/10.1146/annurev.matsci.28.1.271
[84] U.G. Wegst, et al., Bioinspired Structural Materials, Nat Mater 14(1) (2015) 23-36. https://doi.org/10.1038/nmat4089
[85] Q. Liu, et al., When Does Nanotube Grafting on Fibers Benefit the Strength and Toughness of Composites?, Compos Sci Technol 188 (2020) 107989. https://doi.org/10.1016/j.compscitech.2020.107989
[86] H. Qian, et al., Carbon Nanotube-Based Hierarchical Composites: A Review, Journal of Materials Chemistry 20(23) (2010) 4751. https://doi.org/10.1039/c000041h
[87] G.C. Papanicolaou, et al., The Concept of Boundary Interphase in Composite Mechanics, Colloid and Polymer Science 256(7) (1978) 625-630. https://doi.org/10.1007/bf01784402
[88] Q. Liu, et al., The Interplay between Multiple Toughening Mechanisms in Nanocomposites with Spatially Distributed and Oriented Carbon Nanotubes as Revealed by Dual-Scale Simulations, Carbon 142 (2019) 141-149. https://doi.org/10.1016/j.carbon.2018.10.005
[89] Q. Liu, et al., Spatial Distribution and Orientation of Nanotubes for Suppression of Stress Concentrations Optimized Using Genetic Algorithm and Finite Element Analysis, Materials & Design 158 (2018) 136-146. https://doi.org/10.1016/j.matdes.2018.08.019
[90] N. Domun, et al., Improving the Fracture Toughness and the Strength of Epoxy Using Nanomaterials--a Review of the Current Status, Nanoscale 7(23) (2015) 10294-329. https://doi.org/10.1039/c5nr01354b
[91] G. Lubineau, A. Rahaman, A Review of Strategies for Improving the Degradation Properties of Laminated Continuous-Fiber/Epoxy Composites with Carbon-Based Nanoreinforcements, Carbon 50(7) (2012) 2377-2395. https://doi.org/10.1016/j.carbon.2012.01.059
[92] H. Yao, et al., Optimization of Interfacial Microstructure and Mechanical Properties of Carbon Fiber/Epoxy Composites Via Carbon Nanotube Sizing, Applied Surface Science 347 (2015) 583-590. https://doi.org/10.1016/j.apsusc.2015.04.146
[93] C. Deng, et al., Influence of Carbon Nanotubes Coatings onto Carbon Fiber by Oxidative Treatments Combined with Electrophoretic Deposition on Interfacial Properties of Carbon Fiber Composite, Applied Surface Science 357 (2015) 1274-1280. https://doi.org/10.1016/j.apsusc.2015.09.178
[94] A. Battisti, et al., Single Fiber Push-out Characterization of Interfacial Properties of Hierarchical Cnt-Carbon Fiber Composites Prepared by Electrophoretic Deposition, Compos Sci Technol 95 (2014) 121-127. https://doi.org/10.1016/j.compscitech.2014.02.017
[95] X. Sui, et al., Interfacial and Fatigue-Resistant Synergetic Enhancement of Carbon Fiber/Epoxy Hierarchical Composites Via an Electrophoresis Deposited Carbon Nanotube-Toughened Transition Layer, Composites Part A: Applied Science and Manufacturing 92 (2017) 134-144. https://doi.org/10.1016/j.compositesa.2016.11.004
[96] G. Gong, et al., Development of Electrophoretic Deposition Prototype for Continuous Production of Carbon Nanotube-Modified Carbon Fiber Fabrics Used in High-Performance Multifunctional Composites, Fibers 6(4) (2018) 71. https://doi.org/10.3390/fib6040071
[97] M.S. Zainol Abidin, et al., Enhanced Fracture Toughness of Hierarchical Carbon Nanotube Reinforced Carbon Fibre Epoxy Composites with Engineered Matrix Microstructure, Compos Sci Technol 170 (2019) 85-92. https://doi.org/10.1016/j.compscitech.2018.11.017
[98] W. Bauhofer, J.Z. Kovacs, A Review and Analysis of Electrical Percolation in Carbon Nanotube Polymer Composites, Compos Sci Technol 69(10) (2009) 1486-1498. https://doi.org/10.1016/j.compscitech.2008.06.018

[99] J.N. Coleman, et al., Small but Strong: A Review of the Mechanical Properties of Carbon Nanotube–Polymer Composites, Carbon 44(9) (2006) 1624-1652. https://doi.org/10.1016/j.carbon.2006.02.038
[100] G. Gkikas, et al., Effect of Dispersion Conditions on the Thermo-Mechanical and Toughness Properties of Multi Walled Carbon Nanotubes-Reinforced Epoxy, Composites Part B: Engineering 43(6) (2012) 2697-2705. https://doi.org/10.1016/j.compositesb.2012.01.070
[101] B. Natarajan, et al., Multiscale Metrologies for Process Optimization of Carbon Nanotube Polymer Composites, Carbon 108 (2016) 381-393. https://doi.org/10.1016/j.carbon.2016.07.028
[102] G. Pagani, et al., Competing Mechanisms and Scaling Laws for Carbon Nanotube Scission by Ultrasonication, Proc Natl Acad Sci U S A 109(29) (2012) 11599-604. https://doi.org/10.1073/pnas.1200013109
[103] S.G. Advani, Z. Fan, Dispersion, Bonding and Orientation of Carbon Nanotubes in Polymer Matrices, (2006) 61-98. https://doi.org/10.1142/9789812772473_0002
[104] M.R. Zakaria, et al., Hybrid Carbon Fiber-Carbon Nanotubes Reinforced Polymer Composites: A Review, Composites Part B: Engineering 176 (2019) 107313. https://doi.org/10.1016/j.compositesb.2019.107313
[105] Z. Fan, et al., Experimental Investigation of Dispersion During Flow of Multi-Walled Carbon Nanotube/Polymer Suspension in Fibrous Porous Media, Carbon 42(4) (2004) 871-876. https://doi.org/10.1016/j.carbon.2004.01.067
[106] F.H. Gojny, et al., Influence of Nano-Modification on the Mechanical and Electrical Properties of Conventional Fibre-Reinforced Composites, Composites Part A: Applied Science and Manufacturing 36(11) (2005) 1525-1535. https://doi.org/10.1016/j.compositesa.2005.02.007
[107] L. Ci, J. Bai, The Reinforcement Role of Carbon Nanotubes in Epoxy Composites with Different Matrix Stiffness, Compos Sci Technol 66(3-4) (2006) 599-603. https://doi.org/10.1016/j.compscitech.2005.05.020
[108] J.A. Nairn, S. Hu, The Initiation and Growth of Delaminations Induced by Matrix Microcracks in Laminated Composites, International Journal of Fracture 57(1) (1992) 1-24. https://doi.org/10.1007/bf00013005
[109] S. Ogihara, N. Takeda, Interaction between Transverse Cracks and Delamination During Damage Progress in Cfrp Cross-Ply Laminates, Compos Sci Technol 54(4) (1995) 395-404. https://doi.org/10.1016/0266-3538(95)00084-4
[110] K. Bilge, M. Papila, Interlayer Toughening Mechanisms of Composite Materials, (2015) 263-294. https://doi.org/10.1016/b978-1-78242-279-2.00010-x
[111] L. Tong, et al., 3d Fibre Reinforced Polymer Composites, Elsevier Science, Oxford, 2002.
[112] H. Yao, et al., Effect of Polymer-Grafted Carbon Nanofibers and Nanotubes on the Interlaminar Shear Strength and Flexural Strength of Carbon Fiber/Epoxy Multiscale Composites, Composite Structures 195 (2018) 288-296. https://doi.org/10.1016/j.compstruct.2018.04.082
[113] F.L. Shan, et al., Effect of Deposited Carbon Nanotubes on Interlaminar Properties of Carbon Fiber-Reinforced Epoxy Composites Using a Developed Spraying Processing, Polymer Composites 34(1) (2013) 41-50. https://doi.org/10.1002/pc.22375
[114] J. Vázquez-Moreno, et al., Preparation and Mechanical Properties of Graphene/Carbon Fiber-Reinforced Hierarchical Polymer Composites, Journal of Composites Science 3(1) (2019) 30. https://doi.org/10.3390/jcs3010030
[115] L.L.a.L.L. Shen, Influence of Cnt Buckypaper on the Interlaminar Shear Strength of Laminates, 20th International Conference on Composite Materials, Copenhagen, 2015.
[116] S.U. Khan, J.-K. Kim, Improved Interlaminar Shear Properties of Multiscale Carbon Fiber Composites with Bucky Paper Interleaves Made from Carbon Nanofibers, Carbon 50(14) (2012) 5265-5277. https://doi.org/10.1016/j.carbon.2012.07.011

[117] X. Ni, et al., Static and Fatigue Interlaminar Shear Reinforcement in Aligned Carbon Nanotube-Reinforced Hierarchical Advanced Composites, Composites Part A: Applied Science and Manufacturing 120 (2019) 106-115. https://doi.org/10.1016/j.compositesa.2019.02.023
[118] R. Guzman de Villoria, et al., In-Plane Strength Enhancement of Laminated Composites Via Aligned Carbon Nanotube Interlaminar Reinforcement, Compos Sci Technol 133 (2016) 33-39. https://doi.org/10.1016/j.compscitech.2016.07.006
[119] E. Kalfon-Cohen, et al., Synergetic Effects of Thin Plies and Aligned Carbon Nanotube Interlaminar Reinforcement in Composite Laminates, Compos Sci Technol 166 (2018) 160-168. https://doi.org/10.1016/j.compscitech.2018.01.007
[120] B.L. Wardle, Nanocomposites and Hierarchical Nanoengineered Mechanical and Multifunctional Performance, 8th International Conference on Carbon Nanoparticle based Composites, London, 2019.
[121] S. Singh, I.K. Partridge, Mixed-Mode Fracture in an Interleaved Carbon-Fibre/Epoxy Composite, Compos Sci Technol 55(4) (1995) 319-327. https://doi.org/10.1016/0266-3538(95)00062-3
[122] H. Qian, et al., Mapping Local Microstructure and Mechanical Performance around Carbon Nanotube Grafted Silica Fibres: Methodologies for Hierarchical Composites, Nanoscale 3(11) (2011) 4759-67. https://doi.org/10.1039/c1nr10497g
[123] A.Y. Matveeva, et al., Debonding at the Fiber/Matrix Interface in Carbon Nanotube Reinforced Composites: Modelling Investigation, Computational Materials Science 159 (2019) 412-419. https://doi.org/10.1016/j.commatsci.2018.10.031
[124] E.T.T. E. Bekyarova, A. Yu, H. Kim, J. Gao, J. Tang, H. T. Hahn, T.-W. Chou, M. E. Itkis, R. C. Haddon, Multiscale Carbon Nanotube-Carbon Fiber Reinforcement for Advanced Epoxy Composites, Langmuir 23(7) (2007) 3970-3974.
[125] Q. An, et al., Electrophoretic Deposition of Carbon Nanotubes onto Carbon-Fiber Fabric for Production of Carbon/Epoxy Composites with Improved Mechanical Properties, Carbon 50(11) (2012) 4130-4143. https://doi.org/10.1016/j.carbon.2012.04.061
[126] J. Jiang, et al., Influence of Carbon Nanotube Coatings on Carbon Fiber by Ultrasonically Assisted Electrophoretic Deposition on Its Composite Interfacial Property, Polymers (Basel) 8(8) (2016). https://doi.org/10.3390/polym8080302
[127] M. Zhao, et al., Layer-by-Layer Grafting Cnts onto Carbon Fibers Surface for Enhancing the Interfacial Properties of Epoxy Resin Composites, Compos Sci Technol 154 (2018) 28-36. https://doi.org/10.1016/j.compscitech.2017.11.002
[128] Y. Deng, et al., Effects of Grafting Strength and Density on Interfacial Shear Strength of Carbon Nanotube Grafted Carbon Fibre Reinforced Composites, Compos Sci Technol 168 (2018) 195-202. https://doi.org/10.1016/j.compscitech.2018.09.025
[129] Y.-T. Liu, et al., Grafting of Carbon Nanotubes onto Carbon Fiber Surfaces by Step-Wise Reduction of in-Situ Generated Diazonium Salts for Enhancing Carbon/Epoxy Interfaces, Materials Letters 134 (2014) 75-79. https://doi.org/10.1016/j.matlet.2014.07.053
[130] R.L. Zhang, et al., Polyhedral Oligomeric Silsesquioxanes/Carbon Nanotube/Carbon Fiber Multiscale Composite: Influence of a Novel Hierarchical Reinforcement on the Interfacial Properties, Applied Surface Science 353 (2015) 224-231. https://doi.org/10.1016/j.apsusc.2015.06.156
[131] W. Zhang, et al., Improving Interfacial and Mechanical Properties of Carbon Nanotube-Sized Carbon Fiber/Epoxy Composites, Carbon 145 (2019) 629-639. https://doi.org/10.1016/j.carbon.2019.01.063
[132] W. Zhang, et al., Improved Interfacial Properties of Carbon Fiber Composites by Building Stress Transition Layer with Carbon Nanotubes, Advances in Polymer Technology 37(7) (2018) 2510-2519. https://doi.org/10.1002/adv.21926
[133] Z.-G. Zhao, et al., The Growth of Multi-Walled Carbon Nanotubes with Different Morphologies on Carbon Fibers, Carbon 43(3) (2005) 663-665. https://doi.org/10.1016/j.carbon.2004.10.013

[134] D.E. Boura O, Aggelis D, Barkoula N-M, Gournis D, Paipetis AS, Carbon Nanotube Growth on High Modulus Carbon Fibres and Interfacial Characterization, 14th European conference on composite materials, Budapest, Hungary, 2010, p. 10.
[135] R. Li, et al., Hierarchical Carbon Nanotube Carbon Fiber Unidirectional Composites with Preserved Tensile and Interfacial Properties, Compos Sci Technol 117 (2015) 139-145. https://doi.org/10.1016/j.compscitech.2015.04.014
[136] G. Lee, et al., Low-Temperature Grafting of Carbon Nanotubes on Carbon Fibers Using a Bimetallic Floating Catalyst, Diamond and Related Materials 68 (2016) 118-126. https://doi.org/10.1016/j.diamond.2016.06.012
[137] O. Shishkina, et al., Stress Distribution around a Broken Carbon Fibre and How It Is Affected by Carbon Nanotubes in the Interface Region, Composite Interfaces 26(6) (2018) 507-524. https://doi.org/10.1080/09276440.2018.1511108
[138] R. Sharma, et al., Dynamic Observations of the Effect of Pressure and Temperature Conditions on the Selective Synthesis of Carbon Nanotubes, Nanotechnology 18(12) (2007) 125602. https://doi.org/10.1088/0957-4484/18/12/125602
[139] F. Zhao, et al., Formation of a Carbon Fiber/Polyhedral Oligomeric Silsesquioxane/Carbon Nanotube Hybrid Reinforcement and Its Effect on the Interfacial Properties of Carbon Fiber/Epoxy Composites, Carbon 49(8) (2011) 2624-2632. https://doi.org/10.1016/j.carbon.2011.02.026
[140] X. He, et al., Direct Measurement of Grafting Strength between an Individual Carbon Nanotube and a Carbon Fiber, Carbon 50(10) (2012) 3782-3788. https://doi.org/10.1016/j.carbon.2012.03.053
[141] C. Wang, et al., The Role of Grafting Force and Surface Wettability in Interfacial Enhancement of Carbon Nanotube/Carbon Fiber Hierarchical Composites, Carbon 69 (2014) 239-246. https://doi.org/10.1016/j.carbon.2013.12.020
[142] M.S. Islam, et al., Grafting Carbon Nanotubes Directly onto Carbon Fibers for Superior Mechanical Stability: Towards Next Generation Aerospace Composites and Energy Storage Applications, Carbon 96 (2016) 701-710. https://doi.org/10.1016/j.carbon.2015.10.002
[143] J. Karger-Kocsis, et al., All-Carbon Multi-Scale and Hierarchical Fibers and Related Structural Composites: A Review, Compos Sci Technol 186 (2020) 107932. https://doi.org/10.1016/j.compscitech.2019.107932
[144] H. Qian, et al., Hierarchical Composites Reinforced with Carbon Nanotube Grafted Fibers: The Potential Assessed at the Single Fiber Level, Chemistry of Materials 20(5) (2008) 1862-1869. https://doi.org/10.1021/cm702782j
[145] A. Hampe, et al., An Advanced Equipment for Single-Fibre Pull-out Test Designed to Monitor the Fracture Process, Composites 26(1) (1995) 40-46. https://doi.org/10.1016/0010-4361(94)P3628-E
[146] X. Yao, et al., Comparison of Carbon Nanotubes and Graphene Oxide Coated Carbon Fiber for Improving the Interfacial Properties of Carbon Fiber/Epoxy Composites, Composites Part B: Engineering 132 (2018) 170-177. https://doi.org/10.1016/j.compositesb.2017.09.012
[147] Z. Zhao, et al., Mechanical, Thermal and Interfacial Performances of Carbon Fiber Reinforced Composites Flavored by Carbon Nanotube in Matrix/Interface, Composite Structures 159 (2017) 761-772. https://doi.org/10.1016/j.compstruct.2016.10.022
[148] V. Rao, et al., A Direct Comparison of the Fragmentation Test and the Microbond Pull-out Test for Determining the Interfacial Shear Strength, The Journal of Adhesion 34(1-4) (1991) 65-77. https://doi.org/10.1080/00218469108026506
[149] A. Kelly, C. Zweben, Poisson Contraction in Aligned Fibre Composites Showing Pull-Out, Journal of Materials Science 11(3) (1976) 582-586. https://doi.org/10.1007/bf00540944
[150] L. Zhang, et al., Carbon Nanotube-Grafted Carbon Fiber Polymer Composites: Damage Characterization on the Micro-Scale, Composites Part B: Engineering 126 (2017) 202-210. https://doi.org/10.1016/j.compositesb.2017.06.004

[151] N.A. Siddiqui, et al., Tensile Strength of Glass Fibres with Carbon Nanotube–Epoxy Nanocomposite Coating, Composites Part A: Applied Science and Manufacturing 40(10) (2009) 1606-1614. https://doi.org/10.1016/j.compositesa.2009.07.005
[152] H.S. Bedi, et al., Quantitative Determination of Size and Properties of Interphases in Carbon Nanotube-Based Multiscale Composites, Carbon 132 (2018) 181-190. https://doi.org/10.1016/j.carbon.2018.02.059
[153] J.D.H. Hughes, The Carbon Fibre/Epoxy Interface—a Review, Compos Sci Technol 41(1) (1991) 13-45. https://doi.org/10.1016/0266-3538(91)90050-y
[154] M. Li, et al., Interfacial Improvement of Carbon Fiber/Epoxy Composites Using a Simple Process for Depositing Commercially Functionalized Carbon Nanotubes on the Fibers, Carbon 52 (2013) 109-121. https://doi.org/10.1016/j.carbon.2012.09.011
[155] L. Yang, et al., Interfacial Shear Behavior of 3d Composites Reinforced with Cnt-Grafted Carbon Fibers, Composites Part A: Applied Science and Manufacturing 43(8) (2012) 1410-1418. https://doi.org/10.1016/j.compositesa.2011.11.012
[156] J.D. Schaefer, et al., Effects of Electrophoretically Deposited Carbon Nanofibers on the Interface of Single Carbon Fibers Embedded in Epoxy Matrix, Carbon 49(8) (2011) 2750-2759. https://doi.org/10.1016/j.carbon.2011.02.070
[157] Q. Li, et al., Interfacial Characterization and Reinforcing Mechanism of Novel Carbon Nanotube – Carbon Fibre Hybrid Composites, Carbon 109 (2016) 74-86. https://doi.org/10.1016/j.carbon.2016.07.058
[158] K. Tsirka, et al., Optimal Synergy between Micro and Nano Scale: Hierarchical All Carbon Composite Fibers for Enhanced Stiffness, Interfacial Shear Strength and Raman Strain Sensing, Compos Sci Technol 165 (2018) 240-249. https://doi.org/10.1016/j.compscitech.2018.07.003
[159] V. Lutz, et al., Ex-Pan Carbon Fibers Vs Carbon Nanotubes Fibers: From Conventional Epoxy Based Composites to Multiscale Composites, European Polymer Journal 106 (2018) 9-18. https://doi.org/10.1016/j.eurpolymj.2018.06.023
[160] S. Aziz, et al., Experimental Evaluation of the Interfacial Properties of Carbon Nanotube Coated Carbon Fiber Reinforced Hybrid Composites, Polymer Composites 36(10) (2015) 1941-1950. https://doi.org/10.1002/pc.23103
[161] K.M. Kim T, Natori J, Kawada H, Fabrication of Cnts Grafted Hierarchical Multiscale Composite and Evaluation of Its Mechanical Properties, ECCM16 – 16th European conference on composite materials, Seville, Spain, 2014, p. 8.
[162] N. Lachman, et al., Fracture Behavior of Carbon Nanotube/Carbon Microfiber Hybrid Polymer Composites, Journal of Materials Science 48(16) (2013) 5590-5595. https://doi.org/10.1007/s10853-013-7353-2
[163] K.J. Kim, et al., Improved Tensile Strength of Carbon Fibers Undergoing Catalytic Growth of Carbon Nanotubes on Their Surface, Carbon 54 (2013) 258-267. https://doi.org/10.1016/j.carbon.2012.11.037
[164] O. Boura, et al., Carbon Nanotube Growth on High Modulus Carbon Fibres: Morphological and Interfacial Characterization, Surface and Interface Analysis 45(9) (2013) 1372-1381. https://doi.org/10.1002/sia.5292
[165] A.Y. Tolbin, et al., Preparation of Bicomponent Fibers by Surface Modification with Fibrous Carbon Nanostructure Filler, Fibre Chemistry 44(4) (2012) 252-258. https://doi.org/10.1007/s10692-012-9441-5
[166] N. Lachman, et al., Application of Continuously-Monitored Single Fiber Fragmentation Tests to Carbon Nanotube/Carbon Microfiber Hybrid Composites, Compos Sci Technol 72(14) (2012) 1711-1717. https://doi.org/10.1016/j.compscitech.2012.06.004
[167] P. Lv, et al., Increasing the Interfacial Strength in Carbon Fiber/Epoxy Composites by Controlling the Orientation and Length of Carbon Nanotubes Grown on the Fibers, Carbon 49(14) (2011) 4665-4673. https://doi.org/10.1016/j.carbon.2011.06.064

[168] E.T. Thostenson, et al., Carbon Nanotube/Carbon Fiber Hybrid Multiscale Composites, Journal of Applied Physics 91(9) (2002) 6034-6037. https://doi.org/10.1063/1.1466880
[169] H. Zheng, et al., The Direct Architecture of Carbon Fiber-Carbon Nanofiber Hierarchical Reinforcements for Superior Interfacial Properties of Cf/Epoxy Composites, Polymers for Advanced Technologies 30(3) (2019) 620-630. https://doi.org/10.1002/pat.4498
[170] Y. Wang, et al., Preparation and Properties of Carbon Nanotube/Carbon Fiber Hybrid Reinforcement by a Two-Step Aryl Diazonium Reaction, RSC Advances 5(55) (2015) 44492-44498. https://doi.org/10.1039/c5ra04117a
[171] Y. Li, et al., Tuning the Interfacial Property of Hierarchical Composites by Changing the Grafting Density of Carbon Nanotube Using 1,3-Propodiamine, Compos Sci Technol 85 (2013) 36-42. https://doi.org/10.1016/j.compscitech.2013.05.016
[172] Q. Peng, et al., Chemically and Uniformly Grafting Carbon Nanotubes onto Carbon Fibers by Poly(Amidoamine) for Enhancing Interfacial Strength in Carbon Fiber Composites, Journal of Materials Chemistry 22(13) (2012) 5928. https://doi.org/10.1039/c2jm16723a
[173] L. Mei, et al., Multiscale Carbon Nanotube-Carbon Fiber Reinforcement for Advanced Epoxy Composites with High Interfacial Strength, Polymers and Polymer Composites 19(2-3) (2011) 107-112. https://doi.org/10.1177/0967391111019002-309
[174] F.-H. Zhang, et al., Interfacial Shearing Strength and Reinforcing Mechanisms of an Epoxy Composite Reinforced Using a Carbon Nanotube/Carbon Fiber Hybrid, Journal of Materials Science 44(13) (2009) 3574-3577. https://doi.org/10.1007/s10853-009-3484-x
[175] L. Li, et al., Remarkable Improvement in Interfacial Shear Strength of Carbon Fiber/Epoxy Composite by Large-Scare Sizing with Epoxy Sizing Agent Containing Amine-Treated Mwcnts, Polymer Composites 39(8) (2018) 2734-2742. https://doi.org/10.1002/pc.24263
[176] B. Yu, et al., Enhanced Interphase between Epoxy Matrix and Carbon Fiber with Carbon Nanotube-Modified Silane Coating, Compos Sci Technol 99 (2014) 131-140. https://doi.org/10.1016/j.compscitech.2014.05.021
[177] W. Liu, et al., Fabrication of Carbon Nanotubes/Carbon Fiber Hybrid Fiber in Industrial Scale by Sizing Process, Applied Surface Science 284 (2013) 914-920. https://doi.org/10.1016/j.apsusc.2013.08.045
[178] E. Moaseri, et al., Fabrication of Multi-Walled Carbon Nanotube–Carbon Fiber Hybrid Material Via Electrophoretic Deposition Followed by Pyrolysis Process, Composites Part A: Applied Science and Manufacturing 60 (2014) 8-14. https://doi.org/10.1016/j.compositesa.2014.01.009
[179] J. Guo, et al., Effect of Electrophoretically Deposited Carbon Nanotubes on the Interface of Carbon Fiber Reinforced Epoxy Composite, Journal of Materials Science 47(6) (2011) 2831-2836. https://doi.org/10.1007/s10853-011-6112-5
[180] X. Du, et al., Improving the Electrical Conductivity and Interface Properties of Carbon Fiber/Epoxy Composites by Low Temperature Flame Growth of Carbon Nanotubes, RSC Advances 6(54) (2016) 48896-48904. https://doi.org/10.1039/c6ra09839h
[181] G. Lee, et al., Improved Tensile Strength of Carbon Nanotube-Grafted Carbon Fiber Reinforced Composites, Composite Structures 220 (2019) 580-591. https://doi.org/10.1016/j.compstruct.2019.04.037
[182] H.S. Bedi, et al., Interfacial Shear Strength of Carbon Nanotubes Based Hybrid Composites: Effect of Loading Rate, Frattura ed Integrità Strutturale 13(48) (2019) 571-576. https://doi.org/10.3221/igf-esis.48.55
[183] L. Zheng, et al., Scalable Manufacturing of Carbon Nanotubes on Continuous Carbon Fibers Surface from Chemical Vapor Deposition, Vacuum 152 (2018) 84-90. https://doi.org/10.1016/j.vacuum.2018.03.011
[184] C. Ren, et al., Analyses of Reinforcing Effects of in Situ Grown Cnts on Carbon Fibre Fabric/Epoxy Composites at Micro- and Macroscale, Micro & Nano Letters 7(3) (2012) 240. https://doi.org/10.1049/mnl.2012.0065

[185] F. An, et al., Preparation and Characterization of Carbon Nanotube-Hybridized Carbon Fiber to Reinforce Epoxy Composite, Materials & Design 33 (2012) 197-202. https://doi.org/10.1016/j.matdes.2011.07.027
[186] F. An, et al., Preparation of Vertically Aligned Carbon Nanotube Arrays Grown onto Carbon Fiber Fabric and Evaluating Its Wettability on Effect of Composite, Applied Surface Science 258(3) (2011) 1069-1076. https://doi.org/10.1016/j.apsusc.2011.09.003
[187] T.R. Pozegic, et al., Development of Sizing-Free Multi-Functional Carbon Fibre Nanocomposites, Composites Part A: Applied Science and Manufacturing 90 (2016) 306-319. https://doi.org/10.1016/j.compositesa.2016.07.012
[188] S.Y. Jin, et al., Hybrid Carbon Fibre–Carbon Nanotube Composite Interfaces, Compos Sci Technol 95 (2014) 114-120. https://doi.org/10.1016/j.compscitech.2014.02.015
[189] M. Park, et al., Strain-Dependent Electrical Resistance of Multi-Walled Carbon Nanotube/Polymer Composite Films, Nanotechnology 19(5) (2008) 055705. https://doi.org/10.1088/0957-4484/19/05/055705
[190] N. Hu, et al., Tunneling Effect in a Polymer/Carbon Nanotube Nanocomposite Strain Sensor, Acta Materialia 56(13) (2008) 2929-2936. https://doi.org/10.1016/j.actamat.2008.02.030
[191] T.W. Tombler, et al., Reversible Electromechanical Characteristics of Carbon Nanotubes under Local-Probe Manipulation, Nature 405(6788) (2000) 769-72. https://doi.org/10.1038/35015519
[192] J.d.J. Ku-Herrera, et al., Selective Damage Sensing in Multiscale Hierarchical Composites by Tailoring the Location of Carbon Nanotubes, Journal of Intelligent Material Systems and Structures 29(4) (2017) 553-562. https://doi.org/10.1177/1045389x17711790
[193] B. Yang, et al., Simultaneously Enhancing the Ifss and Monitoring the Interfacial Stress State of Gf/Epoxy Composites Via Building in the Mwcnt Interface Sensor, Composites Part A: Applied Science and Manufacturing 112 (2018) 161-167. https://doi.org/10.1016/j.compositesa.2018.06.006
[194] S.-l. Gao, et al., Glass Fibers with Carbon Nanotube Networks as Multifunctional Sensors, Advanced Functional Materials 20(12) (2010) 1885-1893. https://doi.org/10.1002/adfm.201000283
[195] A. Goldel, et al., Selective Localization and Migration of Multiwalled Carbon Nanotubes in Blends of Polycarbonate and Poly(Styrene-Acrylonitrile), Macromol Rapid Commun 30(6) (2009) 423-9. https://doi.org/10.1002/marc.200800549
[196] Alamusi, et al., Piezoresistive Strain Sensors Made from Carbon Nanotubes Based Polymer Nanocomposites, Sensors (Basel) 11(11) (2011) 10691-723. https://doi.org/10.3390/s111110691
[197] N. Hu, et al., Investigation on Sensitivity of a Polymer/Carbon Nanotube Composite Strain Sensor, Carbon 48(3) (2010) 680-687. https://doi.org/10.1016/j.carbon.2009.10.012
[198] E.T. Thostenson, T.W. Chou, Carbon Nanotube Networks: Sensing of Distributed Strain and Damage for Life Prediction and Self Healing, Advanced Materials 18(21) (2006) 2837-2841. https://doi.org/10.1002/adma.200600977
[199] E.T. Thostenson, et al., Electrical Anisotropy in Multiscale Nanotube/Fiber Hybrid Composites, Applied Physics Letters 95(7) (2009) 073111. https://doi.org/10.1063/1.3202788
[200] G.J. Gallo, E.T. Thostenson, Electrical Characterization and Modeling of Carbon Nanotube and Carbon Fiber Self-Sensing Composites for Enhanced Sensing of Microcracks, Materials Today Communications 3 (2015) 17-26. https://doi.org/10.1016/j.mtcomm.2015.01.009
[201] E.T. Thostenson, T.W. Chou, Real-Time in Situ Sensing of Damage Evolution in Advanced Fiber Composites Using Carbon Nanotube Networks, Nanotechnology 19(21) (2008) 215713. https://doi.org/10.1088/0957-4484/19/21/215713
[202] L. Böger, et al., Load and Health Monitoring in Glass Fibre Reinforced Composites with an Electrically Conductive Nanocomposite Epoxy Matrix, Compos Sci Technol 68(7-8) (2008) 1886-1894. https://doi.org/10.1016/j.compscitech.2008.01.001

[203] D. He, et al., Design of Electrically Conductive Structural Composites by Modulating Aligned Cvd-Grown Carbon Nanotube Length on Glass Fibers, ACS Appl Mater Interfaces 9(3) (2017) 2948-2958. https://doi.org/10.1021/acsami.6b13397
[204] Q. An, et al., Tailored Glass Fiber Interphases Via Electrophoretic Deposition of Carbon Nanotubes: Fiber and Interphase Characterization, Compos Sci Technol 166 (2018) 131-139. https://doi.org/10.1016/j.compscitech.2018.01.003
[205] S. Tamrakar, et al., Tailoring Interfacial Properties by Controlling Carbon Nanotube Coating Thickness on Glass Fibers Using Electrophoretic Deposition, ACS Appl Mater Interfaces 8(2) (2016) 1501-10. https://doi.org/10.1021/acsami.5b10903
[206] J. Zhang, et al., Functional Interphases with Multi-Walled Carbon Nanotubes in Glass Fibre/Epoxy Composites, Carbon 48(8) (2010) 2273-2281. https://doi.org/10.1016/j.carbon.2010.03.001
[207] L. Tzounis, et al., The Interphase Microstructure and Electrical Properties of Glass Fibers Covalently and Non-Covalently Bonded with Multiwall Carbon Nanotubes, Carbon 73 (2014) 310-324. https://doi.org/10.1016/j.carbon.2014.02.069
[208] A. Godara, et al., Interfacial Shear Strength of a Glass Fiber/Epoxy Bonding in Composites Modified with Carbon Nanotubes, Compos Sci Technol 70(9) (2010) 1346-1352. https://doi.org/10.1016/j.compscitech.2010.04.010
[209] Q. An, et al., Hierarchical Composite Structures Prepared by Electrophoretic Deposition of Carbon Nanotubes onto Glass Fibers, ACS Appl Mater Interfaces 5(6) (2013) 2022-32. https://doi.org/10.1021/am3028734
[210] J.A. Rodríguez-González, et al., Piezoresistive Response of Spray-Coated Multiwalled Carbon Nanotube/Glass Fiber/Epoxy Composites under Flexural Loading, Fibers and Polymers 20(8) (2019) 1673-1683. https://doi.org/10.1007/s12221-019-8711-8
[211] D.F. Adams, J.M. Busse, Suggested Modifications of the Short Beam Shear Test Method, Proceedings of the 49th International SAMPE Symposium, Long Beach, California, 2004.
[212] J.M. Whitney, C.E. Browning, On Short-Beam Shear Tests for Composite Materials, Experimental Mechanics 25(3) (1985) 294-300. https://doi.org/10.1007/bf02325100
[213] R. Li, et al., Woven Hierarchical Aerospace Composite Laminates with Aligned Carbon Nanotube Bulk Reinforcement, (2016). https://doi.org/10.2514/6.2016-0149
[214] R. Li, et al., Unidirectional Hierarchical Laminates with Interlaminar Shear Reinforcement, (2019). https://doi.org/10.2514/6.2019-1464
[215] J.L. Abot, et al., Novel Carbon Nanotube Array-Reinforced Laminated Composite Materials with Higher Interlaminar Elastic Properties, Compos Sci Technol 68(13) (2008) 2755-2760. https://doi.org/10.1016/j.compscitech.2008.05.023
[216] K. Adhikari, et al., Effect of the Localized Application of Swnt Modified Epoxy on the Interlaminar Shear Strength of Carbon Fiber Laminates, (2006). https://doi.org/10.2514/6.2006-1855
[217] V.K. Srivastava, et al., Effect of Nanomaterial on Mode I and Mode Ii Interlaminar Fracture Toughness of Woven Carbon Fabric Reinforced Polymer Composites, Engineering Fracture Mechanics 180 (2017) 73-86. https://doi.org/10.1016/j.engfracmech.2017.05.030
[218] M. Fogel, et al., Manufacturing of Conductive Structural Composites through Spraying of Cnts/Epoxy Dispersions on Dry Carbon Fiber Plies, Composites Part A: Applied Science and Manufacturing 100 (2017) 40-47. https://doi.org/10.1016/j.compositesa.2017.04.020
[219] M. Tarfaoui, et al., Mechanical Properties of Carbon Nanotubes Based Polymer Composites, Composites Part B: Engineering 103 (2016) 113-121. https://doi.org/10.1016/j.compositesb.2016.08.016
[220] M. Siegfried, et al., Impact and Residual after Impact Properties of Carbon Fiber/Epoxy Composites Modified with Carbon Nanotubes, Composite Structures 111 (2014) 488-496. https://doi.org/10.1016/j.compstruct.2014.01.035

[221] M.K. Hossain, et al., Improved Thermomechanical Properties of Carbon Fiber Reinforced Epoxy Composite Using Amino Functionalized Xdcnt, Journal of Applied Polymer Science 131(17) (2014) n/a-n/a. https://doi.org/10.1002/app.40709
[222] C.Y.L. Naveed A. Siddiqui, Youshan Yu, Peng Cheng Ma, Jang-Kyo Kim, Prepregging and Mechanical Properties of Cnt-Cfrp Hybrid Composites, 17th Int. Conf. Compos. Mater., 2009.
[223] A. Godara, et al., Influence of Carbon Nanotube Reinforcement on the Processing and the Mechanical Behaviour of Carbon Fiber/Epoxy Composites, Carbon 47(12) (2009) 2914-2923. https://doi.org/10.1016/j.carbon.2009.06.039
[224] S.-B. Lee, et al., Processing and Characterization of Multi-Scale Hybrid Composites Reinforced with Nanoscale Carbon Reinforcements and Carbon Fibers, Composites Part A: Applied Science and Manufacturing 42(4) (2011) 337-344. https://doi.org/10.1016/j.compositesa.2010.10.016
[225] A.J. Rodriguez, et al., Mechanical Properties of Carbon Nanofiber/Fiber-Reinforced Hierarchical Polymer Composites Manufactured with Multiscale-Reinforcement Fabrics, Carbon 49(3) (2011) 937-948. https://doi.org/10.1016/j.carbon.2010.10.057
[226] C. Fang, et al., Interlaminar Improvement of Carbon Fiber/Epoxy Composites Via Depositing Mixture of Carbon Nanotubes and Sizing Agent, Applied Surface Science 321 (2014) 1-9. https://doi.org/10.1016/j.apsusc.2014.09.170
[227] S. Khan, et al., Augmenting Mode-Ii Fracture Toughness of Carbon Fiber/Epoxy Composites through Carbon Nanotube Grafting, Engineering Fracture Mechanics 204 (2018) 211-220. https://doi.org/10.1016/j.engfracmech.2018.10.014
[228] Y. Wang, et al., High Interlaminar Shear Strength Enhancement of Carbon Fiber/Epoxy Composite through Fiber-and Matrix-Anchored Carbon Nanotube Networks, ACS Appl. Mater. Interfaces 9(10) (2017) 8960-8966.
[229] B.L.W. Anastasios John Hart, Enrique J. Garcia, Alexander H. Slocum, Continuous Process for the Production of Nanostructures Including Nanotubes, Massachusetts Institute of Technology, Cambridge, MA (US), 2007.
[230] B.A.G.S.M.S.P.G.T.M.Q.G.L.S.G.M.A.G.G.E. [GB], Production of Composite Material, IMPERIAL INNOVATIONS LIMITED, GB, 2010.
[231] K. Tao, et al., Effects of Carbon Nanotube Fillers on the Curing Processes of Epoxy Resin-Based Composites, Journal of Applied Polymer Science 102(6) (2006) 5248-5254. https://doi.org/10.1002/app.24773
[232] J. Sumfleth, et al., Comparison of Rheological and Electrical Percolation Phenomena in Carbon Black and Carbon Nanotube Filled Epoxy Polymers, Journal of Materials Science 46(3) (2010) 659-669. https://doi.org/10.1007/s10853-010-4788-6
[233] R. Li, et al., Interlaminar Shear Reinforcement of Aerospace Laminates with Radially-Aligned Carbon Nanotubes, (2018). https://doi.org/10.2514/6.2018-0907
[234] Hexcel Composites, Hextow™ As4c Carbon Fiber, Data Sheet (2009).
[235] Hexcel Composites, Hextow™ As4 Carbon Fiber, Data Sheet (2009).
[236] Saint-Gobain Quartz, Quartzel® Fused Quartz Textiles, 2007, p. 24.
[237] Hexion, Technical Data Bulletin: Epon™ Resin 828, 2005.
[238] Gurit, Prime™ 20ulv Ultra Low Viscosity Epoxy Infusion System.
[239] F.C. Technology, Technical Data: Epoxy Resin L 20, (2010).
[240] K.H. Hung, et al., Growth of Carbon Nanofibers on Carbon Fabric with Ni Nanocatalyst Prepared Using Pulse Electrodeposition, Nanotechnology 19(29) (2008) 295602. https://doi.org/10.1088/0957-4484/19/29/295602
[241] B.O. Boskovic, et al., Low Temperature Synthesis of Carbon Nanofibres on Carbon Fibre Matrices, Carbon 43(13) (2005) 2643-2648. https://doi.org/10.1016/j.carbon.2005.04.034
[242] K.H. Hung, et al., Processing and Tensile Characterization of Composites Composed of Carbon Nanotube-Grown Carbon Fibers, Composites Part A: Applied Science and Manufacturing 40(8) (2009) 1299-1304. https://doi.org/10.1016/j.compositesa.2009.06.002

[243] K.J. Kim, et al., Degradation and Healing Mechanisms of Carbon Fibers During the Catalytic Growth of Carbon Nanotubes on Their Surfaces, ACS Appl Mater Interfaces 4(4) (2012) 2250-8. https://doi.org/10.1021/am3002499
[244] H. Qian, Carbon Nanotube Grafted Fibres: A Route to Advanced Hierarchical Composites, Department of Chemistry, Imperial College London, 2009.
[245] D.B. Anthony, et al., Applying a Potential Difference to Minimise Damage to Carbon Fibres During Carbon Nanotube Grafting by Chemical Vapour Deposition, Nanotechnology 28(30) (2017) 305602. https://doi.org/10.1088/1361-6528/aa783f
[246] K.K.C. Ho, et al., Wet Impregnation as Route to Unidirectional Carbon Fibre Reinforced Thermoplastic Composites Manufacturing, Plastics, Rubber and Composites 40(2) (2013) 100-107. https://doi.org/10.1179/174328911x12988622801098
[247] K.K.C. Ho, et al., Continuous Atmospheric Plasma Fluorination of Carbon Fibres, Composites Part A: Applied Science and Manufacturing 39(2) (2008) 364-373. https://doi.org/10.1016/j.compositesa.2007.10.008
[248] S.A. Steiner, 3rd, et al., Circumventing the Mechanochemical Origins of Strength Loss in the Synthesis of Hierarchical Carbon Fibers, ACS Appl Mater Interfaces 5(11) (2013) 4892-903. https://doi.org/10.1021/am4006385
[249] J.I. Goldstein, et al., Scanning Electron Microscopy and X-Ray Microanalysis, 2003.
[250] M.S. Dresselhaus, et al., Raman Spectroscopy of Carbon Nanotubes, Physics Reports 409(2) (2005) 47-99. https://doi.org/10.1016/j.physrep.2004.10.006
[251] A. Bismarck, et al., Influence of Oxygen Plasma Treatment of Pan-Based Carbon Fibers on Their Electrokinetic and Wetting Properties, J Colloid Interface Sci 210(1) (1999) 60-72. https://doi.org/10.1006/jcis.1998.5912
[252] S. Wu, Polymer Interface and Adhesion, 2017.
[253] A. Bismarck, et al., Surface Characterization of Glass Fibers Made from Silicate Waste: Zeta-Potential and Contact Angle Measurements, Journal of Materials Science 39(2) (2004) 401-412.
[254] B.S. Institution, Carbon Fibre – Determination of the Tensile Properties of Single-Filament Specimens, BS ISO, 11566, 1996, pp. 1-5.
[255] A. international, Astm D3039 / D3039m-17, Standard Test Method for Tensile Properties of Polymer Matrix Composite Materials, 2017. www.astm.org
[256] C.R. Ramirez-Jimenez, et al., Identification of Failure Modes in Glass/Polypropylene Composites by Means of the Primary Frequency Content of the Acoustic Emission Event, Compos Sci Technol 64(12) (2004) 1819-1827. https://doi.org/10.1016/j.compscitech.2004.01.008
[257] A. international, Astm D2344 / D2344m-16, Standard Test Method for Short-Beam Strength of Polymer Matrix Composite Materials and Their Laminates,, (2016). https://doi.org/10.1520/D2344_D2344M-16
[258] S. Feih, et al., Strength Degradation of Glass Fibers at High Temperatures, Journal of Materials Science 44(2) (2009) 392-400. https://doi.org/10.1007/s10853-008-3140-x
[259] R. Guzman de Villoria, et al., Continuous High-Yield Production of Vertically Aligned Carbon Nanotubes on 2d and 3d Substrates, ACS Nano 5(6) (2011) 4850-7. https://doi.org/10.1021/nn2008645
[260] H. Qian, et al., Synthesis and Characterisation of Carbon Nanotubes Grown on Silica Fibres by Injection Cvd, Carbon 48(1) (2010) 277-286. https://doi.org/10.1016/j.carbon.2009.09.029
[261] M. Bedewy, et al., Population Growth Dynamics of Carbon Nanotubes, ACS Nano 5(11) (2011) 8974-89. https://doi.org/10.1021/nn203144f
[262] M. Xu, et al., Alignment Control of Carbon Nanotube Forest from Random to Nearly Perfectly Aligned by Utilizing the Crowding Effect, ACS Nano 6(7) (2012) 5837-44. https://doi.org/10.1021/nn300142j
[263] D.-H. Kuo, M.-Y. Su, The Effects of Hydrogen and Temperature on the Growth and Microstructure of Carbon Nanotubes Obtained by the Fe(Co)5 Gas-Phase-Catalytic Chemical

Vapor Deposition, Surface and Coatings Technology 201(22-23) (2007) 9172-9178. https://doi.org/10.1016/j.surfcoat.2007.04.083
[264] Y. Murakami, et al., Growth of Vertically Aligned Single-Walled Carbon Nanotube Films on Quartz Substrates and Their Optical Anisotropy, Chemical Physics Letters 385(3-4) (2004) 298-303. https://doi.org/10.1016/j.cplett.2003.12.095
[265] P. Fernberg, et al., Piezoresistive Performance of Long-Fiber Composites with Carbon Nanotube Doped Matrix, Journal of Intelligent Material Systems and Structures 20(9) (2008) 1017-1023. https://doi.org/10.1177/1045389x08097387
[266] M.H.G. Wichmann, et al., Glass-Fibre-Reinforced Composites with Enhanced Mechanical and Electrical Properties – Benefits and Limitations of a Nanoparticle Modified Matrix, Engineering Fracture Mechanics 73(16) (2006) 2346-2359. https://doi.org/10.1016/j.engfracmech.2006.05.015
[267] A. Baltopoulos, et al., Exploiting Carbon Nanotube Networks for Damage Assessment of Fiber Reinforced Composites, Composites Part B: Engineering 76 (2015) 149-158. https://doi.org/10.1016/j.compositesb.2015.02.022
[268] J. Sumfleth, et al., A Comparative Study of the Electrical and Mechanical Properties of Epoxy Nanocomposites Reinforced by Cvd- and Arc-Grown Multi-Wall Carbon Nanotubes, Compos Sci Technol 70(1) (2010) 173-180. https://doi.org/10.1016/j.compscitech.2009.10.007
[269] B.L. Wardle, et al., Fabrication and Characterization of Ultrahigh-Volume- Fraction Aligned Carbon Nanotube-Polymer Composites, Adv Mater 20(14) (2008) 2707-14. https://doi.org/10.1002/adma.200800295
[270] T. Prasse, et al., A Comparative Investigation of Electrical Resistance and Acoustic Emission During Cyclic Loading of Cfrp Laminates, Compos Sci Technol 61(6) (2001) 831-835. https://doi.org/10.1016/s0266-3538(00)00179-2
[271] F. Dahmene, et al., Acoustic Emission of Composites Structures: Story, Success, and Challenges, Physics Procedia 70 (2015) 599-603. https://doi.org/10.1016/j.phpro.2015.08.031
[272] R. Gutkin, et al., On Acoustic Emission for Failure Investigation in Cfrp: Pattern Recognition and Peak Frequency Analyses, Mechanical Systems and Signal Processing 25(4) (2011) 1393-1407. https://doi.org/10.1016/j.ymssp.2010.11.014
[273] A.E. Goode, et al., High Resolution and Dynamic Imaging of Biopersistence and Bioreactivity of Extra and Intracellular Mwnts Exposed to Microglial Cells, Biomaterials 70 (2015) 57-70. https://doi.org/10.1016/j.biomaterials.2015.08.019
[274] R. Plonka, et al., Adhesion of Epoxy/Glass Fibre Composites Influenced by Aging Effects on Sizings, Composites Part A: Applied Science and Manufacturing 35(10) (2004) 1207-1216. https://doi.org/10.1016/j.compositesa.2004.03.005
[275] S. Erden, et al., Continuous Atmospheric Plasma Oxidation of Carbon Fibres: Influence on the Fibre Surface and Bulk Properties and Adhesion to Polyamide 12, Plasma Chem. Plasma P. 30(4) (2010) 471-487.
[276] A. Magrez, et al., Catalytic Cvd Synthesis of Carbon Nanotubes: Towards High Yield and Low Temperature Growth, Materials 3(11) (2010) 4871-4891. https://doi.org/10.3390/ma3114871
[277] D.B.A. Jian Wang, Carlos A. Fuentes, Hugo G. De Luca, Dongxing Zhang, Alexander Bismarck, Aart Willem Van Vuure, Milo S.P. Shaffer, David Seveno, Wettability of Carbon Nanotube-Grafted Carbon Fibers and Their Interfacial Properties in Polypropylene Thermoplastic Composite, 2021.
[278] W. Szmyt, et al., Protective Effect of Ultrathin Alumina Film against Diffusion of Iron into Carbon Fiber During Growth of Carbon Nanotubes for Hierarchical Composites Investigated by Ptychographic X-Ray Computed Tomography, Carbon 115 (2017) 347-362. https://doi.org/10.1016/j.carbon.2016.12.085